Photonic discrimination and specific targeting of vascular stem cells.

A dissertation submitted for the degree of PhD

by Claire Molony BSc.

Under the supervision of

Prof. Paul A. Cahill

October 2017

Vascular Biology & Therapeutics Lab

School of Biotechnology

Faculty of Science and Healthy

Dublin City University, Dublin 9, Ireland

Declaration

I hereby certify that this material, which I now submit for assessment on the programme of study leading to the award of PhD is entirely my own work, and that I have exercised reasonable care to ensure that the work is original, and does not to the best of my knowledge breach any law of copyright, and has not been taken from the work of others save and to the extent that such work has been cited and acknowledged within the text of my work.

Signed:_____

I.D. No: 59308636

Date:_____

Dedication

This thesis is dedicated to my parents.

For Terri Molony who taught me that *'everything is impossible until it isn't'* and Jack Molony who reminded me that *'one of the most important things to have in life is choice'.*

Acknowledgements

First and foremost, I would like to express my gratitude to Professor Paul Cahill for the opportunity to work in his lab and carry out this work. I would also like to acknowledge him for going above and beyond the call of any supervisor in providing constant encouragement and support throughout this whole process.

Next, I would like to thank the members of the VBT lab past and present. In particular, Joseph Mackle, Dorota Kozlowska, Abi Olayinkai, Emma Fitzpatrick, Eimear Kennedy and Roya Hakimjavadi (along with Paul Cahill) for teaching me almost everything I know. To my colleague Roa Bashmail who has been with me since the start, thanks for always making me smile. Thanks to Gillian Casey, who was there for a good time but not a long time! Thank you to Mariana Di Luca for always helping whenever you can, even if its just a listening ear. To the newbies Eoin Corcoran, Denise Burtenshaw and Yusof Gusti I wish you the best of luck in your own projects and thank you for your patience with me while I finished up! I hope we will all work together again in the future.

I would also like to thank the many collaborators who helped to make this research possible, especially Bryan Hennelly, Jennifer McIntyre, Hugh Byrne, Damien King, Albina Julius and Eileen Redmond. It was a pleasure working with you all.

I would like to acknowledge the Biological Research Society and all of its members, past and present, who made the last 4 years eventful to say the least! Especially Kim Connick, Niamh Hunt, Gillian Casey and Denise Burtenshaw who have been my colleagues, committee panel, team mates and will hopefully be life-long friends.

Finally, I would like to thank my parents again, for working so hard their whole lives to provide me with the opportunity to pursue my education. To my sisters, Karen and Jenni, for being my role models who I will always look up to and to Carrie McMeel and Aaron Dolan for being so understanding and supportive, especially over the last few months.

Table of Contents:

List of figures

List of tables

Abbreviations

1-Aza	1-Azakenpaullone
AF	Auto-fluorescence
APS	Ammonium per sulfate
Bio	(2'Z,3'E)-6-Bromoindirubin-3′-oxime
BCA	BSA
BSA	Bovine Serum Albumin
CNN1	Calponin1
CVD	Cardiovascular Disease
DAPI	4,6-diamidino-2-phenylindole
FTIR	Fourier Transfer Infrared
dSMC	differentiated SMC
ddSMC	de-differentiated SMC
DEPC	Diethylpyrocarbonate
DES	Drug eluting stent
DLS	Dynamic Light Scattering
DMEM	Dulbecco's Modified Essential Medium
DMSO	Dimethylsulfoxide
DNA	Deoxyribose Nucleic Acid
EDTA	Ethylenediamine Tetracetic Acid
EMEM	Eagle's Minimum Essential Medium
FBS	Fetal Bovine Serum
GFP	Green Fluorescent Protein
GSK	Glycogen Synthase Kinase
Hes	Hairy enhancer of split
Hey	Hairy enhanced of split related with YRPW motif
HPLC	High Performance Liquid Chromatography
HRP	Horseradish Peroxidase
ICC	Immunocytochemistry
Jag-1	Jagged-1

NICD	Notch Intracellular Domain
mAb	Monoclonal antibody
MNP	Magnetic Nanoparticle
Myh11	Myosin heavy chain 11
MSC	Mesenchymal Stem Cell
MVSC	Multipotent Vascular Stem Cell
PBS	Phosphate Buffered Saline
PLGA	Poly(D,L-lactide-co-glycolide)
PVA	Polyvinyl Alcohol
RNA	Ribonucleic Acid
RIPA	Radioimmunoprecipitation Assay
RT-PCR	Reverse Transcriptase PCR
SDS	Sodium Dodecyl Sulphate
SEM	Scanning Electron Microscopy
siRNA	small interfering RNA
SMC	Smooth Muscle Cell
αSMA	Smooth Muscle alpha Actin
SM22α	Transgelin 2
St-Osteo	Stem Cell derived Osteocyte
St-SMC	Stem Cell derived Smooth Muscle Cell
TEM	Transmission Electron Microscopy
TGF-β_1	Transforming Growth Factor beta
vSMC	vascular Smooth Muscle Cell

Units

℃ degrees celcius
µg microgram
µl microliter
µm micrometer
µM micromoles
AU arbitrary unit
AF unit of autofluorescence
cm centimetres
d days
g grams
H Hours
kDa Kilo Dalton
M Molar
mg milligram
Min Minute
ml millilitre
mV millivolt
ng nanogram
nm nanometer
RPM revolutions per minute
s second
x g G force

Presentations: Poster

Molony, C., Di Luca, M., McIntyre, J., Hennelly, B., Byrne, H., Cahill, P.A. (2016) Vibrational spectroscopy discriminates differentiated vascular smooth muscle cells from mesenchymal stem cells and their vascular progeny. ATVB Meeting, May 2016, Nashville, Tennessee.

Presentations: Oral

Molony, C., Cahill, PA. (2016). Cellular Footprints: Discriminating cells using spectroscopy. Research day, January, School of Biotechnology, Dublin City University, Dublin, Ireland.

Molony. C., Cahill, PA, (2015) Second generation therapeutics for drug-eluting stents. Transfer to PhD, August 2015, Dublin City University, Dublin, Ireland.

Molony, C., Cahill, PA (2015) The generation of GSK3βi-loaded-PLGA-MNPs. Research Day, January, School of Biotechnology, Dublin City University, Dublin, Ireland.

Manuscripts:

Molony, C., McIntyre, J., Hakimjavadi, R., Burtenshaw, D., Di Luca, M., Casey, G., Maguire. A, Hennelly, B., Byrne, H., Cahill, PA. (2017) Label-free discrimination analysis of de-differentiated vascular smooth muscle cells, mesenchymal stem cells and their vascular and osteogenic progeny using vibrational spectroscopy. *BBA.* (in press)

Molony, C., King, D., Julius A., Fitzpatrick E., Di Luca, M., Casey, G., Kernan, D., Redmond, E., Ducree, J., Cahill, PA. Photonic detection and discrimination of vascular cells. (In preparation).

Abstract

Photonic discrimination and specific targeting of vascular stem cells.
Claire Molony

Cardiovascular disease remains the leading cause of death and disability world-wide. The current treatment options include balloon angioplasty and the deployment of drug-eluting stents (DES) coated with anti-mitotic drugs to prevent intimal-medial thickening (IMT). Despite this, an unacceptably high failure rate remains due to non-specific targeting of cells and drug-depletion over time. The source of the cells contributing to IMT remains controversial; one theory suggests a reprogramming of native differentiated vascular smooth muscle cells (SMC) while the other proposes myogenic differentiation of resident vascular and/or circulating stem cells. Resolution of this controversy through identification of the source of the contributing cells would greatly assist in the development of future drug targeting strategies using novel DES platforms.

The use of photonics and vibrational spectroscopy is gaining popularity for disease diagnosis. Both platforms have the ability to yield cellular and molecular information about cells and tissues label-free, making them attractive technologies for analysing biological specimen. The first main objective of this work was to analyse individual cells from normal (healthy) and arteriosclerotic (diseased) vessels *ex vivo* using autofluorescence (AF) in response to broadband light and to compare their AF signatures to undifferentiated stem cells and their myogenic progeny *in vitro.* The second aim was to use vibrational spectroscopy (Raman and FTIR) to examine undifferentiated stem cells, their myogenic and osteogenic progeny and and further compare their spectra to re-programmed differentiated SMC.

Finally, a novel therapeutic platform for targeting stem cell-derived myogenic progeny using magnetic nanoparticles was developed. Using pharmacological inhibitors of glycogen synthase 3 beta (GSK3β), the effects on Notch, a well known mediator of myogenic differentiation were first evaluated *in vitro.* Further to this, a prototype GSK3β inhibitor was incorporated into a novel drug delivery system consisting of polymer coated Fe_30_4 magnetic nanoparticles which can be systemically administered and specifically targeted to bare-metal stents by an external magnetic field.

Chapter 1

General Introduction

1.1.1 Cardiovascular Disease Statistics

According to the World Health Organisation (WHO), cardiovascular disease (CVD) is the leading cause of death globally (WHO., 2017). One CVD related death is reported every 40 seconds in America. (Benjamin et al., 2017). In Europe, CVD accounts for 47% of all deaths (Nichols et al., 2014). CVD is not only detrimental to the health of the world's populations, it also has a significant societal impact on national healthcare budgets. The total number of cardiovascular related operations in the U.S. increased by 28% from 2000 to 2010 with the total cost of CVD related treatments increasing to $321.6 billion (Go et al., 2013). The incidence of CVD diagnosis and mortality is set to rise significantly and it is estimated that by 2030, 23.6 million people will die a year from CVD (WHO, 2017). Faced with statistics such as these, it is imperative solutions are found for this global dilemma.

1.1.2 The Vasculature

The cardiovascular system is a complex system consisting of the heart i.e the pump and an array of connected tubes with various functions. The efferent tubes (vessels) consist of the arteries and arterioles that deliver nutrients and oxygen to the capillaries that can transport the materials to surrounding tissue. The afferent vessels consist of the veins and venules that transport the waste products from the surrounding tissue back to the heart.

The average adult artery consists of three general layers, the intimal layer, the medial layer and the adventitia (Lilly et al., 2012).

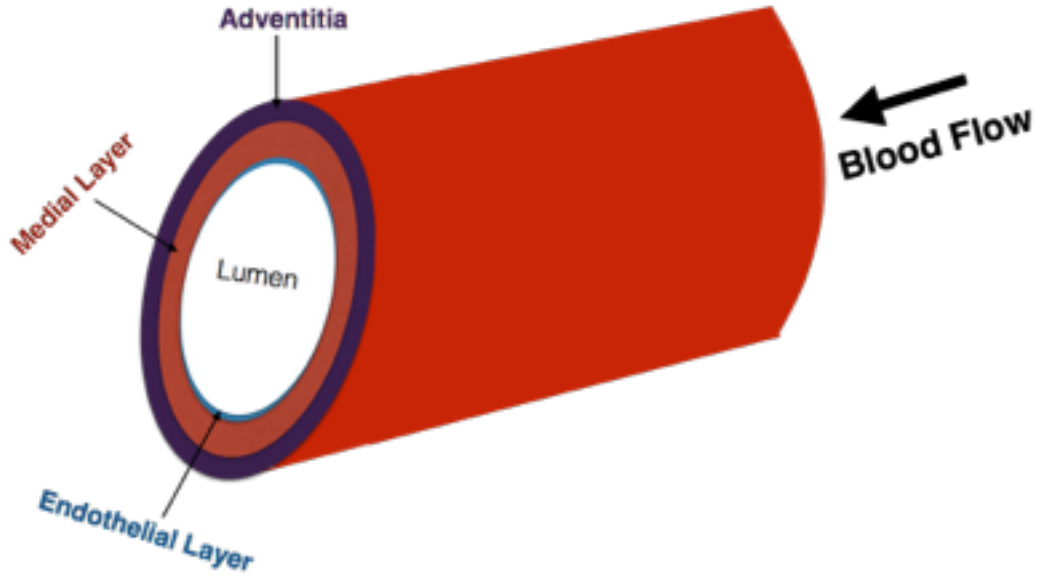

Figure 1.1 Basic Arterial Structure. The structure of a regular healthy artery with the three forming layers. The innermost endothelial layer (blue), the middle 'medial layer' containing SMC/stem cells (red) and the outermost adventitial layer containing fibroblasts/stem cells (purple). The lumen space inside the arterial layers is wide for regular blood flow.

The intimal layer, which is the innermost layer of the artery, consists of a wall of endothelial cells one cell thick in most rodents (Alberts et al. 2002). The endothelial layer is the initial layer formed during development (Grittenberger-De-Groot et al. 1998). In humans, the endothelial or intimal layer thickens normally with age and is composed of extracellular matrix proteins, α-actin^{+} smooth muscle-like cells and proteoglycans. Excessive intimal thickening in human coronary arteries before intimal lipid depositions is now considered the initiation of coronary atherosclerosis (Subbotin et al., 2016). Nakashima et al., performed the most detailed analysis of normal human vessels and demonstrated that (i) the normal adult coronary tunica intima is thicker than the tunica media; and (ii) the tunica intima comprises numerous cell layers of α-actin^{+} smooth muscle-like cells which are arranged in dense manner and comprise two-thirds of the intimal thickness. The cell layer density progressively increases toward the internal elastic lamina (Nakashima et al., 2002).

The primary function of the intimal endothelial cell lining the internal elastic lamina is to regulate vascular tone through modulation of the

underlying medial vascular smooth muscle layer and the expansion and contraction of the blood vessel to accommodate blood flow. The endothelial cells in response to various factors such as shear stress or metabolic conditions produce a host of vasoactive molecules, including nitric oxide, endothelin, prostacyclin and other prostanoids which act as a relaxation/contraction factors to control vascular one and maintain homeostasis. Nitric oxide diffuses onto the vascular smooth muscle cells (vSMCs) in the medial layer stimulating the production of guanylate cyclase to generate cyclic GMP which decreases the intracellular calcium, relaxing the vSMCs and subsequently widening the artery (Lilly et al., 2012).

The medial layer, which as the name suggests is the middle layer, is composed of a high concentration of vSMCs (Karrer et al., 1961) and a small population of resident multipotent vascular stem cells (MVSCs) (Tang et al., 2012). During development, the mesoderm begins to acquire vascular smooth muscle cell markers; firstly, α-actin (SMA, ACTA2) and later SMC markers such as transgelin (SM-22α), calponin1 (CNN1) and smooth muscle myosin heavy chain 11 (Myh11) (Gittenberger-De-Groot, 1998). A heterogeneous population of vSMCs in the medial layer has been widely reported (Gittenberger-De-Groot, 1998; Rensen et al., 2008; Shanahan & Weissberg, 1998). Many of these reports purport that these vSMC subpopulations undergo phenotypic switching (or re-reprogramming) from contractile to synthetic phenotypes in response to certain physiological/pathophysiological stimuli where vSMCs go from resident vascular tone ‘regulators’ to migratory ‘pro-proliferative’ cells that accumulate within the expanding medial and intimal layers (Li et al. 1999). In addition, a small population of resident vascular stem cells (MVSCs) have been identified in the medial layer however the precise function of these cells remains controversial (Tang et al., 2012, Huang et al., 2015).

Finally, the outer adventitial layer is made up of connective tissue, fibroblasts and a small niche of resident vascular stem cells; adventitial

Sca1+ progenitor stem cells (APCs). The adventitia has many functions including facilitation of crosstalk between endothelial cells and smooth muscle cells, controlling the movement of cells in and out of individual layers and facilitating microvessel formation that permeate the vessel wall (Majesky et al., 2011).

1.1.3 Vascular Disease

CVD manifests itself as an obstruction within the blood vessel wall that restricts normal blood flow. This puts a mechanical strain on the heart and causes high blood pressure i.e. hypertension, that can lead to more serious conditions such as stroke or heart failure (Hollander et al., 1976).

Atherosclerosis accounts for 75% of cardiovascular related deaths. The initial step in atherosclerosis is intimal medial thickening (IMT) that occurs throughout ageing but, if exaggerated, facilitates the build-up of LDL (low density lipoprotein) particles within the intimal layer of the vessel wall (Sun et al., 2000, Subbotin et al., 2016). LDL are proteins that transport and deposit cholesterol around the body (Insull et al., 2009). High LDL concentrations can be attributed to various risk factors such as diet, abdominal obesity, metabolic syndromes e.g. hyperglyceredaemia and chemical toxins e.g. nicotine all of which are related to each other and can be reduced by ceasing smoking, eating more plant based foods and exercising regularly (Reddy et al., 2010). The build-up of the LDL-particles activates the endothelial cells which in turn activate the vSMCs. The activated endothelial and vSMCs then recruit inflammatory cells such as leukocytes, monocytes and neutrophils to the arterial wall progressing the next major step in intimal thickening (Insull et al., 2009). The monocytes are subsequently activated in the sub-endothelial space where they are encouraged to present receptors on their surface that initiate the digestion of oxidised lipids which stimulates the transition from activated monocyte cells to macrophage foam cells.

The macrophage foam cells undergo apoptosis and their debris forms most of the lipid rich plaque which promotes further inflammation, therefore more inflammatory cells are recruited to the site and additional formation of macrophage foam cells. Vascular SMC-like cells accumulate and constitute up to 90% of the neointimal lesion. The vSMCs then synthesise a collagen-rich extracellular-matrix that forms the fibrous cap of the lipid plaque, providing structure and stability (Hunt et al., 2002). The lipid plaque and collagen rich fibrous cap is highly thrombogenic and may rupture causing a clotting cascade and further occlusion of the blood vessel (Sherif et al., 2010).

In an attempt to lower the incidence of atherosclerosis, high-risk individuals are prescribed cholesterol-lowering drugs, Statins. Statins inhibit the enzyme HMG-CoA Reductase that is essential in the conversion of dietary fatty acids to cholesterol. However, atherosclerosis is a silent disease and mostly proceeds un-diagnosed until a cardiac event occurs (Yamashita et al., 2010).

The most common treatment of a vessel occlusion is balloon angioplasty and stent placement. Balloon angioplasty is minor surgery that involves inserting a balloon inside the occluded vessel at the plaque site. The balloon is then inflated to crush the plaque against the vessel wall and facilitate resumed blood flow through the artery. However, in 40% of patients, this can result in a re-occlusion of the artery due to elastic recoil (White et al., 2005). Cardiologists therefore began to insert bare metal stents during balloon angioplasty to keep the artery open after the balloon angioplasty procedure. However, even after stent placement, 25% of patients display renewed intimal medial thickening (IMT) termed ‘in-stent restenosis’ (ISR) (Dangas et al., 2002).

The pathology of ISR differs from atherosclerosis and is a form of more symmetrical internal thickening, referred to as arteriosclerosis.

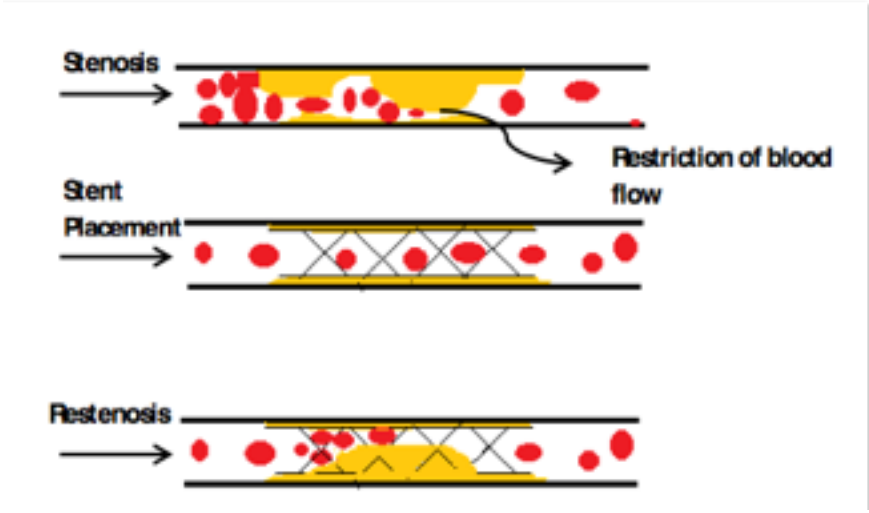

Figure 1.2 In-Stent Restenosis. Represents the original occlusion of the artery, the mechanism for combating this occlusion with a stent and the incidence of re-occlusion at the site of stent placement.

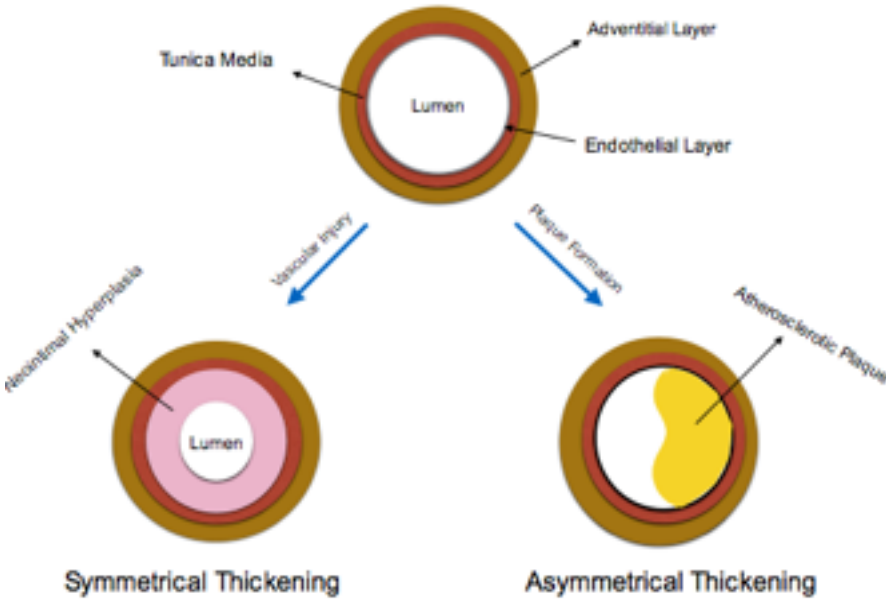

Figure 1.3 Arteriosclerosis & Atherosclerosis: Cross sections of a healthy artery with a wide lumen area with a normal medial size; symmetrical thickening of the medial layer and neointima formation leading to a luminal reduction of an arteriosclerotic artery; and the asymmetrical thickening and subsequent loss of luminal layer due to plaque build up of atherosclerotic artery.

There are four main mechanisms reported to be involved in restenosis, particularly ISR. The first mechanism is vasoconstriction of the vessel due

to endothelial disruption from e.g., a stent placement. This occurs within 24 hours and results in initial narrowing of the artery. The second step is the activation of local platelets and secretion of thrombin, forming a mural thrombus. This response occurs 2-3 weeks after stent placement. The third mechanism, and possibly the most important, is the formation of a neointimal lesion. This occurs from 48 hours to months after the stent placement (Kibos et al., 2007). Schiele et al., reported that the number of cells representing α-actin in the neointima increased from day 7 to day 30 to 98% (Schiele et al., 2005) suggesting that the majority of cells forming the neointima are vSMCs-like cells and their associated matrix (Schiele et al., 2005). The fourth mechanism of restenosis is vascular remodelling. This is the change in the arterial wall size due to the first 3 mechanisms.

1.1.4 The source of neointimal SMCs…the central dogma

As mentioned above, up to 98% of the cells that present in the restenotic lesion are primarily vascular smooth muscle-like cells (Schiele et al., 2005). Originally, it was purported by many investigators that these neointimal SMC-like cells originated from differentiated SMCs that switched phenotype to become de-differentiated and began proliferating/ migrating to the site of injury to form the neointima. Subsequent lineage tracing studies have provided further compelling evidence in support of SMC switching and re-programming by demonstrating that neointimal SMCs (Nemenoff et al., 2011; Herring et al., 2014; Shankman et al., 2015) and a considerable number of neointimal macrophage-like cells (Shankman et al., 2015) may be derived from ‘marked’ medial differentiated SMC *in vivo* (Cherepanova et al., 2016; Shankman et al., 2015; Majesky et al., 2016; Chappell et al., 2016). Furthermore, it appears not all ‘marked’ differentiated SMCs are responsible but rather there exists a discrete subpopulation of ‘plastic’ medial SMCs (Chappell et al., 2016). Moreover, epigenetic modifications indicative of SMC lineage identity at the Myh11 locus (H3K4me2:histone 3 lysine 4 dimethylation) are retained in de-differentiated SMCs that are no longer

transcriptionally active. These signatures have been used to further suggest that neointimal SMCs and macrophage-like cells are derived from differentiated SMCs *in vivo* (Gomez et al., 2015; Shankman et al., 2015).

However, several recent reports have challenged this idea of SMC phenotypic switching and re-programming by demonstrating the presence of stem cell markers within rodent and human vascular lesions, and the isolation and characterisation of these cells as multipotent mesenchymal stem like cells *in vitro* (Torsney et al., 2011; Hu et al., 2004). The putative role of the resident vascular stem cells undergoing myogenic differentiation and contributing to the neointimal lesion has been evaluated by several research groups. Circulating and resident mesenchymal stem-like cells have been reviewed for their contribution to lesion formation and calcification (Klein, 2016). MSC-like $CD44^+$, $CD90^+$ and $CD105^+$ cells have been isolated from the wall of the thoracic aorta raising the possibility of MSCs driving vascular remodelling and triggering calcification (Klein et al., 2011). To demonstrate the presence of circulating bone marrow MSCs (bm-MSCs) in the neointima, Sata et al., transplanted the bone marrow from ROSA26 mice expressing β-galactosidase (LacZ) to control mice and reported that 63% of the neointimal cells were LacZ positive indicating they were derived from the bm-MSCs (Sata et al., 2002). Double staining further showed that the $LacZ^+$ cells in the neointima were also either α-actin or CD31 positive which would suggest that the bm-MSCs differentiated to SMCs or endothelial cells following injury (Sata et al., 2002). While the contribution of bone-marrow derived stem cells has since been clarified (Hoglund et al., 2010), the origin of neointimal SMC-like cells stills remains contentious and incompletely understood.

A controversial *Nature Communications* paper was published by Song Li's group in 2012 wherein they challenged the role of de-differentiated

vSMCs and concluded that the data were misinterpreted and an overstatement of differentiated vSMC function (Tang et al., 2012). The researchers identified a small niche of multipotent resident vascular stem cells (MVSCs) within the medial layer of the adult rat, mouse and human arteries that were Myh11 and CNN1 negative but positive for stem cell markers S100β, Sox17 and Sox10. Parallel lineage tracing analysis provided further evidence that neointimal SMC-like cells were derived from this Myh11 negative population. They further argued that previous studies provided no direct evidence for de-differentiation/re-programming of vSMCs to conclude that the proliferating neointimal vSMCs originated from a native SMC source (Tang et al., 2012).

Subsequent lineage tracing studies here too have provided important evidence that a significant subset, if not the majority of neointimal SMC-like cells may be derived from medial resident stem cells (Tang et al., 2012; Wan et al., 2012), adventitial stem cells (Shikatani et al., 2016; Kramann et al., 2016; Kramann et al.,2015) and mesenchymal stem cells (EndMT)(Cooley et al, 2014) following (EndoMT) using various models of vascular injury in mice. Indeed, follow-up lineage tracing studies by Song Li's group that mapped $Sox10^{+}$ cells following injury clarified the presence of neointimal SMC-like cells derived from a parent $Sox10^{+}$ population in addition to cells from a $Myh11^{+}$ population (Yuan et al., 2017).

Importantly, drivers of myogenic differentiation are commonly found in neointimal lesions (Majesky et al. 1991; Kanzaki et al. 1995; Otsuka et al. 2006; Tsai et al. 2009; Liao et al. 2016; Sakata et al. 2004; Gridley et al. 2010; Caolo et al. 2011). For example, transforming growth factor beta (TGF-β_1) has repeatedly been implicated with neo/intimal lesion progression (Majesky et al. 1991; Kanzaki et al. 1995; Otsuka et al. 2006; Tsai et al. 2009; Liao et al. 2016). In addition, TGF-β_1 has been associated with various stem cells undergoing myogenic differentiation. Specifically, TGF-β isoforms (TGF-β_1, TGF-β_2 and TGF-β_3) contribute to

myogenic differentiation of embryonic stem cells (Wang et al., 2015), C3H T10 1/2 cells (Guo & Wang, 2009), mesenchymal stem cells (Kurpinski et al. 2010), multipoint vascular stem cells (MVSCs) (Tang et al. 2012) and endothelial derived MSCs (EndoMT) (Chen et al. 2015; Evrard et al. 2016; Zeisberg et al. 2007) *in vitro.* Gene expression analysis studies of TGF-β_1 stimulated stem cells revealed another smooth muscle associated molecule commonly found in lesions, Jagged-1 (Jag-1). Jag-1 is one of many Notch ligands associated with coronary artery disease (CAD) models (Sakata et al., 2004; Gridley et al., 2010; Caolo et al., 2011). Stimulation of Notch in embryonic stem cells (Kurpinski et al., 2010), mesenchymal stem cells (Doi et al., 2006; Kurpinski et al., 2010, Mooney et al., 2015), neural crest stem cells (High et al. 2007), endothelial derived MSCs (Chang et al., 2011) and multipotent vascular stem cells (Tang et al.,2012) promotes myogenic differentiation. The presence of drivers of myogenic differentiation within neointimal lesions further supports the evidence of stem cells as the major source of the SMC-like cells in injured/arteriosclerotic vessels and provides a new therapeutic platform when considering the rate of restenosis after vascular ballooning and stenting.

Overall, excessive intimal hyperplasia in human coronary arteries before intimal lipid depositions is considered the initial event leading to coronary atherosclerosis (Subbotin et al., 2016). The evidence supporting a role for resident vascular stem cell(s) contributing to intimal hyperplasia is growing, however the subject still remains controversial (Tang et al., 2012). Therefore, classification and characterisation of these cells is vital before determining the best treatment option to target restenosis after vascular ballooning and stenting.

1.2 Photonics for disease diagnosis

The use of light to assess health and treat disease has become increasingly popular over the last number of years. In as early as 1903, Niels Finsen won the Nobel Prize in Physiology and Medicine for his use of ultraviolet (UV) light to treat lupus vulgars. The direction of photonics in medicine has more recently focused on the diagnostic power rather than healing power of this technology. To understand how it can be used to characterise biological samples and diagnose disease, it is important to note the fundamentals of light interactions with a material. The interaction of light with matter, such as tissue, can result in a scattering or absorption of that light. When a sample interrupts the direct path of light and alters it to produce scattered light, the states of scattering can be recored and mapped to give discrete information about that sample. On the other hand, when light is absorbed by the sample, the energy from the photons changes to vibrational or electronic energy and can result in inelastic scattering or accoustomechanical waves which can be recorded to yield physical, biochemical and molecular information about a sample (Yun & Kwok., 2017). In this section, two methods of light scattering, auto-fluorescence and Raman spectroscopy, and one method of light absorption, Fourier-transform infrared spectroscopy, will be described in the context of characterising biological samples and disease.

1.2.1 The LiPhos Project

LiPhos (living photonics) is a project involving microfluidic technologies and auto-fluorescent signalling. It relies on the principles of elastic light scattering, which is also the basis of the well-known flow cytometry technique. The elastic scattering of light from a cell depends on the size, shape, morphology and refractive index of the cell from the surrounding medium. The project utilises microfluidic systems to capture single cells before exposure to broadband light to generate auto-fluorescence signatures and patterns for individual cell populations. Using this technique, the cell is subjected to a single laser beam only, and the

measurement of the scattering from that cell is recorded, without the interference from any other cell or laser beam. The resulting scattered light is interpreted through mathematical models such as the Muller matrix, T-matrix or the Finite-Difference Time-Domain (FDTD) method to provide information on the characteristics of that cell (Kinunnan et al., 2015). Several studies have already been carried out utilising the elastic light scattering technique (ELS) to characterise cells label-free. ELS has been shown to enhance Raman signals (outlined later in this section) and the combination of the two techniques have been used to compare and characterise lymphocytes and granulocytes (Watson et al., 2004). Red blood cells undergoing heamolysis have also been studied and changes in refractive index were noted between cell samples (Popescu et al., 2005).

1.2.2 Autofluorescence Imaging for disease diagnosis

To date, label-free autofluorescence (AF) readings are not a widely used method to diagnose disease. In fact, there are only two main applications for label-free autofluorescence readings in the area of disease diagnosis in the literature. The first is for identifying changes in fluorophores in the fundus of the eye to identify ocular diseases or degradation. In this case, confocal scanning lasers are used with broadband emission wavelengths and alterations in the eye in response to disease can be detected. For example, alterations in the retinal pigment epithelium or alterations in the blood vessels of the eye have been reported (Fleckenstein et al., 2010). The other clinical application of autofluorescence spectra for disease diagnosis are skin autofluorescence readings (SAF). SAF exploits the accumulation of advanced glycation end products and collagen, which are novel risk factors of CVD and chronic kidney disease (CKD), particularly in skin biopsies. It has been widely reported that elevated skin autofluorescence is associated with atherosclerosis and also to be a predictor of a serious cardiac event in diabetic patients (McIntyre et al., 2011; Noordzig et al., 2012; Dekker et al., 2013; Wong et al., 2014).

At a cellular level, AF detection has been applied in the areas of cancer, neurodegeneration and stem cell differentiation models. Much of the autofluorescence cellular studies so far are based on the naturally fluorescent nicotinamide adenine dinucleotide (NADH) to study cell state metabolism. NADH is commonly known to be involved in many cellular processes such as mitochondrial function, calcium homeostasis, metabolism, ageing, oxidative stress and apoptosis. Therefore, alterations in NADH levels can be indicative of diseases such as cancer and Alzheimers disease. Researchers have taken advantage of this fluorophore and identified changes in AF readings in different cancer cell lines and alterations in AF readings based on NADH of ovarian and bladder cancer cells in response to chemotherapy. As NADH is a good indicator of mitochondrial function, it is an ideal biomarker for neurodegenerative diseases such as Alzheimers disease. Varying AF levels in senile plaques ex vivo of mice have been reported compared to healthy controls. This pattern of autofluorescence is considered a good photonic biomarker for Alzheimers disease (Heikal, 2010). There are some reports detecting changes in AF readings for stem cells following differentiation. AF readings have been shown to decrease for MSCs differentiating to osteocytes and adipocytes, increase for mESCs differentiating to embryoid bodies and mESCs to neural stem cells (Quinn et al., 2013; Rice et al., 2007; 2010; Thimm et al., 2015). As stem cells have been implicated in tumourogenesis (Miranda-Lorenzo et al., 2014) and now vascular diseases (Klein, 2016), AF analysis of stem cells and their progeny may become novel biomarkers for disease.

1.2.3 Microfluidic Systems for Single Cell Analysis

The concept of optically analysing cells in aqueous solution has been around since the 1930's leading to the development of Flow Cytometry in the 1970's. The first microfluidic device to trap biological particles for singular optical analysis was reported by Arthur Askin in the 1970's (Yun, 2013). Microfluidics has significantly advanced since then and microfluidic devices now have the potential to mix fluids, pump liquids, determine

optimal reaction conditions and even culture cells. The microfluidic devices have also been miniaturised making them easily portable and suitable for point-of-care diagnostics (Godin et al., 2008). Microfluidic devices which perform multiple operations on a single platform are known as Lab-on-a-chip (LOC) devices and can be used for a range of analytical techniques (Greiner et al., 2004). There are five common microfluidic platforms which vary mainly on their dominant fluid propulsion principle. These techniques are capillary (lateral flow), pressure, electrokinetic, acoustic driven flow and finally, the most relevant to this thesis, centrifugal microfluidics (Mark et al., 2010).

1.2.4 Methods of microfluidic transport

- **Lateral Flow**

Lateral flow devices are typically wettable test strips that contain chemicals or antibodies within to react with the sample to give a read-out. The liquid is transported via capillary action through the test-strip for detection (Mark et al.,2010).

- **Pressure Driven Laminar Flow**

The flow of liquid through micro-channels is typically laminar. Using external or internal pressure pumps, the liquid can be hydrodynamically controlled for purposes such as predictable velocity profiles, controllable diffusing mixing and stable phase arrangements. However, the necessity for internal or external pumps reduces the devices portability and automation (Mark et al.,2010).

- **Electrokinetic**

Electrokinetic systems are controlled by electric fields acting on the electrical charge of the sample which can induce several electrokinetic effects such as electroosmosis, electrophoresis and dielectrophoresis. The surface of the microchannels can be electrically charged and

charged particles in the sample can transport electrostatically to the corresponding electrode. Components of a liquid sample can thus be separated due to their electrical charge and this technique forms the basis of the commonly known capillary electrophoresis (Mark et al. 2010)

- **Surface Acoustic Waves**

The surface acoustic wave platform uses mechanical waves from piezoelectric transducer chips to exert acoustic pressure on liquids places on hydrophobic surfaces. The acoustic waves can then manipulate droplets of the liquid around the microfluidic device. The device can only be used with very small samples, in the nanoLitre range, and the chip:sample interaction is not particularly stable (Mark et al., 2010).

- **Centrifugal Microfluidics**

Centrifugal microfluidics works on the principle of centrifugal forces propelling fluid. The frequency of rotation of the microstructured substrate controls the flow of the fluid radially outwards from the inner to outer edge of the substrate. The technique of using external centrifugal forces means there is no need for pumps or electrodes within the system making the devices cheap to make and easily portable (Lindström et al., 2011).

1.2.5 Approaches for single cell capturing on a microfluidic system

The purpose of utilising microfluidic devices in research is to facilitate capture of individual cells in liquid medium on a microfluidic chip for single cell analysis. Currently, there are numerous methods for capturing single cells within microfluidic devices such as mechanical traps, micropatterning, encapsulation, magnetic trapping, optical trapping, and hydrodynamic trapping. Briefly, mechanical traps are compartments in the device such as microwells that are capable of trapping a cell within for analysis. The shape, size and number of microwells can be altered during device manufacture depending on the required experimental parameters. Micropatterning involves formulating a pattern of extracellular matrices such as fibronectin and laminin onto specific regions of the device to

promote the adhesion of adherent cells to the surface. The patterns can also be arranged in any order to suit the experiment. Encapsulation is the capture of cells in small droplets of liquid, however, controlling the amount of cells per droplet remains an issue. Magnetic trapping is a popular method of trapping cells in microfluidic devices and involves the attachment of a superparamagnetic bead with a conjugated anti-body specific to the cell within the microfluidic chamber. Passing cells bind to the conjugated antibody and are held for analysis. Optical trapping, most often optical tweezers, are optical forces generated from laser beams that attract the cell towards the focal point of the beam where it can be held or moved using the laser beams. Finally, hydrodynamic trapping – the method used in this research thesis work – involves obstacles in the device that capture cells from the fluid as the liquid transports through the chip. Cup shaped traps are most commonly used for this purpose with the size of the cup generated to capture one single cell at a time (Lindström et al., 2011).

1.2.6 Portable centrifugal microfluidic chip for single cell capture

One widely used portable device for the analysis of single cells in aqueous solution is the Lab-on a-Disc (LoaD) platform first described by Burger et al., (2015) (Burger et al., 2015). This was an adaptation of a cell culture array previously described Carol et al., (2006) (Carlo et al., 2006). The system relies on centrifugal force to manipulate cells in suspension into a microfluidic chamber which leads to an array of v shaped cups to singularly capture cells for photonic analysis. These chips are constructed of polydimethylsiloxane (PDMS) containing the pre-moulded cup arrays and microfluidic chambers bonded to PDMS coated PMMA discs. Microfluidic chips were originally constructed with glass or silicon however these substrates are expensive and are therefore unsuitable as disposable devices. Currently, PDMS, poly(methyl methacrylate) PMMA, high density polyethylene (HDPE), low density polyethylene (LDPE), polyamide 6 and SU-8 are the most commonly used polymers for

microfluidic chip fabrication. The polymeric chips are typically formulated using the 'soft-lithographic technique'. Soft-lithography is a family of fabrication techniques of micro-fluidic devices made from mechanically soft material. The soft nature of the materials means patterns, such as arrays, and chambers can be developed in the chip structure making these types of chips ideal for biomedical applications. PDMS is the most commonly used polymer for the chips due to its desirable low cost, safety and opaqueness (Friend et al., 2016).

The centrifugal microfluidic platform is ideal for blood analysis as parameters such as glucose, proteins, lipids and electrolytes identified in blood can yield information about the body. Kuo et al. (2014) used a centrifugal microfluidic platform to separate blood plasma from whole blood using inertial force. The sample was then further aliquoted in the system for a creatine test (Kuo et al., 2014). Nwankire et al., (2015) used a similar technique to separate blood plasma but this time with valves in the chip to aliquot plasma into separate chambers to perform a rapid liver assay (Nwankire et al., 2015). The technique has also been adapted and utilised for the identification of bacteria in urine samples for rapid diagnosis of urinary tract infections (UTIs). Schroder et al., loaded the chips with urine from patients with known UTI's and exposed the captured single cells to Raman spectroscopy. Raman spectra were recorded for E. Coli and E. faecilis and were successfully identified in patient samples. With the use of the portable Lab-on-a-Disc, bacterial diagnosis was performed within one hour (Shroder et al., 2015). The Burger LoaD platform was further adapted using a loaded disc with live rat cardiomyocytes and cells interrogated for growth and beat pattern over time (Espulgar et al., 2015). Although this particular technique has shown great promise over the last numbers of years, the majority of the focus has been on photonically characterising biological material (tissue and cells) and diagnosing disease using vibrational spectroscopy techniques such as Raman spectroscopy and FTIR which are discussed below.

1.3 Vibrational Spectroscopy as a method for identification of cells contributing to vascular remodelling:

Vibrational spectroscopy methods such as Raman spectroscopy and FTIR have been utilised to characterise cells through their cellular 'footprint' i.e., a unique light scattering pattern. These methods are gaining huge attention as diagnostic tools, particularly in the area of cancer and some initial vascular studies. The concept and success of these tools will be discussed below with the potential of this tool to discriminate vascular stem cells, which may contribute to the accumulation of smooth muscle-like cells in the vascular lesion, to be kept in mind.

1.3.1 Background to vibrational spectroscopy of cells

The concept of spectroscopy has been reported from as early as the 17th century. Sir Isaac Newton introduced the word 'spectrum' following the observation of spectral dispersion through a glass prism (Newton 1704, Rehman et al., 2013). It wasn't until 1800 that infrared radiation (IR) was discovered by William Herschel (Ring et al., 2000), with the first IR spectrometer dated 1937 (Gershinowiltz et al., 1978). Raman spectroscopy was discovered by Raman himself in 1928 (Smith et al., 2016).

One of the first reports of using spectroscopy for the analysis of biological samples, was carried out by Elliot and Ambrose (1950) and published in *Nature*. Elliot and Ambrose reported a change in spectra between folded and extended polypeptide chains. Although their conclusions were later proven to not be entirely correct (Miyazawa and Blout 1961; Krimm et al., 1962) it heralded the beginning of a new era using methods such as vibrational spectroscopy and photonics to study biological molecules.

The most common spectral bands using Raman spectroscopy and IR spectroscopy as experimental tools for different components of the plant cells such as proteins, amino acids, lipids, fatty acids, carbohydrates,

phenols and terpenoids has been reviewed (Schultz and Baranska, 2007). As the majority of the plant cell components are present in the animal cell, the characteristic bands can be translated across and contribute to animal cell molecule identification (Rehman et al., 2013).

1.4. Raman Spectroscopy for the analysis of biological samples

Raman spectroscopy is a form of vibrational spectroscopy that has been employed to extract molecular information from a substance. Vibrational spectroscopy relies on the interaction of electromagnetic radiation with molecules. The electromagnetic radiation causes a transition in energy state of molecules in a sample, giving off energy that can be quantified (Sathyanarayana et al., 2004). When an atom of electromagnetic radiation (photon) interacts with a molecule and the scattered photon has the same frequency as the initial interacting photon (incident photon) it is referred to as Rayleigh scattering. When the scattered photon has more or less energy than the incident photon due to transfer of energy between the photon and the molecule, it is referred to as Raman scattering. There is also phenomena called stokes and anti-stokes Raman scattering where stokes scattering is the excitation of a molecule from ground to a higher energy state and anti-stokes is the scattering of the molecule from the higher energy state to the ground state. Typically, spectra are obtained from the Raman scattering in the stokes state only (Rehman et al., 2007).

Raman spectra are plots of the difference in initial and final vibrational energy levels when a sample is hit with a monochromatic laser. Individual molecules can be uniquely identified by this method by analysing the frequency difference between Raman-scattered and non-Raman scattered (incident) light for that molecule. This forms a peak in the spectrograph with each band representing a molecule (Rehman et al., 2007).

Raman spectroscopy has been widely used to characterise cells based on their vibrational molecular ‘fingerprint’. The fingerprint region is

generally between 400-2000 cm^{-1} wavenumber with regions in the wavenumbers that have been characterised as proteins (1500-1700 cm^{-1}), nucleic acids (785-788, 1090, 1262, 1319, 1341, 1585, 1662 cm^{-1}) carbohydrates (470-1200 cm^{-1}) and lipids (1451, 2855, 2889, 2930 cm^{-1}) (Butler et al., 2016, Kiselev et al., 2016). Due to detectable differences in the fingerprint regions of biological samples, Raman spectroscopy is rapidly evolving as a highly specific diagnostic technique.

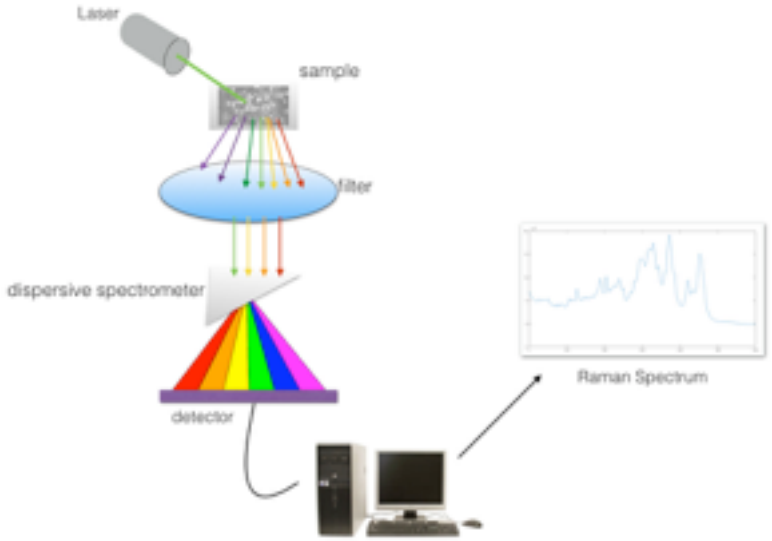

Figure 1.4 Raman Spectroscopy. Simple Raman Spectroscopy schematic adapted from Salvas et al. 2010. Diagram of the direction of laser light to a sample and the filtration and dispersion of the emitted light through filters and spectrometers to a detector (camera) to produce a spectrum.

The focus of much of the research with Raman spectroscopy relates to various types of cancer models, including breast and prostate cancer which are the most common in women and men respectively (Vardaki et al., 2016). Indeed there has been significant research carried out for breast (Haka et al., 2005; Pichardo-Molina et al., 2007), prostate (Crow et al., 2003; 2005; Li et al., 2014; Patel et al., 2010; 2011), brain (Jermyn et al., 2015;2016; Zhou et al., 2012; Baker et al., 2014; Gajjar et al., 2012;; Beljebbar et al., 2010) bladder (Crow et al., 2005; Draga et al., 2010; Mourant et al., 1995; Jong et al., 2006; Kerr et al., 2016) cervical (Lyng et

al., 2007; Rubina et al., 2013; Kim et al., 2016; Krishna et al., 2006; Utzinger et al., 2001) colon (Chen et al., 2006; Molckovsky et al., 2003; The et al., 2008, Li et al., 2016) lung (Huang et al., 2003; Mcgregor et al., 2016) skin (Lieber et al., 2008; Zhao et al., 2008; Lui et al., 2012) and leukemia cancers (Gonzales-Solis et al., 2014; Chan et al., 2008; Manago et al., 2016; Happillon et al., 2015). Many peaks and wavenumbers have been identified in these studies to be associated with cancer cells in comparison to their control counterparts (see Table 1.1)

1.3.3 Raman Spectroscopy Peaks for Cancer Cells

Cancer Type	Peaks Associated	Author(s)
Breast	1445 cm^{-1} and 1551 cm^{-1}	Pichardo-Molina
Prostate	721, **783**, 827, 1096, 1250, 1305, 1450, 1577, 1568 cm^{-1} (Crow) 1445 cm and 1586 cm^{-1} (Li) **781-787 cm^{-1}** (Patel)	Crow 2005; Li 2014; Patel 2010.
Brain	**1548**, 1587-1605, 1732 cm^{-1} (Zhou) 721 cm^{-1} and 782 cm^{-1} (Baker) 1001 and 1670 cm^{-1} (Gajjar) 1063, 1086, 1131, 1300 and 1739 cm^{-1} (Koljenovic) 1005, 1126, 1176, **1548** and 1578 cm^{-1} (Beljebbar)	Zhou 2012; Baker 2014; Gajjar 2012; Belijebbar 2010.
Bladder	**1003**, 1083, 1260, 1310, 1446, 1665 cm^{-1} (Crow) 680, 789**, 1003**, 1170, 1180, 1208, 1370, 1386, 1560 cm^{-1} (Draga) 1584 cm^{-1} (Shapiro)	Crow 2005; Draga 2010; Shapiro 2011.
Cervical	**1655 cm^{-1}** (Lyng) **1450 cm** and 1660 cm^{-1} (Rubina) **1448 cm^{-1}** (Kim) 620, 644, 719, 757, 1004, 1033, 1270, 1461, 1671, 1092, 1128, 1300, 780, 1340, 1492 cm^{-1} (Krishna) **1454-1656 cm^{-1}** (Utzinger)	Lyng 2007; Rubina 2013; Kim 2016; Krishna 2006; Utzinger 2001.

Colon	1265, 1305, **1450** and **1660 cm**$^{-1}$ (Teh) 788, 1034**, 1446, 1657 cm**$^{-1}$ (Chen)	Teh 2008; Chen 2006
Lung	752, 1004, 1223, 1336, **1445**-1655 cm^{-1} (Huang)	Huang 2003
Leukaemia	917 cm^{-1} (Gonzales-Solis) 1126, 1605, 1615 cm^{-1} (Chan) 1447 cm^{-1} (Manago) 796, 1106, 1380, 1454, 1498, 1556, 1585 and 2954 cm^{-1} (Happillon)	Gonzales-Solis 2014; Chan 2008; Manago 2016; Happillon 2015.

Table 1.1 Raman spectral peaks associated with various cancer types. Peak wavelengths in bold represent signatures that are common in more than one study.

Interestingly, peaks from the 1445-1450 cm^{-1} range that are attributed to proteins and lipids (Kiselev et al., 2016) were identified by at least one article per cancer type outlined in Table 1 above to be elevated in cancerous samples, except for the brain (Pichardo-Molina et al., 2007; Crow et al., 2005; Li et al., 2014; Rubina et al., 2013; Kim et al., 2016; Utzinger et al., 2001; Teh et al., 2008; Chen et al., 2006; Huang et al., 2003; Happillon et al., 2015). Using the differences in these peaks, the researchers could employ statistical algorithms to discriminate between cancerous and non-cancerous samples with high accuracy.

Raman spectroscopy is not limited to cancer models. It has also been implicated in the field of microbiology, particularly for bacterial identification (Butler et al. 2016; Jarvis et al., 2004; Maquelin et al., 2002; Neugebauer et al., 2006; Pahlow et al., 2015; Ashton et al., 2011) and in the diagnosis of infectious microorganisms (Tien et al., 2016; Avci et al., 2015; Kusters et al., 2016). As mentioned previously, there has also been extensive research of Raman spectroscopy in plants, as reviewed by Schultz and Baranska (Schultz and Baranska 2007). Since then, the technique has been adopted for many areas in plant science including monitoring plant health and development (Butler et al., 2015), early detection of plant diseases (Yeturu et al., 2016) and the characterisation of plant-associated bacteria (Paret et al., 2010).

Raman spectroscopy has been widely used in the pharmaceutical sector as a non-invasive tool to, for example, analyse pharmaceutical products such as tablets and capsules and also monitor crystallisation of pharmaceutical formulations as reviewed by Buckley et al. (Buckley et al., 2011). Raman microscopy, which involves both Raman spectroscopy and high power optical imaging, is more common in the pharmaceutical sector (Smith et al., 2015). Raman spectroscopy has been further applied in pharmaceutical sciences to distinguish between visually indistinguishable pharmaceuticals (Jahme et al., 2016), compound detection in unknown pharmaceutical products (Boiret et al., 2016), quality control for pharmaceutical compound formulations (Meek et al., 2016) and quantifying and evaluating the uniformity of pharmaceutically active ingredients in drug products (Li et al., 2016).

The focus of Raman spectroscopy for this research thesis is the utilisation and current trends of Raman spectroscopy in the broad area of heart disease and in particular vascular remodelling.

1.3.4 Raman & Atherosclerosis

Atherosclerosis is responsible for 75% of cardiovascular related deaths (Insull et al., 2009). It is characterised by an asymmetrical thickening of an artery due to the formation of what is called a ‘plaque’. The plaque is an obstruction in the artery composed of cholesterol, lipids, inflammatory cells such as macrophages and lymphocytes and a high concentration of smooth muscle-like cells. The plaque is usually contained by a fibrous cap which can become vulnerable to rupture and cause a thrombus formation (Libby & Theroux., 2005). Diagnosing atherosclerosis is a tricky business as most patients do not present any symptoms and access to the arteries is very limited. The most common method to diagnose atherosclerosis is still catheterised coronary angiography. The catheter leads the x-ray source to the site of obstruction and records x-ray images of the plaque or stenosis. There are various other methods to image atherosclerotic plaques such as coronary computed tomographic

angiography, magnetic resonance angiography, optical coherence tomography, CT scan and PET-CT scans as outlined in the recent review by Tarkin et al. (2017) (Tarkin et al., 2017).

The limitation of all of these techniques is the inability to extract biochemical information from the presented plaque or obstruction. The techniques can record images of the obstruction and observe the phenotype of the disease, but that means the plaque has to be already present in the patient before detection. Therefore, methods such as optical spectroscopy, which can extract biochemical information from biological tissues, are ideal for early detection of subtle changes within the vasculature that contribute to disease progression. Many researchers have recognised the power of Raman spectroscopy for this purpose.

Wrobel et al., constructed a thorough table outlining the Raman band assignments corresponding to atherosclerotic plaques that presented in the literature to that date. This table provides a foundation for a Raman library for the detection of atherosclerosis biomarkers such as cholesterol, smooth muscle cells, collagen fibre/fibrous cap, fat cells, foam cells and calcification (Wrobel et al., 2014). Further research to expand the Raman library for atherosclerosis biomarkers would be beneficial to the early detection of atherosclerosis.

1.3.5 Raman & Vascular Remodelling

Vascular remodelling can occur spontaneously throughout ageing or in response to risk factors such as hypertension or vascular injury by catheterisation or stenting. In these cases, the resulting obstruction is not due to the presence of a fatty plaque, but a build up of primarily neointimal smooth muscle-like cells with an additional small population of inflammatory cells and endothelial cells. The accumulation of smooth muscle-like cells in the vasculature is therefore an early biomarker for stenosis (Schiele et al., 2005). Although much work has been done so far

with Raman and atherosclerosis, there is scant information available for analysing non-atherosclerotic vascular lesions. However, some work has been carried out using Raman analysis of vascular smooth muscle cells and associated extracellular matrix proteins, collagen and elastin, which could serve as spectral early biomarkers for non-atherosclerotic stenotic progression. Table 1.2 outlines the current literature for the biochemical peaks for SMCs and extracellular matrix proteins collagen and elastin.

Peak Number	Attributed to	In Vascular	Reference
853/940/1034 940/1034 1030; 935; 850 cm^{-1} 853cn^{-1} + 936/938 cm^{-1}	C-C or C-H Bending C-C and C-H bending C-C or C-H bending C-C or C-H bending + C-C stretching of protein backbones	SMC-like cell dSMCs dSMCs Myosin	Buschman 2001 Peres 2011 Abubaker 2007 Pascut 2011
855 cm^{-1}	C-C Stretching Mode of Proline	Collagen	Buschman 2001
876 cm^{-1}	Gly-Pro-X and Gly-X-Hyp.	Collagen	Latterman 2013
921 cm^{-1}	Gly-Pro-X and Gly-X-Hyp	Collagen	Latterman 2013
933 cm^{-1}	C-C Stretching Mode of Proline	Collagen	Buschman 2001
938, 1001, 1260, 1305, 1555, 1657		SMC-like cell	Lopes 2011
1004 cm^{-1} 1004 cm^{-1} 1004 cm^{-1} 1004 cm^{-1}	Phenylalanine Phenylalanine Phenylalanine Phenylalanine	SMC-like cell dSMCs Remodelled Tunica Media dSMCs	Buschman 2001 Peres 2011 Marcez 2015 Abubaker 2007
1104 cm^{-1}	Desmosine/Isodesmosine	Elastin	Buschman 2001
1244 cm^{-1}	Amide III	Remodelled Tunica media	Marcez 2015
1264 cm^{-1} 1265 cm^{-1}	Amide III	Collagen	Buschman 2001 Abubaker 2007
1255 cm^{-1} 1256 cm^{-1}	Amide III Amide III	Elastin/Collagen Aortic Intima SMC-like cell	Peres 2011 Manohoran 1995 Lopez 2011
1268 cm^{-1} 1268 cm^{-1}	Amide III Amide III	SMC-like cell dSMCs	Buschman 2001 Peres 2011
1270 cm^{-1}	Amide III	dSMCs	Abubaker 2007

1336 cm^{-1} 1336 cm^{-1} 1335 cm^{-1} 1334 cm^{-1}	Desmosine/Isodesmosine C-C and C-H bending C-C and C-H bending	Elastin dSMCs SMC-like cell dSMCs	Buschman 2001 Peres Lopes 2011 Abubaker 2007
Decrease in 1338 cm^{-1}		Elastin/Disease	Manoharan 1995
1440; 1100 cm^{-1}	Desmosine/Isodesmosine	Elastin	Abubaker 2007
1452 cm^{-1} 1455 cm^{-1} 1455 cm^{-1} 1452 cm^{-1} 1450 cm^{-1} 1451 cm^{-1}	CH_2 Bending Amide III C-C or C-H bendingSMCs CH bending C-C or C-H Bending	Elastin/Collagen Elastin Aorta Intima SMC-like cell	Peres 2011 Abubkaer 2007 Manoharan 1995 Buschman 2001
1660 cm^{-1} 1660 cm^{-1} 1660 cm^{-1} 1660 cm^{-1} 1660 cm^{-1}	Amide I Amide I Amide I Amide I Amide I	SMC-like cell Remodelled tunica media dSMCs Aortic intima dSMCs	Buschman 2001 Marcez 2015 Abubaker 2007 Manoharan 1995 Peres 2011
1664 cm^{-1} 1665 cm^{-1} 1663 cm^{-1}	Amide I Amide I Amide I	Elastin dSMCs Elastin	Buschman 2001 Peres 2011 Abubaker 2007

Table 1.2. Raman spectroscopy table for SMCs and associated extracellular matrix proteins collagen and elastin. differentiated SMC (dSMC) represents SMCs analysed directly from a healthy vessel, SMC-like cells represent the smooth muscle like cells present in hyperplasia or diseased models.

It is interesting to note the spectral similarities for differentiated SMCs (dSMCs) analysed straight from healthy tissue and the SMC-like cells identified in diseased models as outlined in various Raman spectroscopy studies. The similar peaks are often associated with extracellular matrix proteins collagen and elastin which is known to be associated in dSMC extracellular matrix proteins and also to be produced by stem cell derived SMCs (Bank et al. 1996; Naryanan et al. 1976; Wanjare et al. 2015). These Raman peaks can be used to identify the presence and accumulation of SMC-like cells in the intima of patient arteries, indicating the initiation of a neointimal formation that could begin to occlude the artery.

Recently, a lot of attention has been focused on the role of stem cells to the contribution of vascular remodelling including atherosclerosis and arteriosclerotic disease (Yuan et al., 2017; Tang et al., 2012; 2013; Majesky et al., 2015). With this in mind, the presence of stem cells and their respective progeny within the neointima of an artery is another potential early marker for vascular remodelling that can be exploited by Raman spectroscopy.

The role of vibrational spectroscopy including Raman spectroscopy for identifying stem cells and their differentiated progeny has recently been reviewed (Sule-Sulo et al., 2014; Askoy et al., 2012). Table 1.3 below is a summary of the stem cells that have been studied by Raman spectroscopy and the peaks that have been identified as important for stem cells and their differentiated progeny. Interestingly, stem cells had higher RNA and DNA values at 813 cm^{-1} and 788 cm^{-1} than their respective differentiated cells (Notingher et al., 2004; Chan et al., 2009; Downes et al., 2011; El-Said et al., 2015). These studies were reported over a period of ten years and include mESCs, MSCs and neural stem cells. Further investigation into the wide range of stem cells, particularly at those markers, could provide an identifiable spectral marker for stem cells recruited to vascular lesions.

Stem Cell Type	Peak Number	Attributed to	Phenotype	Reference
mESC	813 cm^{-1} 788 cm^{-1}	O–P–O stretch vibration - RNA Cytosine ring vibration - DNA	Both higher in SCs than differentiated	Notingher 2004
hESC	811 cm^{-1} 785 cm^{-1} 1090 cm^{-1}	RNA DNA DNA	All higher in SCs than differentiated	Chan 2009
hESC	1003 cm^{-1} 1308 cm^{-1} 1448 cm^{-1} 1669 cm^{-1}	Phenylalanine Lipid CH_2 Twist CH deformation Amide I	Strong hESC bands	Chen 2011

hESCs to cardiomyocytes	482 cm^{-1} 577 cm^{-1} 858 cm^{-1} 937 cm^{-1} 1083 cm^{-1} 1340 cm^{-1}	Carbohydrate Carbohydrate CH bending C-O-C glycosidic bond-H bending vibration	Increase during differentiation to CMs	Pascut 2013
MSCs	785 cm^{-1} 811 cm^{-1} 828 cm^{-2}	DNA RNA RNA	All higher in SCs than differentiated	Downes 2011
hMSC to osteocytes	950-970 cm^{-1} 1030 cm^{-1} 1070 cm^{-1}	Phosphate groups	hMSC differentiation to osteocytes	McManus 2011
hMSCs and fibroblasts			Distinguish fibroblasts from MSC cultures	Pudlas 2011
Rat Adult Neural Stem Cells SERS (gold substrate)	755 cm^{-1} 838 cm^{-1} 913 cm^{-1} 955 cm^{-1} 1155 cm^{-1} 1440 cm^{-1} 1540 cm^{-1} 690 cm^{-1} 1120 cm^{-1}	A and Trp RNA/DNA Proline Proline Proline Carbohydrate Trp & amideIII DNA Carbohydrate	755-1540 cm^{-1} higher in SC than differentiated Increased during differentiation	El-Said 2015
Mouse Neural Stem Cells	650 cm^{-1} 828 cm^{-1} 1160 cm^{-1} 738 cm^{-1} 1617 cm^{-1} 1001 cm^{-1} 1580 cm^{-1}	Tyr DNA/RNA Proline Trp Proline Phenylalanine DNA/RNA	Appeared and increased for up to 2 week sand then disappeared Decreased Increased	El-Said 2015

Table 1.3. Collection of Raman studies for various types of stem cells. Raman spectroscopy table for stem cells and their myogenic progeny.

The current library for Raman spectra for cells involved in vascular remodelling is somewhat limited but further research into this area could identify specific spectral signatures for this disease.

1.3.6 FTIR of Biological Samples

Fourier Transform Infrared Radiation (FTIR) is another method of

vibrational spectroscopy but in contrast to Raman spectroscopy it relies on the absorption of infrared radiation rather than the scattering of light from a laser beam. Each chemical bond in a molecule has defined vibrational frequencies that can be absorbed by the FTIR – giving biochemical information for each molecule (Sule-Suso et al., 2014). In the case of FTIR, infrared radiation is passed through the sample via a laser beam which vibrates the atoms in the molecules. For a molecule to be infrared active, the electric dipole moment must change in response to atomic displacement. The FTIR quantifies the vibrational modes. FTIR relies on one laser beam splitting to two via an interferometer yielding a signal that is a function of the difference in path length between the two beams. The resulting signal is an amplified signal with the noise reduced(Stuart et al., 2004).

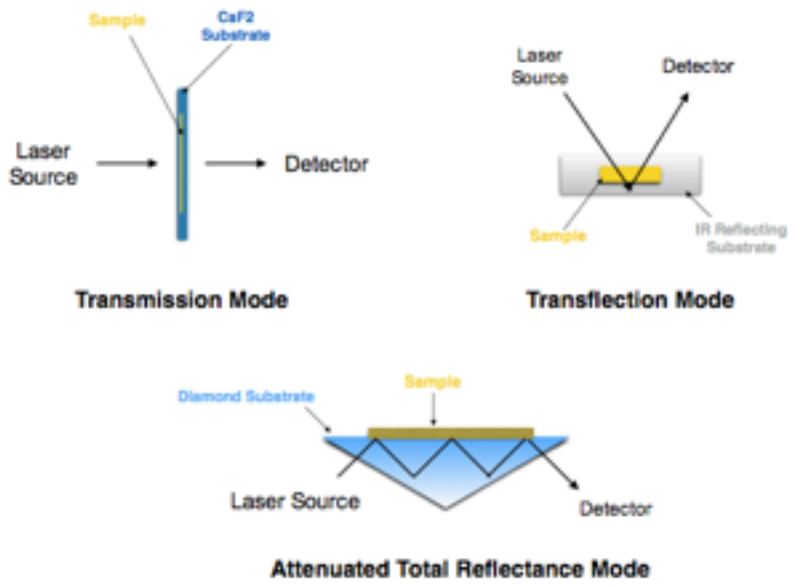

Figure 1.5. Modes of FTIR. Common modes of FTIR; adapted from Baker et al. 2014. The three main modes of FTIR (1) transmission mode, directing a laser through a sample to the detector, (2) transflection mode, reflecting the laser source from the sample to the detector, (3) attenuated total reflectance mode (ATR), directing a laser source through a highly refractive element to the detector.

There are three main modes of FTIR, transflection, transmission and

attenuated total reflection (ATR). Transflection directs the laser beam through the sample to an IR-reflective surface that sends the beam back to the detector. Transmission sends the beam through the sample and substrate to the detector below. Attenuated total reflection involves directing the beam through an internal reflective element with a high refractive index, for example a diamond. The mode depends on the thickness of the sample, for example, can the beam get through the sample in transmission mode? Most cell samples are thin enough for transmission mode to be used. However, ATR could be used for a tissue sample (Baker et al., 2014).

For biological samples, the 'fingerprint' region lies between 600-1450 cm^{-1} of the spectra (Baker et al., 2014). A detailed table outlining the peak assignments for the FTIR fingerprint region have been reported (Movasaghi et al. 2008). In broad terms, the fingerprint region of mammalian cells can generally be divided into sections of the spectrum where the region of approximately 1000 cm^{-1} corresponds to carbohydrates, from 1050 cm^{-1} to 1400 cm^{-1} is attributed to nucleic acids, 1400 cm^{-1} to 1800 cm^{-1} corresponds to proteins and lipids and finally the high wavenumber region from about 2800 cm^{-1} relates to lipids (Baker et al., 2014).

Like Raman spectroscopy, a lot of the research has focused on cancer detection. FTIR and spectral imaging were carried out in conjunction with conventional Haemotoxylin and Eosin (H&E) staining for breast cancer tissue. FTIR spectroscopy accurately assembles a clusteral graph mimicking the histological pattern of axillary lymph nodes and metastatic breast cancer tissue (Bird et al., 2008). ATR-FTIR was also used to distinguish between epithelial, myoepthelial and stromal tissue in benign or cancerous tumours. It also is capable of identifying terminal ductal lobular units (TDLU) which are commonly the primary site of breast cancer and can be difficult to diagnose by histology in malignant tumours (Walsh et al., 2012). Focusing on the collagen region of the FTIR spectra, Ooi et al., demonstrated that the FTIR collagen region was higher in

cancerous samples than healthy samples in relation to tissue samples from mastectomy, mammoplasty and excisional biopsy which was attributed to the structural disruption of collagen in cancerous tissues (Ooi et al., 2008). Complementary to the previous studies, FTIR has been shown to identify the main cell types in breast tissue sections including epithelial, stromal, lymphocytes, vascular, connective tissue and erythrocytes, to distinguish between cancerous and healthy tissue sections and present spectral differences between the stroma spatially close and un-associated stroma to the tumour (Verdonck, 2016). In 2010, Backhaus et al., utilised the unsupervised learning technique to classify breast cancer spectrally from serum samples in total of 196 patients. The clusteral analysis had a sensitivity of 98% and specificity of 95%. Using a supervised learning technique, the sensitivity of 92% and specificity of 100% was achieved for classifying cancerous samples (Backhaus et al., 2010). Similarly, FTIR spectroscopy has been employed to compare normal, dysplastic, early carcinoma and advanced carcinoma in rat colon cancer models with an accuracy of 100%, 94%, 97.5% and 100% respectively (Cheng et al., 2009). Complementary results have been reported in the field of colon cancer including correlating FTIR maps with histopathological sections (Piva et al., 2015), detection of colon and rectum cancer in vitro and in vivo (Li et al., 2005) and comparing healthy tissue with cancerous and post-chemotherapy tissue (Kaznowskia et al., 2017).

A detailed review on the sample preparation, spectral acquisition, data processing and applications of FTIR for prostate cancer has been recently published (Siquiera et al., 2016). In the case of brain tumours, FTIR successfully discriminated normal brain tissue, tumours and tissue surrounding tumours and can diagnose cancer compared to non-cancer serum samples with a sensitivity of 93.75% an specificity of 96.53% (Hands et al., 2014). For cervical cancer, FTIR has a higher classification accuracy than the basic Pap-Smear, 72% vs 43% respectively (Njoroge et al., 2006). Further studies utilised FTIR for cervical cancer screening and achieved results of 85% sensitivity, 91% specificity, a positive

predictive value of 19.5% and negative predictive value of 99.5% (El-Tawil et al., 2008). As the commonly used pap smear frequently obtains false positives, this study demonstrates the true benefit of using FTIR as a diagnostic tool for cervical cancer over the typical pap smear (El-Tawil et al., 2008). As FTIR successfully detects biochemical changes in a cell, pre-cancerous cervical cells can be identified by FTIR before the morphological changes occur that are usually detected by microscopy. A system coupled with multivariate statistical analysis that could successfully identify pre-cancerous cervical cells with an accuracy of 92% was subsequently developed, further demonstrating the application of FTIR in particular in the area of cervical cancer diagnostics (Jusman et al., 2016). FTIR has also been deployed to assess bladder cancer for diagnostic purposes. A 100% sensitivity for classifying bladder carcinoma in human bladder wash samples has been reported (Gok et al., 2016). Cancerous and non-cancer bladder tissue has also been assessed and successfully discriminated (Al-Muslet et al., 2011) while FTIR classified urinary bladder cancer from urinary tract infections from patient blood samples with a classification accuracy of 80%, and sensitivity and specificities of 78% and 81% respectively (Ollesch et al. 2014).

The focus of FTIR in the area of cancer research has been primarily on classification and the diagnostic potential of FTIR rather than the specific biochemical and biomarker identification which is more the focus of much of the Raman research. As the techniques are complementary, the use of FTIR for the classification of cancerous versus non cancerous models with the use of Raman spectroscopy for the sensitive molecular identification within the models could provide a gold standard vibrational spectroscopy system to accurately diagnose and study cancers.

The study of FTIR and biological cells has also not been limited to cancer models. The application of FTIR to analyse diseases resulting of protein mis-folding or aggregation such as Alzheimer's, Parkinson's, Huntington's, sclerosis and prions disease has been reviewed (Miller et al., 2013). Since then, Tidy et al., identified a distinct peak in the Amide 1

region at approximately 1630-1625 cm^{-1} which appears during protein aggregation disease models of Alzheimer's disease and stroke (Tidy et al., 2016). A more detailed review of the common peaks in neurological disorders has identified the peak at approximately 1630-1625 cm^{-1} in studies including Alzheimer's disease, Parkinson's disease, multiple sclerosis and brain tumours suggesting a common peak for neurological disorders (Caine et al., 2012).

FTIR has also been utilised in the pharmaceutical industry mostly to analyse the content of formulated drugs. FTIR was first successfully used to assess the quantity of ibuprofen in pharmaceutical formulations (Matkovic et al. 2005) while ATR-FTIR was used to successfully predict solution concentration in a compound produced by the solution crystallisation method (Togkalidou et al. 2002) and distinguish between polymorphs in a pharmaceutical mixture (Salari et al., 1998). FTIR has also been applied to microbiological cells and tissue (Naumann et al., 1991) and has been utilised in the analysis of E. Coli biofilm dynamics (Holman et al., 2009), the identification of unknown bacteria and also in the analysis of yeast and fungi (Beekes et al., 2010).

The focus of this section of the review however, is the utilisation and current trends of FTIR in the broad area of heart disease and in particular vascular remodelling.

1.3.7 FTIR & Atherosclerosis

The frequent FTIR spectra features of atherosclerotic plaques has also been addressed (Wrobel et al., 2014). Table 1.4 provides a foundation for an infrared radiation (IR) library for the detection of atherosclerosis biomarkers such as oligosaccharides and polysaccharides (1041 cm^{-1}), cholesterol (1055 cm^{-1}, 3035 cm^{-1}), phospholipids, glycolipids and calcification (1080-1095 cm^{-1}), glycogen (1080-1095 cm^{-1}, 1151 cm^{-1}), cholesterol esters (1170 cm^{-1}), collagen (1203 cm^{-1}), lipids (1395-1377 cm^{-1}, 1460 cm^{-1}, 1733-1750 cm^{-1}, 2850 cm^{-1}, 2925 cm^{-1}, 2954 cm^{-1}) and proteins (1552 cm^{-1}, 1666 cm^{-1}, 2873 cm^{-1}, 3080 cm^{-1}, 3500-3200 cm^{-1}).

Further research to expand the FTIR spectra library for atherosclerosis to facilitate the early detection of atherosclerosis has been desirable (Wrobel et al. 2014). FTIR analysis of human atherosclerotic carotid arteries has been performed to determine the biochemical markers of mechanical stiffness during atherosclerosis and revealed that a decrease in lipid content and an increase in calcification in the plaque groups displaying mechanical stiffness (Barrett et al. 2015). FTIR spectra for atherosclerotic plaques from ApoE/LDLR$^{-/-}$ mice fed on a normal diet and on a low carbohydrate high protein diet (LCHP) have been generated and compared with higher cholesterol and cholesterol esters found in the LCHP mouse model (Wrobel et al., 2014). Chemical changes in grey and white matter of brains from C57/BL6 and ApoE/LDLR$^{-/-}$ mice have also revealed higher lipid to protein content and cholesterol, in contrast to lower haem groups in the red blood cells of the white matter demonstrating that atherosclerosis can effect brain tissue and therefore could contribute to brain-related diseases (Kochan et al., 2016). Finally, the effects of pravastatin on the FTIR spectra from ApoE/LDLR$^{-/-}$ mice have also been evaluated (Kostogrys et al., 2017). Pravastatin decreased the effects of a pro-atherogenic diet on lipid content, cholesterol and cholesterol esters and the levels of phospholipids but increased the levels of unsaturated compounds compared to control or atherosclerotic mice. The study demonstrated the potential of FTIR to not only compare control, diseased and diseased treated models but also to identify the biochemical changes in each of the groups (Kostogrys et al., 2017). The application of FTIR to atherosclerosis models is currently well characterised and demonstrates great potential for the diagnosis of atherosclerosis.

1.3.8 FTIR and Vascular Remodelling

One of the first studies reporting the use of FTIR for vascular tissue was carried out on rabbit aortas. FTIR identified several peaks in the tunica media as outline in Table 1.5 (Colley et al., 2004). FTIR was also performed on aortic tissue and diseased (aneurysm) aortic tissue to

evaluate the diagnostic potential of the technique. Healthy and diseased aortic tissue could be distinguished from one another with 95% confidence (Bonnier 2008). The structure of elastin which is a structural component of the aorta and can be modified in disease progression was originally mapped by FTIR (Debelle et al.,1998) and was subsequently used to analyse the elastin and collagen content of the aorta and track structural changes in the extracellular matrix of the aorta during disease progression (Cheheltani et al., 2014). FTIR spectra of the proteins from human vSMCs versus vSMCs cultured with aggregated LDL were also analysed to map changes elastin content (Table 1.6, Samouillan et al., 2012). Sham and injured (arteriosclerotic) arteries treated Connective Tissue Growth Factor (CTGF) were also analysed by FTIR and displayed a 50% decrease in the 1338/AM2 area ratio and a 600% increase in the 1660/1690 peak height ratio (attributed to collagen). The CTGF treated samples reversed these ratios back to control sham levels (Herman et al., 2009). All of these studies contain valuable information of the peaks present in various parameters of vascular remodelling and have been recorded in Table 6 as a basis of an FTIR 'library' for vascular remodelling which can be expanded with further research.

Peak	Attributed to	Vascular Relation	Reference
530	ν(S-S)	SMC protein	Samouillan 2012
930	ν(Cα-C) characteristic of α-helices.	SMC protein	Samouillan 2012
1039	ν(C-C), ν(C-O), Phe, Ser	SMC protein	Samouillan 2012
1178	γ(CH2) Pro, Tyr	SMC protein	Samouillan 2012
1206	δ(COH)Tyr	SMC protein	Samouillan 2012
1224	amide III δplan (N-H)	SMC protein	Samouillan 2012
1408	ν(COO-)	SMC protein	Samouillan 2012
1464-1452	δ(CH2,CH3) aliphatic side chains	Smooth muscle cell protein	Samouillan 2012

1548	Amide II v(CN), ∂NH	Smooth muscle cell protein	Samouillan 2012
1591	V(C-C) ring Tyr, Phe	Smooth muscle cell protein	Samouillan 2012
1651, 1632	Amide I v(C=O)	Smooth muscle cell protein	Samouillan 2012
2955, 2922, 2850, 2827	v(C-H) aliphatic	Smooth muscle cell protein	Samouillan 2012
3446; 3361; 3197	Amide A H-bonded v(O-H) and v(N-H)	Smooth muscle cell protein	Samouillan 2012
969; 1063; 1241; 1378; 1464; 1539; 1645; 1734; 2854; 2927; 2958; 300-3450		Aggregated LDL	Samouillan 2012
1030 1080 1163 1403 1456	C-O Stretching C-O Stretching CH_2 Wagging C-H deformation C-H stretch of protein	Aortic wall (Collagen and elastin)	Bonnier 2008
525; 645; 752; 836 852; 905; 928; 960; 1004; 1031; 1103; 1123; 1175; 1207; 1246; 1313; 1336; 1414; 1452; 1565; 1613; 1659	V(S-S) bridge G-G-T; Tyr; Tyr; v(C-C) v(C-C); v(C-C); Phe Phe; v(C-N); Tyr Tyr, Phe; Amide II; ∂(CH); $(C0)_2$;∂(CH_2CH_1) Phe; Phe/Tyr; Amide I	Human Elastin	Debelle 1998e
1338 1480-1580 1580-1718	CH_2wagging vibration of proline side chains Amide II Amide I	Elastin/Collagen Elastin/Collagen Collagen Scar deposition in cardiac tissue sections	Cheheltani 2014
1610-1645 1643-1667	β Sheets Amide I	Elastin	Cheheltani 2014
1338 1660/1690	Collagen Integrity Collagen Maturity	Vascular Remodelling Vascular Remodelling	Herman 2009
1237 1448 1634 ;1529 3081; 2934	Phospholipids Protein Protein Saturated C-H modes	Tunica Media Tunica Media Tunica Media Tunica Media	Colley 2004 Colley 2004

Table 1.4: FTIR and Vascular Remodelling. Table of peaks reported in

the literature.

As mentioned above, the role of stem cells in contributing to vascular remodelling has come into focus in the recent literature. With that in mind, Table 1.5 below is a collection of peaks attributed to stem cells and differentiation that have been outlined in the literature so far.

Stem Cell Type	Peak	Attributed To	Phenotype	Reference
hESC and hMSC	2920 cm^{-1} & 2850 cm^{-1} 1740 cm^{-1}	CH_2 stretching mode of methylene chains; carbonyl C=O stretching mode.	Membrane lipids Phospholipids both higher in hESC than hMSC	Pijanka et al. 2010
hESC differentiation to neural stem cells	2959 cm^{-1}; 2923 cm^{-1}; 2853 cm^{-1}; 1659 cm^{-1} &1637 cm^{-1}	CH_2 CH_3 stretching vibrations Amide I	Lipids & Proteins Increase during differentiation	Tanthanuch et al. 2010
mESC Spontaneous Differentiation	1692 cm^{-1} & 1657 cm^{-1} 994 cm^{-1}; 914 cm^{-1}; 966 cm^{-1} 899 cm^{-1}	Amide I Nucleic Acid DNA	Proteins; increase during differentiation Decrease during differentiation Appeared during differentiation	Ami et al. 2008
rBM-MSC differentiation to hepatocytes	3012 cm^{-1} 2952 cm-^{1} 2854 cm^{-1} 1722 cm^{-1}	C=O stretch $V_{as}CH_3$ stretch $_{vs}CH_2$ stretch C=O stretch All from lipids	Triglycerides and fatty acids.	Ye et al. 2012

Stem Cell Type	Peak	Attributed To	Phenotype	Reference
mPSCs to differentiated pancreatic cells (DPCs)	1650 cm^{-1} 1540 cm^{-1} 1030 cm^{-1} 1080 cm^{-1} 992 cm^{-1} 914 cm^{-1} 986 cm^{-1} 899 cm^{-1}	Amide I Amide II Glycogen Phosphate Nucleic Acid Nucleic Acid Nucleic Acid DNA	broadens in DPCs decrease in DPCs Increase during differentiation Decrease during differentiation Appears in late differentiation stage	Vazquez-Zapien et al. 2016
mPSCs to differentiated kidney cells (DKCs)	16751 cm^{-1} 1650 cm^{-1} 1633 cm^{-1}	Asparagine Glutamine Arginine	All lower in DKCs than mPSCs	Mata-Miranda et al. 2017
hMSCs to chondrocytes	1338 cm^{-1} 1230 cm^{-1} 1203 cm^{-1} 1152 cm^{-1} 1107 cm^{-1} 1080 cm^{-1} 1019 cm^{-1} 993 cm^{-1}	Amide III P-O stretching-C-O-C stretching Aggrecans	Collagen type II (all higher chondrocytes Higher in chondrocytes	Chonanant et al. 2011
murine haematopoietic stem cells (HSCs) from bm-MSCs	966 cm^{-1} 1088 cm^{-1} 1240 cm^{-1}	DNA bands	Higher in mHSCs than BM-MSCs	Zelig et al. 2010

Table 1.5. FTIR peaks for stem cells and their progeny. Table of stem cell FTIR peaks reported in the literature.

The substantial evidence of the specificity and sensitivity of Raman and FTIR as diagnostic tools suggests that these platform technologies are critical to the future of biomedical diagnostics. Further research is required in the areas of CVD and in particular vascular remodelling. The first aim of this research was to determine if the cells composing the injured and healthy vessel models could be discriminated from one another, and if so, could the aforementioned photonic platforms be sensitive enough to discriminate a variety of stem cells from their myogenic progeny, differentiated smooth muscle cells and de-differentiated smooth muscle cells.

1.4 GSK3β and Notch in Myogenic Differentiation

Recent evidence suggests that the source of the SMC-like cells in the vascular lesion are of a stem cell origin. There are no current drugs on the market to target this pathway for in-stent restenosis. Therefore, the mechanisms for vascular stem cell transition to smooth muscle-like cells will be discussed with the aim of identifying a suitable drug target for vascular remodelling due to the accumulation of stem cell-derived progeny.

1.4.1 Mechanisms for myogenic differentiation

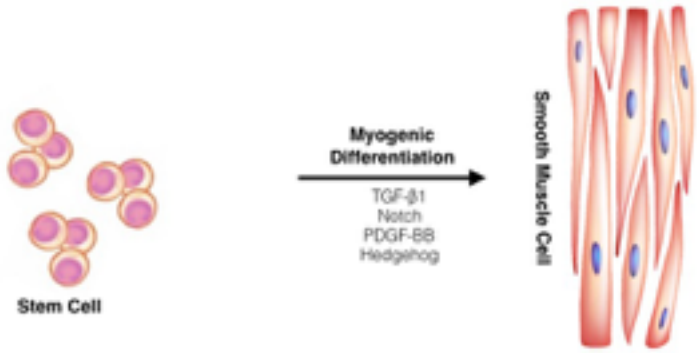

Figure 1.6 Myogenic Differentiation of stem cells to smooth muscle-like cells. Process of vascular stem cell differentiation to smooth muscle cells through signalling molecules TGF-β_1, Notch, PDGF-BB and Hedgehog.

The formation and remodelling of vessels during development and disease, respectively, has been recently reviewed and highlights the importance of smooth muscle cells during angiogenesis, the formation of veins and arteries in the developing embryo, and the recruitment and differentiation of SMCs (Wang, 2015). Two of the factors that are critical for smooth muscle cell formation are platelet-derived growth factor (PDGF-BB) and TGF-β_1, both of which are multifunctional during development. Further to this, another factor identified to be essential for

vascular development is the morphogen, sonic hedgehog (SHh) which up-regulates PDGF-BB and Akt phosphorylation to stimulate SMC migration for neovessel formation (Wang, 2015).

1.4.2 TGF-β_1 Signalling Contributes to Myogenic Differentiation

Not surprisingly, TGF-β in its three isoforms TGF-β_1, TGF-β_2 and TGF-β_3 is involved in SMC differentiation, proliferation, survival and apoptosis with significant detrimental effects observed in mice deficient in TGF-β_1/ TGF-β_2/TGF-β_3 in vivo. TGF-β_1 signalling positively regulates Myh11 and smooth muscle alpha actin (ACTA2) expression through the SMAD complex and Notch signalling in embryonic stem cells and suggests that TGF-β_1 contributes to myogenic differentiation both in vitro and in vivo (Wang 2015).

The mechanisms of TGF-β_1 induction of stem cells to smooth muscle-like cells has been assessed by many groups and involves four signalling pathways (i) the TGF-β_1 control element, (ii) the Smad binding elements (SBE), (iii) the CArG box, (iv) cross-talk with Notch and regulation with microRNAs. Briefly, the TGF-β1 control element has been found in the promotor region of the SMC marker genes SM-22α, SMA, CNN1 and SMMHC (Myh11). TGF-β1 forms a complex with TCE and up-regulates SM-22α and SMA. In a C3H T10/2 mesenchymal like stem cell model, over-expression of Kruppel like factor-4 (KLF4) attenuates the stimulation of TGF-β1 induction of smooth muscle markers. Inhibition of KLF-4 has also been shown to increase SMA and Myh11 markers (Liu et al., 2003; Guo & Chen, 2012).

The Smad binding element (SBE) is essential in the promotor region of the SMC marker genes. The SBE provides a binding region in its sequence for the Smad proteins which regulate TGF-β_1 induced gene expression. In particular, the SM22α promotor SBE is a direct binding site for Smad3. Another pathway shown to be involved in the Smad

dependent TGF-β1 induction of stem cells to SMCs is RhoA. RhoA inhibits Smad2 and Smad3 phosphorylation which is essential for TGF-β_1 gene expression and thus attenuates SMC marker expression. Smad-dependent promotor activity is enhanced by constitutively active RhoA (Chen et al., 2006b; Guo & Chen, 2012).

The CArG box AKA serum response factor (SRF) is also involved in TGF-β_1 induction of SMCs. Enhanced expression of SRF leads to an increase in SMC marker expression in C3H 10T1/2 cells. Mutations in the SRF lead to attenuation of SMC marker expression. Myocardin, a co-factor of SRF, enhances the effect of TGF-β_1 on the SM22α promotor of C3H 10T1/2 cells and increases the Smad3-mediated up-regulation of SM22α, SMMHC (Myh11) and SMA. Although myocardin is critical in development and enhances TGF-β_1 induction of SMCs, there is evidence in the literature that demonstrates that myocardin is not essential for myogenic differentiation (Guo & Chen, 2012).

Notch signalling is also involved in SMC differentiation. The binding of Notch ligands (Delta and Jagged) up-regulates SMC genes SMA, SM22α, Cnn1 and Myh11 in numerous cell lines. Notch increases the binding of TGF-β1 to the Smad promotor and TGF-β_1 increases Notch ligand Jag-1 expression in hMSCs suggesting a cross-talk between Notch and TGF-β_1 signalling. (Kurpinski et al., 2010; Guo & Chen., 2012).

1.4.3 PDGF-BB and myogenic differentiation

PDGF-BB is involved in neo-vessel formation during development and myogenic differentiation. PDGF-BB increases SMC marker expression in C3H 10T1/2 cells and Sca1+ and Flk1+ progenitors (Wang 2015). PDGF-BB was also induces SMC marker expression in human bm-MSCs (Wu et al., 2007) and rat $CD34^+$ resident vascular wall stem cells (Shen et al., 2016).

1.4.4 Notch signalling contributes to myogenic differentiation.

Notch signalling has been shown to be critical during embryogenesis, particularly in vasculogenesis. Mutations in the Notch receptors Notch-1, Notch-2, Notch-3 and Notch-4 and Notch ligands, Delta-like 1, Delta-like 2, Delta-like 3, Delta-like 4, Jag-1 and Jagged-2 have resulted in abnormalities and sometimes fatalities in the developing embryo (Gridley, 2010).

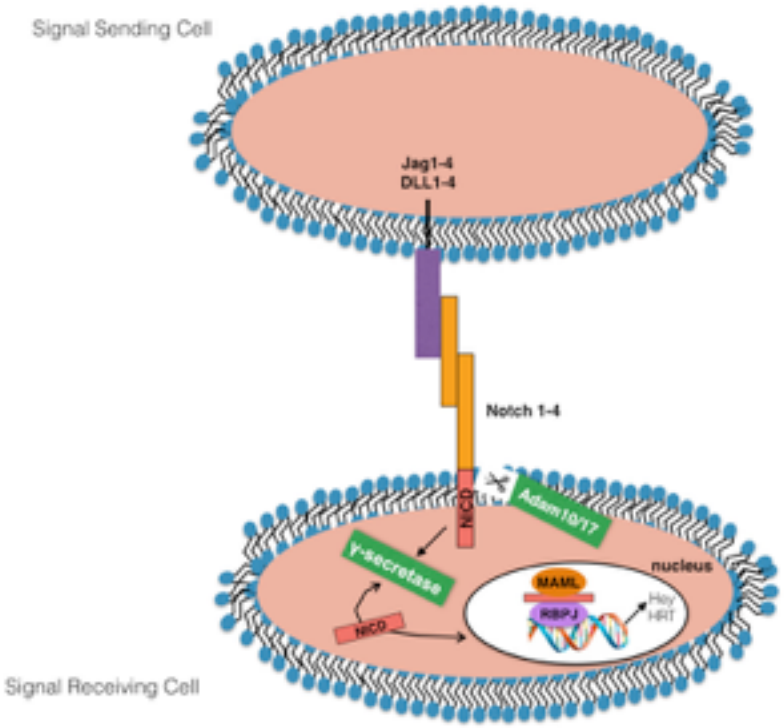

Figure 1.7 Notch signalling in the vasculature, as adapted by Gridley, 2007. The binding of Notch ligands Jagged or delta-like ligands (1-4) from a signalling cell to an adjacent Notch (1-4 receptor) of a receiving cell. The diagram demonstrates the cleavage of the Notch intracellular domain (NICD) by a disintegrin and metalloproteinase domain containing protein (ADAM) and translocation of the NICD by γ-secretase. The NICD then binds to the transcription factor RBJ-k through the mastermind like protein (MAML) to turn on transcription of Notch target genes e.g. Hey, Hes, HRT.

The Notch receptor is a trans-membrane protein that requires the binding of its ligand to undergo a series of proteolytic cleavage steps. The first step, initiated by furin convertase aids in the ligand receptor binding of Notch to the adjacent cell. The second proteolytic step is mediated by

disintegrin and metalloproteinase domain containing protein 10 or 17 (ADAM10/ADAM17) which internalises the Notch receptor by cleaving its extracellular domain (Andersson & Lendahl, 2014). The next step which is driven by Ɣ secretase releases Notch from the membrane to allow it to translocate to the nucleus through the signals in the Notch intracellular domain (NICD). The NICD then binds to the RBP-Jk transcription factor and mastermind like protein (MAML) that can turn on the Notch target genes, hairy and enhancer of split (HES-1, -5, -7), HES-related repressor protein (HERP-1 to -3) and hairy/enhancer of split related with YRPW motif protein (Hey1 to 3) in humans (Gridley, 2010).

1.4.5. Notch signalling in arterial development.

One of the major roles of Notch signalling in arterial development is the fate specification of arterial endothelial cells. Notch signalling has been shown to be downstream of the vascular endothelial growth factor A (VEGF-A). In cell culture, stimulation of VEGF-A in human arterial endothelial cells resulted in an up-regulation of the Notch ligand Dll4 expression (Liu et al., 2013). In vivo, injection of zebrafish with VEGF-A mRNA increased arterial differentiation markers, inhibition of VEGF-A led to a loss of dorsal aortic arterial markers, but injection of Notch-1 mRNA rescued the arterial marker expression in VEGF-A deficient zebrafish demonstrating the role of Notch in VEGF-A directed arteriogenesis (Lawson et al., 2002; Gridley, 2010).

Notch signalling has also been demonstrated to specify smooth muscle cell fate. In particularly, Notch-3 has been reported in the literature to be present in arteries but not veins. Notch-3 deficient mice presented arterial defects such as thinner weakened arteries and also the smooth muscle cells isolated from Notch-3 deficient mice had a downregulation of SMC markers smoothelin and SM22α (Domenga et al., 2004; Gridley, 2010).

1.4.6 Notch signalling in disease.

Notch signalling has been implicated in disease and injury models. Liedner et al., first performed in situ hybridisation of denuded rat carotid arteries (to induce IMT) and compared the gene expression for Jagged 1 and 2, and Notch 1-4. Low levels of Jagged 1, Jagged 2 and Notch-1 were found in the uninjured model, however these levels (along with Notch-2 to -4 levels) significantly increased after injury (Liedner et al., 2001). In Hey2 knockout mice, the levels of neointima formation following injury were markedly reduced compared to wildtype mice and isolated SMCs from the Hey2 deficient mice exhibited reduced proliferation capabilities compared to control SMCs (Sakata et al., 2004). The neointima of heterozygous Notch-$1^{+/-}$ mice and mice with a smooth muscle cell specific Notch-1 deletion resulted in a 70% neointimal reduction compared to wildtype or Notch-3 deficient mice (Li et al., 2009). Perivascular delivery of Notch-1 siRNA can inhibit neointima formation following mouse carotid ligation (Redmond et al., 2014). Levels of Notch-1 protein and mRNA have also been shown to increase in conjunction with levels of sonic hedgehog following carotid ligation in mice (Morrow et al., 2009). Finally, Notch-1, -2 and Jagged 1 are up-regulated in rat carotid arteries following balloon injury. The addition of soluble Jagged1 (which when solubilised is inhibitory for Notch signalling) attenuates this response and the formation of the neointima is disabled (Caolo et al., 2011).

1.4.7 Notch signalling in myogenic differentiation.

Several recent studies have demonstrated a putative role for Notch signalling in promoting myogenic differentiation. Mesenchymal C3H/ 10T1/2 cells were used to examine the role of Notch signalling in controlling myogenic differentiation in response to Jag-1 stimulation. Jag-1 increased Myh11 expression independent of the myocardin serum response factor – CarG complex but dependent on the Notch

transcription factor RBP-jk complex (Doi et al., 2006). Similarly, human embryonic stem cells (hESCs) and bm-MSCs undergo myogenic differentiation through a TGF-β1/Notch signalling axis. The myogenic differentiation response was dependent on the activation of SMAD3 and Rho kinase. In addition, Jag-1 knockdown partially blocked smooth muscle α actin ACTA2 and CNN1 expression and completely blocked MYOCD expression, suggesting that Jag-1 plays an important role in TGF-β1-induced expression of SMC markers. Notch activation also resulted in an increase of neural markers and a decrease of endothelial markers in hESCs (Kurpisnki et al., 2010). Jag-1 also increased CNN1 and smooth muscle α actin (ACTA2) levels in rat mesenchymal stem cells, a response that was attenuated following inhibition with a Notch γ-secretase inhibitor, DAPT (Mooney et al., 2015). In addition, neural crest stem cells from explanted neural tubes undergo myogenic differentiation and increase their expression of SM22α and smooth muscle α-actin. However, neural crest stem cells from explanted tubes of Cre-Pax mice with dominant negative MAM (Mastermind, a complex critical for Notch signalling) had a significant reduction in myogenic cell differentiation capability compared to the control, demonstrating a role for Notch signalling in neural crest stem cell differentiation to smooth muscle-like cells (High et al., 2007). MVSCs have also been shown to differentiate to smooth muscle-like cells in the presence of Notch. Co-cultured MVSCs grown with OP9-Delta 1 feeder cells to supply Notch ligand stained positive for SM-MHC (Tang et al., 2012).

Collectively, these studies suggest that Notch is an important regulator of myogenic differentiation in vitro and neointimal formation in vivo. The presence of resident vascular stem cells and their myogenic progeny in arteriosclerotic lesions suggests that the Notch pathway may be activated during neointimal formation making Notch a potential therapeutic target for inhibiting myogenic differentiation and the accumulation of stem-cell derived myogenic progeny within a lesion.

1.5 Targeting Notch

Several methods to specifically target and inhibit Notch signalling have been reported (Andersson & Lendahl, 2014). Targeting Notch signalling at the first proteolytic step and ligand/receptor binding phase has been addressed. Inhibition of furin convertase has no effect on Notch-2 and little effect on Notch-1 signalling (Kidd & Lieber, 2002). As furin convertase is a multifunctional enzyme and inhibition of it did not have significant effects on Notch signalling, the risk of off target effects outweighs the benefit of inhibition and therefore is not an optimal target for Notch inhibition. Similar off target effects are associated with inhibiting the ADAMs that internalise the Notch receptor to the cell as they are involved with vital proteins tumour necrosis factor (TNF-α) and interleukin-receptor 6 (IL-6) (Andersson & Lendahl, 2014).

It is not surprising, that the enzyme γ-secretase that releases the NICD to turn on transcription of its target genes is the most popular target for Notch inhibition. Many γ-secretase inhibitors have been developed by pharmaceutical companies and have made it to clinical trials. These include DAPT (Eli Lili), BMS-906024 (BMS), MK0752 (Merck), PF-03084014 (Pfizer) and RO4929097 (US National Cancer Institute). The focus of these clinical trials were both Alzheimer's disease or cancer, where Notch signalling has been roundly implicated. The Eli Lily γ-secretase inhibitor trials had to be stopped prematurely due to the discovery that the Alzheimer's patients performed worse compared to the placebo control. The Merck MK-0752 clinical trial and RO4929097 trials had mixed results, particularly when translating the therapy to children but showed a reduction in colonic and glioblastoma tumours respectively. The Pfizer PF-03084014 was also reported to significantly reduce tumour size and decrease Notch target gene mRNA expression in desmoid tumours (Andersson & Lendahl, 2014).

Single chain antibodies have been generated for the Notch ligand binding domain in Notch-1 and -2, but have only been proven to be effective in

mouse models (Falk et al., 2012; Andersson & Lendahl, 2014). The monoclonal antibodies have also been developed for the DLL4 ligand and were shown to be more effective than the gold standard γ-secretase inhibitor in postponing tumour growth in mice. However, this study was limited to a cancer and not vascular model (Liu et al., 2011).

The Notch intracellular domain also undergoes several post-translational modifications that can affect it's signalling and functions. This includes phosphorylation by GSK3β, cyclin-dependent kinase 8 and atypical protein kinase C. These enzymes, in particular GSK3β has been evaluated for its ability to inhibit Notch signalling.

1.5.1 Glycogen synthase kinase 3 beta (GSK3β)

Glycogen synthase kinase 3β is a serine threonine kinase that cross-talks with Notch to regulate it's signalling. It was initially discovered in the glycogen synthase pathway, hence its name (Hall et al., 2001). GSK has two structurally similar domains denoted the α-domain (51kDa) and the β-domain (47kDa) (Woodgett et al., 1990). GSK3β has a broad range of substrates and is unique because of the priming phosphorylation the majority of substrates undergo before further phosphorylation by GSK3β. Basal levels of GSK3β are expressed in resting cells. The activation of GSK3β is due to phosphorylation of it's tyrosine residue at the 216 site (Wang et al., 1994). It is negatively regulated in response to phosphorylation at the serine 9 residue (Pearl & Barford, 2002) .This phosphorylation causes the N-terminal domain of the kinase to fold over and block the site from a substrate (Doble & Woodgett, 2003). GSK3β has been implicated in many diseases such as Alzheimer's disease, tumorigenesis, diabetes and CVD (Guha et al., 2011; Kim et al., 2002).

1.5.2 GSK3β in embryonic development

GSK3β is crucial for development as GSK3β knockdown leads to embryonic death in late development in mice. This is thought to be due to hyperproliferation of early cardiomyocyte precursors that could be

regulated by GSK3β (Force & Woodgett., 2009). GSK3β was first implicated in development in the drosophila model where genetic analysis showed that the GSK3β homologue 'shaggy' was important for cell fate specification in the developing embryo. Wingless, a β-catenin homologue, switched on shaggy during embryogenesis. β-catenin belongs to the Wnt signalling pathway which has an essential and highly conserved role in the embryogenesis of drosophila, zebrafish and mammals. Briefly, the hallmark of the canonical Wnt pathway is accumulation of β-catenin within the nucleus. In the absence of Wnt, cytoplasmic β-catenin is enzymatically degraded by a complex including GSK3β, Axins, casein kinase 1α, adenomatosis polyposis coli and protein phosphatase 2a (Komiya et al., 2008). In the presence of Wnt binding to its receptor complex, frizzled and LRP5/6 disrupts the β-catenin destruction complex releasing β-catenin for signalling. Another protein, disheveled, can bind to the frizzled-LRP5/6 complex and inhibit the destruction complex by inactivating GSK3β which results in an intact and stabilised β-catenin for accumulation in the cytoplasm. The accumulated β-catenin is transported to the nucleus where it binds to the LEF/TCF DNA binding transcription factor complex and turns on genes for embryogenesis. Some of these genes include Twins and Siamois which are organiser-specific genes. The Wnt pathway has also been associated in the anterior head formation, neural patterning, posterior patterning, tail formation and the formation of the internal organs. Due to its crucial role in many pathways in development, Wnt/β-catenin needs to be highly regulated and GSK3β has been shown to regulate Wnt signalling at the β-catenin level (Komiya et al., 2008).

The presence of GSK3β is crucial for vascular development. Targeted knockdown or pharmacological inhibition of GSK3β in developing zebrafish embryos has significant phenotypic defects including incorrect patterning and positioning of blood vessels. This suggest a positive role for GSK3β in the specification of cell fate in the vasculature (Lee et al., 2014). However, inactivation of GSK3β signalling has also been shown to be of importance in angiogenesis. Previously it has been shown that β-

catenin signalling increases following the inactivation of GSK3β and the subsequent formation of capillaries from endothelial cells in Matrigel plug assays in vivo. In contrast to this, the activation of GSK3β inhibited the angiogenesis pattern suggesting that GSK3β regulates angiogenesis at the nodal point of endothelial cell signalling (Kim et al., 2002).

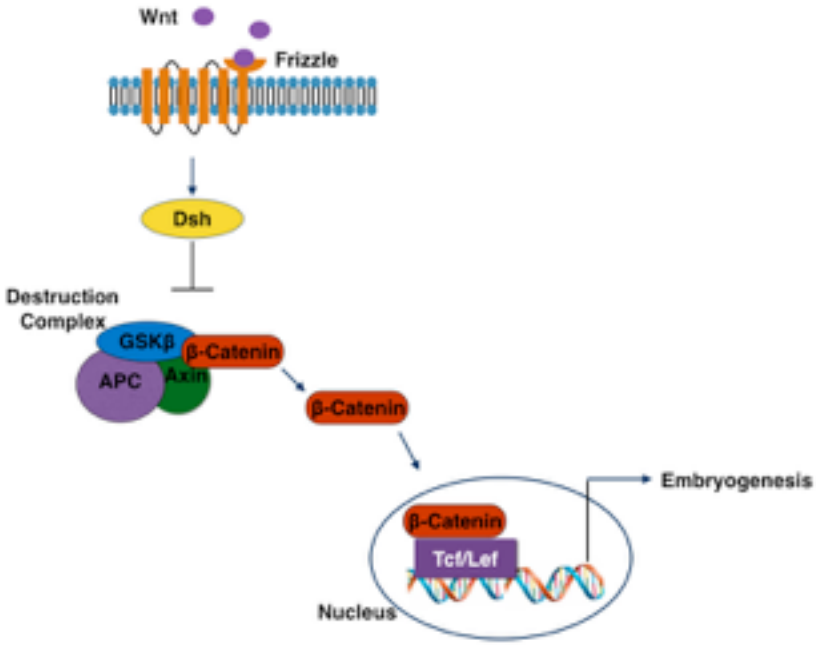

Figure 1.8 Wnt and GSK3β signalling in embryonic development. Demonstration of the Wnt ligand binding its receptor frizzled and activating dishevelled to inactivate the destruction complex including GSK3β to release β-catenin for translocation to the nucleus to drive transcription of embryogenesis genes. Figure adapted from Majid et al., 2012.

1.5.3 Targeting GSK3β

GSK3β has been evaluated as a drug target for diseases such as Alzheimer's and cancer. The initial prescribed GSK3β inhibitor was lithium, which was prescribed to patients with neurological disorders such as depression. Lithium simply phosphorylates GSK3β to its inactive state and studies have shown a decrease in active GSK3β signalling within 2 days of lithium treatment and stabilisation in patient moods (Jope et al., 2003). Lithium has also been used in clinical trials involving bone marrow

transplants and was shown to aid in the mobilisation of haematopoietic stem cells. Lithium carbonate has also reached clinical trials for Alzheimer's and bipolar disorder. In cancer research, lithium has been shown to suppress cell migration in spheroid cultures of glioma cells (McCubrey et al., 2016). There have been many pharmaceutically derived GSK3β inhibitors manufactured. Some of these include AR-A014418, AZD1080, CHIR-99021, SB216763, SB415286 and TDZD-8. The majority of the inhibitors do not discriminate between the α- and β-forms of GSK3 and work in an ATP-competitive manner. GSK3β inhibitors including Tideglusib has made it to clinical trails for Alzheimer's treatment and Divalproex for mood disorders. In pre-clinical cancer trials, GSK3β inhibitors such as SB415286 were shown to inhibit proliferation, promote cell cycle arrest and cause apoptosis in leukaemia cells. Other inhibitors SB216763, GSK-3 IX and allsterpaullone have also shown to suppress leukemia cell growth (McCubrey et al., 2014).

Although inhibition of GSK3β has been shown to be highly successful for the treatment of mood disorders, Alzheimer's disease and some cancers so far, the focus for this thesis work is vascular remodelling. In 2009, Ma et al., compared restenosis rates in rabbits that contained bare metal stents, stents coated with a typical drug rapamycin, stents coated with AR-A014418 or stents coated with rapamycin and AR-A014418. The researchers found that the neointimal size was 45% lower in the GSK3βi coated stent than bare metal stent and 49% lower compared to the rapamycin only stent. The researchers also showed that the combination of the GSK3βi and rapamycin resulted in faster re-endothelialisation on the stent (Ma et al., 2009).

Initial studies targeting GSK3β inhibitors have shown success however much of the focus has been directed towards endothelial cells. The aim of this thesis is to evaluate the role of GSK3β inhibition on stem cell transition to SMCs, particularly through the Notch pathway which has been shown by us and others to be significant in vascular remodelling (Redmond et al., 2014, Morrow et al., 2009, Li et al., 2009).

1.5.4 GSK3β Signalling in the vasculature

GSK3β signalling is functional within vascular smooth muscle cells. Pharmacological inhibition and siRNA knock down of GSK3β showed an attenuation in myocardin and smooth muscle markers CNN1, SMA and SM22α in human vascular smooth muscle cells. Complementary to this, enhanced GSK3β expression through a constitutively active mutant showed an increase in the myocardin/SMC markers (Zhou et al., 2016).

1.5.5 GSK3β in vascular disease

Several studies have addressed the putative role of GSK3β in vascular disease. Woulfe et al. (2010) generated a mouse model that allowed for inducible deletion of GSK3β and reported an improvement in ventricular diameter and function and subsequently vascular remodelling following knockdown (Woulfe et al., 2010). In another mouse, pharmacological inhibition of GSK3β resulted in a significant attenuation of atherogenesis in hyperglycaemic ApoE-deficient mice compared to the no-drug control (Bowes 2009). Inhibition of GSK3β also improved vessel diameter and blood flow in porcine vascular disease models (Potz et al., 2016). In a rat atherosclerotic model, there was a significant decrease in inactivated GSK3β (Ser9) which would suggest a concomitant increase in activated GSK3β signalling along with typical atherosclerotic markers such as increased total cholesterol, triglycerides and LDL and a decrease in LDL (Wang et al., 2013). Similarly, the levels of inactive GSK3β phosphorylated at Ser9 were substantially lower within the neointima following carotid artery ligation suggesting the accumulation of the active form of GSK3β (Guha et al. 2011).

1.5.6 GSK3β and Notch Signalling

GSK3β has previously been shown to act downstream of Notch in drosophila models (Ruel et al., 1993) and to regulate and phosphorylate the Notch intracellular domain (NICD) (Foltz et al., 2002). Using GSK3β null and wildtype mice the levels of phosphorylated Notch NICD increase

following the addition of GSK3β suggesting that GSK3β directly phosphorylates the Notch intracellular domain and aids in Notch signalling by protecting the intracellular domain from proteosomal degradation (Foltz et al., 2002). A similar role of GSK3β in Notch signalling in rat aortic smooth muscle cells (SMCs) has also been reported (Guha et al., 2011). Notch-3 NICD and Notch target genes Hey1 and Hey2 were enhanced following ectopic expression of GSK3β whereas these levels decreased following either siRNA knockdown of GSK3β or pharmacological inhibition of GSK3β. These results suggest that active GSK3β is essential for Notch signalling in vascular SMCs (Guha et al., 2011).

1.6 Nanoparticles as drug delivery platforms for stents

1.6.1 In-Stent Restenosis (ISR)

The most common form of therapy for cardiovascular related events is balloon angioplasty and subsequent stent placement. Balloon angioplasty involves minor surgery inserting a balloon inside the vessel occluded with the plaque, inflating the balloon so that the plaque is pushed back against the vessel wall and thus the artery is opened (White et al., 2005). However, up to 40% of patients resulted in a re-occlusion of the artery, this is referred to as restenosis. Clinicians then began to insert bare metal stents during balloon angioplasty to hold the artery open after the procedure. Even after stent placement, 25% of patients displayed what is called 'in-stent restenosis' (Dangas et al., 2002). Other than the necessity to identify and further target the cells that contribute to the neointimal hyperplasia, another issue contributing to the high failure rate of stents is the eventuality that all drugs will deplete over time. It is a secondary aim of this thesis to develop a novel delivery platform for replenishing the stents with drugs.

Various types of stents have been developed over the last number of years to combat in-stent restenosis (See Table 1.6).

Stent Type	Composed of	Advantages	Drawbacks	Reference
Stainless Steel	Iron and chromium	Re-opens occluded artery	Disrupts endothelium and causes restenosis	Alberts et al., 2002; Palmaz et al., 1992
Cobalt Chromium	Cobalt Chromium	Thinner than stainless steel	Causes restenosis	Kereikas et al., 2003
Absorbable Metal Stent	Biodegradable magnesium	Reduces restenosis rate compared to stainless steel	Causes restenosis	Bose et al., 2006
Polymer coated stent	Coatings e.g. phosphorylcholine and polyvinyl purrolidone	Prevents contact of metal stent with blood	TBD	Yin et al., 2014

Stent Type	Composed of	Advantages	Drawbacks	Reference
Drug eluting stent	Metal mesh stents coated with drugs e.g. rapamycin and sirloins	Reduces neointimal formation compared to bare metal stents	Drugs deplete over time e.g. rapamycin by day 30 and sirolimus by day 14	Lüscher et al., 2007; Halkin et al., 2004

Table 1.6. Table of DES stent types used for CVD models.

The original stent introduced was the stainless steel bare-metal stent that resulted in restenosis in 25% of patients (Dangas et al. 2002). Following that, cobalt chromium stents were employed in a clinical trial where 15.7% of patients suffered binary restenosis by day 180 (Kereikas et al., 2003). Clinical trials were also carried out for absorbable metal stents such as biodegradable magnesium stents and binary restenosis was detected by 1 year (Bose et al., 2006). Various polymers are being constructed as stent models and for coating of stents to attempt to reduce restenosis rates in patients, however none have made it to market yet (Yin et al., 2014). Stents coated with drugs such as rapamycin and sirolimus are currently used in up to 90% of patients (Jeremias et al. 2008) yet the rate of restenosis is still unacceptably high (White et al. 2005). In vitro studies have determined that the commonly used drugs rapamycin and sirolimus deplete after 30 and 14 days, respectively (Lüscher et al., 2007; Halkin et al., 2004) which suggests a reason for current failure rate of drug-eluting stents (DES). The ability to replenish a stent with a drug is an attractive solution to the current issue.

1.6.2 Nanoparticles for drug delivery

The first nanoparticles developed for drug use were formulated by Speiser and colleagues in the late 1960's. They were initially developed to achieve a controlled release of antibodies from tetanus vaccines (Kreuter et al., 2007). Nanoparticles are particles that range between 1 and 100 nm in size and show great promise as drug delivery vehicles due to their small size. Nanocarriers ranging from approximately 50 to 400 nm can easily transport drugs around the blood-stream, whilst nanoparticles

of less than 1 nm in size can even cross the blood-brain barrier (Siafaka et al., 2016). Nanoparticles are therefore, ideal vehicles for drug delivery and targeting.

1.6.3. Important characteristics of nanoparticles for drug delivery systems

- **Size**

Particle size is the most important characteristic when considering nanoparticles for drug delivery systems. The size of the NP determines the toxicity, in vivo distribution, stability, drug release (smaller the particle, the closer to the surface the drug is for release) from the nanoparticle, cellular uptake in vitro and in vivo, and if small enough, can cross the blood-brain barrier. The most common method to determining the size of nanoparticles is Dynamic Light Scattering (DLS), which relies on scattering of light from nanoparticles in response to a laser source (Singh et al., 2009).

- **Surface Properties**

Nanoparticles can be recognised as foreign particles by the body and therefore functionalisation of nanoparticles, as discussed below, can aid nanoparticles to evade the immune response and increase cellular uptake by cells. Also, the surface charge, or zeta potential, is of critical importance. Nanoparticles with a surface charge of ±30mV have greater stability in suspension as the charged particles will repel each other and thus prevent aggregation. Zeta potential is also determined by DLS. (Singh et al., 2009; Zhang et al., 2008).

- **Drug Release**

The rate of release of a drug from a nanoparticle must be carefully monitored to prevent toxicity but also to ensure enough is released for disease targeting. Drug release from nanoparticles usually occurs by diffusion through or dissociation from the encapsulating matrix. Rapid

release from nanoparticles can occur if the drug weakly binds the associated matrix. More sustained drug release can be attained by incorporating the drug inside a shell such as a polymer. Release studies are most commonly carried out by controlled agitation and centrifugation or by dialysis whereby the drug released from nanoparticles are in supernatants (Singh et al., 2009). In this context, a Her2 receptor ligand humanised mAb trastuzumab has been conjugated to nanoparticles and targeted to breast tumour cells in vitro and in vivo and is currently being evaluated as a specific breast cancer detection probes for MRI contrast agent (Bazak et al., 2015). Passive targeting on the other hand involves incorporating the therapeutic agent inside the nanoparticle for cellular uptake.

• **Passive targeted nanoparticles for dug delivery**

One of the main benefits to using nanoparticles is the potential to specifically target cells and tissue. There are various types of nanoparticle formulations described for targeted transport of drugs to cells. These include but are not limited to, lipid-based nanocarriers, liposomes, chitosan nanoparticles, hyaluronic acid and polymers. Each of these formulations are outlined briefly below (Siafaka et al., 2016).

- **Lipid-Based Nanoparticles**

Lipid based nanoparticles are desirable nanocarriers for hydrophobic drugs as they enhance the stability of the drug in solution. Lipids are naturally variable in their physiochemical, absorption and digestible properties and therefore there are a wide range of lipid-based nanoparticles to choose from based on the properties and target of the drug (Siafaka et al., 2016).

- **Solid Lipid Nanoparticles**

Solid lipid nanoparticles are nanocarriers consisting of a solid hydrophobic core containing a solid lipid matrix that the drug can be dispersed or dissolved in. The lipids can be anything from triglycerides,

glycerides, fatty acids to steroids and waxes. Drugs such as pilocarpine, paclitaxel, doxorubicin (DOX), timolol, tobramycin, diazepam, nifedipine, hydroxcortisone and desoxycorticosterone have been successfully loaded into SLNs (Siafaka et al., 2016).

- Lipid Nanocarriers (NLNs)

Nanostructured lipid nanocarriers are lipid nanoparticles containing a solid and liquid core matrix. NLNs have shown greater drug solubility, bioavailability, permeability, decreased adverse effects and prolonged half-life in comparison to solid lipid nanoparticles. Therefore, they are a more attractive nanocarrier to the SLN provided the inner core can tolerate the hydrophobicity of the drug (Siafaka et al., 2016).

- Liposomes

Liposomes are lipid nanoparticles of an aqueous core entrapped in a lipid bilayer. The hydrophobic and hydrophilic portions of the liposome make it possible to incorporate hydrophobic or hydrophilic drugs. Liposomes have been widely successful so far. For example, liposomes functionalised with polyethylene glycol (PEG) and folate have been shown to be ideal carriers for paclitaxel to the lymphatic system. Liposomes functionalised with a specific breast cancer targeting peptide (H6, YLFFVFER) has successfully targeted Her2 positive cancer cells in vitro and in vivo. Finally, PEGylated liposomes modified with ox26 and chlorotoxic have managed to cross the blood brain barrier to promote brain glioma cell transfection with anti-cancerous plasmid DNA (Jia et al., 2016; Siafaka et al., 2016).

- Chitosan NP

Naturally occurring cationic polymer chitosan can be found in the exterior skeleton of crustaceans and is showing promise as a nanocarrier system. Due to the active amino and hydroxyl groups on its surface, chitosan can be easily modified for functionality. For example, pure chitosan based Nanoparticles have been used in conjunction with sodium alginate beads

to improve the oral delivery of DOX and PEGylated CS functionalised with folate and with paclitaxel incorporated has shown to enhance tumour penetration of PTX (Li et al., 2016; Siafaka et al., 2016).

- **Hyaluronic Acid**

Hyaluronic acid (HA) is a cyto- and histo-compatible polysaccharide consisting of D-glucuronic acid and D-N-acetylglucosamine. HA can be used as a nanocarrier itself or as a functionalizing agent for some of the aforementioned nanoparticles. PEGylated HA nanoparticles have been developed for anti-cancer drugs. HA Nanoparticles modified with cholesterylhemisuccinate have been used to incorporate docetaxal for tumour tissue targeting. The major drawback of HA is that it can accumulate in the liver and therefore could be harmful in high doses (Song et al., 2014; Siafaka et al., 2016).

- **Nanocarriers of synthetic polymers**

Synthetic polymers such as poly(lactic acid) (PLA), poly(e-caprolactone) (PCL) and poly(lactic acid co-glycolic acid) (PLGA) have been examined as potential nanocarriers for various drugs over the last decade. They are all aliphatic polyesters and other than PCL have been generally regarded as safe by the FDA. PCL has crystallinity issues making it a less attractive carrier than PLA and PLGA. Like the aforementioned nanoparticles, polymer nanoparticles such as PLA and PLGA can be further functionalised by coatings such as PEG or HA (Siafaka et al., 2016).

Coating PLA with PEG has been shown to aid the transport of PLA nanoparticles to the intestine and subsequently to the epithelium. Multiblock polymer nanoparticles consisting of PLA and poly(methacrylic acid) have been utilised to incorporate paclitaxel and target intestinal cancer (Luo et al., 2014). PLA has also been functionalised with a folate-core polylactide-D-α-tocopheryl polyethylene glycol 1000 succinate (FA-PLA-TPGS) to load emtansine (DM1) to target breast cancer in vitro and in vivo and resulted in greater anti-cancer activity than the non-drug

loaded copolymer nanoparticles (Tang et al., 2013). Similarly, FA-PLA-TPGS nanoparticles loaded with paclitaxel have shown greater activity than free paclitaxel. Multiblock polymer of thiolated chitosan-modified-PLA-PCL-TPGS-PTX successfully targeted lung cancer orally (Jiang et al., 2013).

Similar to the PLA copolymer model, PLGA functionalised with TPGS and cholic acid were employed as transport agents for docetaxal to cervical cancer cells (Zeng et al., 2013). PEGylated PLGA loaded with oleanolic acid expressed greater cancer cell cytotoxicity in vitro. PEGylated PLGA Nanoparticles have also been functionalised with HA to target ovarian cancer cells (Vangara et al., 2013; Siafaka et al., 2016).

1.6.4. Externally controlled drug delivery system:

The most recent method of specific targeting involves the use of magnetic nanoparticles that can be externally targeted to the site of injury or tumour based on an external magnetic field (Li et al., 2012).

The most extensively studied magnetic nanoparticle for biomedical purposes is the iron oxide Fe(II)Fe(III) nanoparticle, Fe_3O_4 NP. In general, the iron oxide magnet nanoparticle (MNP) has a net zero magnetic charge although it has randomly aligned magnetic moments. This means that the MNP requires external magnetic fields to align the magnetic moments and activate the magnetic property of the nanoparticle. The most common form of magnetic nanoparticle is the superparamagnetic iron oxide nanoparticle (SPION) which is characterised by its small size (<20 nm) and its single magnetic domain region. The SPION is the more attractive form of the MNP for biomedical applications as it requires external magnetic fields for magnetisation and exhibits no residual magnetism post magnetisation which reduces the risk of aggregation of the MNPs in vivo (Mohammod et al., 2017).

MNPs must be polymer coated to become more biocompatible and reduce toxicity. The main methods of coating are ligand addition or ligand exchange. Ligand addition involves the hydrogen bonding or hydrophobic interactions of, most commonly, a polymer to the surface of the MNP. This can result in the encapsulation of the MNP inside the polymer coat. Ligand exchange involves replacing the surface of the nanoparticle with functional groups, this can be done with a polymer. A range of polymers have been used to coat MNPs in the literature and include, but are not limited to, PEG, PVA, PLGA, dextran, gelatin and chitosan (Mohammod et al., 2017).

There has been much success in drug loading polymer coated MNPs, particularly, in the areas of cancer. The use of the external magnetic field to specifically target drugs to disease cells results in higher specificity of drug targeting in vitro and in vivo. Anti-cancer drugs DOX, PTX, methotrexate (MTX) and epirubicin have all been reportedly formulated with MNPs. MNPs loaded with MTX and targeted to cancer cells with an external magnetic field resulted in controlled release of MTX in vivo (Kohler et al., 2006). DOX and curcumin loaded PVA-PAA (polyacrylic acid) coated MNPs resulted in higher tumour suppression in mice than DOX alone (Fang et al., 2014). Chitosan functionalised MNPs loaded with PTX have been reported for targeted delivery in lung cancer and Fe_3O_4-carboxymethyl chitosan nanoparticles loaded with rapamycin have also been targeted to cancer cells (Mangaiyarkarasi et al., 2016). Some SPIONs have been clinically approved for drug delivery, mainly in the area of cancer treatment. These include Feridex® and Resovist® for liver cancers, Abdoscan® and Lumirem® for bowel cancers and Feraheme® for the vasculature (Mohammod et al., 2017).

1.6.5 Methods to generating polymer coated SPIONs

Various methods for synthesising SPIONs and particularly encapsulated SPIONs have been described in the literature and has been described in detail in a review by Wu et al. (2015). The most common technique for

synthesising MNPs is the co-precipitation method. Briefly, the method involves combining ferric and ferrous oxide ions at a 1:2 molar ratio in basic conditions at room temperature to give the resulting Fe_3O_4-NP. Following this, the synthesised MNPs are typically encapsulated into polymers or undergo ligand exchange with polymers, as described above, with or without drugs for functionalisation. Magnetic nanoparticles are typically encapsulated in polymers such as PLGA or PEG by either the single or double oil in water emulsion solvent evaporation method. This method involves adding the magnetite to the polymer and adding this phase to an aqueous phase containing a stabilising superfactant. This solution is then agitated or most commonly sonicated to form polymer-magnetite droplets, or nanoparticles, in the aqueous phase. The organic solvent at which the polymer and magnetite were dissolved in, prior to mixing with the aqueous phase, subsequently evaporates leaving hardened nanoparticles (Massart, 1981; Wu et al., 2015).

1.6.6 Drug-Carrying Nanoparticles for Drug Eluting Stents

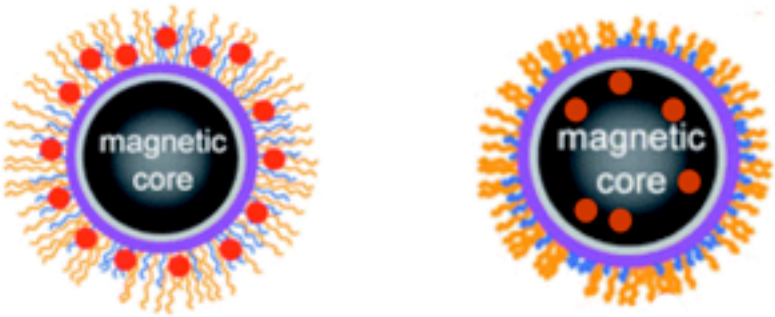

Figure 1.9. Drug loading of magnetic nanoparticles. Magnetic nanoparticles coated in polymers and co-polymers with the therapeutic agent attached to the surface or incorporated inside the nanoparticle. Figure adapted from Luoguet et al. (2012).

One of the first studies to use nanoparticles for in-stent restenosis treatment was carried out by Danenberg et al., in 2002. This group incorporated a bisphosphonate agent (clodronate), to target monocytes and macrophages at the site of injury, into a liposome and targeted

neointima formation in rabbits. The results showed a significant reduction in neointimal formation following balloon angioplasty and treatment with the liposome clodronate (Danenberg et al., 2002). The group also compared methods of delivery of the liposome by administering the liposome clodronate intraluminally, IV and subcutaneously. They reported systemic delivery as the best delivery platform to have the greatest effect on restenosis in rabbits (Danenberg et al., 2003).

Alendronate, a bisphosphinate agent, encapsulated into a polymer PLGA nanoparticle, has also shown success in inhibiting macrophage like cells and smooth muscle like cells in vitro by 98% and 61% respectively. In vivo, the alendronate PLGA-NPs (ALN-NPs) reduced the neointima to media ratio by 52.7% and stenosis rate by 39.7% in rabbits after 28 days (Cohen-Sela et al., 2006).

Paclitaxel loaded PLGA:PEG polymer shells which were functionalised with heptameric peptides referred to as ‘nanoburrs’ were targeted to rat coronary arteries after balloon angioplasty. The nanoburr treated group had the greatest reduction in N/M ratio at 0.662+- 0.169, approximately 53% lower than the control group. A free paclitaxel group also exhibited a lower rate of restenosis than the control but not as significantly reduced as the nanoburr group at 0.937±0.126μM which is approximately 25% less than the sham control. The NP only group had the least N/M ratio reduction at 1.063±0.097μM which is approximately 11% less than the untreated control (Chan et al., 2011).

Paclitaxel loaded polymer coated MNPs (like Figure 1.9) have recently inhibited 98% of smooth muscle cells growth, however this result was dependent on an external uniform magnetic field. Without the presence of a magnet, only 45% of SMC proliferation was inhibited. In vivo, there was a 4 fold increase in MNPs localised to a rat carotid stent when the external magnetic field was applied and this led to a 63% reduction in neointimal formation compared to a traditional stent control. The PTX-

MNPs under non-magnetic conditions had a statistically insignificant effect on neointimal formation compared to the traditional stent control (Chorny et al., 2010).

MNPs loaded into endothelial cells (ECs) have been targeted stents in rat carotid arteries using a uniform magnetic field. This results in a 1.7 fold less loss of lumen diameter and 2.1 fold reduction in stenosis in the EC-MNP treated group compared to the non-treated control (Polyak et al., 2016). In a similar concept, endothelial cells genetically modified with enhanced eNOS (endothelial nitric oxide synthase) were loaded with MNPs and targeted to the vascular wall following injury via an external magnetic field. The injured vessel wall showed an increase in the vasoprotective eNOS marker and restoration of endothelial function following eNOS EC-MNP treatment compared to the control (Vosen et al., 2016).

Although polymer coated SPIONs have shown great promise for specific drug delivery and improved drug targeting and effects, most of the research is limited to cancer models. Within the area of vascular diseases, the focus has been on targeting stents with SPIONs to improve re-endothelialization following injury. The aim of the research in this thesis therefore, is to incorporate an inhibitor into a polymer coated SPION to attenuate resident vascular stem transition to smooth muscle-like cells which may be used in the future as a novel method of inhibiting in-stent restenosis (ISR).

1.7 Aims & Objectives:

The following aims and objectives were addressed:

Aim 1: To establish whether stem cell-derived myogenic progeny could be distinguished from differentiated (normal healthy, dSMCs) and de-differentiated (arteriosclerotic, ddSMCs) vascular smooth muscle cells in vitro using microfluidic capture of individual cells and measurement of the autofluorescence (AF) signatures in response to broadband light.

- **Objective 1:** Evaluate AF photonic differences between healthy differentiated vascular smooth muscle cells (dSMCs) and injured arteriosclerotic de-differentiated medial and neointimal cells (ddSMCs) following carotid artery injury.

- **Objective 2:** Generate AF photonic signatures for undifferentiated stem cells, their myogenic progeny and differentiated smooth muscle cells.

- **Objective 3:** Compare AF photonic signatures for stem cell-derived myogenic progeny with differentiated vascular smooth muscle cells (dSMCs) and arteriosclerotic medial and neointimal cells following carotid artery ligation-induced injury.

- **Objective 4:** Identify the specific role of auto-fluorescent molecules collagen and elastin in contributing to the the spectral differences between undifferentiated stem cells, their myogenic progeny.

Aim 2: To establish whether stem cell-derived myogenic progeny (St-SMCs) could be distinguished from de-differentiated (arteriosclerotic,

ddSMCs) vascular smooth muscle cells in vitro using vibrational spectroscopy, FTIR and Raman.

- **Objective 1:** Validate FTIR and Raman spectroscopy at discriminating undifferentiated mesenchymal stem cells (bm-MSCs) from their osteogenic progeny (St-Osteo).

- **Objective 2:** Generate photonic signatures and discriminate populations of undifferentiated stem cells (bm,-MSCs), their myogenic progeny (St-SMCs) from de-differentiated smooth muscle cells (ddSMCs) in vitro using FTIR.

- **Objective 3:** Generate photonic signatures and discriminate populations of undifferentiated stem cells (bm,-MSCs), their myogenic progeny (St-SMCs) from de-differentiated smooth muscle cells (ddSMCs) in vitro using Raman spectroscopy.

- **Objective 4:** Identify the specific molecular signatures that contribute to the spectral differences between undifferentiated stem cells, their myogenic progeny and de-differentiated ddSMCs by Raman spectroscopy.

- **Objective 5:** Establish a novel platform that discriminates stem derived myogenic and osteogenic progeny from the same undifferentiated stem cell population.

Aim 3: Identify an effective GSK-3β inhibitor of myogenic differentiation and incorporate the inhibitor into novel polymer-coated magnetic nanoparticles *in vitro.*

- **Objective 1:** Identify a suitable GSK-3β inhibitor to attenuate myogenic differentiation of undifferentiated resident vascular stem cells *in vitro*.

- **Objective 2:** Optimise the fabrication of polymer coated magnetic nanoparticles and functionalisation with a GSK-3β inhibitor using an oil in water emulsification technique

- **Objective 3:** Determine the functionality of inhibitor-loaded magnetic nanoparticles *in vitro*.

Chapter 2

Materials & Methods

2.1 Materials

All materials were of the highest purity commercially available and were of cell culture standard where applicable. See appendix A for a full list of materials.

2.2 Cell Culture & Maintenance

All cell culture techniques were carried out in a clean and sterile environment using a Bio air 2000 MAC laminar flow cabinet. Cells were visualised using an Olympus CK30 phase contrast microscope and maintained in a Hera water jacket cell incubator at 37˚C in an atmosphere humidified with 5% CO_2.

2.2.1 Primary Aortic Smooth Muscle Cell Isolation and Culture

The thoracic aorta was isolated from Sprague-Dawley rats and C57/BL6 mice and placed in Hanks balanced salt solution (HBSS), pH 7.4, before adipose fat and the endothelium were removed by gentle rubbing. Once the aorta was cleaned, it was placed into a Dulbecco's Modified Essential Medium (DMEM) solution containing 0.7 mg/ml collagenase (Sigma/ C9891-500 mg) in TNS (Soybean Trypsin Inhibitor in MEM with 0.1% FBS, Roche, Dublin/Ireland) for 20 min at 37°C to loosen the adventitia before complete removal using a fine-forceps under a dissecting microscope. The remaining medial layer was placed in the DMEM solution containing 1.25 mg Elastase Type III (Sigma, E0127) and incubated at 37°C for a further 2h with repeated gentle agitation until the medial layer was completely dissociated. Once fully dissociated, the aortic medial cells were centrifuged and washed twice in complete medium (DMEM supplemented with 10% FCS and 1% penicillin/ streptomycin) before the cells were plated and grown in RPMI-1640, 20% FBS (Sigma, F9665) and 1% Penn-Strep (Sigma, P4333) to passage 4. The mouse aortic medial cells were generally fixed with 3.7%

formaldehyde, dissociated and added directly to the microfluidic chip rather than cultured.

2.2.2 Primary Multipotent Vascular Stem Cell Isolation and Culture

Multipotent vascular stem cells (MVSCs) were isolated from rats as described by Tang et al. (2012). Briefly and as described above, the aorta from Sprague-Dawley rats were isolated and stripped of fat and the endothelium in Hanks balanced solution (HBSS), pH 7.4. To remove the adventitia, the aorta was cleaned and was placed into a Dulbecco's Modified Essential Medium (DMEM) solution containing 3.5 mg/ml collagenase (Sigma/C9891-500 mg) in TNS (Soybean Trypsin Inhibitor in MEM with 0.1% FBS, Roche, Dublin/Ireland) for 20 min at 37°C to loosen the adventitia before complete removal using a fine-forceps under a dissecting microscope. The resulting media was finely sliced and placed on tissue culture plates. The explanted cells were then grown in maintenance media containing DMEM (ATCC-30-2002), 1% FBS (ATCC-SCRR-30-2020), 1X B-27 supplement (Gibco A17504-044), 1X N2 supplement (Gibco A13707-01), 2% chick embryo extract (Seralab CE-650-J), 20 mg/ml of rmFGF (3139-FB-025; Bio-techne), 10mM retanoic acid (R2625) and 500μM β-mercaptoethanol (M7522; Sigma).

2.2.3 Cell Line Culture

Rat and mouse mesenchymal stem cells (Gibco S1601-01, Gibco S1502-01 respectively) and mouse C3H 10T ½ cells (ATCC-CCL-226) cells were purchased and cultured as per the manufacturers instructions. Cells were grown in alpha MEM + Glutamax and Eagles Modified MEM respectively with 10% stem cell qualified FBS (ATCC-SCRR-30-2020) and 1% penicillin/streptavadin (Sigma; P4333-100 ml). Cells were subcultured by washing three times with PBS, incubating the adherent cells with Triple E Select (Thermofisher; 12563029) for 3 minutes. The Triple E was neutralised with serum containing media and the cells were

centrifuged at 400 x g. The resulting pellet was resuspended in fresh medium and seeded based on experimental requirements.

2.2.4 Carotid Artery Ligation

Sham and ligated carotids from the same C57/BL6 mouse were obtained from a collaborator, Prof Redmond at the University of Rochester (NY). Briefly, cervical incisions were made to anaesthetised mice and the left carotid artery was ligated using a 6-0 silk structure near the carotid bifurcation. The sutures were closed and the animals allowed recover. Vessels were harvested 14 days post-ligation. The morphometric analysis was carried out in collaboration with Prof Eileen M Redmond at the University of Rochester, Rochester NY.

2.2.5 Stem Cell Myogenic Differentiation

To induce osteogenic differentiation, rat mesenchymal stem cells were grown in StemPro Osteogenesis medium (Thermo-fisher A1007201) for 21 days as per the manufacturers protocol. Myogenic differentiation was achieved with TGF-β_1 (R&D 7666-MB-05) (2-10ng/ml) for 2-14 days or Jagged1-1Fc (2 μg/ml) (R&D, 599-JG-100). The dose chosen to treat cells was decided by a trial and error approach where the least dose that elicited a significant effect was used for all similar experiments. The time chosen for myogenic differentiation was dependent on the process intended to up regulate whereby promotor activity takes the least time and protein expression takes the most time.

To immobilise Jag-1 to a cell culture plate, each well was first immobilised with protein G (MSC 21193) (20 μg/ml) overnight at 4˚C. Following the overnight incubation, the wells were washed three times with sterile PBS and blocked with 1% BSA for 2 hours at room temperature. This was then removed and the wells washed as before before addition of 2 μg/ml control IgG-Fc (R&D, 110-HG-100) or Jag-1-Fc and further incubation for 2 hours. This solution was removed and the wells washed again before

cells were seeded at a density of 20,000 cells/well directly onto the treated plates and incubated at 37˚C for 1-7 days.

2.2.6 RNA Interference and gene manipulation

The Mirus TransIT-X2 Dynamic Delivery System was used for all siRNA transfections and was carried out as per the manufacturers instructions. Briefly, approximately 20,000 cells/well were seeded on 6-well plates 24 hours prior to transfection. On the day of transfection, 25 nm of siRNA was added to 250µL of opti-MEM I reduced serum media and 7.5µL of TransIT-X2. This was left for 25 minutes to allow complexes to form. The complexes were then added and incubated for up to 72 hours before RNA was isolated for gene expression analysis and 7 days for LiPhos measurements.

2.2.7 Pharmacological Inhibition of GSK3β activity

Inhibitors of GSK3β: SB-216763 (S3442), Bio (B1686) and 1-Azakenpaullone (1-Aza) (A3734) were compared for their inhibitory actions.

2.3 Living Photonics (LiPhos) of individual cells

LiPhos platforms are biophotonic tools deployed to interrogate individual cells using microfluidics and determine their photonic fingerprint (PIN) to broadband light.

2.3.1 Biochip Preparation and Microfluidic Testing: Biochips were prepared as described previously [Burger 2015]. Briefly, the biochip was fabricated in PDMS (Sylgard 184, Dow Corning GmbH, Germany) in pre-casted PDMS moulds that were surface micromachined using SU8-3025 (Microchem, USA) to include the V-cup array (47 x 24 cups) and reservoirs. The middle chip supporting layer consisted of poly(methyl meth-acrylate) (PMMA) with a thin layer of pressure sensitive adhesive

(PSA), this layer was defined using a laser cutter (Epilog Zing Laser, Epilog USA) and a microscope slide was bound to the PSA. The chip was treated by air plasma (1000 mTorr) for 5 minutes and assembled.

2.3.2 Biochip Sample Loading The device was placed in a vacuum prior to introducing the liquids for a minimum of 30 minutes ensure complete and bubble-free filling. Other than the fresh aortas that were already in suspension and the pre-fixed carotids in suspension, all cells that had finished their treatments were washed three times and then trypsinized with trypLE Select (ThermoFisher 12563029). The trypLE was inhibited with media and resulting cell suspension centrifuged and washed twice with media. Cells (including the digested aorta) were then fixed in suspension with 3.7% formaldehyde in media after which time they were washed twice with media and resuspended in the appropriate media. The PDMS chips were then primed in the respective media and the cells in suspension were added to the chips. In all cases, the sedimentation in absence of flow led to significantly increased occupancy of the V-cups (≥ 95%) compared to common, flow-driven methods.

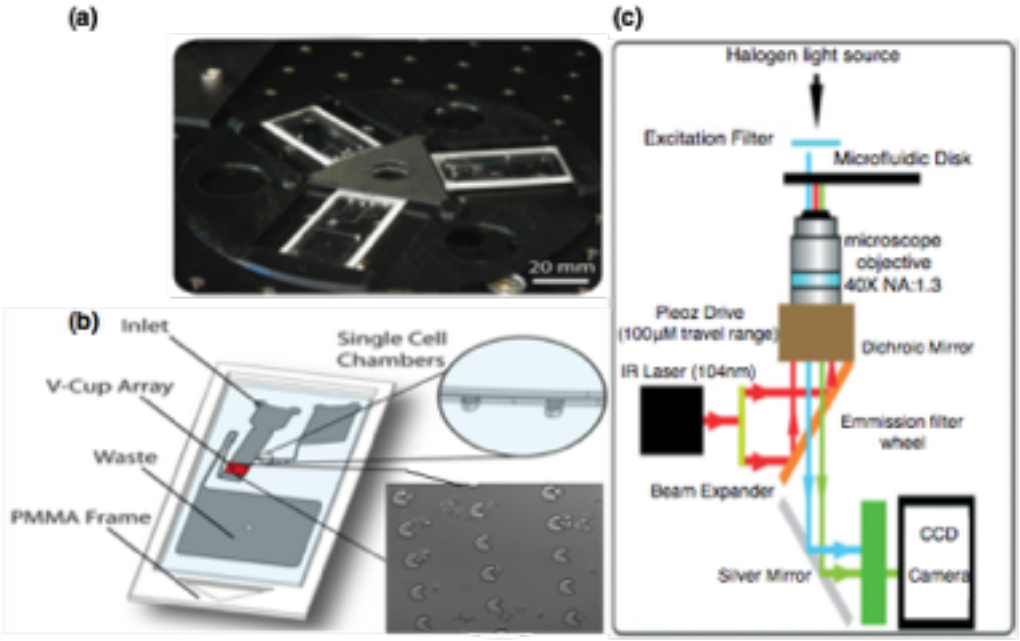

Figure 2.1 Liphos method. Methods for loading, capturing and analysing cells by the centrifugal microfluidic method. (a) microfluidic chips on the spin stand for centrifugation; (b) components of the microfluidic chip and

in particularly the cell chambers and v-cup array; (c) set up of the microscope and lasers for auto-fluorescent analysis of cells.

2.3.3 Auto-fluorescence imaging Cells captured in the biochip were imaged with an Olympus IX81 motorised inverted microscope with an attached Hamamatsu ORCA - ER digital camera C4742-80 using a 10x and 20x objective. Excitation was performed to allow both broadband light (λ = 360 - 800 nm) and emission wavelengths were 465 ± 20 nm, 530 ± 20 nm, 565 ± 20 nm, 630 ± 20 nm and 670± 20 nm.

2.3.4 Data Analysis LiPhos: Images were analysed by the open-source software ImageJ (version 1.46r). Cell signal intensity was quantified by 'region of interest' (ROI) analysis. Each signal was divided by it's respective background signal to give fold signal over background. All results are reported as mean values ± standard errors (where s = standard deviation and n = number of cells). Statistical differences were analysed by t-tests or Wilcoxon t-tests depending on the normality of the data and probability levels below 5% were considered significant.

2.4 FTIR & Raman Spectroscopy

2.4.1 Sample preparation for Spectroscopic analysis.

For both FTIR and Raman spectroscopic analyses, cells were seeded on calcium fluoride slides in 6 well plates at approximately 10,000 cells/well. After 24 hours, the medium was changed and the cells were treated in the respective maintenance or myogenic differentiation media for 14 d before the cells were washed three times with PBS and formalin fixed for 15 minutes. After fixation, the slides were washed with PBS and placed briefly in distilled water. The slides were left to air dry before recording spectra.

2.4.2 FTIR Spectroscopy.

IR absorption measurements were carried out using a Perkin Elmer Spotlight 400N FTIR imaging system. The system is also equipped with an AutoImage microscope system operating with a x 40 Cassegrain objective, and can operate in transmission or reflection mode. FTIR images were acquired in transmission mode with 10 scans of a 150 X 150µm area of the slide. Individual spectra are acquired with a liquid nitrogen cooled mercury cadmium telluride (MCT-A) line detector of pixel size 6.25 µm x 6.25 µm at a spectral resolution of 4 cm^{-1}, interferometer speed of 1.0 cm/s and the useable spectral range is restricted to 1000-4000 cm^{-1}. Background measurements were acquired on a region with no tissue with 120 scans per pixel whereas 32 scans per pixel were recorded from the sample.

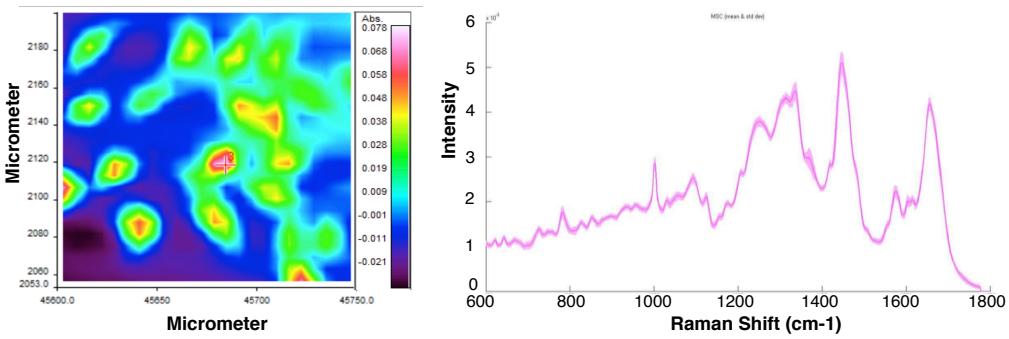

Figure 2.2 Raw FTIR and Raman dataset. Sample raw read outs from FTIR and spectral read out from Raman. (a) Sample IR heat map from FTIR before undergoing spectral processing. (b) Sample Raman spectra that has been meaned and normalised.

2.4.3 Raman Spectroscopy.

Raman spectra were recorded using a custom-built Raman micro-spectroscopy system (Kerr et al., 2016a; Kerr et al., 2016b). Briefly, this system employs a 150 mW laser with a wavelength of 532 nm (Laser Quantum, Torus), spectrograph (Andor, Shamrock 500) operating with a 600 lines/mm grating, and a CCD camera (Andor; DU420A-BR-DD) cooled to –80°C. A 50x microscope objective, with numerical aperture of

0.8 (Olympus, UMPlanFl), was used to image the spectral irradiance to a 100 µm confocal aperture, which isolates the signal from the cell nucleus, and minimises background noise from the sample substrate, as well as from optical elements in the system. The system provides a spatial resolution of 3 µm from the cell nucleus. A long pass filter (Semrock, LP03-532RU-25) and a dichroic beamsplitter (Semrock, LPD-01-532RS) are also used to filter the laser wavelength from reaching the spectrograph, while transmitting the longer Raman scattered wavelengths. A dichroic short pass filter (Edmund Optics, 69-202) permits imaging of the sample to a digital camera (Basler, acA2000-340km). All spectra were recorded using the Andor Solis software system and were recorded within the 400-1800 cm^{-1} range with an acquisition time of 30s each. Two spectra were recorded from the same location within the nucleus of each cell to allow for cosmic ray removal. The system was wavelength calibrated using a Neon lamp as described previously (Hutsebaut et al., 2005) with further design considerations for a custom-built Raman micro-spectroscopy system, as outlined previously (Kiselev et al., 2016).

2.4.4 Data Processing and Analysis.

The different data pre-processing and analysis steps were performed using Matlab (Mathworks, USA). For FTIR data, the resonant Mie scattering correction algorithm (RMieS-EMSC) was employed to remove scattering effects from FTIR spectra as has been successfully demonstrated in a number of studies (Hughes et al., 2010). The algorithm utilises a scatter-free reference spectrum (ZZ_{Ref}), to correct the raw cellular spectrum ($_{Raw}$). In the current work, a Matrigel (a commercial artificial extra cellular matrix) spectrum was employed as reference. Other variable parameters for the algorithm included the number of iterations (20), the number of principle components (Byrne et al., 2016), the Mie theory option with Resonant Mie (RMieS) correction, a lower range of the scattering particle radius (2 µm), an upper range of the scattering particle radius (8 µm), lower range of scattering particle average refractive index

(1.1), and upper range of scattering particle average refractive index (1.5). For Raman data, cosmic ray removal is followed by application of an extended multiplicative signal correction (EMSC) algorithm as described in detail elsewhere (Kerr et al., 2016a). This algorithm computes a background signal in the form of an N-order polynomial to remove the baseline signal that results from the cells auto-fluorescence or from Mie scattering due to the cell morphology. The background signal from the substrate itself is minimised by depositing the cells on CaF_2 Raman grade substrates which are known to produce a relatively flat Raman spectrum in the fingerprint region (Kerr et al.,2016a; Kerr et al., 2015). For this study, a 5th order polynomial was used in the EMSC subtraction algorithm for all datasets, and similar results were found for n=3. Following the EMSC correction all spectra were smoothed with a Savitzky-Golay filter (k = 3; w = 7) to reduce noise.

After pre-processing, Principal Components Analysis (PCA) was employed as an unsupervised multivariate analysis tool to differentiate the data recorded from different cell phenotypes. PCA allows the reduction of the number of variables in a multidimensional dataset, the order of the PCs denoting their importance in the dataset, whereby PC1 describes the highest amount of variation (Ling et al., 2002; Romero et al. 2013). The combination of PCA-LDA has been demonstrated to be a powerful classification technique in vibrational spectroscopic analysis of cells and tissues (Byrne et al., 2016). While PCA identifies differences between the data sets, Linear Discriminant Analysis (LDA) maximises these differences so as to group similar spectral sets. PCA performs a feature reduction of the data and LDA classifies the data into one of two or more classes. Thus, if a group of spectra have a similar correlation to the shape defined by PC1 and that defined by PC2; they are identified as the same class. The loading of the PCs provides valuable information on the origin of the differentiation, in this case spectral signatures of biochemical differences. LDA was then performed on each of the datasets scores independently and a 10-fold cross validation was performed to produce confusion matrices. In the case of FTIR, LDA

accuracy was calculated using a 10-fold cross validation on increasing numbers of latent variables (PC scores) for the classification of all cell phenotypes. The classification which resulted in the maximum accuracy while keeping the number of latent variables to a minimum was chosen for all successive models. In the case of the classification of all cell phenotypes, from a plot of accuracy as a function of increasing number of latent variables, the maximum accuracy was found when 4 principal components were used in the classification. Further addition of principal components only increased the complexity of the model without further improving the performance. In the case of Raman, LDA accuracy was determined using a leave one out procedure, utilising the number of principal components that accounted for at least 85% of the total variance in the dataset.

2.5 Cell Characterisation and Analytical Techniques

2.5.1 Immunocytochemistry

Cells were grown and treated with inductive stimuli and fixed with 3.6% formaldehyde for 15 mins. The cells were then washed three times with PBS and permeabilised with 0.1% Triton-X100. Cells were blocked with 5% bovine serum albumin (BSA) in PBS for 1 hour at room temperature before they were incubated overnight at 4°C with the primary antibody at the appropriate dilution (anti-CD44, Abcam ab24504 at a 1:100 dilution, anti-calponin1, Abcam ab46794 at a 1:200 dilution, anti-SM-MHC (Myh11), Santa Cruz Sc-79079 at a dilution of 1:100, anti-nestin Abcam ab11306 at 1:100 and anti-Sox10 R&D MAB2864 at a 1:100 dilution). The cells were then washed three times and incubated with the corresponding secondary antibody (Biosciences, anti-goat A-11055, anti-rabbit A11008, anti-mouse A11030) at a dilution of 1:1000 for one hour at room temperature. Cells were washed twice with PBS containing 0.1% tween and cell nuclei were stained using DAPI: PBS (D9542-5 mg Sigma) (dilution 1:1000) at room temperature for 15 min. For each secondary

antibody used, a control was prepared with no primary antibody to assess nonspecific binding of the secondary antibody to cells.

An Olympus CK30 microscope with Cell^F software was used to capture images. A threshold of background staining was defined using the secondary antibody control and exposure rates were limited in order to rule out false positives. At least five images from the Olympus CK30 microscopy per experimental group (minimum n=3) were analysed using ImageJ software as previously described (Kennedy et al., 2014a; Kennedy et al., 2014b).

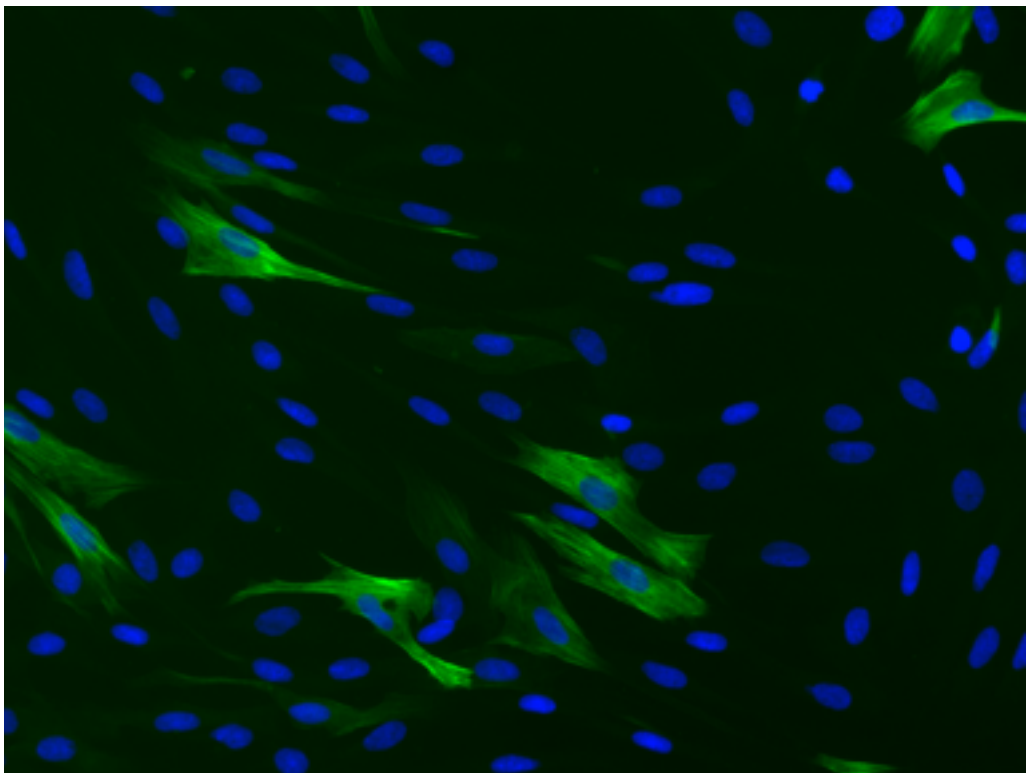

Figure 2.3 Sample immunocytochemical staining. Sample immunocytochemical read out with DAPI staining (blue) and calponin1 (CNN1)/alexafluor488 staining (green).

2.5.2 RNA & DNA isolation

Harvested cultured cells were centrifuged at 400 rcf for 5 minutes to produce a pellet. The RNA/DNA was then isolated using the Magcore HF16 Plus system and using the Magcore Total RNA Cultured Cells Kit

610 (MRC-02SP; MSC) for RNA and Magcore Cultured Cells DNA Kit 110 for DNA (MCC-01SP; MSC). RNA was extracted from tissue samples by crushing the tissue using a pestle and mortar in a small quantity of liquid nitrogen before carrying out the Trisure (Bioline, Bio-38032) protocol.

2.5.3 Quantitative Realtime qRT-PCR

Realtime qRT-PCR: Quantitative real-time RT-PCR was performed using the Rotor Gene (RG-3000, Corbett Research) with either the Quantitect™ Primer assay system using Quantitect mouse and rat primers (Qiagen, Hilden, Germany) or the BioLine Sensifast No Rox kit (MSC, Bio-72005) with PrimeTime® IDT primers. The sequence of the primers were as follows:

Gene	Sequence
mHPRT	5'-GGC TAT AAG TTC TTT GCT GAC CTG -3'
Myh11 Transcript 1	5'-GCA GTG AGC TCT CAG TCA TC-3'
Calponin 1	5'-CTC AGC CCT CCT CAA TGA AGG-3'
Hey1	5'-CAC TTC TGT CAA GCA CTC TCG-3'
HeyL	5'-ATT CCC GAA ACC CAA TAC TCC-3'

Table 2.1 IDT PrimeTime® primer sequences for q-RT-PCR.

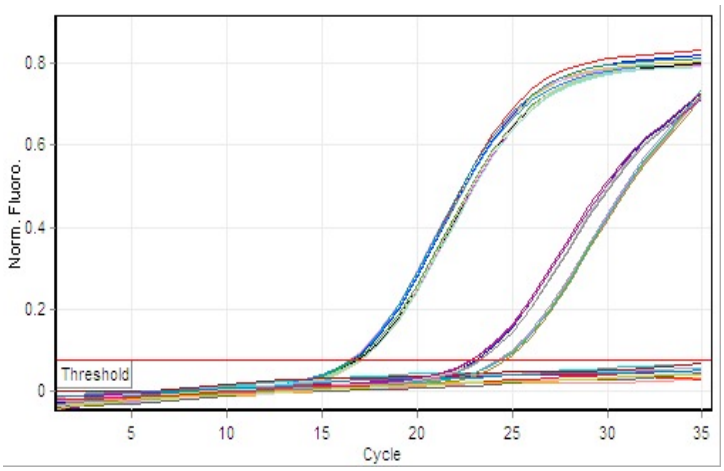

Figure 2.4 Sample cycling amplification curve: HPRT and Myh11 for IgG-Fc versus Jag-1-Fc.

2.5.4 Chromatin Immunoprecipitation Assay (ChIP Assay).

Briefly, 5 × 10^6 cells were cross-linked and used for each immunoprecipitation. DNA was sheared to 500-1000 bp by sonication. Protein G Dynabeads (Invitrogen, BioSciences Ireland) were used to pulldown the antibody-antigen complexes immunoprecipitated with antibodies against H3K4me2 and H3K27me3 (Cell Signalling, Leiden, The Netherlands) using the MAGnify™ Chromatin Immunoprecipitation System (InVitrogen, Bioscience Ireland, cat no 49-2024) according to the manufacturer's instruction. IgG was also included as a negative control. Immunoprecipitated DNA was extracted with phenol-chloroform, ethanol precipitated and eluted. Recovered DNA was analysed by qRT-PCR. Primers spanning the promoter regions (within 2500 bp of transcription start site) of SM-MHC (Myh11) were used to amplify input and immunoprecipitated DNA. Primers were designed to span a CArG (CC(A/T)6GG) element and sequences were (For - 5' - CCC TCC CTT TGC TAA ACA CA - 3' and Rev- 5' - CCA GAT CCT GGG TCC TTA CA - 3'). All samples were performed in triplicate, from at least three independent experiments and data were normalised to % input. This work was carried out in collaboration with Roya Hakimjavadi, Mariana Di Luca and Denise Burtenshaw (DCU).

2.5.5 Myh11-promoter luciferase assay.

The cells were maintained in their respective maintenance growth media before plasmid transfection was performed using TransIT-X2® Dynamic Delivery System (Mirus Bio, Madison, WI) in OptiMEM according to the manufacturer's instruction. For the luciferase assay, 1 µg of the Myh11 reporter plasmid (Myh11-GLuc, GeneCopoeia, Inc. Cat No; MPRM16957-PG02) and 0.1 µg of Renilla reporter plasmid (Promega, Madison, WI) were transiently transfected into cells for 24 h. The total amount of plasmid DNA among samples was kept equal by adding corresponding control vector plasmids. The promoter was activated following treatment with TGF-β_1 (2ng/ml) before dual luciferase assays (Promega) were

conducted 24 h after treatment. Luciferase reporter activities were determined by the Gaussia luciferase activities normalised to the activity of internal control Renilla luciferase activities using the dual luciferase assay system described by the manufacturer (Promega, Madison, WI). All assays were performed in triplicate in collaboration with Gillian Casey (TCD).

2.5.6 SDS- Polyacrylamide Gel Electrophoresis (SDS-PAGE)

Cells were treated either in T75 Flasks or seeded at 10,000 cells/well in 6 well plates. Cells were scraped in media and spun down @ 1500rpm for 5 minutes. The pellet was resuspended in 100µl RIPA buffer (Sigma) containing 1µl protease inhibitor cocktail and phosstop (Roche). This was kept at -20°C overnight. The lysed protein was then thawed and centrifuged at 8000rpm for 10 minutes. The soluble fraction (supernatant) was taken and the protein concentration was determined using the BCA Assay (Pierce). 50 parts of BCA Assay Part A was mixed with 1 part BCA Assay part B. 40µl of this was then added to 5µl of the protein and incubated at 37°C for 30 minutes. The absorbances were read using the Tecan Safire II. The protein was then diluted accordingly in RIPA buffer.

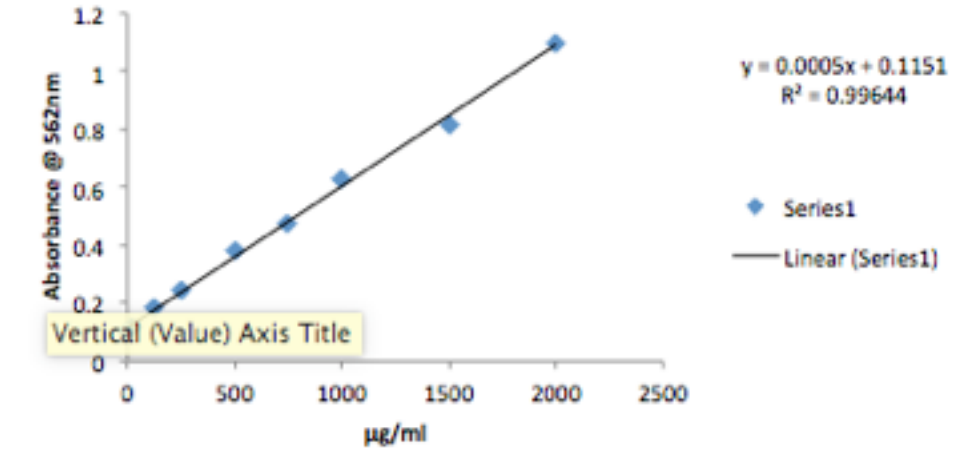

Figure 2.5. Sample BCA Assay. Sample BCA Assay plot of rMVSC protein concentration (µg/ml) versus absorbance readings at 562 nm.

Samples were prepared using 4X Laemelli Buffer with 3 parts protein and 1 part LB containing 10% β-mercaptoethanol and this was sonicated for 10 seconds at 10% amplitude using a probe sonicator.

Gels were prepared as per the following table:

Component	Stacking Gel	12.5% Gel	7.5% Gel
1.5M Tris-HCl	----	1.875 ml	1.875 ml
0.5M Tris-HCl	625ul	----	----
10% SDS	25ul	75ul	75ul
dH_2O	1.54 ml	2.385 ml	3.63375 ml
10% APS	12.5ul	37.5ul	37.5ul
Bis-Acrylamide 30%	325ul	3.12375 ml	1.875 ml
TEMED	10ul	15ul	15ul

Table 2.2. SDS-Page Gel Components. Components and concentrations used to prepare 12.5% and 7.5% bis-acrylamide gels and stacking gels.

Running the Gel

Gels were pre-ran for 30 minutes at 15mA per gel. The running buffer was made up at a 5X concentration as follows:

Component	Quantity
Tris Base (Trizma base sigma)	15.1g
Glycine	95.4g
10%w/v SDS	50 ml
dH2O	950 ml

Table 2.3. Running buffer components. All components and quantities to prepare a 1L sample of running buffer.

This was diluted to 1X accordingly. Gels were then ran at 15mA per gel. Pre-stained protein markers (Fischer) were also ran with the proteins. Empty wells were loaded with laemelli buffer to balance the gel.

2.5.7 Western Immunoblotting.

The MSC G-Blotter system was used to transfer proteins. Nitrocellulose membranes were used for the transfer. Membranes were immersed in Ponceau stain (except the membranes with phosphoproteins) to ensure efficient transfer has ensued.

Membranes were blocked in 5% w/v BSA in TBS containing 0.1% Tween for 1 hour at room temperature. The membranes were then washed 3 times with TBST for 5 minutes each time. The membranes were then incubated with the optimised amount of primary antibody overnight at 4°C. . The total GSK-3β XP® antibody and the phospho-GSK3β-(ser9) antibody were diluted at 1:500 in blocking buffer. The primary antibody is washed off three times again with TBST for 5 minutes each time. The membranes are then incubated in secondary antibody (1:1000) conjugated to HRP for 1 hour at room temperature. This is washed again as before. The bands are developed using TMB (sigma).

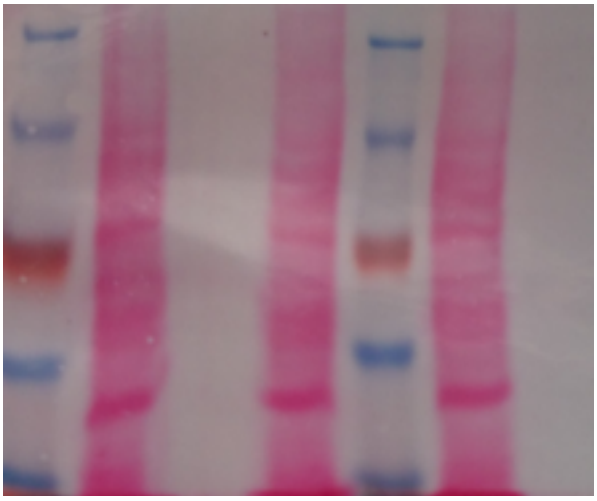

Figure 2.6 Sample Ponceau stain. Ponceau S stain of mSMC protein transferred onto nitrocellulose membrane for Western Blot analysis.

2.5.8 Data Analysis:

Protein bands were plotted using the gel analysis software in ImageJ. Peaks for each protein band were generated by ImageJ and the areas of

each peak were quantified so that each protein band could be directly compared to one another.

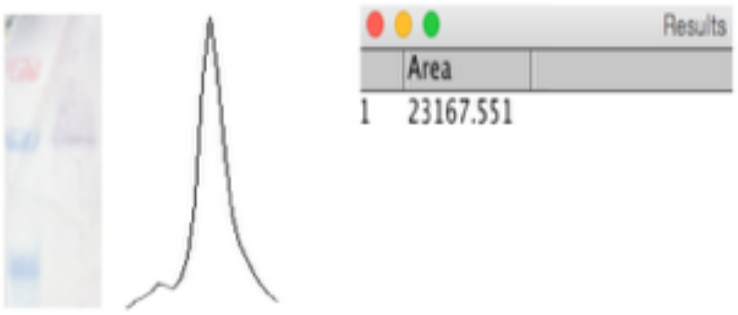

Figure 2.7 Sample western blot densitometry peak. Sample western blot band and resulting densitometry peak and peak area generated using the ImageJ software.

2.6 Nanoparticle Formulation and Analysis

2.6.1 Nanoparticle preparation:

Blank and drug-loaded polymeric magnetic nanoparticles were developed in a technique adapted from McCall et al. (2013). Briefly, 22.5 mg of poly(lactic-co-glycolic acid) (PLGA) (P2066) was weighed out and placed in a 13mm X 100mm test tube. The crystals were dissolved in 225µL of dichloromethane (650463) and the top of the tube was sealed with parafilm. The level of solvent was marked and the polymer was left to dissolve overnight. Meanwhile, 200µL of MNPs (700312) were aliquoted into a 13mm X 100mm test tube and placed under nitrogen gas overnight to evaporate off the toluene. On the day of formulation, or the day previously, 10 ml of 0.3% PVA (363138) and 450µL of 5% PVA in dH_2O were prepared and boiled at 90°C until dissolved (approximately 45 minuets). The 10 ml 0.3% PVA solution was placed in a 50 ml conical

flask and the 5% solution placed in a 16mm X 150mm test tube. The dissolved PLGA in dichloromethane was added to the dried MNPs to dissolve them in the polymer complex. This was vortexes for 10 seconds to ensure mixing. In the drug-loaded samples, the drug was added at the desired concentration at this point to the polymer:Fe_3O_4-NP mix and vortexes for another 10 seconds. The PLGA:DCM;Fe_3O_4NP:Drug solution was added drop wise to the 5% PVA whilst under vortex. The solution was vortexed for a further 15 seconds and typically an emulsion would form. The emulsion was then sonicated on ice at a 40% amplitude for 10 seconds (X3) with a 5 second interval in between each sonication. For the fluorescently mAB-loaded PLGA-MNPs or fluorescently tagged siRNA PLGA-MNPs, the fluorescent agents were added at this step. The resulting emulsion was then poured to the 0.3% PVA and stirred over night to allow the nanoparticles to harden (McCall et al. 2013).

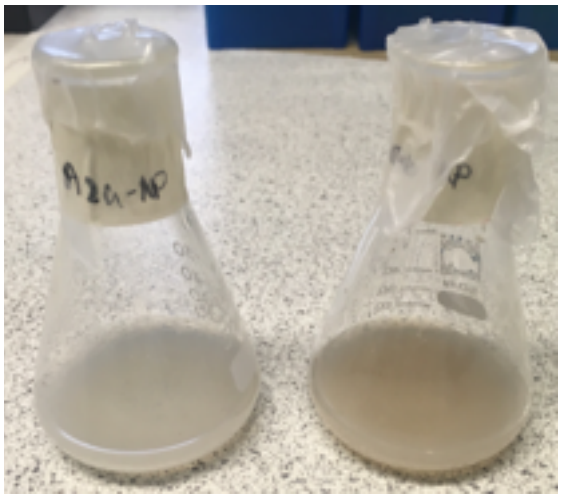

Figure 2.8 Sample MNP image. Representative image of freshly formulated 1-Aza-loaded NPs and blank NPs.

2.6.2 Nanoparticle Collection

Nanoparticle solutions were centrifuged with the Sorvall RC 5B Plus centrifuge with the Sorvall SA-600 rotor at 17000g for one hour. The

supernatant was collected and kept for HPLC analysis. The nanoparticle pellet was then re-suspended in 10 ml dH_2O, if the nanoparticles aggregated upon re-suspension the solution was sonicated twice for 30 seconds each at 20% to break up the aggregates, if any. The nanoparticle solution was then aliquoted out into 10 1 ml aliquots which were centrifuged again at 17000g for 1 hour. The supernatant was kept for analysis. The nanoparticle pellets were then placed in the "DNA Speed Vac DNA110" for 1-2 hours to remove excess liquid and then stored at -80°C.

2.6.3 Analysis of Nanoparticles:

2.6.4 High Performance Liquid Chromatography (HPLC)

The Agilent 1100 HPLC system was used in conjunction with the silica packed Supelco Discovery C18 Column (568523-U) to separate the molecules in the supernatant samples. The Supelco Discovery C18 column contains porous silica beads packed inside to separate the molecules based on their size. The smaller the molecules, the more they will penetrate the pours and interact with the column and therefore the slower it will elute from the column to be detected. The time at which it takes for a molecule to be eluted and detected from the column is called the 'retention time' and varies based on the molecule size, this is referred to as size exclusion chromatography.

High pressure pumps transport the mobile phase through the system and pump meters regulate the flow rate, usually in millilitres per minute (ml/min). The mobile phase typically consisted of either 50:50 or 70:30 acetonitrile:dH_2O (Sigma 34851) depending on the hydrophobicity of the drug. The flow rate was typically 0.5 ml/min to 1 ml/min. An injector takes the sample to be analysed and injects it into the mobile phase stream to be separated by the column. Once it passes through the column it passes by the detector , usually a UV or fluorescence detector, which sends an electrical signal to the computer to generate a chromatogram. A

wavelength scan was performed for each drug on a Tecan NanoQuant Infinite M200 to determine the optimum wavelength for detection of the drug by HPLC.

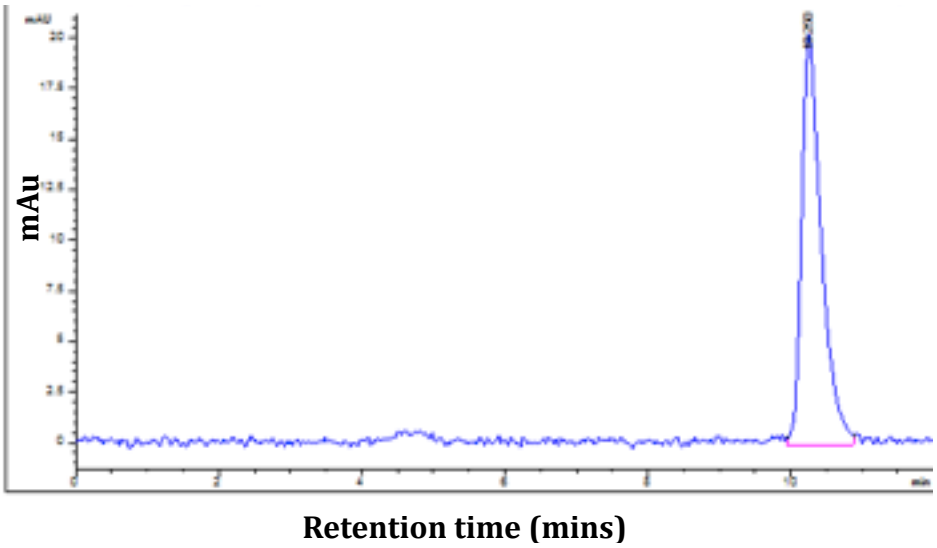

Figure 2.9 HPLC Chromatogram Example chromatogram for 1-Aza (5µM) as it appears by HPLC at 336 nm.

2.6.5 Drug Incorporation Efficiency

To determine the incorporation efficiency of the drugs into the MNPs, the previously collected supernatants were subjected to HPLC. The peak area of the drug was compared to a standard curve performed on the same day to determine the concentration of drug from the supernatant. The concentration of drug detected in the supernatant was then subtracted from the theoretical drug loaded to give the concentration of drug incorporated. The following equation was then used to calculate the incorporation efficiency:

(Concentration of drug incorporated/Theoretical drug loaded) X 100 = % of drug incorporated.

2.6.6 Drug release studies:

To study the release of drug from the nanoparticles, the stored nanoparticle pellets were re-suspended in 1 ml of dH_2O and were left for up to 14 days at room temperature and 37°C in the presence or absence of pulsed magnetisation (30s on, 10s off for 5 minutes) from the external Dextran magnet (Dexter Magnetic Technologies, 2501008). Pulsed magnetisation has previously been shown to increase cellular uptake of nanoparticles (Min et al., 2013) and a similar study performed with PTX-PLGA-MNPs found the short magnetisation time of 5 minutes sufficient to inhibit restenosis *in vivo* (Chorny et al., 2010). The nanoparticles were centrifuged at 17000 x g after 24hrs, 48hrs, 72hrs, 7 days and 14 days in the various environmental conditions and the supernatants were analysed by HPLC for the presence of drug in the supernatant. The percentage of drug released at each time point was calculated as follows:

(Concentration of drug in supernatant/concentration of drug incorporated) X 100 = % of drug released from nanoparticle.

Total percentage drug released at each time was simply calculated as the percentage released at that time point plus previous time points.

2.6.7 Dynamic Light Scattering:

DLS (Malvern Zetasizer Nano) was performed to determine the size and colloidal stability of the nanoparticles. Dynamic Light Scattering is a laser based system which sends a laser beam through a polariser to the sample and measuring the scatter light to yield information about molecules in a solution. 100µL of nanoparticles were added to 0.9 ml of ultrapure water and filtered through a 0.45µM disposable plastic cuvette for size and disposable folded capillary cuvette for zeta potential and covered with parafilm. The automated protocol for magnetite in water was followed on the Zetasizer software. 12 reads at 30 seconds each were performed for each sample in triplicate.

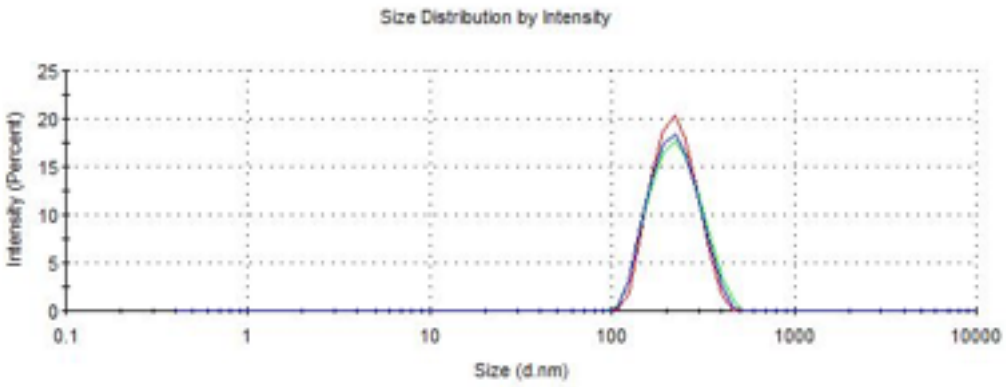

Figure 2.10 DLS Sizing Peaks Sample DLS triplicate reading of blank nanoparticles.

2.6.8 TEM and FeSEM

A 100µL of nanoparticles was pipetted onto carbon coated copper TEM grids. TEM images were recorded in the University of Limerick and Fe-SEM (Hitachi S5500 FeSEM) images were recorded in the NRF DCU.

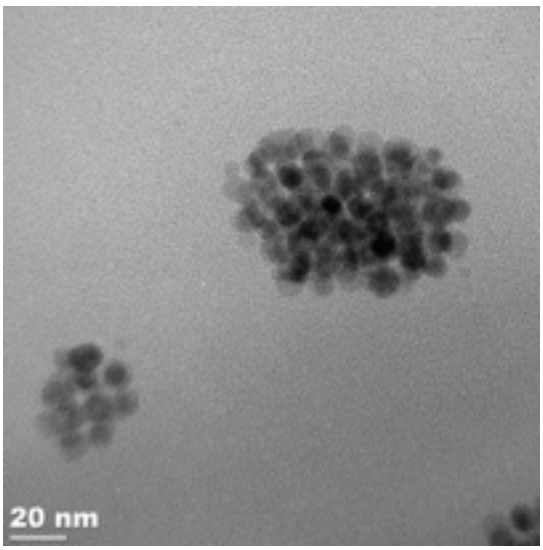

Figure 2.11 TEM image. Representative TEM image of blank nanoparticles.

2.6.9 Statistical Analysis:

All biochemical analysis experiments and autofluorescence experiments were performed in triplicate and data are presented as mean ± SEM for at least three independent runs. Statistical analysis was performed with Prism v6 software package using t-test for parametric data or a Wilcoxon Signed Rank test for non-parametric data.

Raman and FTIR data were analysed as described above (2.2.4) and statistical analysis was performed using the leave one out statistical method whereby one spectra from each population was left out of the analysis and later compared to mean spectra for percentage accuracy.

Chapter 3

Photonic Discrimination of Vascular Stem cells, their myogenic progeny and healthy SMC and arteriosclerotic (diseased) SMCs-like cells by centrifugal microfluidics and label free autofluorescence imaging.

3.1.1 Introduction

The arterial blood vessel consists of three layers of cells; the outer adventitial layer that houses fibroblasts, connective tissue, stem cells and perivascular nerves; the medial middle layer that predominantly contains vascular smooth muscle cells (SMCs) and some resident vascular stem cells and the intimal inner most monolayer of cells called the endothelium. A hallmark of CVD is neointimal thickening of the artery due to SMC accumulation leading to the obstruction of blood flow that can result in a heart attack or stroke (Hoglund et al., 2010). The source of these SMCs has been controversial with either de-differentiated SMCs (Nguyen et al. 2013., Alexander et al., 2012) or progenitor stem cell-derived SMCs (Tang et al., 2013; Tang et al., 2012) playing a putative role. Importantly, progenitor stem cells can develop into differentiated vascular smooth muscle cells (SMCs) and have been shown to originate from both the vasculature itself and/or the bone marrow (BM) (Wang, 2015). TGF-β_1 1 is an important multifunctional cytokine that regulates the promotion of stem cell differentiation to SMCs (Kurpinski et al., 2010). It is proposed that vascular stem cells become activated following injury, transition to SMC and subsequently dictate, in part, the vascular remodelling events that occur leading to vascular disease progression (Wang, 2015). Their role and identification within the vessel wall highlights a potential new diagnostic target for CVD (Majesky et al., 2011; Tang et al., 2012; Wigren et al., 2016).

Label-free technologies have recently attracted significant interest for being both sensitive and quantitative multi-parameter analysis tools to examine biological systems. Several different classes of label-free sensors are currently being developed for bio-analytical applications that include plasmonic detection, photonic detection, electrical detection and mechanical sensors too (Qavi et al., 2009).

Every material has distinct photonic properties depending on its composition and morphology. The innate optical response comprises of scattering, absorbance and auto-fluorescence signals. The combination of several fluorescence and/or absorbance bands together with scattering bands form a specific pattern which is unique for each particular cell (photonic fingerprint). (Yun & Kwok, 2017; Kinnunan et al., 2015). Label-free optical technologies have been developed with highly efficient cell-to-light coupling and in combination with microfluidics has been successfully employed to measure the real-time response of individual cells in a population (Nwankire et al., 2015; Jahnke et al., 2013; Yun et al., 2013).

3.1.2 Objectives:

The main aims of this chapter were:-

1. To determine the AF signature of individual differentiated medial vascular smooth muscle cells (dSMCs) isolated from the mouse carotid artery and differentiated medial vascular dSMCs isolated from the mouse aorta.

2. To determine whether differences exist between the AF signature of normal (healthy) medial differentiated SMCs from carotid and aorta and medial and neointimal cells (arteriosclerotic) from carotid artery following partial ligation.

3. To compare the AF signature of individual undifferentiated bone marrow derived mouse mesenchymal stem cells (mMSCs) and their respective myogenic progeny following treatment with TGF-β_1 or the Notch ligand, Jag-1 for up to 7-28 days in culture.

3.1.3. Strategy

The first main objective of this chapter was to determine whether photonics can be used as a tool to identify and discriminate healthy medial differentiated SMCs from diseased medial and intimal SMC-like cells using a partial carotid artery injury model in mice (Korshunov et al., 2003). In order to achieve this, ligated and sham carotid arteries were cleaned, de-endothelialised (by gentle rubbing) and the adventitia separated from medial layer before SMCs were enzymatically digested and loaded onto PDMS chips and centrifuged into v-cup arrays for single-cell analysis of AF signatures (see Chapter 2.3). The medial SMCs from carotid artery were also compared to medial cells from fresh aorta following similar de-endothelialisation and removal of fat and adventitia.

In a similar manner, individual undifferentiated mesenchymal stem cells (mMSCs) and their myogenic progeny following induction with medial supplemented TGF-β_1 (10ng/ml) or Jag-1 (2 µg/ml) for 7 days (see Chapter 2.2.5) were loaded onto PDMS chips and centrifuged into v-cup arrays for single-cell analysis of AF signatures (see Chapter 2.3). In order to confirm that any differences in the AF signatures were independent of the inductive stimulus and dependent on myogenic differentiation, AF signatures were assessed in stem cells that were treated with two dissimilar myogenic inductive stimuli (TGF-β_1 or Jag-1) and were also compared to a RAMOS β-cell line. Both murine bone-marrow derived mesenchymal stem cells (mMSCs), multipotent embryonic adventitial cells (C3H-10T1/2 cells) and rat multipotent resident vascular stem cells (rMVSCs) derived from rat aorta were treated with TGF-β_1 (10ng/ml) or Jag-1 (2 µg/ml) for 7 days to induce myogenic differentiation before individual cells were captured and analysed.

Hence, the altered light scattering properties of vascular smooth muscle cells from healthy and arteriosclerotic diseased (following carotid artery ligation) vessels were compared to identify a novel AF photonic signature

associated with intimal medial thickening (IMT). Further to this, the AF signatures of undifferentiated stem cells and their myogenic progeny were compared to assess for differences and determine whether these myogenic progeny shared any spectral similarity with SMC-like cells dissociated from remodelled (injured) carotid arteries.

In all analysis, significance testing was carried out using the Prism software. Statistical tests were chosen based on the normal distribution of the data with sets of data with normal distribution analysed by paired or un-paired t-tests and groups that were not normally distributed analysed by paired non-parametric Wilcoxon ranked t-tests.

3.2 Results

3.2.1 Photonic Auto-Fluorescence (AF) analysis of individual vascular cells from diseased and healthy vessels.

Carotid arteries were excised from C57/Bl6 mice 14 days after sham or partial ligation as described in Chapter 2.2.4. The excised vessels were cleaned, sectioned and H&E stained to determine the volume of the lumen, medial and adventitial layers, respectively. The sections were further probed with anti-α-actin (SMA) and anti-Myh11 antibodies to determine the contribution of α-actin and Myh11 positive cells, respectively to the neo-intimal layer. Carotids were prepared and stained by Eileen Redmond, Rochester, NY. The carotid cells, ligated and the matching sham, were also enzymatically digested, loaded onto microfluidic chips for capture, and analysed for their auto-fluorescence (AF) signature to broadband light, as described in Chapter 2.3.

H&E staining shows the medial and intimal layer of the ligated vessel significantly increased in diameter with a concomitant decrease in the lumen volume compared to sham controls [Figure 3.1(a,b)]. Immunohistological staining with α-actin and Myh11 showed the presence of α-actin positive cells in the media of the aorta and uninjured sham vessels and Myh11 in the uninjured media of the sham vessel. The intimal layer of the ligated vessel had decreased Myh11 expression but intense α-actin expression [Figure 3.1(c)]. Single cell analysis measurements from sham and ligated carotids and normal aorta were recorded from individual cells captured on v-cups using the centrifugal Lab-on-a-Disc (LoaD) platform [Figure 3.1(d)]. The auto-fluorescence (AF) pattern of a minimum 55 cells per group were recorded at each wavelength and compared. The cells from the ligated injured carotid had higher AF intensities across all wavelengths compared to the sham control, with the most significant differences in the first 3 wavelengths (465, 530 and 565 nm± 20 nm) [Figure 3.1 (e)]. When comparing isolated differentiated SMC

(dSMC) from both the sham carotid and normal aorta, the AF intensities were much similar, as expected, with minor differences at the 530± 20 nm and 670± 20 nm wavelength and no difference at the 565 nm± 20 nm wavelength [Figure 3.1(f)]. However, there were significant differences in the AF intensities at 465 ± 20 nm and 630± 20 nm wavelengths, respectively [Figure 3.1(f)].

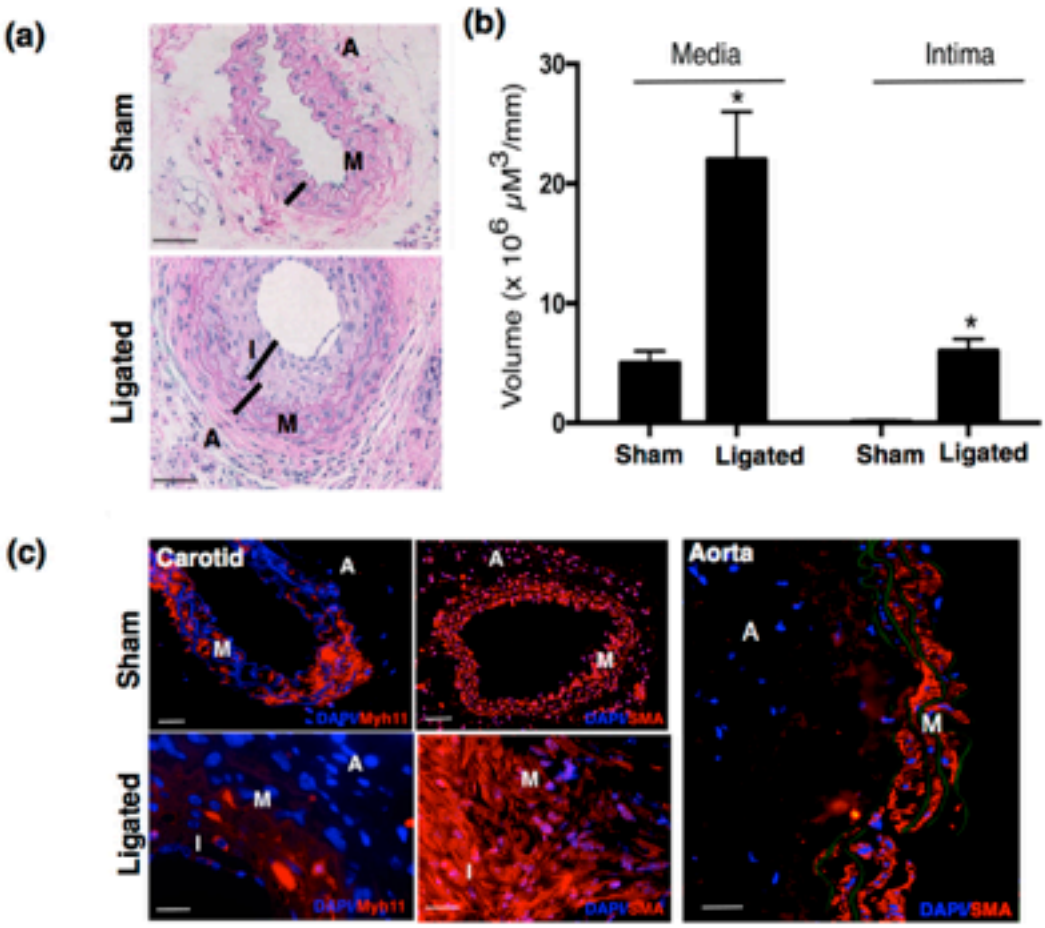

Figure 3.1 (a-c) Photonic AF analysis of cells from ligated and corresponding control carotid arteries. (a) H&E staining of sham and ligated vessels 14 days post-ligation; (b) Morphometric analysis of medial, intimal and adventitial layers in sham and ligated vessels and significance was determined using the Prism software and paired t-tests; (c) Myh11 and α-actin staining (red) and DAPI nuclei staining (blue) or cells in the adventitial, medial and intimal layer of the sham and ligated carotid artery and in the adventitial and medial layer of the aorta. *p<0.05.

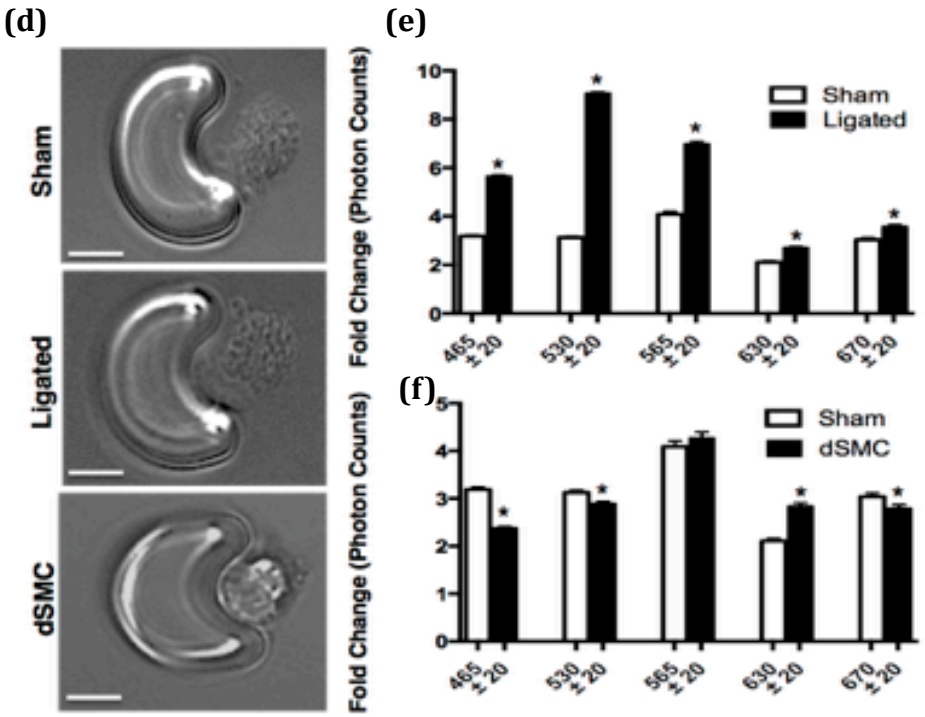

Figure 3.1 (d-f). Photonic AF analysis of cells from sham and ligated carotid arteries and normal aorta. (d) Digested cells from sham and ligated carotids and normal aorta were captured in a v-cup and the AF intensity of cells from each group measured across the five wavelengths from 465±20 nm to 670±20 nm. (e) AF profile of cells from sham and ligated carotids (n=55) (f) AF profile of differentiated SMC from sham and normal aorta (n=55). Standard paired t-tests were carried out for all wavelengths except for the 565±20 nm wavelength, which was not normally distributed and hence a non-parametric Mann-Whitney test was performed. *$p<0.05$ was considered significant for all t-tests. Data are the mean ± SEM of 55 cells/group from 2 pooled vessels, *$p<0.05$ vs sham.

3.2.2 Transforming growth factor beta 1 (TGF-β_1) promotes myogenic differentiation of mesenchymal stem cell and embryonic C3H 10T1/2 mesenchymal stem cells towards a vascular phenotype.

Before photonic AF analysis was performed on undifferentiated stem cells and their myogenic progeny, the cells were directly compared for differences using conventional genetic, biochemical and histological analyses before and after myogenic differentiation [Figure 3.2]. Freshly isolated mRNA from aortic dSMCs and bladder dSMCs were highly differentiated since both preparations were highly enriched for the SMC differentiation marker, Myh11 transcript. In contrast, undifferentiated bone marrow derived mesenchymal stem cells (MSCs), multipotent C2H 10T 1/2 stem cells and embryonic stem cells (ESCs) were devoid of Myh11 transcript [Figure 3.2(a)].

Freshly isolated differentiated aortic dSMCs, subcultured SMCs (ddSMCs), mMSCs and mMSCs treated with (2ng/ml) TGF-β_1 for 7 days were analysed by chromatin immunoprecipitation (ChiP) assays for enrichment of the SMC specific epigenetic mark, di-methlyation of lysine 4 on histone 3 (H3K4me2) at the Myh11 locus (Gomez et al. 2015) and for the stem cell mark tri-methylation of lysine 27 on histone 2 (H3K27me3). The aortic dSMCs were highly enriched for the H3K4me2 mark but devoid of the H3K27me3 mark. Interestingly, the levels of H3K4me2 decreased when mSMCs were grown in culture and become 'de-differentiated" ddSMCs yet still remained enriched for the H3K4me2 mark. The mMSCs were highly enriched for the H3K27me3 mark but with low abundance of the H3K4me2 mark which is typical of a stem cell. After treatment of the mMSCs (2ng/ml) TGF-β_1 for 7 days (the minimum TGF-β_1 dose and time to elicit a significant response), the signature changed so that the mMSCs were now enriched for the SMC mark H3K4me2 and had lost some of the enrichment for the stem mark H3K27me3, further indicating the transition to SMC and myogenic differentiation [Figure 3.2b]. This was work was carried out in collaboration with Dr. Roya

Hakimjavadi, Mariana Soledad di Luca and Denise Burtenshaw (VBT Lab, DCU).

Treatment of mMSCs and C3H T101/2 cells with myogenic inductive media containing TGF-β_1 (2ng/ml) for 48 h that had been transfected with a plasmid encoding the Myh11 promoter resulted in a significant increase in relative luciferase activity (RLU) relative to to both mock transfected cells and vehicle control indicative of specific Myh11-promoter transactivation, carried out by Gillian Casey (TCD) [Figure 3.2c]. The levels of CNN1 and Myh11 mRNA transcripts were also significantly increased following TGF- β1 (10ng/ml) treatment of both mMSCs and C3H 10T1/2 cells when compared to vehicle control [Figure 3.2(d, e)]. Parallel studies using immunocytochemistry for SMC differentiation markers also demonstrated a significant increase in CNN1 and Myh11$^+$ cells compared to the vehicle control. This result was confirmed by analysing protein levels by western blot which also indicated an increase in CNN1 and Myh11 protein levels following TGF-β_1 treatment. [Figure 3.3]. It is noteworthy that a lower dose and treatment time was necessary to activate the Myh11 promotor in the mMSCs and C3H T10 1/2 cells compared to the mRNA and protein levels.

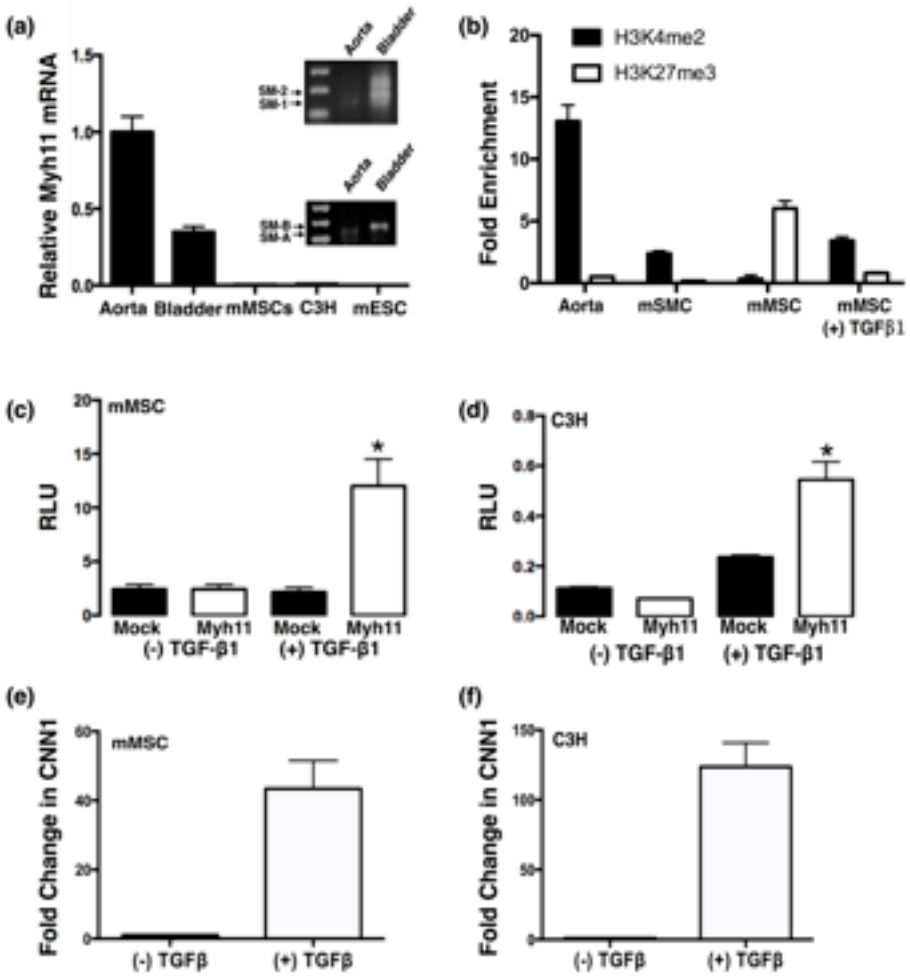

Figure 3.2 TGF-β_1 up-regulates SMC gene expression in stem cells (a) Relative Myh11 levels in aorta, bladder, mMSCs, C3H T10 ½ cells and mESCs; (b) Enrichment of SMC histone modification mark H3K4me2 and stem cell histone modification marker H3K27me3 at the Myh11 promoter in mouse aorta, cultured mSMCs and mMSCs in the absence or presence of TGF-β_1; (c) RLU activity in mMSCs transfected with the Myh11 promotor plasmid in response to TGF-β_1; (d) RLU activity in C3H T10 ½ cells transfected with the Myh11 promotor plasmid in response to TGF-β_1; Data are mean ± SEM of 3 representative experiments performed in triplicate (e) Fold change in calponin1 expression in mMSCs in response to TGF-β_1; (f) Fold change in calponin1 expression in C3H T10 ½ cells in response to TGF-β_1. Data are the mean of triplicate samples within one experiment. Data analysis was carried out using the prism software and the data was tested for significance using appropriate t-tests with *$p<0.05$ considered as significant.

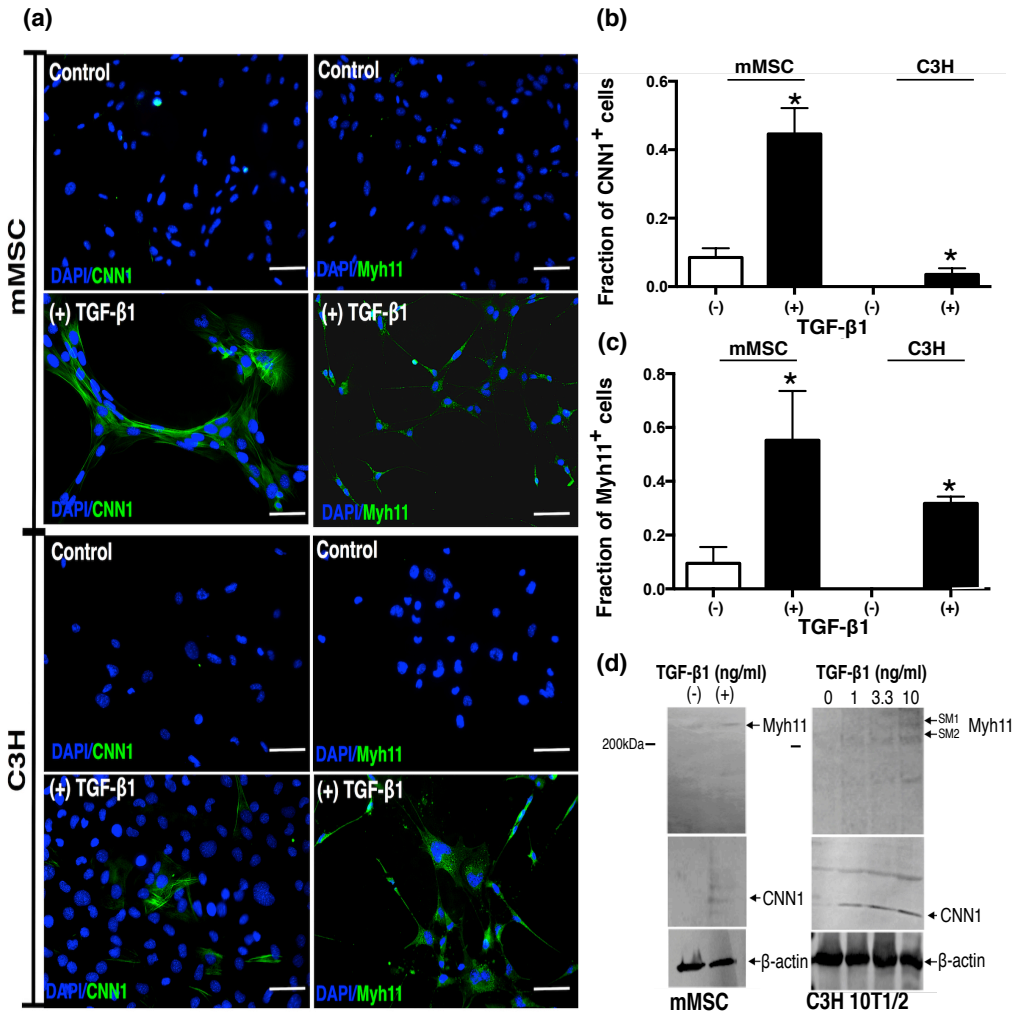

Figure 3.3 TGF-β_1 induced myogenic differentiation of multipotent stem cells (a) Representative immunocytochemical staining of mMSCs and C3H T10 ½ cells with DAPI (blue) and CNN1/Myh11 (green) following TGF-β_1 (10ng/ml) treatment for 7 days; (b) Fraction of CNN1 positive mMSCs and C3H cells following TGF-β_1 treatment in an average of at least 5 images per group; (c) Fraction of Myh11 positive mMSCs and C3H cells following TGF-β_1 treatment in an average of at least 5 images per group in triplicate; (d) Western blot analysis of mMSCs and C3H T10 ½ cell protein levels of Myh11 and CNN1 in the presence and absence of TGF-β_1. Data are mean ± SEM of 3 representative experiments. Data analysis was carried out using the prism software and the data was tested for significance using paired t-tests with *$p<0.05$ considered as significant.

3.2.3 Photonic analysis of murine progenitor stem cells

Individual undifferentiated murine bone marrow derived mesenchymal stem cells (mMSCs) and murine multipotent embryonic fibroblast (C3H T101/2) stem cells were loaded and captured in v-cup arrays using microfluidic chips and exposed to light at different wavelengths, (from 465 nm - 670 nm) before the AF photon intensity at each wavelength was recorded and compared to background noise [Figure 3.4(a, b)]. At each wavelength, the photon counts of the mMSCs [Figure 3.4(a)] and C3H T10 ½ cells [Figure 3.4 (b)] were considerably higher than the background noise – confirming that this technique can detect the AF signature of individual undifferentiated stem cells at various wavelengths [Figure 3.4(a, b)]. In all cases, the data are the mean ± SEM of three samples and are representative of 3 similar experiments. Data analysis was performed using the Prism software and paired t-tests were carried out to test for significance where $p<0.05$ was considered significant.

3.2.4 Photonic analysis for the comparison of stem cells and their myogenic progeny

Murine mMSCs and C3H T101/2 cells were treated with 10ng/ml TGFβ1 for 7 days to induce myogenic differentiation towards a vascular SMC phenotype. Dose and treatment times where extracellular protein changes were confirmed biochemically were chosen for AF analysis. These cells were then captured and analysed on the microfluidic chips for their AF spectra [Figure 3.5(a, b)]. When the mMSCs were treated with TGF-β_1, their AF photon intensity increased compared to untreated mMSCs across all wavelengths {Figure 3.5(a)]. The most significant increase was observed at the 565 nm ± 20 nm wavelength [Figure 3.5(a)]. Similarly, C3H T10 ½ cells had a significant increase in AF intensity at this wavelength compared to the untreated cells, indicating that changes at this wavelength is the most significant when tracking

stem cell differentiation towards a myogenic lineage [Figure 3.5(b)]. In contrast, the AF intensities in response to TGF-β_1 for all other wavelengths for this stem cell decreased [Figure 3.5(b)]. To confirm that the change in auto-fluorescence patterns, particular at the 565 nm ± 20 nm was due to physical differences in the cells following TGF-β_1 stimulation and not an auto-fluorescent pattern due to the inducer itself, a non-vascular human B lymphocyte Ramos cell line was treated with TGF-β_1 for 7 days and the auto-fluorescent profile analysed [Figure 3.5(c)]. The TGF-β_1 treated Ramos B cells had lower auto-fluorescence intensities across all wavelengths, including the 565 nm ± 20 nm, further supporting the notion that this wavelength is the most likely indicator for myogenic differentiation of stem cells *in vitro.*

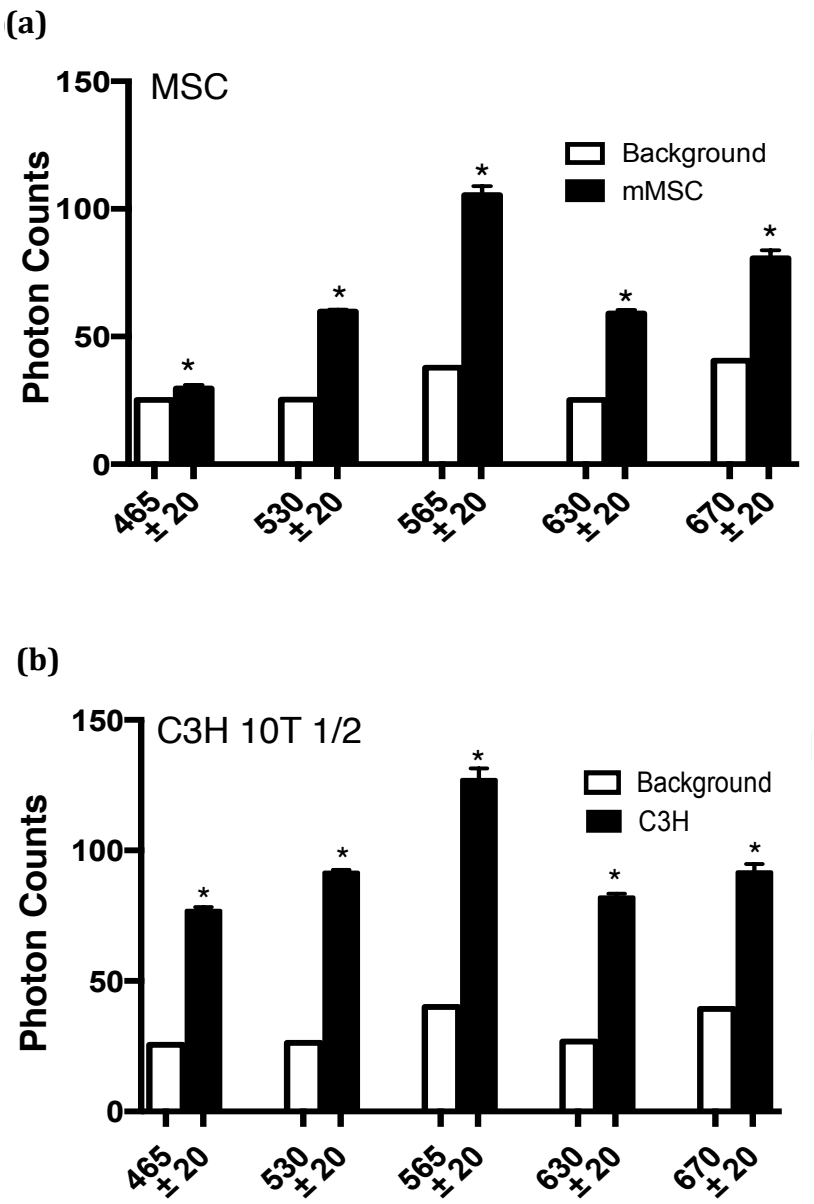

Figure 3.4 Photonic AF analysis of multipotent stem cells. (a) Representative pattern of AF photon intensity of mMSCs compared to the background noise; (b) Representative pattern of AF photon intensity of C3H T10 ½ cells compared to the background noise. Data are the mean ± SEM of 55 cells/group from 3 independent experiments, *$p<0.05$ vs control (without TGF-β1). Paired t-tests were carried out for all samples with *$p<0.05$ considered significant.

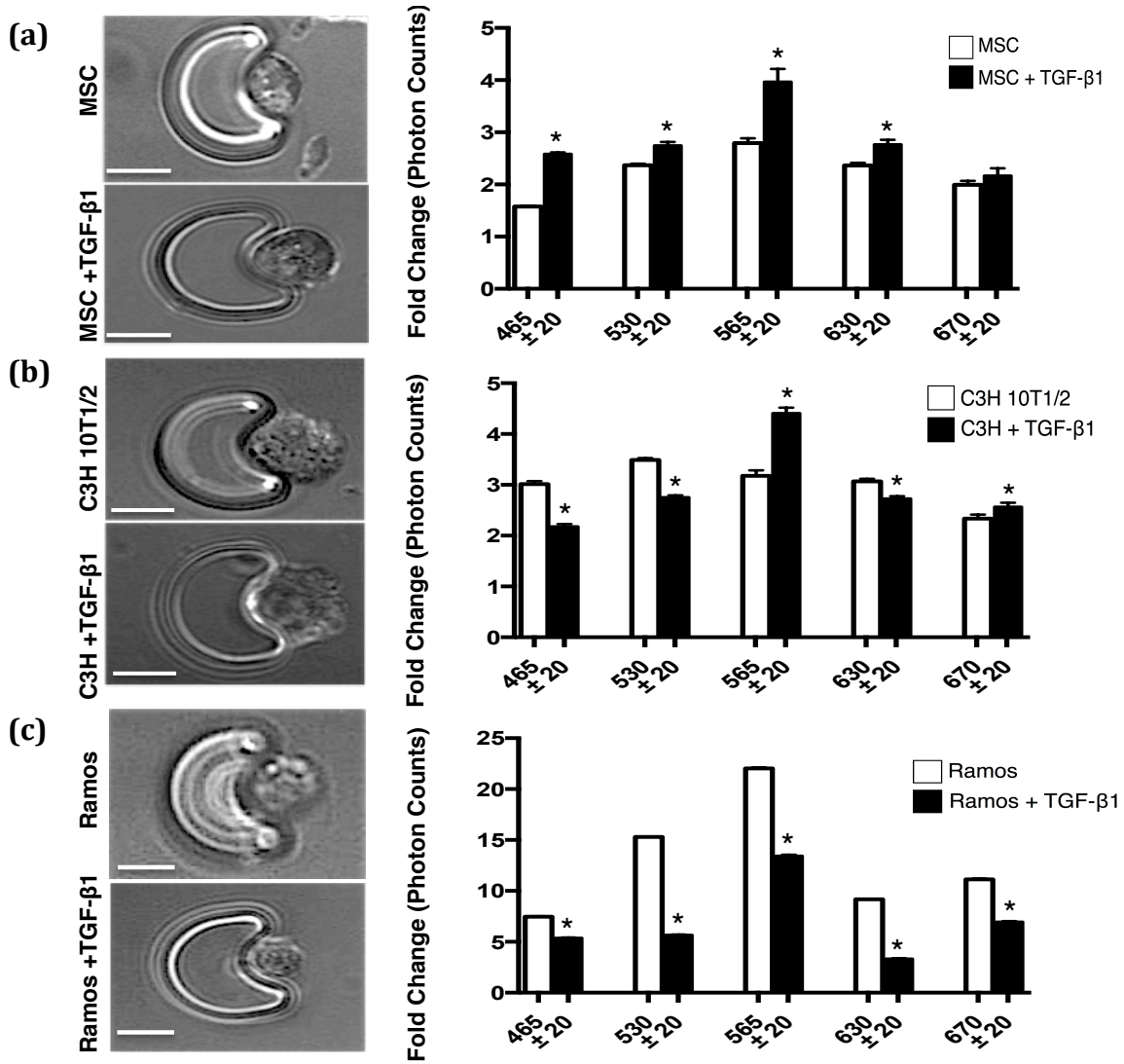

Figure 3.5 Photonic AF analysis discriminates undifferentiated stem cells from their myogenic progeny (a) capture of mMSCs ± TGF-β_1 and the AF intensity in response to broadband light. Wilcoxon t-tests was performed for all wavelengths bar the 465±20 nm which had a standard t-test (b) capture of C3H ± TGFβ-1 and the AF intensity in response to broadband light. Standard t-tests was carried out for C3H ± TGFβ1 at the 530±20 nm and 670±20 nm and Wilcoxon t-tests carried out for all other wavelengths; (c) capture of Ramos B cells ± TGF-β_1 and the AF intensity in response to broadband light. Data are the mean ± SEM of 55 cells/ group from 3 independent experiments, *$p<0.05$ vs control (without TGF-β1). Standard t-tests were carried out for all wavelengths bar the 630±20 nm which had the Wilcoxon t-test due to its data distribution. Data analysis was carried out using the prism software and *$p<0.05$ was considered as significant.

3.2.5 Jag-1-Fc induces myogenic differentiation in stem cells.

Undifferentiated multipotent resident rat vascular stem cells (rMVSCs) treated with control IgG-Fc or Jag-1-Fc (2 μg/ml) for 7 days (Chapter 2.25) were compared for SMC marker expression and change in auto-fluorescence [Figure 3.6]. By trial and error, 2 μg/ml of Jag-1 for 7 days was found to be the optimum dose and time to consistently activate SMC marker genes, particularly Myh11. Scant expression of CNN1 and Myh11 was evident in the control (IgG-Fc) rMVSCs; however rMVSCs treated with Jag-1-Fc showed significant CNN1 and Myh11 expression [Figure 3.6(a)]. The number of CNN1 and Myh11 positive cells was significantly increased following Jag-1-Fc treatment when compared to the IgG-Fc control cells [Figure 3.6(a)]. The levels of CNN1 and Myh11 mRNA transcripts were also significantly increased following treatment with Jag-1-Fc [Figure 3.6(b)]. In all cases, data are the mean ± SEM of three samples and are representative of 3 similar experiments. Data analysis was carried out using the prism software and paired t-tests were used to test for significance. *$p<0.05$ was considered significant.

3.2.6 Auto-fluorescence pattern of stem cells in response to an alternative myogenic stimulus, Jag-1. Undifferentiated rMVSCs were treated with IgG-Fc or the myogenic stimulus, Jag-1-Fc for 7 days before cells were captured on a microfluidic v-cup array and exposed to light at various wavelengths 465±20 nm, 530±20 nm, 565±20 nm, 630±20 nm and 670±20 nm [Figure 3.6c]. The dose and time chosen correlated to changes in protein expression confirmed biochemically. The AF photon intensity of Jag-1-Fc treated cells significantly increased at 565±20 nm. All other AF photon intensities significantly increased following Jag-1-Fc treatment with the exception at the 630±20 nm [Figure 3.6d]

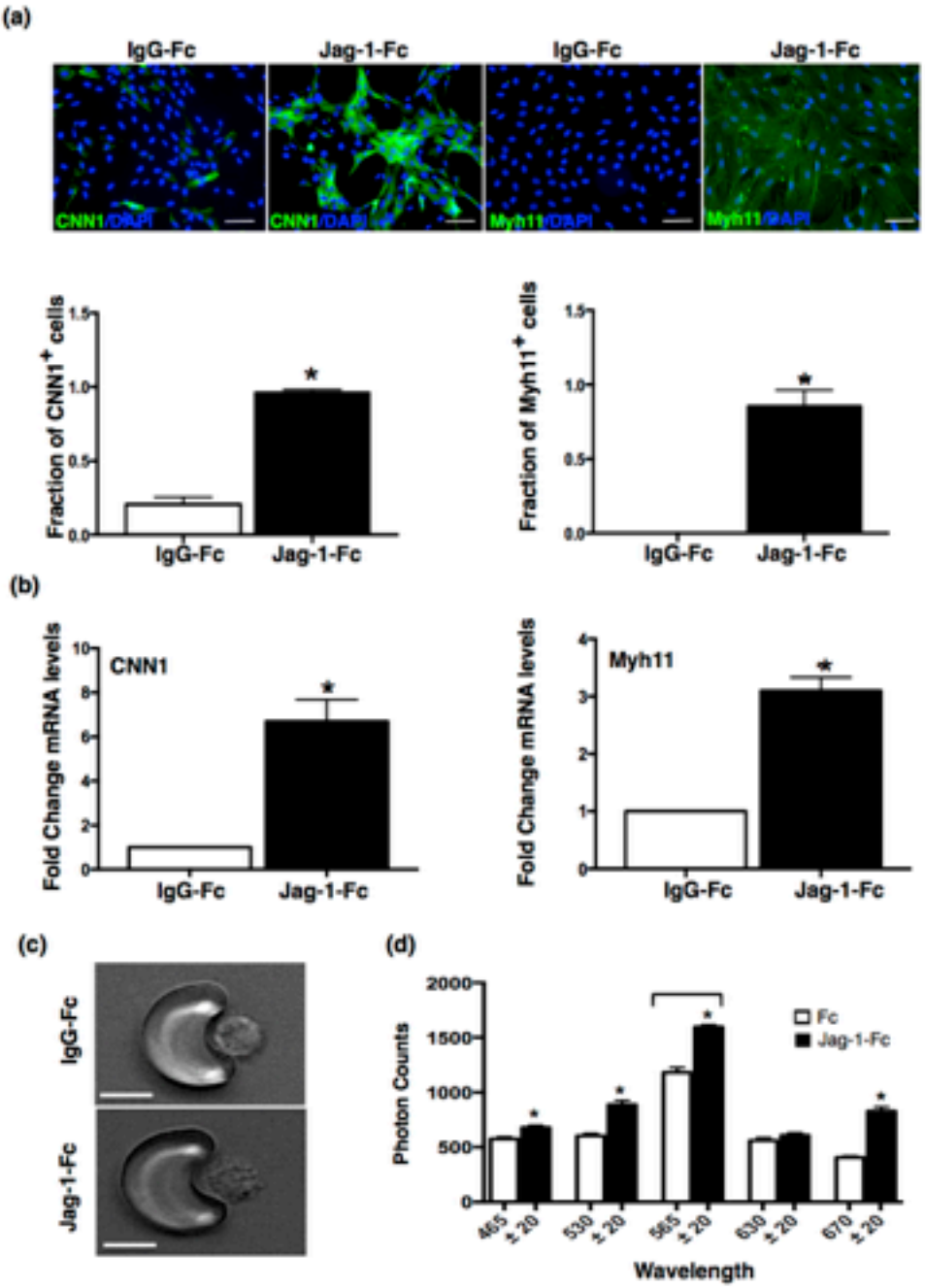

Figure 3.6 Jag-1-Fc induces SMC marker expression and changes in AF photon intensity. (a) representative immunocytochemical image of rMVSCs with DAPI (blue) and CNN1/Myh11 (green) in response to Jag-1-Fc with the fraction of CNN1 and Myh11 positive cells calculated by the average of at least 5 images per treatment group. Scale bars were set to 100µm (b) fold change in CNN1 and Myh11 mRNA expression in rMVSCs in response to Jag-1-Fc; Data are the mean ± SEM from 3 independent experiments (c) Representative phase contract image of rMVSCs treated with IgG-Fc and Jag-1-Fc and captured on v-cups; (d) AF photon intensities of control IgG-Fc and Jag-1-Fc treated rMVSCs across the wavelengths from 465±20 nm to 670±20 nm. Data are the mean ± SEM of 55 cells/group from 3 independent experiments. *$p<0.05$ vs control (without Jag-1).Data analysis was carried out using the prism software and the biochemical data was tested for significance using paired t-tests and the auto-fluorescence data was tested for significance with Wilcoxon t-tests. *$p<0.05$ considered as significant.

3.2.7 TGF-β_1 stimulates auto-fluorescent elastin and collagen expression in stem cells.

Undifferentiated mMSCs and rMVSCs were treated with TGF-β_1 (10ng/ml) for 7 days to evaluate whether the enhanced AF photon intensity of stem cell-derived myogenic progeny at 565 ± 20 nm was due to increased expression of key autofluorescent molecules, elastin and collagen within these cells. The dose and time that demonstrated an AF change was naturally used to evaluate fluorophore gene expression. The expression of elastin, collagen type 1A1, collagen type1A2, collagen type 3A1 and collagen type 3A2 were all increased following TGF-β_1 treatment, however not statistically significant according to Wilcoxon ranked t-tests due to the small sample size [Figure 3.7, 3.8].

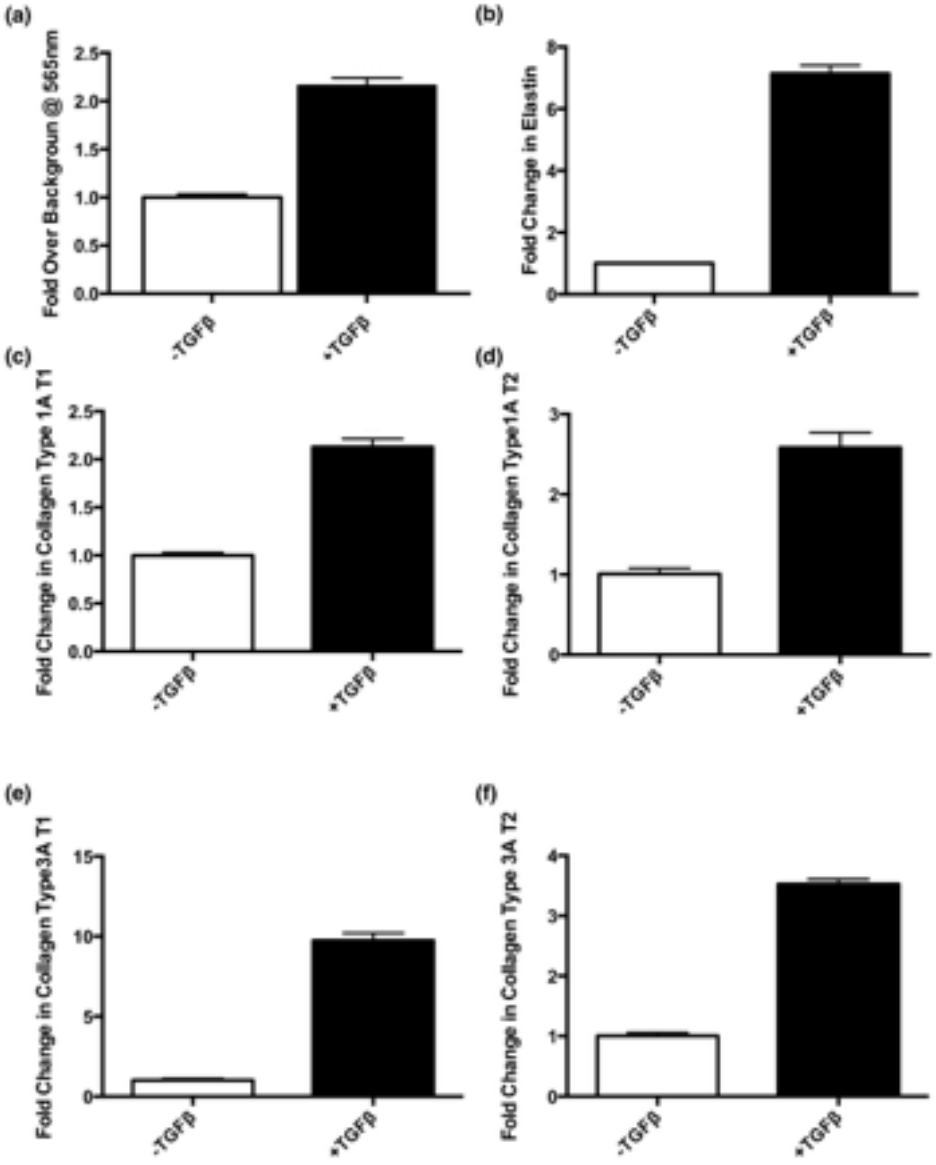

Figure 3.7 TGF-β_1 stimulation of Collagen 1A and Collagen 3A mRNA levels in mMSCs after 7 days. (a) Change in AF photon intensities of mMSCs following treatment with TGF-β_1 for 7 days at the 565±20 nm wavelength; (b) Fold change in elastin mRNA expression in mMSCs in response to TGF-β_1; (c) Fold change in collagen1 alpha 1 mRNA expression in mMSCs in response to TGF-β_1; (d) Fold change in collagen1 alpha 2 mRNA expression in mMSCs in response to TGF-β1; (e) Fold change in collagen3 alpha 1 mRNA expression in mMSCs in response to TGF-β_1 1; (f) Fold change in collagen3 alpha 2 mRNA expression in mMSCs in response to TGF-β_1. Data are the mean ± SEM of triplicate samples. N number of experiments were too low for significance.

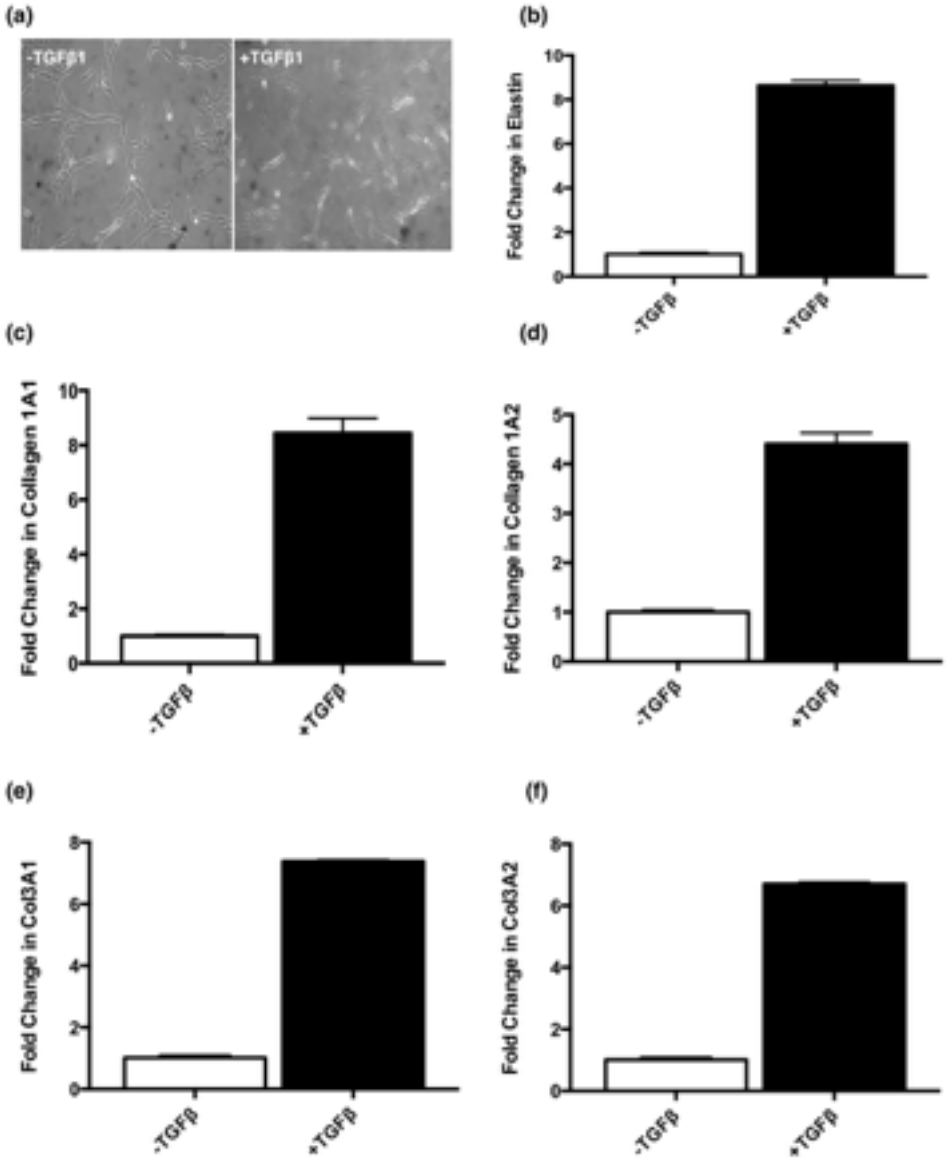

Figure 3.8 TGF-β_1 stimulation of elastin, Collagen 1A and Collagen 3A mRNA levels in rMVSCs after 7 days. (a) Brightfield image of rMVSCs untreated and treated with (10ng/ml) TGF-β_1 for 7 days; (b) Fold change in elastin mRNA expression in rMVSCs in response to TGF-β_1; (c) Fold change in collagen1 alpha 1 mRNA expression in rMVSCs in response to TGF-β_1 (d) Fold change in collagen1 alpha 2 mRNA expression in rMVSCs in response to TGF-β_1; (e) Fold change in collagen3 alpha 1 mRNA expression in rMVSCs in response to TGF-β_1; (f) Fold change in collagen3 alpha 2 mRNA expression in rMVSCs in response to TGF-β_1. Data are the mean ± SEM of triplicate samples. N number of experiments were too low for significance.

3.2.8 Jag-1 stimulates auto-fluorescent elastin and collagen expression in stem cells.

To determine if enhanced expression of collagen and elastin in response to TGF-β_1 was specific to myogenic differentiation, rMVSCs were also treated with Jag-1-Fc and IgG-Fc and analysed in a similar manner. There was a with a significant increase in the AF photon intensities across all wavelengths [Figure 3.9(a)] concomitant with an increase in elastin, collagen 3A1 and collagen 3A2 in rMVSCs following Jag-1-Fc treatment, when compared to the IgG-Fc control. Although the increases are evident they failed the Wilcoxon t-test most likely due to the small sample set. [Figure 3.9(b-d)].

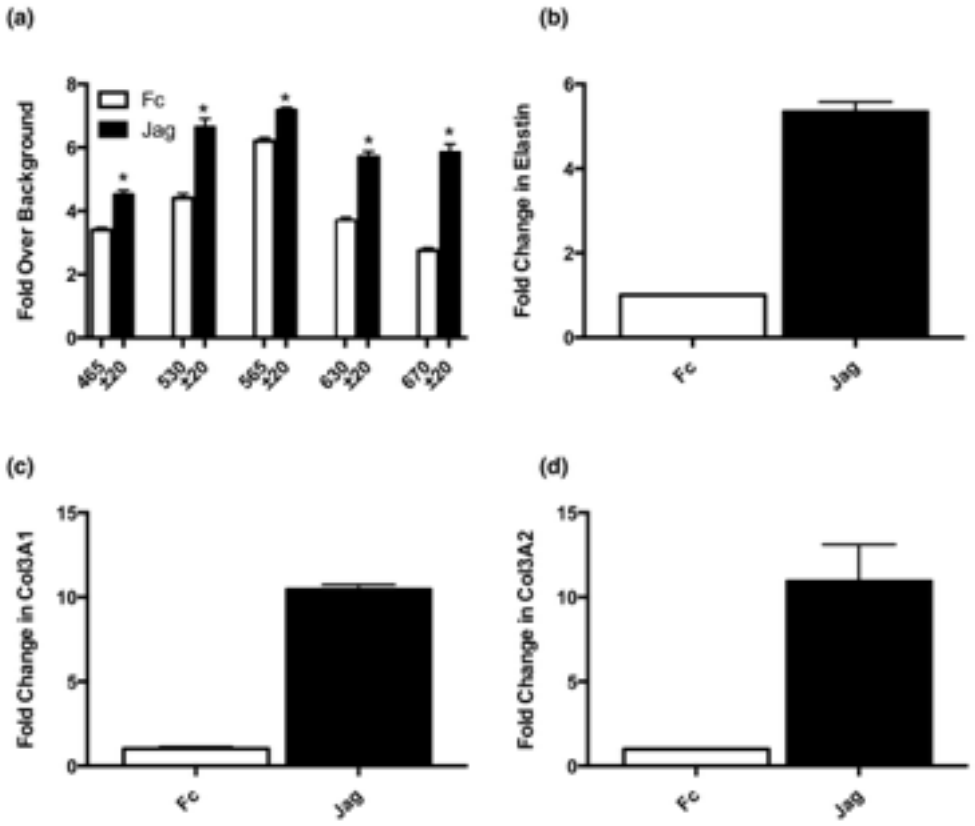

Figure 3.9 Jag-1 stimulation of AF photon intensities and elastin and collagen mRNA levels in rMVSCs. (a) Representative fold change in auto-fluorescence pattern of rMVSCs treated with IgG-Fc and Jag-1 Fc (2 µg/ml); Data are the mean ± SEM of 3 independent experiments (b) fold change in elastin gene expression following treatment with IgG-Fc and Jag-1 Fc (2 µg/ml), (c) Fold change in collagen type 3A1 gene expression following treatment with IgG-Fc and Jag-1 Fc (2 µg/ml); (d) fold change in collagen type 3A2 gene expression following treatment with IgG-Fc and Jag-1 Fc (2 µg/ml). Data are the mean ± SEM of triplicate samples. N number of experiments were too low for significance. *$p<0.05$.

3.2.9 Prolonged treatment of undifferentiated stem cells with TGF-β_1 results in comparable AF profile to ligated cells at the 565±20 nm wavelength

The AF intensity profile at the 565±20 nm wavelength of mMSCs treated with TGF-β_1 (10ng/ml) for 14 and 28 days were analysed and compared to undifferentiated stem cells and neointimal SMC-like cells isolated from ligated carotids after 14 days [Figure 3.10(a)]. Prolonged treatment of cells with TGF-β_1 resulted in an AF photon intensity profile at the 565 ± 20 nm wavelength that mirrored the enhanced AF signature of the neointimal SMC-like cells at this wavelength [Figure 3.10(a)].

3.2.10 Knockdown of collagen significantly reduces auto-fluorescence at the 565 ± 20 nm wavelength.

Undifferentiated mMSCs were transfected with scrambled and siRNA duplexes specific for collagen III and elastin for 72h before the effect of the respective knockdown on the AF photon intensity at the 565±20 nm was assessed. The transfection efficiency of 98% was determined using a fluorescent labelled control siRNA [Figure 3.10(b)]. The effect of collagen III and elastin knockdown on collagen III and elastin mRNA expression was determined by q-RT-PCR (Figure 3.10(c)]. The mMSCs treated with the collagen III siRNA resulted in over 70% knockdown whereas the mMSCs treated with the elastin siRNA had almost complete knockdown [Figure 3.10(c)]. In parallel studies, mMSCs were then captured on the v-cup and exposed to light before the AF photon intensity at 565 ± 20 nm wavelength was recorded. The AF intensity of mMSCs at the 565 ± 20 nm wavelength was slightly reduced in cells following elastin knockdown, but not significantly according to Wilcoxon t-test, when compared to the scrambled control. In contrast, the AF intensity of mMSCs at the 565 ± 20 nm wavelength was significantly reduced in mMSCs following collagen III knockdown, when compared to the scrambled control. These data suggest that collagen III may be

responsible for the AF photon intensity at the 565±20 nm wavelength in stem-cell derive myogenic progeny.

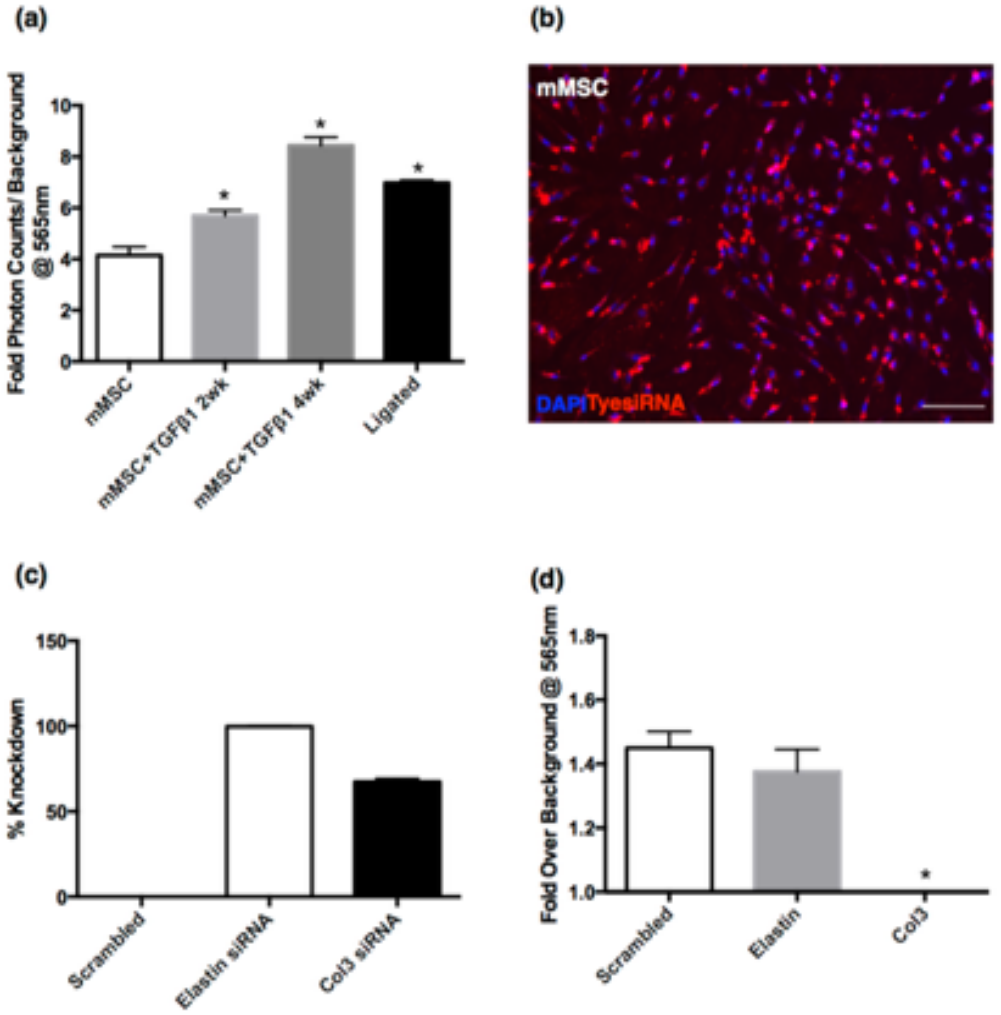

Figure 3.10 Collagen knockdown reduces AF photon intensity at 565 ± 20 nm wavelength in mMSCs. (a) Fold change in AF photon intensity at 565±20 nm of undifferentiated mMSCs and cells treated with TGF-β_1 (10ng/ml) for 14 days and 28 days and compared to cells from ligated vessels. Data are the mean ± SEM of 3 independent experiments. Significance was determined using Wilcoxon t-tests with a $p<0.05$ considered significant (*). (b) representative image of mMSCs transfected with a fluorescent Tye-siRNA imaged after 72 hours; the scale bar was set to 100µm (c) Percentage knockdown of elastin and collagen in response to the elastin and collagen siRNAs, when compared to scrambled control. Significance was tested using the Prism software with the standard paired t-test. Data are the mean ± SEM of triplicate samples. N number of experiments were too low for significance. (d) AF photon intensity of mMSCs following treatment with scrambled siRNA and siRNA targeted against collagen III and elastin. Data are the mean ± SEM of 55 cells/group in 3 independent experiments. Significance was tested using Wilcoxon ranked t-tests with a $*p<0.05$ considered significant.

3.3 Discussion & Conclusion

3.3.1. Discussion

It is widely accepted that the majority of cells composing neointimal lesions are smooth muscle (SMCs)-like cells (Schiele et al., 2005). After the emergence of evidence suggesting that native differentiated SMCs do not appear in the lesion (Tang et al., 2012), conflicting reports on the potential source of these cells have appeared in the literature. On one side of the debate, several investigators propose a re-programming event referred to as 'de-differentiation' is occurring whereby differentiated SMC becomes more plastic and lose differentiated SMC markers before appearing in the lesion (Nemenoff et al., 2011; Herring et al., 2014; Shankman et al., 2015; Cherepanova et al., 2016; Majesky et al., 2016; Chappell et al., 2016). The other side of the debate proposes that resident and/or circulating vascular stem cells and/or endothelial cells that undergo EndoMT differentiate to smooth muscle like-cells, proliferate and accumulate to form the lesion (Torsney et al., 2011; Hu et al., 2004; Klein et al., 2011; Klein 2016; Sata et al. 2002; Hoglund et al. 2010; Tang et al., 2012; Wan et al., 2012; Shikitani et al., 2016; Kramann et al., 2015; Cooley et al., 2014; Yuan et al., 2017). Much of the compelling evidence for de-differentiation and re-programming of SMC comes from lineage tracing experiments where transgenic animals with a Cre recombinase upstream of a smooth muscle marker promotor are bred with animals with a Cre-LoxP specific fluorescent promotor to create an animal where every cell with the SMC promotor are indelibly tagged facilitating high definition tracking using confocal microscopy. However as stem cells may acquire the SMC promotor shortly after injury and themselves become tagged, especially if the inducing stimulus for the Cre (tamoxifen) remains high within tissues, the interpretation of these experiments becomes problematic (Reinert et al., 2012). Moreover, when lineage tracing

analysis is performed using transgenic mice with the Cre upstream of a stem cell specific promoter, nestin (Wan et al., 2012), Gli (Kramann et al., 2015) or S100β (Cahill Lab, unpublished), the tracking suggests a considerable portion of the neointimal and medial SMCs are derived from a non-SMC source. One major drawback with this lineage tracking technique is the requirement for the animals to be sacrificed for tissue extraction and labelling (Kretzschmar & Watt, 2012). In this context, a label-free technology with the potential to track the appearance of cells in vivo would be an excellent platform to resolve this debate.

As outlined in Chapter 1, the interaction of light with cells and tissues produces a scattering of light which can be recorded to generate unique patterns for each cell/tissue type based on their molecular differences (Yun & Kwok, 2017). Lab-on-a-Disc (LOAD) platforms have demonstrated many attractive qualities for cellular analysis and disease diagnosis (Godin et al., 2008). The v-cup array design and auto-fluorescence readings makes it possible to analyse populations of single cells within minutes. Taking advantage of the low cost and ease of use of this platform and the rapid generation of results from this technology, the aim of this chapter was to determine whether the LiPhos LOAD system could detect significant auto-fluorescence differences between individual cells from healthy (medial) and diseased (neointimal and medial) vessels and furthermore, whether similar spectral signatures of individual cells from diseased vessels were evident following myogenic differentiation of undifferentiated stem cells.

Here, for the first time, we utilise auto-fluorescence patterns to compare healthy differentiated SMCs and diseased arteriosclerotic SMCs and stem cells and their vascular progeny.

Sham and ligated carotid arteries were isolated from mice, fixed, sectioned and H&E stained before the intimal and medial volumes assessed. The ligated model had significantly larger media and intima.

The sham carotid displayed α-actin and Myh11 staining whereas the ligated vessel had plenty of the immature α-actin marker and very little of the mature Myh11 marker. The auto-fluorescence patterns were significantly different for the sham and ligated models with the ligated model exhibiting a higher intensity of auto-fluorescence spanning all wavelengths. The differences between the patterns were most prominent at the 475±20 nm, 530±20 nm and 565±20 nm wavelengths. Interestingly, when medial SMCs from sham carotid arteries were compared with aortic SMCs, there was only a slight variation in the signature observed and they had the same auto-fluorescent intensity at the 565±20 nm wavelength. Some amount of variation is to be expected as the differentiated SMCs are derived from two distinct embryological origins (neuroectoderm vs mesoderm) (Cheung et al., 2012). The results demonstrate that auto-fluorescence can be used as a photonic platform to discriminate healthy and diseased vessels label-free. Single cell analysis of the cell populations from ligated vessels showed significant spectral differences to cells from the medial layer of the normal carotid and aorta. As the neointima is composed of primarily SMC-like cells (Schiele et al., 2005) and the medial layer of the vasculature is made of differentiated SMCs (Karrer et al., 1961), this tool can also distinguish neointimal SMC-like cells from native differentiated SMCs. This is not the first study to discriminate healthy and diseased vascular vessels based on auto-fluorescence. Skin auto-fluorescence (SAF) readings have been well characterised in the literature with many reports correlating higher SAF readings in patients with a cardiovascular related issues than in a healthy individual (Noordzig et al., 2012; Dekker et al., 2013; Wong et al., 2014). However, it is the first study, to our knowledge, that discriminates cells isolated directly from diseased and healthy carotids based on their auto-fluorescence patterns.

In an attempt to provide insight to the source of SMC-like cells in the neointima using such auto-fluorescent patterns, the next aim of this chapter was to characterise patterns for stem cells and their myogenic

progeny and compare those patterns to that of the neointimal SMC-like cells.

To do this, TGF-β_1 and Jag-1 were used as drivers of myogenic differentiation. TGF-β_1 is known to activate a heteromeric complex of two serine/threonine kinase receptors [the type IITGF-β receptor (TβRII) and the type I receptor, ALK5], that results in phosphorylation-dependent activation of Smads 2 and 3 that subsequently complex with Smad4 and translocate to the nucleus where they stimulate myogenic gene expression (Massague et al., 2005). Similarly, Jag-1 binds to specific Notch receptors on the plasma membrane that, once cleaved, act as transcriptional activators of myogenic differentiation (Morrow et al., 2008), including activation of the SMA promoter (Noseda et al., 2006).

In this study, mMSCs and C3H T101/2 cells treated with TGF-β_1 (5-10ng/ml) for 7 days resulted in a shift in epigenetic modification, promotor transactivation, gene expression and protein marker expression towards a SMC phenotype. Importantly, mMSCs treated with TGF-β_1 exhibited a higher intensity of auto-fluorescence across all wavelengths. C3H T101/2 cells treated with TGF-β_1 only exhibited greater auto-fluorescence intensity at the 565±20 nm which suggests the change in auto-fluorescence at that particular wavelength may relate to myogenic differentiation.

To evaluate whether the change in auto-fluorescence is due to myogenic differentiation as opposed to a direct effect of TGF-β_1, Ramos B cells were treated in parallel in the same manner and exhibited lower auto-fluorescence across all wavelengths, demonstrating that the auto-fluorescent effect seen with TGF-β_1 is due to a change in the cell phenotype and not an auto-fluorescent effect of the molecule itself. Secondly, an alternative myogenic stimulus Jag-1-Fc was used to evaluate the changes in auto-fluorescence of rMVSCs before and after treatment. Immunocytochemical and gene expression analysis were

performed to confirm the differentiation of rMVSCs to an SMC-like phenotype before cells were captured on the v-cup array. The auto-fluorescent pattern of rMVSCs with and without the myogenic stimulus mimicked that of the mMSCs in the presence and absence of TGF-β_1, further demonstrating that an increase in auto-fluorescence at 565±20 nm in particular occurs concomitant with myogenic differentiation. Moreover, these data suggest that stem cells undergoing myogenic differentiation could also contribute to the increase in intensity of auto-fluorescence of the ligated vessel cells at the 565±20 nm wavelength.

Previous studies have evaluated the change in auto-fluorescence patterns in response to stem cell differentiation using two photon excited fluorescence microscopy for human mesenchymal stem cells and their osteogenic and adipogenic progeny. These studies report a decrease in auto-fluorescence following differentiation to both progeny, however the studies are limited to the 460 nm and 525 nm emission wavelengths (Quinn et al., 2013; Rice et al., 2007; 2010). Multiphoton scanning laser microscopy has also been utilised to evaluate the change in auto-fluorescence of mESCs during spontaneous differentiation and the auto-fluorescence profile increased at the 457 nm emission wavelength (Squirrel et al., 2012) and the 520 nm wavelength (Thimm et al., 2015). In a comparable study, mESCs induced to differentiate to neural stem cells using retanoic acid were analysed for changes in auto-fluorescence. Again, auto-fluorescence intensities increased at 457 nm (emission) following differentiation using multiphoton laser scanning microscopy; however changes at other wavelengths were not investigated (Squirrel et al., 2012).

Much of the data reported to date is limited to the 460±10 nm and 525 nm wavelengths as photonic intensities at those wavelengths have been attributed to auto-fluorescent molecules nicotine adenine dinucleotide (NADH/NAPDH) and flavins, respectively (Bartolome et al., 2015; Quinn et al., 2013; Rice et al., 2007; 2010). As the ratio of NADH/NADPH and

flavins dictate cellular energy and metabolism, alterations in the levels of the molecules can drive the pathogenesis of many diseases such as cancer, neurodegeneration and diabetes. Hence these changes are easily detected label free (Blacker et al., 2014). However, there are many other auto-fluorescent molecules in the cell that may drive detectable changes in auto-fluorescence, such as retinol, folic acid, pyridoxine, lipofuscin, tryptophan, melanin, collagen and elastin (Gosnel et al., 2016). In fact, in one study using multiphoton laser scanning microscopy, researchers detected an increase in auto-fluorescence during mESC differentiation with a concomitant increase of collagen and elastin at 520±35 nm, which suggests other molecules also contribute to auto-fluorescence at that wavelength (Thimm et al., 2015).

In this study, treatment for 7 days with TGF-β_1 and Jag-1, yielded a dramatic spectral change, particularly at the 565±20 nm wavelength. Further treatment of the cells with TGF-β_1 continued to increase the auto-fluorescence at 565±20 nm to comparable levels of the ligated SMC-like cells. One reason suggested for the high level of auto-fluorescence associated with the samples in this study could be due to the elastin and collagen content of the extracellular matrix of SMCs (Bank et al. 1996, Naryanan et al. 1976, Wanjare et al. 2015). Neointimal SMC-like cells have been shown to produce collagen and elastin following injury (Wang et al., 1998; Krishnan et al., 2016; Pahk et al., 2017) and elastin and collagen have been previously shown to exhibit auto-fluorescence (Richards-Kortum and Sevick-Muraca, 1996; Masters and So, 1999; Agarwal et al., 2001; Gosnel et al., 2016). Moreover, stem cells undergoing myogenic differentiation produce collagen and elastin (Swaminathan et al., 2014; Li et al., 2016; Thimm et al., 2015). Of course, de-differentiated smooth muscle cells have also been historically implicated in the high rate of collagen and elastin production in disease. Subcultured primary aortic rat and rabbit SMC-like cells exhibit enhanced collagen production in vitro (Sjolund et al., 1986; Ang et al., 1990; Okada et al., 1990) and in vivo (Hachani et al., 2011). However, none of these

studies address the possibility that the 'de-differentiated SMCs' could actually be stem-cell derived SMCs. Recent evidence suggest that this indeed may be the case since indelibly marked SMCs from Myh11 Cre-LoxP transgenic mice are lost as SMC are cultured in vitro (Yuan et al., 2017). Moreover, during vascular development, SMCs also exhibit very high rates of synthesis of extracellular matrix components including collagen, elastin which is due to myogenic differentiation from early vascular progenitors (Owens et al., 2004). In fact, to the best of our knowledge, there have been no definitive experiments proving that de-differentiated SMCs, and not stem cell-derived SMCs, produce collagen and elastin.

To evaluate whether elastin and collagen could be responsible for the high levels of auto-fluorescence in myogenic progeny samples and the neointimal SMC-like cell sample, gene expression analysis for elastin, collagen type I and collagen type III was carried out for mMSCs and rMVSCs following myogenic differentiation. Targeted siRNA knockdown of those genes was also analysed for the effect on the auto-fluorescence profile at the 565±20 nm wavelength. The elastin and collagen content of mMSCs and rMVSCs increased in response to TGF-β_1 and Jag-1-Fc supporting previous reports that stem cell derived SMCs produce collagen and elastin (Swaminathan et al., 2014; Li et al., 2016). Targeted siRNA knockdown of the collagen III gene showed a depletion in the auto-fluorescence levels at the 565±20 nm wavelength, further indicating that collagen contributes to auto-fluorescence at that wavelength. This correlates with the mESC study mentioned above that also noted an increase in auto-fluorescence in conjunction with an increase in collagen at a nearby wavelength (Thimm et al., 2015). It is interesting to note that collagen type III is associated with the high 565±20 nm auto-fluorescence signature of myogenic progeny in vitro and the ligated SMC-like cells following vascular injury (Wang et al., 1998; Krishnan et al., 2016; Pahk et al., 2017). Moreover, collagen III has been specifically implicated with restenotic plaques in human arterial models, while collagen I is

associated with atherosclerosis but reduces during re-stenosis (Krishnan et al., 2016). Furthermore, Collagen type III levels increase in stented coronary arteries versus un-stented (Vladimirskaya et al., 2017) and deposition of collagen type III has been identified along with neointimal SMC-like cells in a rat carotid model (Pahk et al., 2017).

Collectively, the data presented in this study clearly demonstrate that differentiated SMCs are different to the medial and neointimal SMC. This can be seen clearly from the decreased immunohistochemical staining of neointimal SMC-like cells that lose Myh11 expression and the autofluorescence signature of neointimal SMC-like cell that exhibit higher autofluorescence intensities, in particular, at 565±20 nm. This study also demonstrates that stem cells can be distinguished from dSMCs biochemically based on their gene and protein expression, epigenetically based on their histone modifications and further by their auto-fluorescence profiles. The stem-cell derived myogenic progeny can also be distinguished from undifferentiated stem cells biochemically and epigenetically as they exhibit increased SMC marker gene and protein expression but also acquire the SMC specific histone modification H3K4me2 at the Myh11 promoter. Stem-cell derived myogenic progeny can also be discriminated based on their auto-fluorescence profiles with myogenic progeny characterised by higher auto-fluorescence particularly at the 565±20 nm. Although myogenic progeny increase their expression of SMC markers and acquire the SMC epigenetic modifications, the SMC marker levels and epigenetic H3K4me2 enrichment levels are much lower than the differentiated dSMC which further suggests that stem cell derived SMCs are different to dSMCs. In fact, at an epigenetic level, stem cell-derived SMCs mimic vascular smooth muscle cells in culture which are referred to as 'de-differentiated SMCs', supporting the findings by Tang et al., (2012) which suggest they are the same cell (Tang et al., 2012). Moreover, myogenic progeny reach dSMC auto-fluorescent levels after 7 days but exceed those levels over longer periods of time. Longer treatment with TGF-β_1 actually drives the auto-fluorescence levels to the

neointimal SMC-like cell profile. Based on these biochemical, epigenetic and AF photonic similarities, this study therefore clearly supports the concept that the source of the SMC-like cells present in the neointima may be derived from a stem cell source.

3.3.2 Conclusion

Regardless of the cause for the change in auto-fluorescence patterns of individual cells from sham (healthy) and ligated (arteriosclerotic) carotid arteries this chapter clearly demonstrates the ability of the microfluidic v-cup array and auto-fluorescence studies to fundamentally discriminate between cells from healthy and diseased (arteriosclerotic) vessels, undifferentiated stem cells and their myogenic progeny. While this novel platform is attractive, as it is cheap and easy to use, it lacks the specificity to identify the exact cellular and/or molecular differences relating to the differences in auto-fluorescence signatures.

To address this question in more detail, Chapter 4 outlines the more sensitive vibrational spectroscopic photonic platforms, Raman and FTIR, in discriminating undifferentiated stem cells from their myogenic and osteogenic progeny and also compares their spectral signatures to that of the proposed 'de-differentiated SMC' in culture.

Chapter 4

Photonic Discrimination of vascular stem cells, their myogenic progeny and de-differentiated smooth muscle cells by Raman spectroscopy and Fourier Transform IR

4.1.1 Introduction

Among the various imaging platforms available to interrogate closely related cell populations and discriminate cell-dependent changes in vessel structure due to arteriosclerosis, label-free techniques such as vibrational spectroscopy have shown great promise (Cheng & Xie, 2016). Vibrational spectroscopy is a subset of spectroscopy which analyses vibrations within a molecule (or material), which are characteristic of the molecular structure and, in polyatomic molecules, give rise to a spectroscopic "fingerprint" of that molecule. The spectrum of vibrational energies can thus be employed to characterise a molecular structure, or changes to it due to the local environment or external factors (e.g. radiation, chemical agents). Vibrational energies fall within the mid - Infrared (IR) region of the electromagnetic spectrum and are commonly probed through IR absorption spectroscopy (Miller, 1982). Raman spectroscopy is a complementary technique whereby incident radiation couples with the oscillating polarisation of the molecule and thus generates or annihilates a vibrational quantum, similarly resulting in a vibrational spectrum (Byrne et al., 2016). The differing underlying mechanisms give rise to a complementarity of the two techniques, such that vibrations of asymmetric, polar bonds tend to be strong in IR spectra, whereas Raman is particularly suitable as a probe of symmetric, non-polar groups. Moreover, FTIR monitors the absorption of IR radiation whereas Raman scattering can be employed in the UV, visible or near-IR regions of the spectrum and thus offers intrinsically higher spatial resolution for cellular and sub-cellular mapping or profiling. The limit of resolution is determined classically by the wavelength (<1μm for Raman, ~5-10μM for IR) (Efeoglu et al., 2016). Therefore, the longer wavelength of mid infrared radiation, coupled with the use of multidetector arrays in the Fourier Transform mode, render IR techniques more suitable for mapping larger cell populations or tissue sections (Byrne et al., 2016).

To follow on from Chapter 3, the current study was undertaken to establish whether vibrational spectroscopy could be implemented as a

novel photonic platform to more specifically discriminate undifferentiated bone marrow-derived stem cells from their myogenic progeny following differentiation i*n vitro* and further whether these cell populations could be discriminated from de-differentiated 'synthetic' SMCs and stem cell-derived osteogenic progeny.

4.1.2. Objectives:

The main aims of this chapter were:-

4. To first validate the use of vibrational spectroscopy (Raman and FTIR) to discriminate undifferentiated bone marrow-derived mesenchymal stem cells (bm-MSCs) from their osteogenic progeny *in vitro.*

5. To discriminate undifferentiated mesenchymal stem cells (bm-MSCs), their myogenic progeny (St-SMCs) and de-differentiated smooth muscle cells (ddSMCs) in culture by FTIR as a rapid label-free screening tool.

6. To specifically characterise and discriminate undifferentiated stem cells (bm-MSCs), their myogenic progeny (St-SMCs) and de-differentiated smooth muscle cells (ddSMCs) by Raman spectroscopy to compare and contrast molecular differences between these cell populations.

7. To determine whether Raman and FTIR can discriminate myogenic progeny from osteogenic progeny *in vitro* when derived from the same undifferentiated stem cell population.

4.1.3. Strategy

The main objective of this chapter was to analyse undifferentiated MSCs, their myogenic and osteogenic progeny and 'de-differentiated' subcultured SMCs by FTIR and Raman spectroscopy to evaluate whether these distinct cell populations can be discriminated based on their spectral properties. To achieve this, rat MSCs were cultured with TGF-β_1 (10ng/ml) for 14 days to induce myogenic differentiation or 21 days with osteogenic media to induced osteogenic differentiation. Rat aortic SMCs were enzymatically digested and sub-cultured to the point that they become highly proliferative and lose their contractile Myh11 marker and are termed 'de-differentiated' (ddSMCs). The ddSMCs, undifferentiated stem cells (MSCs) and their myogenic progeny (St-SMCs) were then seeded onto calcium fluoride discs and both FTIR of individual cell populations and Raman spectra of individual nuclei were recorded for each population. The spectra were also transformed using the principle component algorithm to plots of their principle components as a classification system for each cell type so that the system can also be used to classify unidentified cells.

Data analysis for the biochemical data was carried out using the Prism software and paired t-tests for parametric data and Wilcoxon ranked t-tests for non-parametric data.

Spectral pre-processing was carried out using MatLab. FTIR spectra were corrected using a scatter free standard matrigel spectrum previously characterised and background scattering was removed using the Resonant MIE correction algorithm. Similarly, Raman spectra were baseline corrected and subjected to cosmic ray and MIE scattering removal using the extended multiplicative signal correction algorithm. Spectra were finally smoothed using Savitzky-Golay filter (k = 3; w = 7) to reduce noise.

FTIR and Raman spectra were then analysed by the unsupervised multivariate analysis techniques, principle component analysis and linear discriminant analysis, to plot the spectra based on their variances (principle components) and group classes based on their PC scores.

4.2. Results

4.2.1. Validation that Raman and FTIR spectra provide biochemical information about a cell

A sample population of $CD44^+$ bm-MSCs was analysed by both FTIR and Raman spectroscopy, and the raw spectra recorded, processed and the mean spectrum presented [Figure 4.1]. The FTIR bands are labelled with assignments of typical biochemical origin. In the "high wavenumber region", >2500 cm^{-1}, the distinctive vibrations of N-H, C-H and O-H of lipids and proteins can be found, whereas in the "fingerprint region", <2000 cm^{-1}, the features are typically more complex combinations, including the Amide I (1650 cm^{-1}) and Amide II (1520 cm^{-1}) modes of proteins, nucleic acid phosphate stretching modes at 1070 cm^{-1} and 1250 cm^{-1} and lipidic derived features at 1310 cm^{-1} and 1750 cm^{-1}. A more detailed list of band assignments is provided in Table 4.1. Mean Raman spectra for bm-MSC nuclei were also recorded and analysed following cosmic ray removal and EMSC correction and the prominent peaks in bm-MSCs are annotated and presented [Figure 4.1(b), Table 4.2]. It should be noted that, although complementary techniques, the features in the respective spectra of FTIR and Raman have similar origin. Thus, the Raman spectrum of the nucleus exhibits similarly prominent signatures associated with proteins and lipids across the fingerprint region, as well as large peaks related to DNA and RNA at 785 cm^{-1}.

(a)

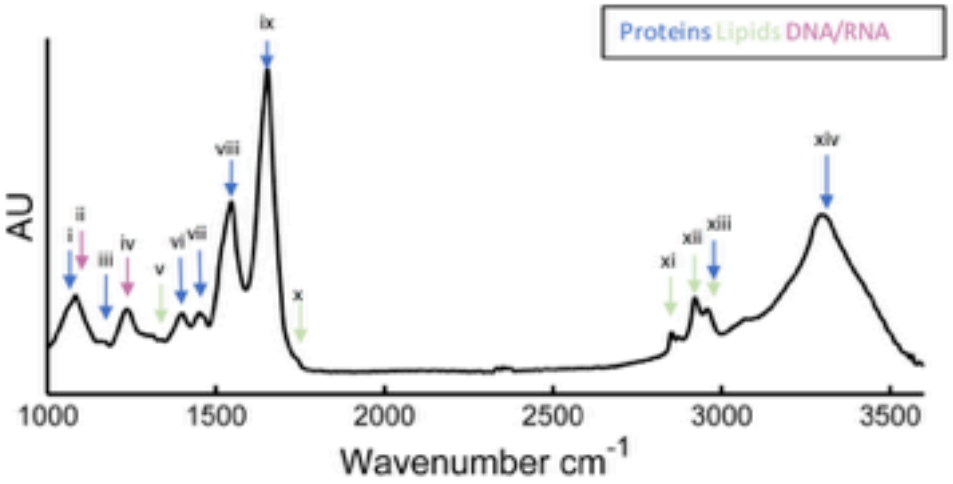

Table 4.1

	Wavenumber	FTIR Peak assignments	Association
(i)	1036	C-C skeletal stretching	Proteins
(ii)	1072	PO_2 symmetric stretching	DNA/RNA
(iii)	1152	C-C and C-O stretching	Proteins
(iv)	1220-1280	PO_2 asymmetric stretching Amide III	DNA/RNA
(v)	1312	CH_2 stretching	Phospholipids
(vi)	1400	CH_3 symmetric stretching	Proteins
(vii)	1456	CH_3 asymmetric stretching	Proteins
(viii)	1546	Amide II	Proteins
(ix)	1620-1700	Amide I	Proteins
(x)	1742	Ester, C=O stretching	Lipids
(xi)	2854	CH_2 symmetric stretching	Lipids
(xii)	2926	CH_2 asymmetric stretching	Lipids
(xiii)	2964	CH_3 asymmetric stretching	Lipids and Proteins
(xiv)	3296	NH asymmetric stretching Amide A	Proteins

Figure 4.1(a). FTIR cell spectra. Representative mean FTIR spectra recorded for bm-MSCs following Resonant Mie (RMieS) correction with classification of relevant peaks and their known association to proteins, nucleic acid and lipids are described in the adjacent **Table 4.1.**

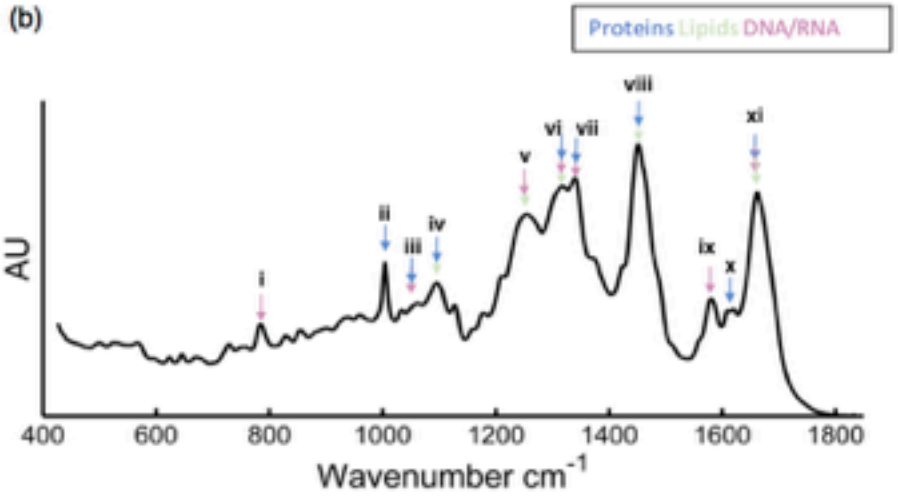

Table 4.2

	Wavenumber	Chemical bond	Association
(i)	785-788	Stretching of DNA related bonds, and DNA/RNA breathing modes	Nucleic Acid
(ii)	1004	Phenylalanine	Protein
(iii)	1090	Stretching of DNA related bonds Stretching of C-N backbone	Nucleic Acid Protein
(iv)	1127	Stretching of C-N backbone Stretching of C-C	Protein Lipid
(v)	1262	DNA/RNA breathing modes Amide III	Nucleic Acid Lipid
(vi)	1319	CH_3, CH_2 twisting DNA/RNA breathing modes CH deformation vibration	Lipid Nucleic Acid Protein
(vii)	1341	DNA/RNA breathing modes CH deformation vibration	Nucleic Acid Protein
(viii)	1451	CH_2 deformation vibration	Protein/Lipid
(ix)	1585	DNA/RNA breathing modes	Nucleic Acid
(x)	1619	Tyrosine; tryptophan	Protein
(xi)	1662	DNA/RNA breathing modes Amide I Fatty acids	Nucleic Acid Protein Lipid

Figure 4.1(b). Raman cell spectra. Raw (110, top) and processed (55, bottom) and mean Raman spectra for bm-MSCs (black) following cosmic ray removal and EMSC correction and their known association to proteins, nucleic acid and lipids are described in the adjacent **Table 4.2.** Also highlighted are nine commonly referenced wavenumber bands within the fingerprint region that can be generally attributed to: proteins, nucleic acids; carbohydrates and lipids.

4.2.2. FTIR and Raman spectroscopy both discriminate bone-marrow derived mesenchymal stem cells from their osteogenic progeny *in vitro*

Osteogenic differentiation of bm-MSC (St-Osteo) was first validated by phase contrast microscopy of gross morphological differences before and after differentiation. St-Osteo cells were morphologically distinct from bm-MSC and exhibited a more osteoblast phenotype with a pronounced, large spherical nucleus [Figure 4.2a(ii-iii)]. Alizarin red staining confirmed the presence of calcium deposits in St-Osteo when compared to bm-MSC [Figure 4.2a (iv-v)], providing evidence for bm-MSC multipotency *in vitro*.

Osteogenic differentiation of bm-MSC to St-Osteo was analysed by FTIR spectroscopy and a spectrally integrated IR map of a representative population of bm-MSC is presented [Figure 4.2a(vi)]. There were notable differences in the St-Osteo mean spectra across the high wavenumber (2000-3500 cm^{-1}) and fingerprint (1000-1800 cm^{-1}) regions [Figure 4.2b], in particular, a strong feature at ~1037 cm^{-1} that overlapped the nucleic acid phosphate backbone band at ~1070 cm^{-1} that is commonly assigned to carbonate groups in apatite (Awonusi et al., 2007). There were also notable differences at 2964 cm^{-1} (corresponding to CH_3 asymmetric stretching of lipids and proteins) where St-Osteo cells had a greater peak intensity. The loading of the discriminating PC1 demonstrated pronounced increases in the feature at 1037 cm^{-1} for St-Osteo and a reduction of the strong Amide I and Amide III features at 1220-1280 cm^{-1} [Figure 4.2b]. PCA identified all significant changes across the FTIR spectroscopic datasets and the scatter plots generated clearly discriminated both groups from each other [Figure 4.2c].

Raman spectra of individual cell nuclei from bm-MSC and St-Osteo were also recorded and the mean spectra are superimposed to reveal clear differences [Figure 4.2d]. The most pronounced was the peak at 960 cm^{-1}, clearly indicating the presence of phosphates associated with mineralisation within the St-Osteo cells [Figure 4.2d] (McManus et al., 2012). Prominent bands at 1030 cm^{-1} and 1070 cm^{-1} associated with

phosphate and carbonate groups respectively, were also evident although they were very much weaker compared to the prominent 960 cm^{-1} feature. Several other peaks were observed that clearly separated bm-MSC from their osteogenic progeny and relate to nucleic acid (DNA/RNA) at 788 cm^{-1}, 1338 cm^{-1}, 1490 cm^{-1}, and 1585 cm^{-1} as well as lipids at 1379 cm^{-1} [Figure 2d]. PCA identified significant changes across the spectrum and the scatter plots generated clearly discriminated both groups from each other [Figure 4.2e].

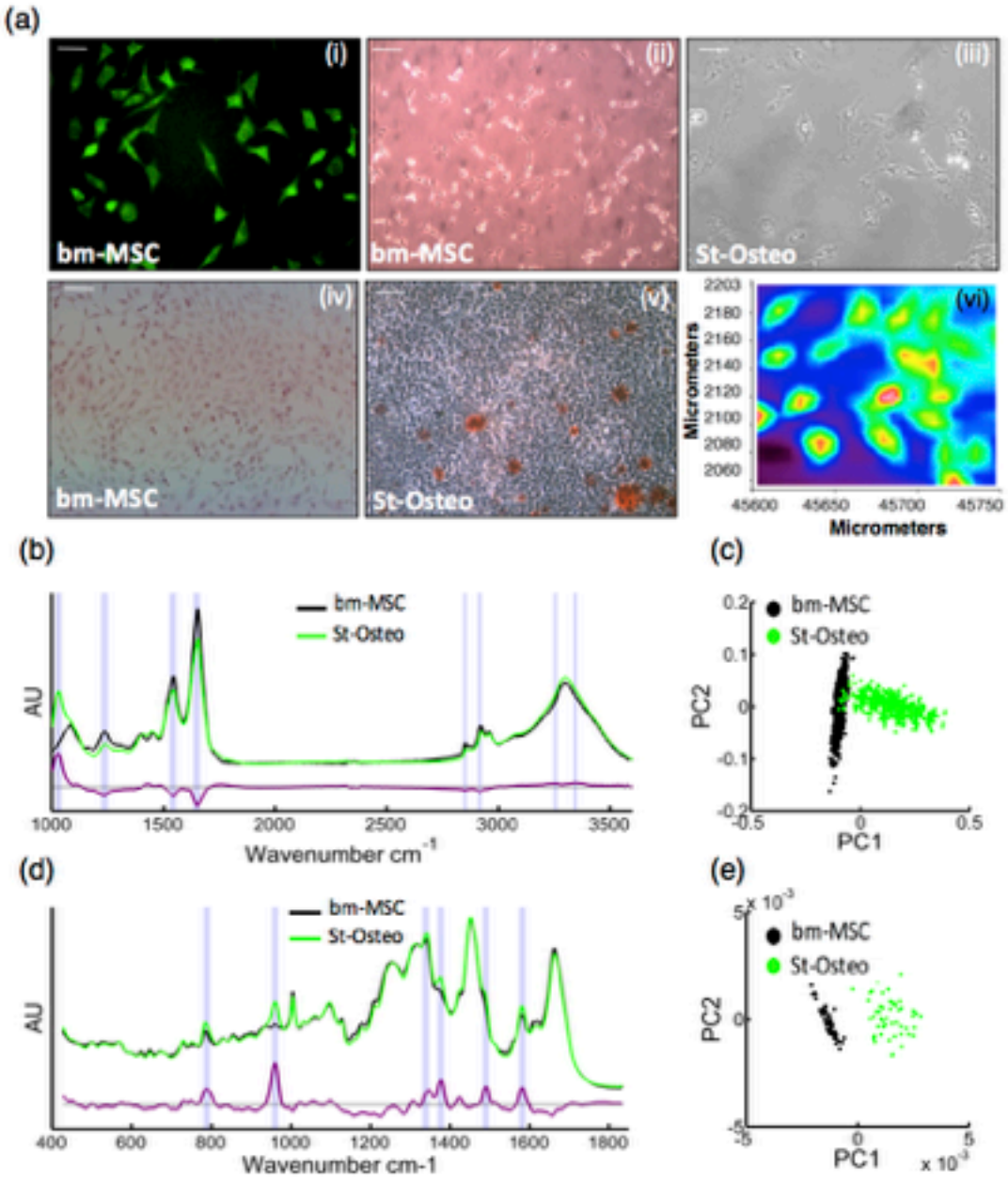

Figure 4.2. Vibrational spectroscopic analysis of bm-MSCs and their osteogenic progeny. (a)(i) Representative immunocytochemical image of $CD44^{+}$ bm-MSC in culture, (ii-iii) phase contrast images and (iv, v) alizarin red staining of bm-MSCs before and after osteogenic differentiation with osteogenic inductive media for 21 d, (vi) representative FTIR heat map of bm-MSCs. (b) Mean FTIR spectra and loading plot of the first principal component and (c) PCA score plot of the bm-MSCs (black) and the St-Osteo (green) cell groups before and after osteogenic differentiation. (d) Mean Raman spectra and loading plot of the first principle component following PCA of the processed bm-MSC and St-Osteo datasets and (e) PCA score plot of bm-MSCs and St-Osteo before and after osteogenic differentiation.

4.2.3. FTIR and Raman spectroscopy discriminates bone-marrow derived mesenchymal stem cells from their myogenic progeny *in vitro*

Myogenic differentiation following treatment of bm-MSC with TGF-β_1 was confirmed by determining the enrichment of a synonymous SMC epigenetic histone mark at the Myh11 promoter, Myh11 promoter transactivation, SMC differentiation marker transcript levels (Myh11, CNN1) and immunocytochemical detection of the number of Myh11 and CNN1 positive cells, respectively [Figure 4.3]. Chromatin immunoprecipitation (ChIP) analysis of freshly isolated rat aortic SMCs confirmed the enrichment of the specific SMC epigenetic mark, di-methylation of lysine 4 on histone H3 (H3K4me2) at the Myh11 locus (Gomez et al., 2015) concomitant with a lack of enrichment of the tri-methylation of lysine 27 on histone H3 (H3K27me3) mark which is consistent with a general repression of developmental genes (Van der Muelen et al., 2015) [Figure 4.3a]. In contrast, bm-MSC were enriched for the H3K27me3 mark at the same locus [Figure 4.3a].

Treatment of bm-MSC with TGF-β_1 (2ng/ml) for 7 d (optimum dose and time for histone modification in this study) increased the level of enrichment of the H3K4me2 mark with a reciprocal diminution of the H3K27me3 mark to levels that were comparable to H3K4me2 and H3K27me3 levels in sub-cultured de-differentiated rat SMCs (ddSMCs) [Figure 4.3a]. This was work was carried out in collaboration with Dr. Roya Hakimjavadi, Mariana Soledad di Luca and Denise Burtenshaw (VBT Lab, DCU). TGF-β_1 treatment also significantly induced Myh11 promoter transactivation [Figure 4.3b] after 2 d concomitant with enhanced Myh11 mRNA levels [Figure 4.3c]. Luciferase readings were carried out by Gillian Casey (TCD).

Furthermore, treatment of bm-MSCs with TGF-β_1 (2ng/ml) for 14 d resulted in a marked increase in the number of Myh11$^+$ and CNN1$^+$ positive cells, when compared to vehicle control [Figure 4.3d]. Similarly,

treatment of bm-MSC with Jag-1-Fc resulted in a significant increase in Myh11 and CNN1 mRNA levels after 48 h [Figure 4.3e] concomitant with a dramatic increase in the number of smooth muscle cell α-actin (SMA^+) and $CNN1^+$ positive cells after 7 d [Figure 4.3f]. As with the mMSCs and C3H T10 1/2 cells in chapter 3, doses and times were chosen by a trial and error approach whereby promotor activity required less TGF-β1 and time for sufficient activation than protein expression. The rat bm-MSCs also required additional time to yield consistent protein changes. Spectra were recorded at the time where protein changes were biochemically confirmed.

FTIR maps and mean spectra were recorded for bm-MSC and their myogenic progeny [Figure 4.3g]. In both cases, there were significant peak intensity increases in myogenic progeny in the high wavenumber region, >2500 cm^{-1}, in particular, between 2800 cm^{-1} and 3000 cm^{-1} [Figure 4.3g] which is associated with acyl chain stretching vibrations from fatty acids of lipids (Movasaghi & Rehman, 2007). There were also significant spectral differences in bands in the C-H stretching region associated with absorbance from lipids (3050-2800 cm^{-1}), the amide I and II region associated with protein absorbance (1700-1500 cm^{-1}), and in the lower wavenumber region associated with nucleic acids (1300-1000 cm^{-1}) [Figure 4.3g]. Notably, PCA of the FTIR spectroscopic data demonstrated that bm-MSCs could be clearly separated from their myogenic progeny according to the first principal component (PC1) [Figure 4.3h]. Moreover, 3-way multivariate statistical analysis revealed that bm-MSC could be clearly discriminated from their myogenic progeny, independent of the inductive stimulus to generate the progeny [Figure 4.3h].

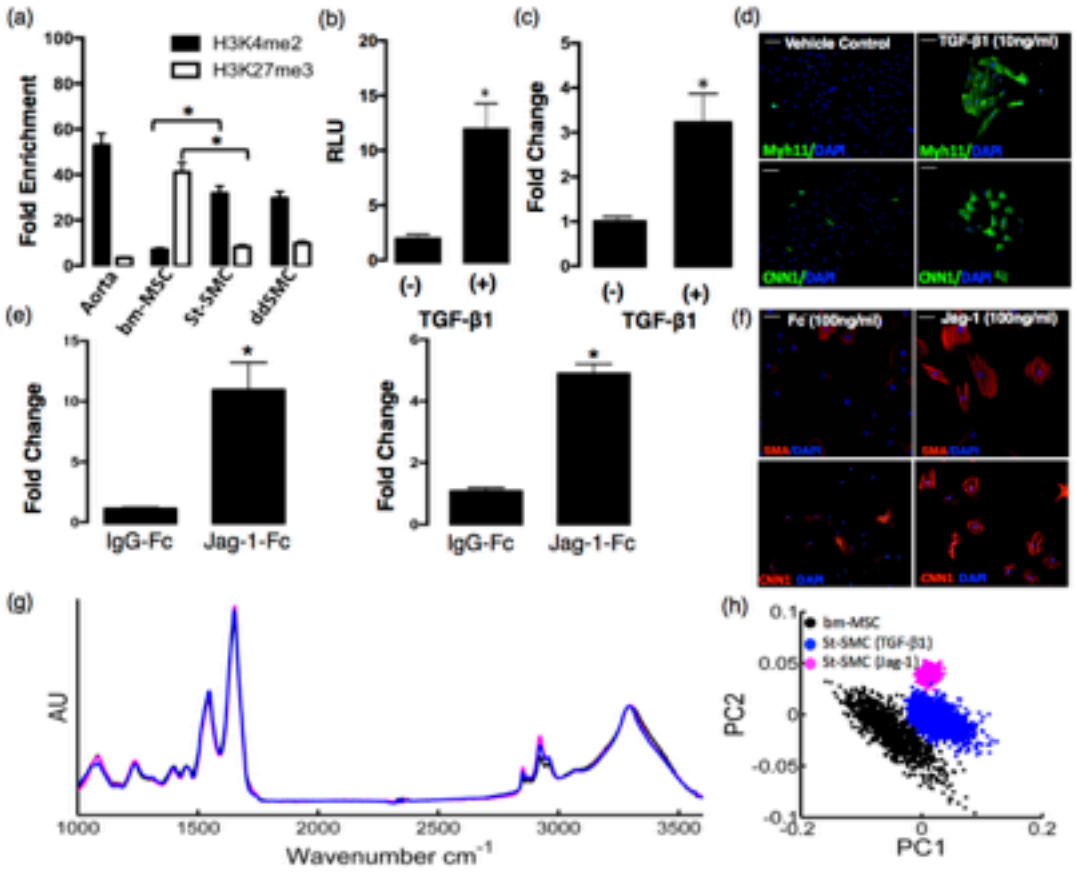

Figure 4.3. FTIR spectroscopic analysis of bm-MSCs and their myogenic progeny. (a) Representative Chromatin Immunoprecipitation(ChIP) analysis of H3K4me2 and H4K27me3 enrichment at the Myh11 locus in freshly isolated differentiated aortic SMCs, sub-cultured ddSMCs and bm-MSCs before and after myogenic differentiation with TGF-β_1 (2ng/ml) for 7 d. Data are the mean ± SEM of three samples and are representative of 3 similar experiments (b) Myh11 promoter transactivation and (c) Myh11 mRNA expression levels in bm-MSCs before and after myogenic differentiation with TGF-β_1 (2ng/ml) for 2 d. Data are the mean ± SEM of three experiments (d) Representative immunocytochemical analysis of the number of Myh11$^+$ and CNN1$^+$ bm-MSCs before and after myogenic differentiation with TGF-β_1 (2ng/ml) for 7 d, (e) n and Myh11 mRNA levels before and after myogenic differentiation with Jag-1 (2 µg/ml) for 2 d and (f) representative immunocytochemical analysis of the number of SMA$^+$ and CNN1$^+$ before and after myogenic differentiation with Jag-1 (100ng/ml) for 5 d. (g) Mean FTIR spectra and (h) Scatter plot of the first principal component after PCA for bm-MSCs before and after myogenic differentiation with TGF-β_1 (2ng/ml) and Jag-1 (2 µg/ml) for 14 d. Data analysis (a)-(e) was carried out using the Prism software and paired t-tests and *p<0.05 considered significant.

4.2.4. FTIR spectroscopic comparisons between de-differentiated SMC, MSCs and stem cell derived SMC progeny.

Dissociated rat aortic SMCs were isolated and grown in culture to the point where they became highly proliferative and lost their SMC MHC marker (approximately passage 4), and were therefore deemed ‘de-differentiated' SMCs (ddSMCs). Morphological analysis of the ddSMCs exhibited strong cytoplasmic refractivity, an oval nucleus and rich cytoplasm and overlapped when confluent, forming typical SMC 'peak-to-valley' growth, as previously reported [Figure 4.4a] [31]. The two major morphological phenotypes were spindle shaped [Figure 4.4a(i), a(ii)] and epithelioid [Figure 4.4a(iii)]. Both phenotypes expressed SMA and Myh11 [Figure 4.4a (iv), (v)], but without the distinctive Myh11 myofilament arrangement within the cytoplasm [Figure 4.4a (v)]. In contrast, the majority of myogenic progeny [St-SMC-TGF-β_1] were spindle-like cells without a strong cytoplasmic refractivity [Figure 4.4a(vi)]. Moreover, the levels of Myh11 mRNA in ddSMC were significantly reduced when compared to that of freshly isolated rat aortic SMCs and were comparable to the levels present in stem cell-derived myogenic progeny [St-SMC-TGF-β_1] [Figure 4.4b].

FTIR maps and mean spectra were recorded and analysed for ddSMCs and compared to both undifferentiated bm-MSCs and their myogenic (St-SMC-TGF-β_1) and osteogenic progeny (St-Osteo), respectively [Figure 4.4c], before PCA analysis of the spectroscopic datasets was performed [Figure 4.4d]. Prominent peaks were observed for ddSMCs across the high wavenumber (2000-3500 cm^{-1}) and fingerprint (1000-1800 cm^{-1}) regions of the spectrum. In particular, the main spectral characteristics for ddSMCs were bands at ~1540 cm^{-1} and 1650 cm^{-1} (amide I and II, respectively), ~1060 cm^{-1}, 1225cm^{-1} and 1460 cm^{-1} (C-C and C-H bending) and ~2850 cm^{-1} - 2960 cm^{-1} and 3325cm^{-1}. The peak at ~1225cm^{-1}, associated with phosphate stretching modes, was noticeably reduced in both ddSMC and St-Osteo cells, when compared undifferentiated bm-MSC and their myogenic progeny [Figure 4.4c],

respectively, as were the peaks at 1380 cm^{-1} and 1660 cm^{-1} (associated with amide I and II proteins) and 2850-2960 cm^{-1} (associated with distinctive vibrations of N-H, C-H and O-H of lipids and proteins) [Figure 4.4c]. In contrast, the ddSMC had a more prominent peak at the ~1036 cm-1 and ddSMC and St-Osteo cells at ~ 3296 cm-1 that are associated with proteins [Table 4.1] [Figure 4.4c].

4.2.5. Raman spectroscopic comparisons between de-differentiated SMC, MSCs and stem cell derived SMC progeny.

All four cell populations were separated by multivariate statistical analysis of Raman spectra using a 4-way PCA scatterplot [Figure 4.4e, f, Table 4.4] with the most notable differences apparent for the St-Osteo spectra. Peak intensities were higher at the 785-788 cm^{-1} and 1585cm^{-1} correlating to nucleic acids, 960 cm^{-1} corresponding to its strong phosphate peak and the 1375cm^{-1} associated with proteoglycans (Gamsjaeger et al., 2014). Many other prominent wavenumbers in the loadings for the first two principal components are also highlighted and the wavenumber associations are discussed below.

Using 4-way multivariate statistical analysis, there was a significant separation of the four populations by FTIR [Figure 4.4d, Table 4.3] as it successfully discriminated ddSMCs, undifferentiated bm-MSCs and their myogenic (St-SMC(TGF-β_1)) or osteogenic (St-Osteo) progeny. Moreover, using PCA/LDA, FTIR could discriminate between undifferentiated bm-MSCs from both their myogenic and osteogenic progeny (St-Osteo) with significant confidence even when these daughter cells originated from the same undifferentiated bm-MSC stem cell population [Table 4.3].

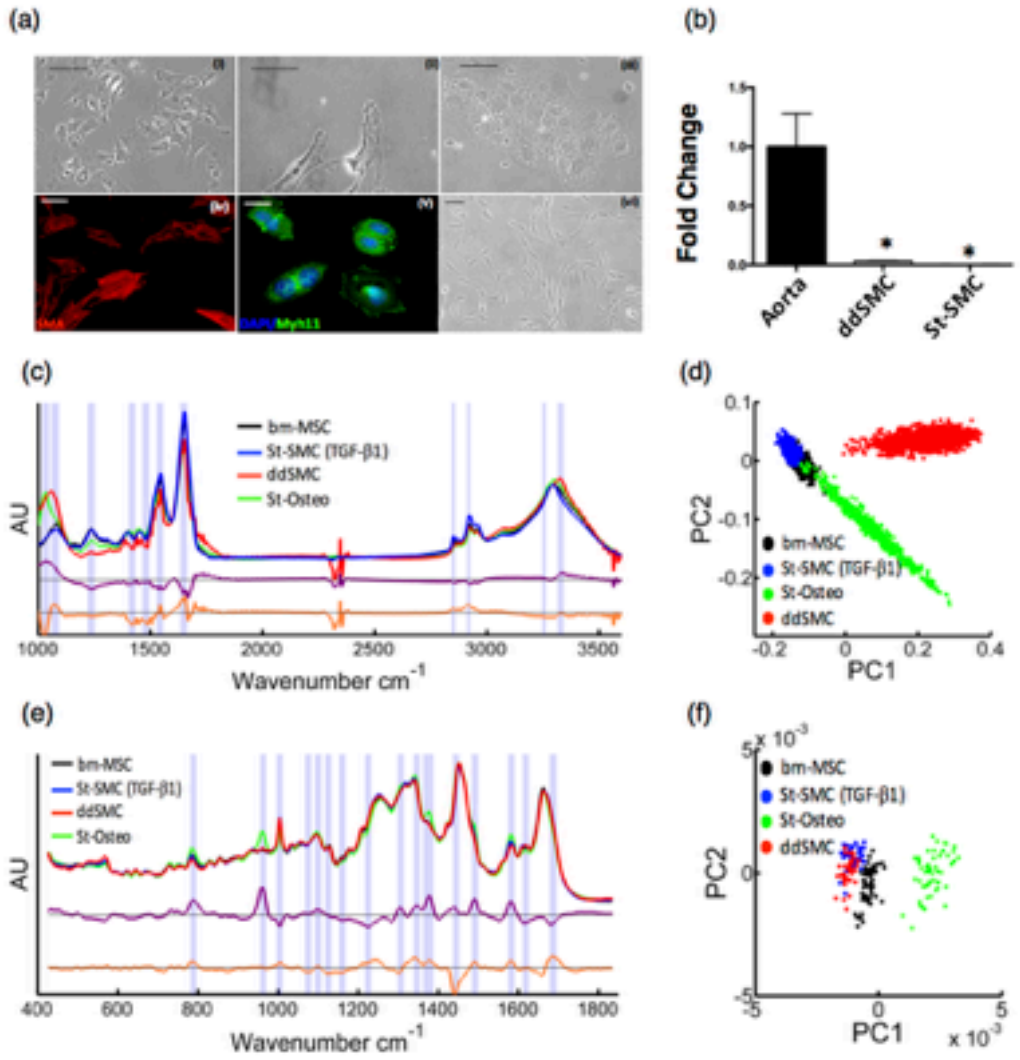

Figure 4.4. Vibrational spectroscopic analysis of bm-MSCs and their osteogenic and myogenic progeny and de-differentiated SMCs. (a)(i-iii) Representative phase contrast images of freshly isolated aortic SMCs and immunocytochemical analysis of (iv) SMA and (v) Myh11 expression in ddSMCs in culture (passage 4) and (vi) phase contrast of St-SMCs following TGF-β_1 induced myogenic differentiation. (b) Myh11 mRNA levels in fresh aortic tissue, ddSMCs and St-SMCs (TGF-β_1). Data analysis was performed using unpaired t-tests in the Prism software with *$p<0.05$ considered significant. (c) Mean FTIR spectra and (d) a 4-way scatter plot of the first two principal components after PCA of bm-MSCs , ddSMCs, St-SMCs (TGF-β_1) and St-Osteo. (e) Mean Raman spectra and (f) a 4-way scatter plot of the first two principal components after PCA for bm-MSCs, ddSMCs, St-SMCs (TGF-β_1) and St-Osteo. *$p<0.05$ considered significant.

	bm-MSC	St-Osteo	ddSMC	St-SMC
bm-MSC	94	0	3	3
St-Osteo	0	100	0	0
ddSMC	7	1	92	0
St-SMC	0	0	0	100

Table 4.3. Confusion matrix for PCA-LDA of FTIR spectral data showing the percentage classification for each cell type. Values on the diagonal represent those correctly identified, off-diagonal values represent those incorrectly identified.

When the Raman spectra for bm-MSC and their myogenic progeny (St-SMC-TGF-β_1) were compared [Figure 4.5a], there was a clear separation across both of the first two components [Figure 4.5b]. Analysis of the prominent spectral features in both PC1 and PC2 for these cells revealed significant spectral differences relating to nucleic acid (DNA/RNA) at 788 cm^{-1}, 1090 cm^{-1}, 1262 cm^{-1}, 1338 cm^{-1}, 1373 cm^{-1}, 1490 cm^{-1} and 1581 cm^{-1}; proteins at 1004 cm^{-1}, 1053 cm^{-1} and 1614-1619 cm^{-1}; and lipids at 1262 cm^{-1}, 1300 cm^{-1}, 1379 cm^{-1}, 1439-1454 cm^{-1} and 1650 cm^{-1}-1695 cm^{-1}, respectively [Figure 4.5a].

When the Raman spectra for ddSMC were compared to bm-MSC [Figure 4.5c], there was a clear separation across only the first component [Figure 4.5d], and the loading for only this component is shown [Figure 4.5c]. Many of the spectral differences recorded for bm-MSC versus St-SMCs (TGF-β_1) were also observed when ddSMC were compared bm-MSC [Figure 4.5c]. In addition to sharing these peaks, more peaks were observed in PC1 that relate to nucleic acid at 813 cm^{-1} and 1420 cm^{-1}; proteins at 1031 cm^{-1}; and lipids at 1220-1250 cm^{-1}, 1420 cm^{-1} and 1554 cm^{-1}.

In contrast, when the Raman spectra of ddSMC were compared to St-SMC (TGF-β_1), there were significant similarities between both spectra with sharp bands at the 1004 cm^{-1}, 1262 cm^{-1}, 1319 cm^{-1}, 1585cm^{-1} and 1662 cm^{-1} [Figure 4.5e]. Some differences were observed at 788 cm^{-1}, 1319 cm^{-1} and 1585 cm^{-1}, corresponding to nucleic acid content, indicative of differences between the DNA/RNA content of the St-SMCs (TGF-β_1) and the ddSMCs [Figure 4.5e]. Further differences were observed in the region of 1262 cm^{-1} attributable to the nucleic acid guanine and amide III and at 1619 cm^{-1} attributable to tyrosine or tryptophan [Figure 4.5e]. Raman spectra of ddSMCs were further compared to St-Osteo and revealed significant differences in the spectra of these two populations, consistent primarily with the onset of mineralization. Finally, PCA analysis of Raman spectra could not directly

separate the St-SMCs (TGF-β_1) and ddSMC groups with 100% accuracy [Figure 4.5f].

However, classification of both cell populations was achieved using a combination of PCA and LDA when applied to each of the four experimental groups. The ddSMC were classified correctly with 89.7% sensitivity and the St-SMC (TGF-β_1) correctly with a 92.7% sensitivity on a leave-one-out cross validation method (Table 4.4).

Using PCA/LDA, Raman spectroscopy discriminated undifferentiated bm-MSCs from both their myogenic (St-SMC-TGF-β_1) and osteogenic (St-Osteo) progeny with significant confidence even when these daughter cells originated from the same undifferentiated bm-MSC stem cell population [Table 4.4].

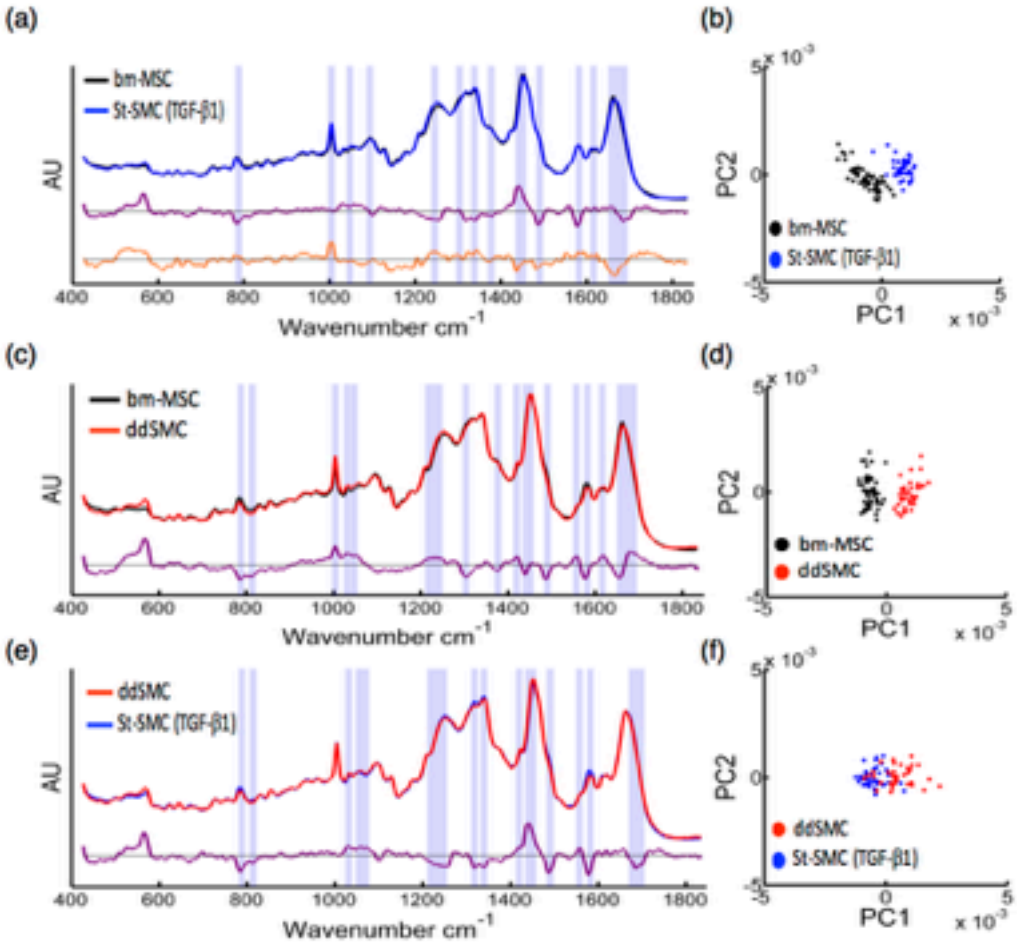

Figure 4.5. (a) Raman spectroscopic analysis of bm-MSCs, myogenic progeny and ddSMCs. Mean Raman spectra and the loadings corresponding to the first two principal components for bm-MSC and the St-SMCs-TGF-β_1 following myogenic differentiation. Significant peaks in the loadings of PC1 and PC2 are highlighted and (b) corresponding scatter plot for the first two principle components for bm-MSC and the St-SMCs-TGF-β_1. Mean Raman spectra and the loadings of the first principle component and corresponding scatter plots for (c, d) bm-MSC versus ddSMCs and (e, f) ddSMCs versus St-SMC. For (c) and (d), only the first loadings are shown, corresponding only to PC1, since separation is found in this component alone.

	bm-MSC	St-Osteo	ddSMC	St-SMC
bm-MSC	100	0	0	0
St-Osteo	0	100	0	0
ddSMC	0	0	89.7	10.3
St-SMC	0	0	7.3	92.7

Table 4.4. Confusion matrix for PCA-LDA of Raman spectral data showing the percentage classification for each cell type. Values on the diagonal represent those correctly identified, off-diagonal values represent those incorrectly identified.

4.3 Discussion & Conclusion

4.3.1. Discussion

Vibrational spectroscopy has shown great promise in functional analysis of single cells and in label-free detection of diseases (Cheng & Xie, 2016). Raman micro-spectroscopy is normally performed in a point to point mapping mode, and thus is considerably slower than FTIR in imaging mode. Nevertheless, its higher spatial and spectral resolution favours it for cellular and sub-cellular analysis, rather than large scale screening of cell population [Byrne et al., 2016; Bryne et al., 2010].

Multivariate statistical techniques such as Principal Components Analysis (PCA) and Discriminant Analysis (DA) have significantly contributed to the development of diagnostic algorithms based on the information recovered in Raman and FTIR spectral signatures. However, before vibrational spectroscopy can be fully implemented as a diagnostic platform, cross-validation with known immunohistochemical platforms for biomarker detection is required (Sule-Suso et al., 2014). In this context, the current study has established for the first time that vibrational spectroscopy can discriminate undifferentiated stem cells from their myogenic and osteogenic progeny in vitro following validation using conventional genetic, biochemical and histological analyses. The further aim was to compare stem cell derived myogenic progeny to de-differentiated SMCs in culture.

While several studies have confirmed the accuracy of Raman spectroscopy in various biological tissues such as the cervical lesions, gastric tissues, colon, thyroid, larynx, skin, bladder amongst others (Cheng & Xie, 2016), data on the interrogation of vascular tissue for early signs of disease have been limited (Motz et al., 2006). The accumulation of neointimal SMC-like cells within the vessel wall leading to the obstruction of blood flow represents a major hallmark of CVD (Bennett et al., 2016). Recent lineage tracing studies in mice and biomarker

identification in human vessels have provided compelling evidence that stem cell-derived myogenic progeny (either directly or via endothelial-mesenchymal-transition) in addition to de-differentiated SMCs may be responsible for neointimal formation (Yuan et al., 2017; Kramann et al., 2016; Chappell et al., 2016; Torsney et al., 2006). Hence the ability to discriminate de-differentiated SMC from undifferentiated stem cells and their myogenic and osteogenic progeny within the vessel wall and map their respective accumulation over time using label-free platforms represents an attractive diagnostic platform for vascular proliferative disease.

The potential of FTIR and Raman to screen cell populations and discriminate undifferentiated stem cells from their differentiated progeny was first established using an osteogenic progeny model. This was used as it is a highly validated method with the added benefit that atherosclerotic plaques are often calcified. In particular, analysis of the FTIR spectra clearly indicated the onset of mineralization via the emergence of the feature at 1037 cm^{-1} which is associated with carbonate groups in apatite (Awonusi et al., 2007). Interrogation of individual cell nuclei by Raman spectroscopy further distinguished a discriminant alteration in phosphate content *in situ* due to the pronounced peak at 960 cm^{-1} (McManus et al., 2012) that facilitated identification of these cells from each other by PCA.

TGF-β_1 and Jag-1 have been previously reported in neointimal lesions and to drive myogenic differentiation (Gridley 2010; Kurpinski et al., 2010; Li et al., 2006; Wang 2015; Morrow et al., 2008). In this study, both of these stimuli promoted myogenic differentiation of bm-MSCs in vitro by inducing specific epigenetic changes at the Myh11 promoter leading to Myh11 promoter transactivation, increased expression of transcript for SMC differentiation markers (Myh11 and CNN1) concomitant with a significant increase in the number of $Myh11^+$, SMA^+ and $CNN1^+$ positive cells. Interrogation of de-differentiated SMCs (ddSMCs), undifferentiated bm-MSC and their myogenic (St-SMCs) and osteogenic progeny (St-

Osteo) by FTIR revealed significant differences in their respective spectral signatures. Notably, the spectra associated with cellular phospholipid content of myogenic progeny decreased when compared to undifferentiated bm-MSC whereas there was a marked increase in levels of -CH_2 symmetric and -CH and -CH_3 asymmetric stretching associated with proteins and lipids. This was in contrast to osteogenic differentiation where there was a notable marked decrease in levels of –CH_2 symmetric and -CH and -CH_3 asymmetric stretching. Furthermore, the similarity in the pattern of FTIR spectral changes for both TGF-β_1 and Jag-1 myogenic progeny when compared to undifferentiated bm-MSC suggests that these differences are independent of the inductive stimulus and were specifically associated with a myogenic inductive stimulus and response. As stem cell-derived myogenic progeny and de-differentiated SMC were also separated by PCA analysis of their corresponding FTIR spectra, these data collectively suggest that FTIR is a reliable platform to screen and map undifferentiated stem cell populations from their myogenic progeny. Indeed, because of the limit of resolution, the longer wavelength of mid infrared radiation, coupled with the use of multidetector arrays in the Fourier Transform mode, render IR techniques very suitable for mapping larger cell populations or tissue sections (Byrne et al. 2016).

Raman spectroscopy of individual cell nuclei from undifferentiated bm-MSC, their myogenic progeny (St-SMC-TGF-β_1) and ddSMCs further defined discrete spectral shifts in these cell populations and quantitatively provided reliable estimates of in situ protein, nucleic acids and lipid content of bm-MSCs before and after myogenic and osteogenic differentiation. Nine distinct wavenumber bands within the fingerprint region 600-1800 cm^{-1} were recorded that correspond to broad biochemical groupings (Kerr et al., 2016; Movasaghi & Rehman., 2007). Analysis of the spectra revealed significant differences that facilitated further discrimination of these cell populations by PCA. Notably, when compared to ddSMC, undifferentiated bm-MSC had higher peaks at 785-788 cm^{-1} and 1585cm^{-1} which are attributable to nucleic acid content. Similar spectral differences were also observed at 785-788 cm^{-1} for St-

SMC. This is not surprising, as stem cells are known to have a higher nucleic acid content than differentiated cells (Chan et al., 2009; Notingher et al., 2004). The peak at 1262 cm^{-1} that corresponds to nucleic acid and lipid content has also been associated with collagen (Buschman et al., 2001) and was found in this study to be higher in the ddSMC when compared to bm-MSC. Other notable differences for St-SMC appear at 1319 cm^{-1} and 1341 cm-1 and are associated with lipids, nucleic acids and proteins in addition to a higher peak at 1585cm-1 which corresponds to nucleic acids.

Importantly, there was a clear separation observed across the first principle component for bm-MSCs and St-SMCs and for bm-MSC and ddSMCs by FTIR suggesting that these cell populations are clearly distinct. However, interrogation by Raman across the first principle components failed to separate the st-SMC and ddSMC populations with 100% accuracy. This is not unexpected since FTIR datasets are from whole cell spectra while Raman spectra were generated exclusively from the cell nucleus. The spectral differences within the cytoplasm may be more pronounced as these cells begin to fate towards a myogenic lineage but still retain significant differences within their cytoplasmic content. Nevertheless, the stem cell-derived SMCs mimic the ddSMCs when compared by Raman analysis of their respective nuclei. This is mirrored epigenetically as the bm-MSCs have remarkably similar histone modifications at they Myh11 promoter to the ddSMCs. Moreover, neither cells are as enriched for the H3K4me2 mark as the differentiated SMCs. Therefore, the results in this study suggest that stem cell-derived progeny and ddSMCs share similar epigenetic and photonic signatures, respectively, to imply that these two cell populations may be derived from the same source. This supports recent studies that demonstrate medial $Sox10^{+}$ resident vascular stem cells predominate in culture and expand at a faster rate than differentiated cells that were indelibly marked using Myh11 CreLoxP transgenic mice (Yuan et al., 2017). Taken together, these data strongly suggest that 'de-differentiated SMCs' may in fact be

stem cell-derived myogenic progeny (Tang et al., 2012; Yuan et al., 2017).

Although PCA analysis did not separate the St-SMCs (TGF-β_1) and ddSMC groups with 100% accuracy, classification of both cell lines was eventually achieved using a combination of PCA and LDA suggesting that there are also important differences, despite these similarities.

The main limitation of these studies is that they are confined to cell culture models. Vibrational spectroscopy for ex vivo analysis of various tissues affected by vascular diseases, including atherosclerotic plaque, vessel wall remodelling and endothelial dysfunction has been performed (Marcez et al., 2015; Buschman et al., 2001). The Raman spectral differences in remodelled vessels following IMT originated mainly from the protein features within the main bands at 1660 cm^{-1} (amide I), 1244 cm^{-1} (amide III), and at 1004 cm^{-1} (phenylalanine). In the spectrum of normal intimal SMCs, major bands due to amide I (1656 cm^{-1}), amide II (1556 cm^{-1}), and CH bending (1457 cm^{-1}) vibrations of the proteins collagen and elastin have also been reported (Motz et al., 2006; Marcez et al., 2015; Peres et al., 2011). In the spectrum of the intima of non-calcified atherosclerotic plaque, major bands due to both proteins and lipids are also observed. The lipid bands at 1734 cm^{-1}, 1468 cm^{-1}, 1171 cm^{-1} and 1058 cm^{-1} were assigned to the C = O (ester) stretch, CH_2 bend, C--O (ester) stretch and C--O stretch, respectively (Motz et al., 2006).

Our current study suggests that St-SMCs exhibit similar enhanced spectral intensities at peaks at 1004 cm^{-1} 1451 cm^{-1} and 1662 cm^{-1} when compared to bm-MSCs and ddSMCs respectively, suggesting that these peak intensities might represent a specific photonic signature for stem cell-derived myogenic progeny that could be exploited using diagnostic platforms. This is interesting as the peaks at 1451 cm^{-1} and 1662 cm^{-1} have been previously associated with collagen and elastin (Peres et al., 2011, Abubaker et al., 2007; and Buscman et al., 2001). This strongly correlates with results from Chapter 3 where the AF photon intensity of mMSCs- and rMVSCs-derived myogenic progeny at 530 ± 20 nm

wavelength significantly increased concomitant with an increase in collagen content. Moreover this photonic signature was attenuated when collagen was reduced following siRNA knockdown.

Furthermore, as vascular lesions are often calcified (Bennett et al., 2016), the ability to discriminate between St-Osteo and St-SMCs is also an advantage. Our data suggests that both FTIR and Raman can detect differences between myogenic and osteogenic progeny even when they are derived from the same undifferentiated stem cell.

4.3.2. Conclusion

Our studies reveal for the first time that FTIR detects specific alterations in the cellular profile of nucleic acid, protein and lipid content of bm-MSC when they progress towards a distinct myogenic phenotype in vitro. Moreover, Raman further distinguished a discriminant alteration in the nuclear spectra for nucleic acid, protein and lipid profiles of these cells. These data highlight the significant screening potential of FTIR and the more analytical potential of Raman at discriminating undifferentiated stem cells from de-differentiated SMCs and stem cell-derived osteogenic and myogenic progeny. Notably, the feasibility of using prototype devices including a laser-scanning fibre endoscope (SFE) to interrogate vascular structure in real-time in vivo and detect the early signs of disease has been validated (Motz et al., 2006; Savastano et al., 2017).

In conclusion, vibrational spectroscopy was successfully applied to the study of bm-MSCs before and after myogenic differentiation in vitro to identify discrete spectral characteristics that could facilitate localisation and detection of myogenic differentiation of resident vascular stem cell populations in vivo. The ability to assess the accumulation of stem cell-derived progeny using label free platforms *in situ* or the shedding of these progeny into the blood during disease progression may facilitate interrogation of these phenotypes by their discrete spectroscopic

signatures using liquid biopsies and microfluidic platforms, such as the lab-on-a-disc platform as described in Chapter 3.

Chapter 5

The Development of a Novel Drug and Delivery Platform Using Bare Metal Stents

5.1.1 Introduction

The findings presented so far in this study have provided further evidence that neointimal SMC-like cells may be derived from a stem cell source (Chapter 3, Chapter 4, Tang et al., 2012, Kramann et al., 2015; Wan et al., 2012). In humans, neointima formation typically follows stent deployment post balloon angioplasty (Dangas et al., 2002). Varying rates of revascularisation following stent deployment (up to 10-17.2% of cases), have been reported in the literature (Terstein et al. 2012). Paclitaxel (Taxol™) and rapamycin (Sirolimus™) are the most commonly used drugs to coat stents to prevent ISR (Ma et al., 2011). Paclitaxel and rapamycin are anti-mitotic drugs typically used to treat tumour growth. However, there is emerging evidence of 'cancer stem cells' present in tumours that drive chemo-resistance due to the presence of adenosine triphosphate binding cassette transporters which shield stem cells from these drugs (Moitra et al., 2011). The evidence presented in this thesis (Chapter 3 and 4) using photonic platforms to analyse cells spectroscopically strongly indicate that stem cell-derived myogenic progeny, de-differentiated ddSMCs in culture and medial/neointimal cells in vivo following vascular injury all possess similar photonic signatures and suggest that these cells populations may be derived from an undifferentiated stem source. Lineage tracing experiments using stem cell promoters to drive Cre-LoxP reporter genes and indelibly mark stem cells have provided further compelling evidence of the presence of stem cell-derived myogenic progeny within vascular lesions during disease progression, at least in murine models (Chapter 3, Chapter 4, Kramann et al., 2015; Wan et al., 2012; Cahill et al., unpublished). Therefore, one contributing factor to the unacceptably high rate of ISR following deployment of DES is most likely the inherent resistance of resident vascular stem cells to these drugs (Moitra et al., 2011). An alternative drug strategy that targets stem cells and the generation of myogenic progeny might prove a better solution to this problem.

Previous studies utilising DES coated with a GSK3β inhibitor demonstrated a marked reduction (~47%) in the incidence of rabbit carotid artery lesions following stenting when compared to the routinely used rapamycin (Sirolimus™) coated DES (Ma et al. 2010). The multi-functional serine-threonine kinase GSK3β is important for its role in arterial development, disease and vascular cell signalling. It has also been characterised to positively regulate Notch in drosophila, embryonic fibroblasts (Foltz et al. 2002), rat smooth muscle cells (Guha et al. 2011), mouse fibroblasts and human embryonic kidney cells (Espinosa et al. 2003; Jin et al. 2009). It has also been shown to regulate SMC markers in vascular SMCs (Zhou et al., 2016). As our group (Morrow et al., 2009, Redmond et al., 2014) and others (Sakata et al. 2004; Gridley et al. 2010; Caolo et al. 2011) have shown that exaggerated Notch signalling is associated with neointimal progression *in vivo* through its role in controlling myogenic differentiation and cell growth (Doi et al. 2006; Kurpinski et al. 2010, Mooney et al. 2015; High et al. 2007; Chang et al. 2011; Tang et al. 2012), Notch presents as a potentially important therapeutic target for combatting stem cell driven ISR.

Another important deficiency with current DES strategies is the natural depletion of targeted drug payloads off stents over time (Halkin et al., 2004). To ensure the continuous attenuation of smooth muscle-like cell accumulation within the stented regions of vessels, nanotechnology has been evaluated and shown great promise for drug-delivery platforms. Lipids and polymers from 10 nm-1000 nm in size have been employed to bind or encapsulate drugs or anti-sense duplexes to target stents in vivo. (Danenberg et al. 2002; Cohen-Sela et al. 2006; Ma et al. 2010; Polyak et al. 2016; Vosen et al. 2016). One of the most notable studies published to date reported a 98% inhibition of smooth muscle cell accumulation at the site of injury using paclitaxel loaded magnetic nanoparticles (MNP's) directed towards the stent using an external magnetic field (Chorny et al., 2010). Using magnetic nanotechnology, the stent was loaded with greater

specificity than non-magnetised nanoparticles and resulted in a 63% reduction of neointimal formation (Chorny et al. 2010). Hence, we chose this is the ideal technology to target GSK3β inhibitors routinely and specifically towards vascular stents.

5.1.2. Objectives:

The main aims of this chapter were:-

1. To identify a pharmacological inhibitor for targeting resident vascular stem cells.

2. To evaluate the effect of GSK3β inhibition on Notch signalling of multipotent resident vascular stem cells *in vitro*.

3. To evaluate the effect of GSK3β inhibition on myogenic differentiation of multipotent resident vascular stem cells *in vitro*.

4. To fabricate novel GSK3βi-loaded magnetic nanoparticles as the basis for a next generation therapeutic platform for drug eluting stents.

5. To determine the functionality of the GSK3βi-loaded magnetic nanoparticles in attenuating myogenic differentiation.

5.1.3. Strategy

To achieve these aims, resident MVSCs were isolated from Sprague-Dawley rats as described in Chapter 2.2.2 and were characterised by immunocytochemistry to confirm that they expressed stem cell markers (Sox10, Nestin) but were negative for a smooth muscle marker, Myh11. The rMVSCs were then treated with three different pharmacological inhibitors of GSK/GSK3β and analysed for their effect on cell growth by counting the number of DAPI nuclei and GSK3β inhibition by western blot using antibodies specific for inactive GSK3β phosphorylation at ser9. The rMVSCs were also treated with Jag-1 (2 μg/ml) for 7 days to induce myogenic differentiation through the Notch pathway and analysed by immunocytochemistry and q-RT-PCR for SMC differentiation marker expression (Myh11 and CNN1). The effect of the GSK3β inhibitors on this pathway were evaluated as free drugs first before the most potent inhibitor was subsequently incorporated into novel polymer coated MNPs by the oil in water emulsification method as described in Chapter 2.6.1 and the success of the formulation was determined by the functionality of the incorporated inhibitor on myogenic differentiation. Although the size of the nanoparticles were >100nm and therefore should be considered as sub micron particles, the magnetic particles in this study will be annotated 'MNPs' in line with similar reports in the literature (Chorney et al., 2010). The ability of the fluorescent labelled MNP's to target bare-metal stents was finally assessed *in vitro* under magnetic conditions.

Data analysis was carried out using paired t-tests pairing each treatment group with its respective control. The non-parametric Wilcoxon ranked t-test was used for sample data sets that did not follow Gaussian distribution.

5.2 Results

5.2.1 Characterisation of rMVSCs with Stem Cell Markers

Multipotent resident vascular stem cells (MVSCs) were isolated from the rat aorta and characterised to confirm a pure culture. The rMVSCs stained positively for the neural stem cell markers Nestin and Sox10 and negatively for the SMC marker, Myh11 [Figure 5.1]. A blue fluorescent stain, 4', 6-diamidino-2-phenylindole (DAPI) was used for nuclear staining. The rMVSCs in this study are $Nestin^{+}$ and $Sox10^{+}$ and $Myh11^{-}$.

5.2.2 Effect of GSKβ Inhibitors on Cell Growth

Three pharmacological inhibitors were chosen to assess the direct effect of GSK3β inhibition on Notch activation of myogenic differentiation of rMVSCs using the specific Notch ligand, Jag-1. The effect of varying doses of each inhibitor were also analysed for their effects on rMVSC growth [Figure 5.2-4]. The DMSO vehicle (<0.05%) had no significant effect on the rMVSC growth in all these studies. Varying doses of SB216763 (SB) 10μM-70μM were added to rMVSCs and cells were DAPI stained before nuclei were counted [Figure 5.2]. Prior studies established a linear relationship between the numbers of cells plated and the number of DAPI nuclei per high power frame (hpf). There was no significant effect of SB216763 on rMVSC cell number. The same experimental approach was applied using varying doses of Bio 1μM-10μM and doses as low as 7μM showed inhibitory effects on rMVSC cell growth [Figure 5.3]. Finally, the same cells were treated with varying doses of 10μM-50μM 1-Aza and no significant effect was observed before treatment with the highest 50μM dose [Figure 5.4]. Based on the images and statistical analysis, appropriate doses were identified as 5μM and 20μM for Bio and 1-Aza respectively. There was no significant effect of SB216763 on rMVSC growth with the chosen doses, however previous

studies using AlamarBlue for cell proliferation capacity and the Annexin-FITC/PI apoptosis assay for mMSCs and mSMCs identified 35μM as the IC_{50} for those cells. Therefore, 35μM was the chosen dose for treatments in these experiments. These inhibitor concentrations were used for all subsequent experiments. The average of 5 images for each sample were compared, plotted and analysed using the Prism software. One way anova was carried out unless otherwise stated using the Prism software and $p<0.05$ was considered significant.

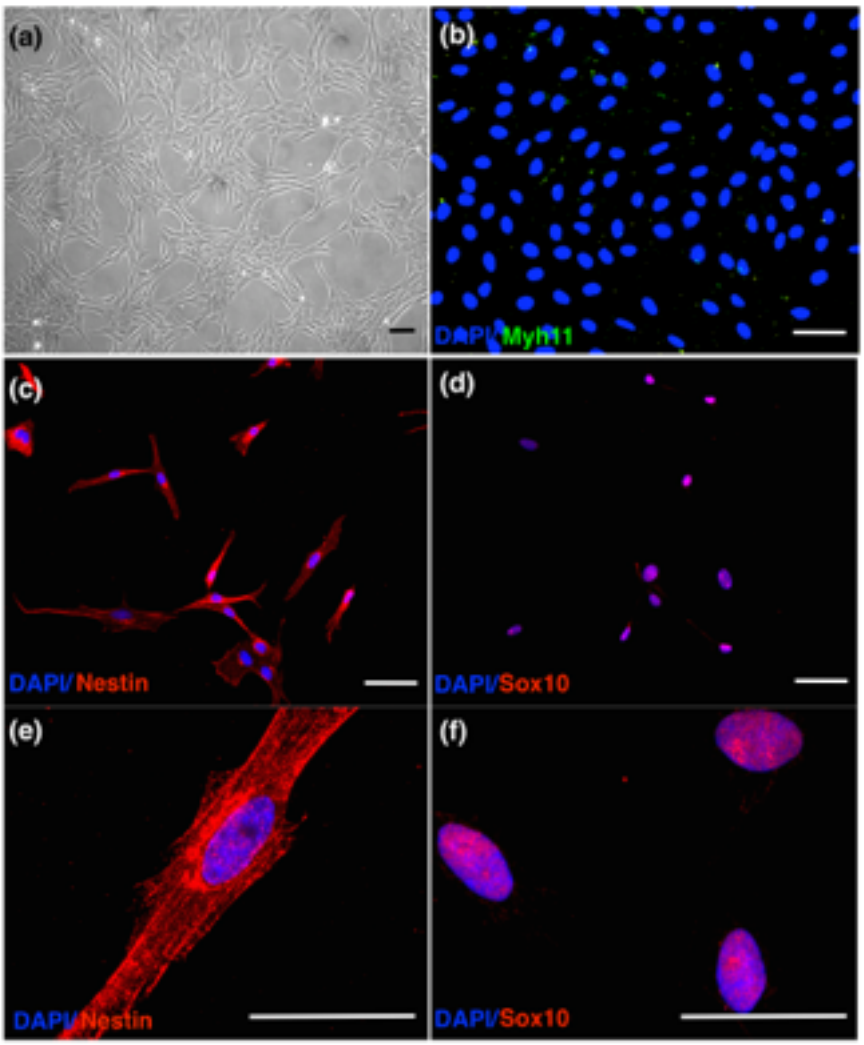

Figure 5.1 Characterisation of rMVSCs. (a) brightfield image of rMVSCs with elongated stem cell morphology and (b-f) representative immunocytochemical images of rMVSCs in culture stained with anti-nestin and anti-sox10 antibodies. Data are representative of at least 5 images per antibody from 3 independent experiments. Scale bars, 100µm.

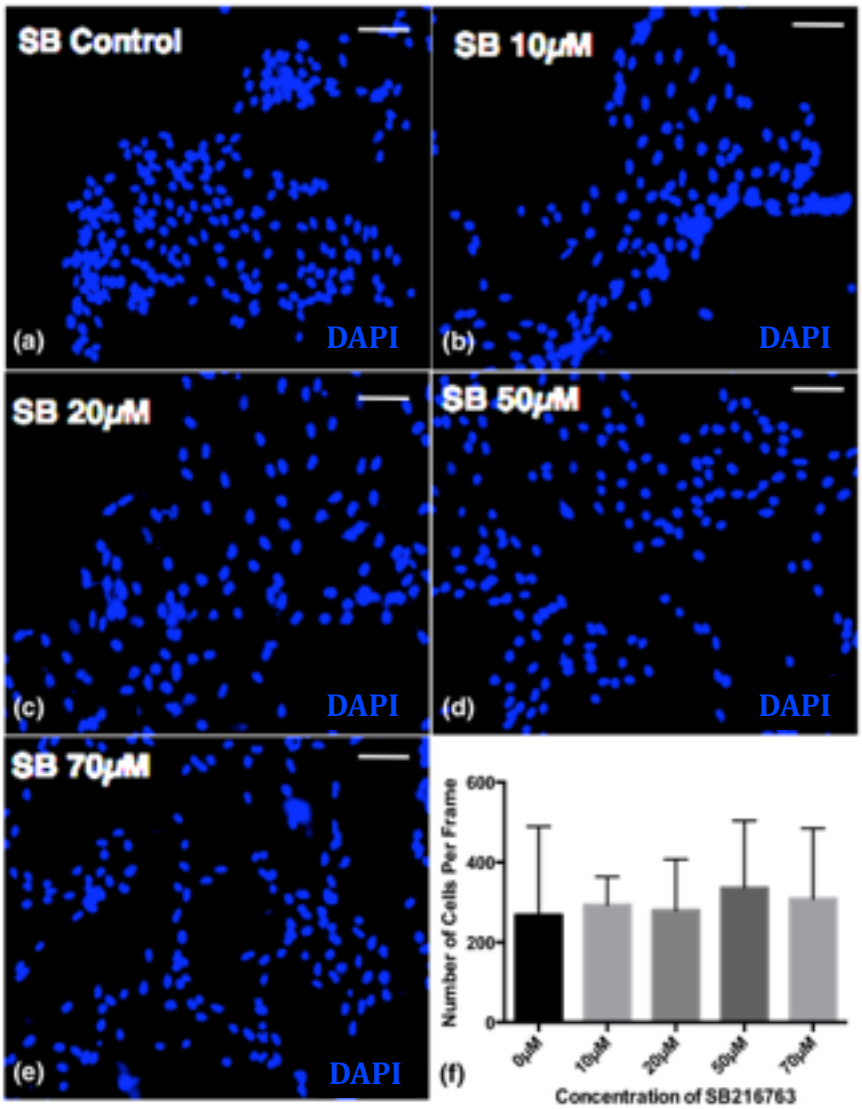

Figure 5.2 Dose response of rMVSCs to SB216763. rMVSCs treated with varying doses of SB216763 for 7 days and DAPI stained before cell counting (a-e). The average of 5 images for each sample were compared, plotted and analysed using the Prism software (f). Data are representative of at least 5 images per treatment in 3 independent experiments. One way anova was carried out using the Prism software and $p<0.05$ was considered significant. Scale bars, 100μm.

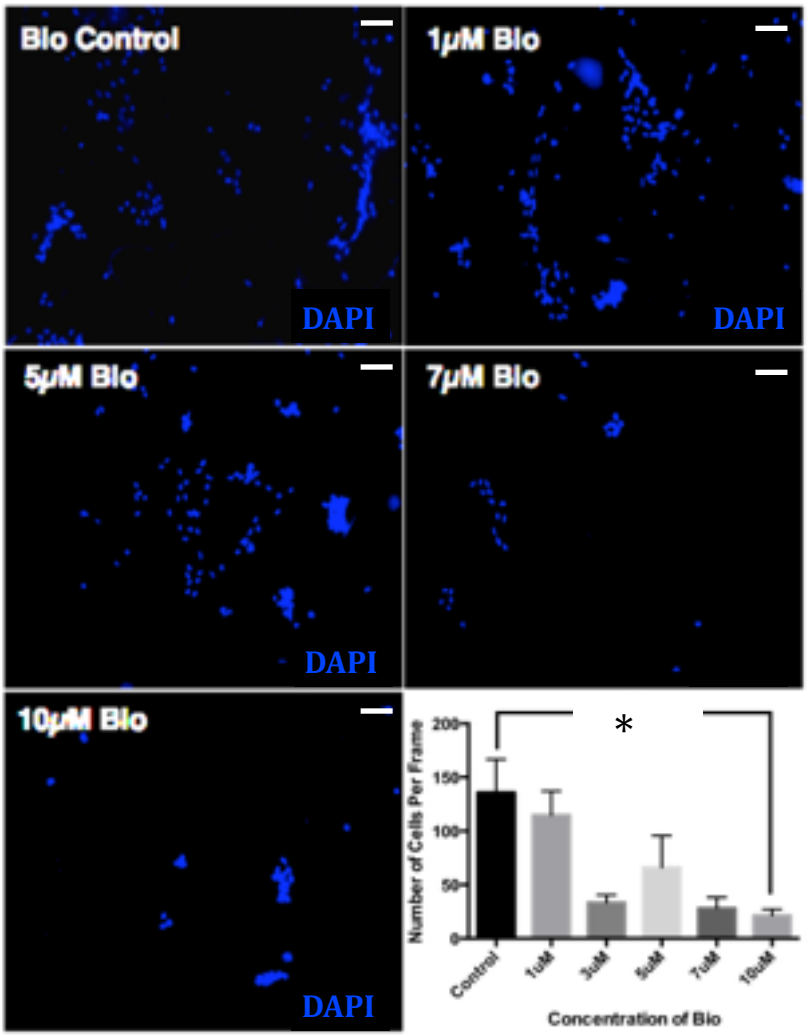

Figure 5.3 Dose response of rMVSCs to Bio. rMVSCs treated with varying doses of Bio for 7 days and DAPI stained before cell counting (a-e). The average of 5 images for each sample were compared, plotted and analysed using the Prism software (f). Data are representative of at least 5 images per treatment in 3 independent experiments. One way anova was carried out using the Prism software and *$p<0.0001$ was considered significant (*). Scale bars, 100μm.

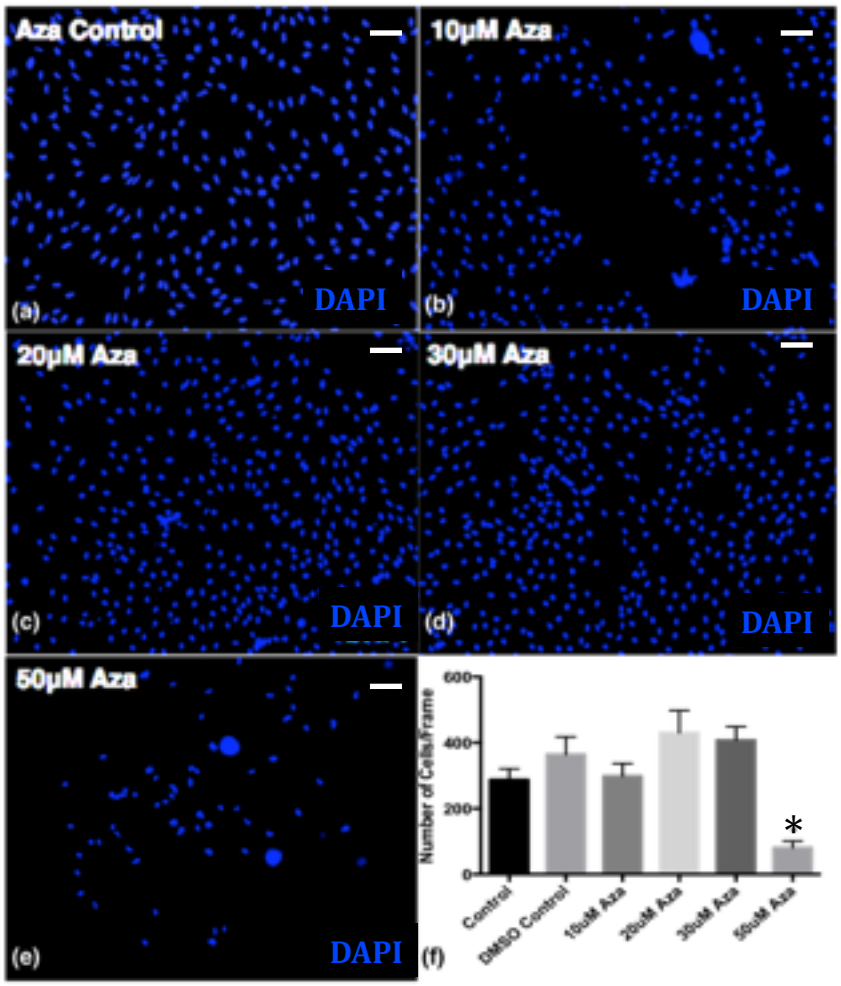

Figure 5.4 Dose response of rMVSCs to 1-Aza. rMVSCs treated with varying doses of 1-Aza for 7 days and DAPI stained before cell counting (a-e). The average of 5 images for each sample were compared, plotted and analysed using the Prism software (f). Data are representative of at least 5 images per treatment in 3 independent experiments. T-tests were carried out using the Prism software and $p<0.05$ was considered significant (*). Scale bars, 100μm.

5.2.3 Determine the best GSKβ Inhibitor for Inactivation of GSKβ

GSK3β is a serine/tyrosine kinase that requires prior phosphorylation to become inactive. If GSK3β is phosphorylated at the serine end, the constitutively active enzyme becomes inactive. If the inactivated GSK3β becomes phosphorylated at the tyrosine end it returns to its naturally active state. To determine the best inhibitor to inactivate GSK3β, protein lysates from rMVSCs treated with each of the inhibitors for 24 h were compared by western blot and stained for GSK3β(ser9). Beta actin staining corrected for equal loading of protein [Figure 5.5a,b]. The total amount of GSK3β was slightly higher in GSK3βi samples than the untreated control but not significantly so [Figure 5.5.c]. Finally, SB and 1-Aza were the only inhibitors to show an increase in GSK3β(ser9) expression indicating an inactivation of GSK3β in response to these inhibitors. Bio on the other hand had similar enzyme inhibition properties as the non-treated control [Figure 5.5.a. and 5.5.d]. SB and 1-Aza were therefore identified as the best pharmacological inhibitors to inactivate GSK3β enzyme activity. Western blot bands were quantified using the gel analysis software in Image J. Gel peaks for GSK3β and GSK3β(ser9) were normalised to the β-actin control. Wilcoxon ranked t-tests were performed for each inhibitor versus the control for GSK3β(ser9) and a p value of 0.25 was assigned to each sample which is not considered statistically significant.

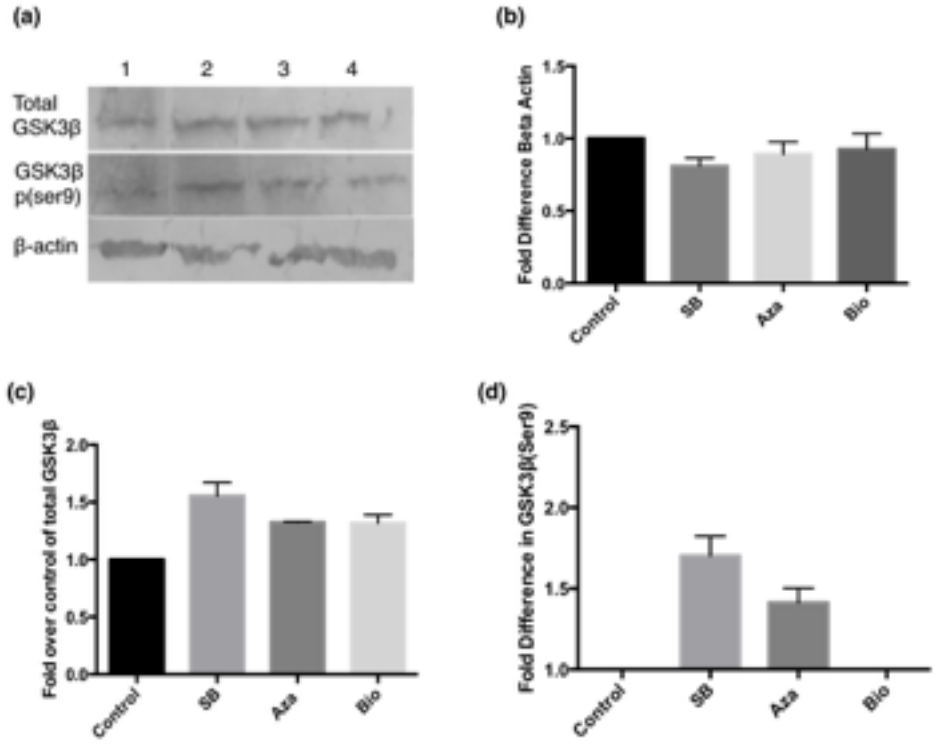

Figure 5.5. Effect of GSK3β on the inactivation of GSK3β (a) Western blot analysis of rMVSCs treated with 3 pharmacological inhibitors for 24 hours to evaluate GSK3β for total GSK3β and inactive GSK3βser9. (b) Densitometry analysis of β-Actin peaks expressed as fold over untreated control. (c) Densitometry of total GSKβ peaks normalised to β-actin expressed as fold over control. (d) Densitometry of GSK3β(ser9) peaks normalised to β-actin expressed as fold over control. Data are representative of 3 similar experiments. N number was too low to determine significance of the data.

5.2.4 Notch signalling drives myogenic differentiation of rMVSCs

rMVSCs treated with 2 μg/ml of Jag-1 for 7 days (previously confirmed as the best dose and time for myogenic differentiation of rMVSCs by a trial and error approach) were evaluated for myogenic differentiation markers Myh11 and CNN1 at the gene and protein level. The mRNA of rMVSCs treated with 2 μg/ml of Jag-1 for 7 days had a significant increase in expression for Myh11 and CNN1 [Figure 5.6.a and Figure 5.6.b]. This increase was concomitant with an increase in Notch target genes Hey1 and HeyL. Data is representative data of a minimum of 3 similar experiments. Significance testing was carried out using Wilcoxon ranked t-tests in the Prism software. $P<0.05$ was denoted *, $p<0.01$ was denoted **, $p<0.005$ was denoted *** and $p<0.0001$ was denoted ****, all of which are considered statistically significant.

In parallel studies, rMVSCs were treated with 2 μg/ml of Jag-1 for 7 days (CNN1) and 14 days (Myh11) and immunocytochemically stained for CNN1 and Myh11 [Figure 5.6.e]. The average of 5 images for each sample were compared, plotted and analysed using the Prism software. The number of CNN1 and Myh11 positive cells significantly increased following Jag-1 treatment according to Wilcoxon ranked t-tests in the Prism software [Figure 5.6.f]. Jag-1 promoted Notch mediated myogenic differentiation of rMVSCs.

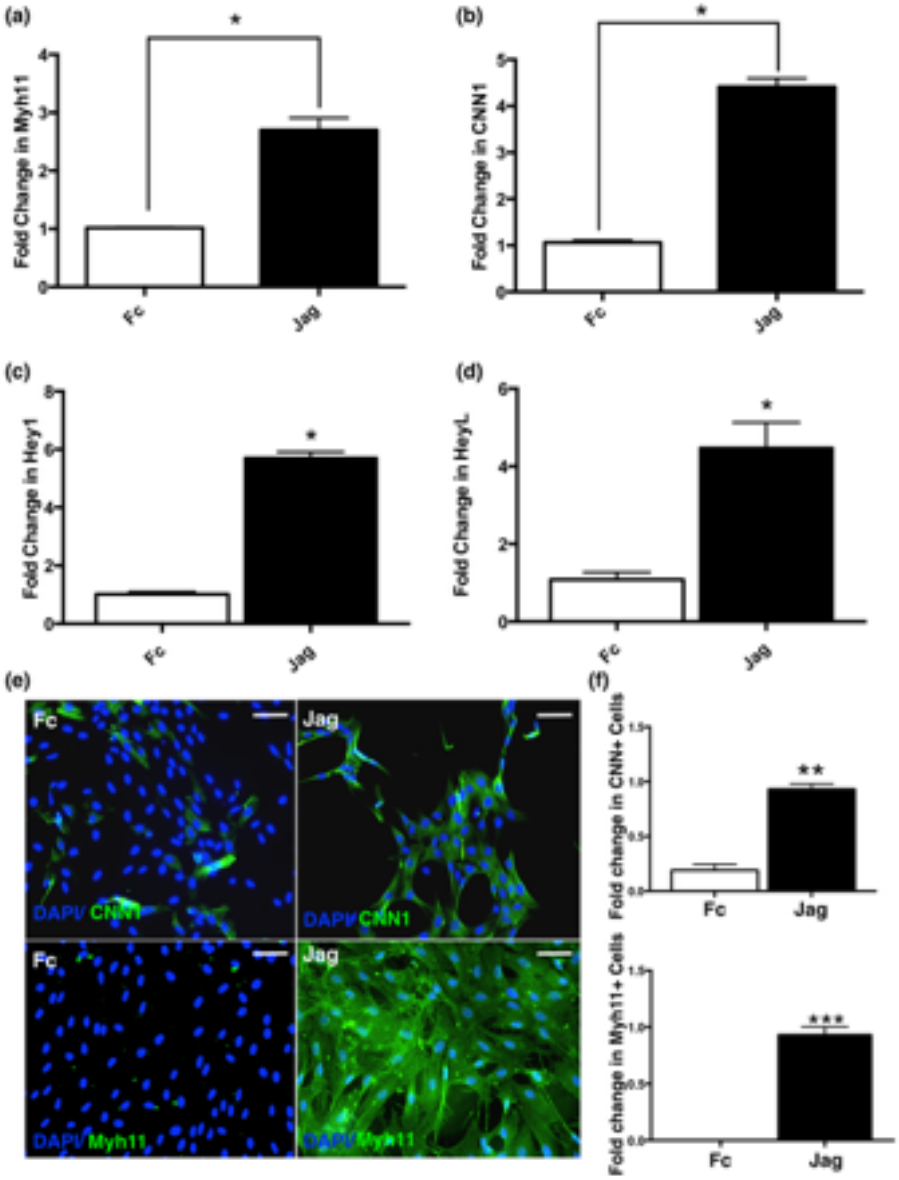

Figure 5.6 Jagged1 stimulates Notch mediated SMC differentiation of rMVSCs. a) Representative CNN1 gene expression in response to Jag-1 (2 µg/ml) treatment for 7 days; b) Representative Myh11 gene expression in response to Jag-1 (2 µg/ml) treatment for 7 days; c) Representative fold change in gene expression of Notch target gene Hey1 in response to Jag-1 (2 µg/ml) treatment for 48 hours; d) Representative fold change in Notch target gene HeyL expression in response to jagged1 for 48 hours; e) Representative immunocytochemistry images of rMVSCs +/- Jag-1 (2 µg/ml) with DAPI nuclei (blue) and CNN1 or Myh11 (green) staining after 7days and 14 days treatment respectively; (f) Fraction of CNN1 and Myh11 positive cells after treatment with Jag-1 for 7 and 14 days respectively as analysed by ImageJ. All data are the mean of triplicate readings from at least triplicate experiments. Wilcoxon ranked t-tests were carried out with *p<0.05; **p<0.005; ***p<0.001 all considered significant. Scale bars, 100µm.

5.2.5 Inhibition of GSK3β blocks Notch mediated myogenic differentiation of rMVSCs

The rMVSCs treated with 2 μg/ml Jag-1 and the IC_{50} of each GSK3β inhibitor were assessed for changes in gene expression for Myh11 and CNN1 [Figure 5.7a and 5.7b]. 1-Aza was the only inhibitor shown to inhibit the Jag-1 mediated Myh11 [Figure 7.a]. 1-Aza and Bio significantly reduced Jag-1 driven CNN1 expression, where SB216763 had little effect [Figure 5.7.b]. 1-Aza was therefore chosen as the best inhibitor to block Notch mediated myogenic differentiation of rMVSCs. The levels of Notch target genes Hey1 and HeyL were then evaluated following Jag-1 treatment and Jag-1 treatment in the presence of 1-Aza [Figure 5.7.c and Figure 5.7.d]. Jag-1 stimulated Hey1 and HeyL expression and 1-Aza attenuated this expression, indicating that 1-Aza blocks myogenic differentiation in rMVSCs through inhibition of Notch. Data is representative data of a minimum of 3 similar experiments and presented as compared to the Fc control.

Parallel immunocytochemistry studies were carried out and 1-Aza was shown to significantly reduce the number of Jag-1 stimulated Myh11 and CNN1 positive cells [Figure 5.7.e and Figure 5.7.f]. This data provides evidence that 1-Aza is a suitable inhibitor of Notch mediated myogenic differentiation of stem cells and could potentially be a novel therapeutic target for stem cell mediated in-stent restenosis. The average of 5 images for each sample were compared, plotted and analysed using the Prism software.

With the attenuation of myogenic differentiation by 1-Aza confirmed, auto-fluorescence readings at the 565±20 nm for IgG-Fc, Jag-1Fc and Jag-1Fc in the presence of 1-Aza were compared [Figure 5.8]. In contrast to the biochemical tests, 1-Aza did not attenuate the myogenic progeny photon counts value [Figure 5.8.a]. As it was suggested in chapter 3 that

Collagen 3 is the protein responsible for high auto-fluorescence in myogenic progeny and neointimal cells, Col3 mRNA expression in rMVSCs was evaluated in response to Jag-1 ± 1-Aza and it was found that 1-Aza did not have an effect on the Jag-1 induction of collagen 3 [Figure 5.8.b]. As the auto-fluorescence readings at the 565 nm± 20 nm wavelength are apparently reliant on collagen 3 and 1-Aza does not seem to block collagen 3, this unfortunately is not a reliable method to analyse 1-Aza inhibition of rMVSC myogenic differentiation.

Significance testing for all experiments in this section was carried out using Wilcoxon ranked t-tests compared to the Fc control, $p<0.05$ denoted * was considered statistically significant.

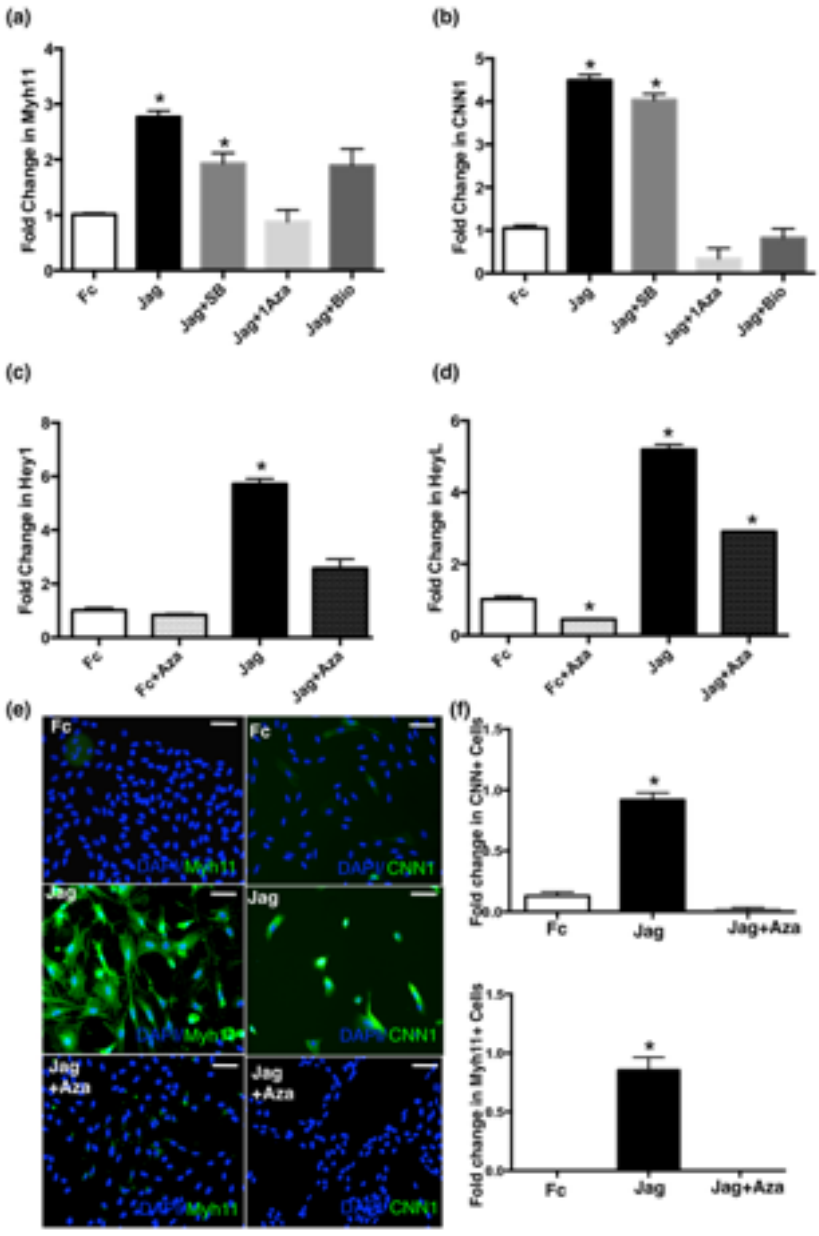

Figure 5.7. Effect of GSK3β inhibitors on Notch mediated myogenic differentiation. (a) Representative fold change in Myh11 gene expression in response to rMVSCs treated with IgG-Fc, Jag-1 Fc, Jag-1 Fc + SB216763, 1-Aza or Bio for 7 days; (b) Representative fold change in CNN1 gene expression in response to rMVSCs treated with IGG-Fc, Jag-1 Fc, Jag-1 Fc + SB216763, 1-Aza or Bio for 7 days; (c) Fold change in Notch target gene Hey1 gene expression in response to IgG-Fc, Jag-1 Fc, Jag-1 Fc with 1-Aza for 48 hours; (d) Fold change in Notch target gene HeyL gene expression in response to IgG-Fc, Jag-1 Fc, Jag-1 Fc with 1-Aza for 48 hours; (e) Representative images of rMVSCs treated with IGG-Fc, Jag-1 Fc, Jag-1 Fc with 1-Aza stained with DAPI (blue) and CNN1 or Myh11 (green) for 7 and 14 days respectively. Scale bars, 100μm. All data are the mean of triplicate readings from at least triplicate experiments. *p<0.05 considered significant.

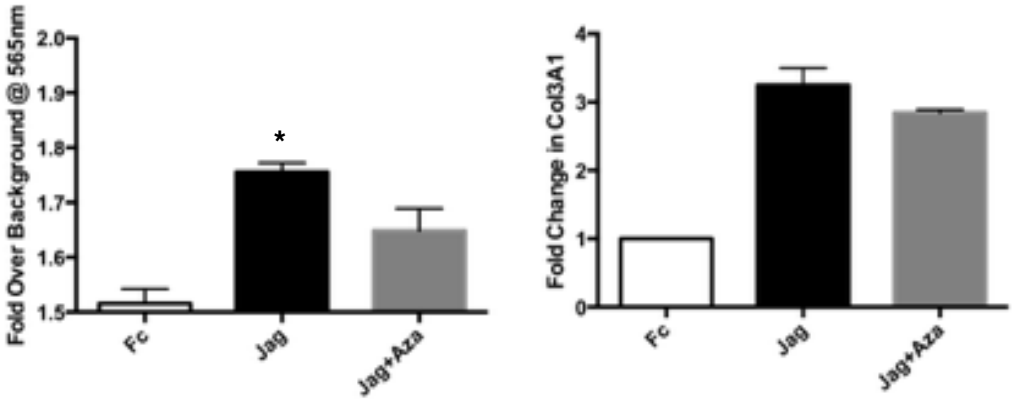

Figure 5.8. Photon count analysis of 1-Aza inhibition of myogenic differentiation. (a) Representative fold over background photon counts for rMVSCs treated with IgG-Fc; Jag-1-Fc and Jag-1-Fc + 1-Aza. (b) Representative collagen 3 mRNA expression for rMVSCs in response to Jag-1 and Jag-1 + 1-Aza. Data analysis was performed for using Wilcoxon ranked t-tests comparing treatment groups with control groups. Data are the mean ± SEM of 55 cells per group from duplicate experiments, *$p<0.05$.

5.2.6 Polymer coated MNPs are round and relatively uniform in size.

FeSEM images at 12X and 20X demonstrate the round shape of the polymer-coated magnetic nanoparticles and the differences in sizes depend on the number of MNPs incorporated into the PLGA shell [Figure 5.9a, b]. At 300X, the polymer can be seen to be blurring and this can be a result from the shrinking of the polymer when exposed to the electron beam [Figure 5.9c].

High power TEM images show the grouping of the small 10 nm MNPs together to form a larger nanoparticle that would be encapsulated by the polymer for functionalisation [Figure 5.9.d].

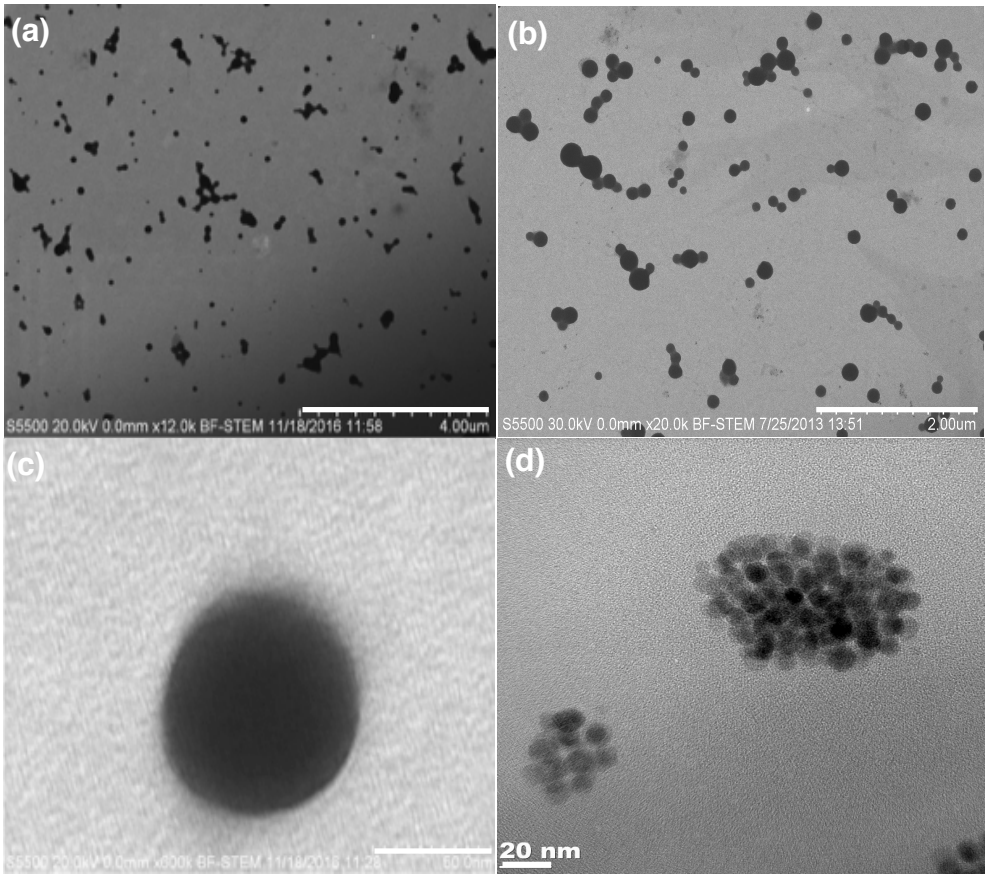

Figure 5.9 FeSEM and TEM images of polymer coated MNPs. (a) FeSEM image of PLGA/PVA coated Fe_3O_4-NPs s at 12X. (b) FeSEM image of PLGA/PVA coated Fe_3O_4-NPs at 20X. (c) FeSEM image of PLGA/PVA coated Fe_3O_4-NPs at 300X. (d) TEM image of PLGA/PVA coated Fe_3O_4-NPs at 100KX.

5.2.7 Characterisation of 1-Aza-loaded MNPs

The size of 1-Aza loaded MNPs is similar to blank-MNPs and measure at 232±2.97 nm and 214±4.3 nm respectively [Figure 5.10 a (blank), b (1-Aza-MNP) and c]. The zeta potential of nanoparticles refers to the electrostatic potential of the nanoparticle or as it is commonly known, the stability of the nanoparticle. Nanoparticles with a zeta potential of less than -30mV are thought to have better dispersion stability (Zhang et al., 2008). The zeta potential of the representative 1-Aza-PLGA-MNPs [Figure 5.10.d] was -24.1±6.9mV. This is slightly higher than the optimum zeta potential however the negative charge should still electrostatically repulse nanoparticles to prevent aggregation (Zhang et al., 2008).

The incorporation efficiency of 1-Aza into the PLGA-MNPs was determined by evaluating the concentration of 1-Aza in supernatants by HPLC directly following 1Aza-MNP generation. The concentration of 1-Aza in the supernatants was subtracted from the concentration of 1-Aza introduced to the nanoparticles and a percentage of 1-Aza incorporated was determined [Figure 5.10e]. On average, 96±2.4% of 1-Aza was incorporated into PLGA-MNPs. The release of 1-Aza from the nanoparticle in the presence and absence of an external magnetic field was again determined by the concentration of 1-Aza in the supernatants by HPLC. Every 24 hours following magnetisation, the 1-Aza-MNPs were centrifuged at 170000 x g for 1 hour and the supernatants were collected and analysed [Figure 5.10.f]. When exposed to a uniform magnetic field, 1-Aza was released at a faster and more stable rate than in the non-magnetic conditions. The percentage release of 1-Aza compared to the percentage of 1-Aza incorporated was 3.4±1.56% in the presence of an external magnetic field and 1±0.53% in the absence of an external magnetic field. 1-Aza was released up to 72 hours and typically no more was released at this time point.

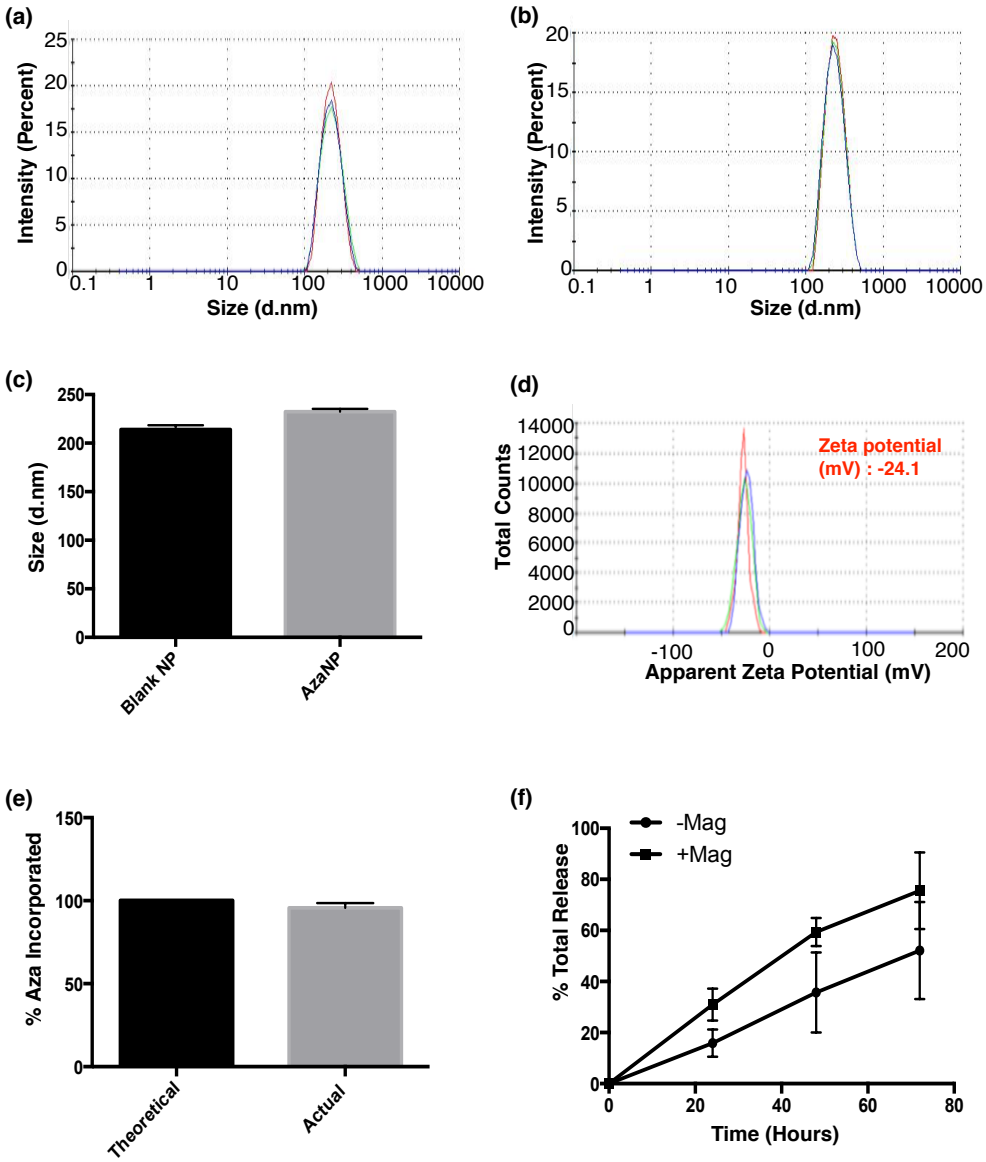

Figure 5.10. Characterisation of 1-Aza loaded polymer coated Fe3O4-NPs. (a) DLS size measurements of blank-NPs; (b) DLS size measurements of 1-Aza-NPs; (c) direct comparison of sizing of blank- or 1-Aza-NPs; (d) zeta potential of blank-NPs; (e) Percentage of incorporation of 1-Aza into nanoparticle as analysed by HPLC; (f) The percent of total release of 1-Aza from nanoparticles with respect to time in the presence and absence of an external magnetic field as analysed by HPLC. All data are the mean ± SEM from a minimum of 3 independent experiments.

5.2.8 Functionality of 1-Aza-MNPs

To determine whether 1-Aza loaded into PLGA-MNPs retained their anti-myogenic effect, rMVSCs treated with Fc and Jag in the presence of blank PLGA-MNPs and 1-Aza loaded PLGA-MNPs were compared for their CNN1 mRNA expression [Figure 5.11.a]. Jag-1 Fc stimulated CNN1 mRNA expression compared to the IgG-Fc control in the presence of blank MNPs. This effect was attenuated in the presence of 1-Aza-PLGA-MNPs in the presence of a uniform magnetic field indicating 1-Aza retains its function even when incorporated into a PLGA-MNP. The attenuation of CNN1 mRNA expression in response to Jag-1 Fc is dependent on the dose of 1-Aza-PLGA-MNPs with the more fold dilutions of the 1-Aza-PLGA-MNPs leading to a reduction in attenuation response [Figure 5.11.b]. Data is representative of at least 3 experiments and statistical analysis was carried out in the form of paired t-tests in Prism with *$p<0.05$ significant.

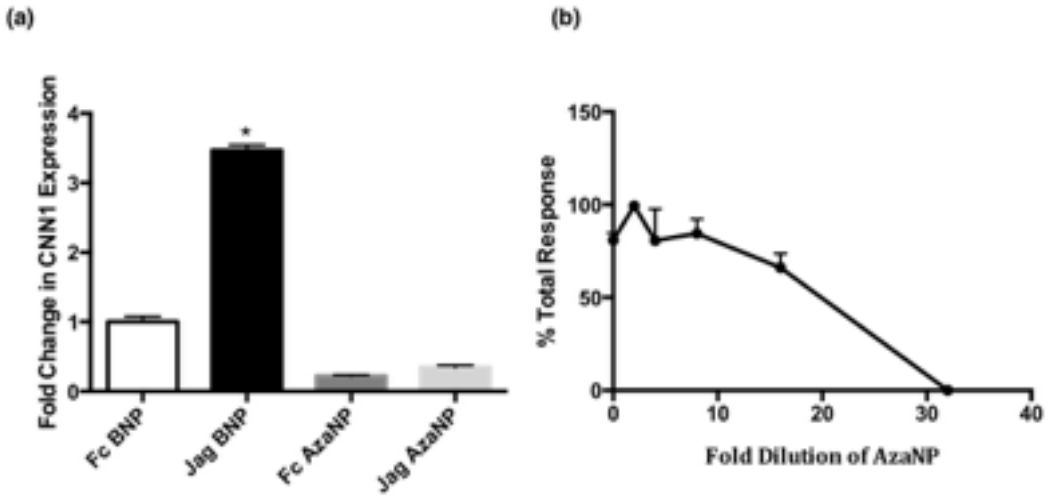

Figure 5.11. Functionality of 1-Aza following incorporation into PLGA-MNPs. (a) CNN1 mRNA expression of rMVSCs when treated with Fc and Jag in the presence of blank nanoparticles and 1-Aza loaded nanoparticles for 7 days. Significance was determined by t-tests compared to Fc BNP control. Data is the mean ± SEM of triplicate readings from 3 independent experiments (b) The percentage response of rMVSCs treated with varying dilutions of 1-Aza-NPs in terms of CNN1 mRNA expression. Statistical analysis was carried out in the form of Wilcoxon ranked t-tests with *$p<0.05$ considered significant.

5.2.9 Magnetic nanoparticles require an external magnetic field to be targeted to stents

To determine whether an external magnetic field is required to target MNPs to stents, fluorescent-tagged PLGA coated MNPs were targeted to bare metal stents in the presence and absence of a magnetic field in vitro [Figure 5.12.a]. Trace amounts of fluorescent-tagged MNPs were found in the absence of a magnetic field compared to high levels in the presence of a magnetic field. AlexaFlour tagged IgG (488) were then incorporated into PLGA-MNPs and targeted to the stent in the presence of a magnetic field to confirm the binding of various agent-loaded PLGA-MNPs. The IgG-loaded PLGA-MNPs were present on the stent following magnetic field application [Figure 5.12.b].

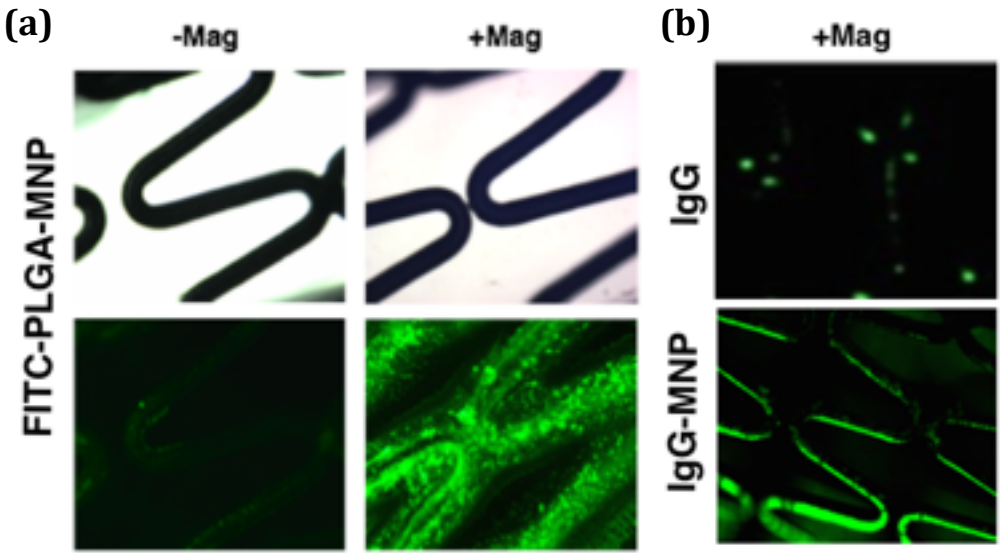

Figure 5.12. Targeting of nanoparticles to stents. (a) Targeting and binding of fluorescent-tagged PLGA coated nanoparticles to bare metal stents in the presence and absence of an external magnetic field; (b) Targeting and binding of alexafluor-488 IgG nanoparticles to bare metal stents in the presence of an external magnetic field.

5.3 Discussion & Conclusion

5.3.1. Discussion

Vascular disease presents as an obstruction (stenosis) of key blood vessels (coronary, carotid) due to the presence of a vascular lesion. Treatment options include percutaneous transluminal coronary angioplasty (PTCA) and the insertion of a stent – a metal mesh tube – into the obstructed vessel to keep the artery open. However, the vessel can become re-occluded due to neointimal formation that forms as a result of accumulation of vSMCs within the stented area. The introduction of the 1st generation DES has resulted in a paradigm shift for the treatment of ISR with significant improvement in therapeutic outcomes.

However, while polymer-coated DES have significantly reduced the incident of in-stent restenosis, current DESs treatment regimes lack the fundamental capacity for (i) adjustment of the drug dose and release kinetics and the (ii) ability to replenish the stent with a new drug on depletion. This limitation can be overcome by a strategy combining magnetic targeting via a uniform field-induced magnetisation effect and a biocompatible magnetic nanoparticle (MNP) formulation designed for efficient entrapment and delivery of specific drugs.

There is now considerable evidence for the presence of stem cell-derived progeny within neointimal lesions and they are likely to be a contributing factor to the accumulation of SMC-like cells leading to in-restenosis (ISR) (Torsney et al., 2011; Hu et al., 2004; Klein 2016; Sata et al., 2002; Hoglund et al., 2010; Tang et al., 2013; Majesky et al., 2010; Kurpinski et al., 2010). There are two main reasons for the recurring failure of DES. The first is the lack of specificity of the anti-mitotic drugs taxol (paclitaxel) and sirolimus to target the correct source of the SMC-like cells (Moitra et

al., 2011). Indeed, if anything, these dugs may exacerbate the problem since sirolimus induces progenitor cell migration and myogenic differentiation via CXCR4 and epidermal growth factor receptor/ extracellular signal–regulated kinase/β-catenin signal pathways, thus implicating a novel mechanism of restenosis formation after sirolimus-eluting stent treatment (Wong et al., 2013). More importantly, the levels of these drugs are depleted over time with significant amounts released as early as 14 days after stent placement (Halkin et al., 2004).

The final aim of this work was to pharmacologically inhibit resident vascular stem cell myogenic differentiation in vitro and incorporate this targeted therapy into novel magnetic nanoparticles as a delivery platform for therapeutic delivery to bare-metal vascular stents in vivo.

Using a series of GSK3β inhibitors and targeted siRNA duplexes, the putative role of inhibiting GSK3β activity and myogenic differentiation of stem cells was assessed before Fe_3O_4 PLGA-PVA nanoparticles were fabricated, functionalised with GSK3β inhibitors and assessed for activity and binding to a bare-metal stent under a magnetic field in vitro.

Resident MVSCs are present in the medial layer of adult arteries and differentiate into SMC-like cells in vitro and in murine injury models in vivo (Tang et al. 2013, Yuan et al., 2017). Following isolation and cell culture MVSCs from rat aorta were characterised as $Myh11^-$, $Nestin^+$ and $Sox10^+$ as previously reported (Tang et al., 2013, Kennedy et al., 2014a, Kennedy et al., 2014b; Huang et al., 2015).

Two ATP-competitive inhibitors of GSK3α/β, SB216763 (SB) and Bio, and one cell permeable selective inhibitor of GSK3β, 1-Aza (1-Aza), were compared for their effect on MVSC cell growth after 7 days. The effects of varying doses of each inhibitor was analysed by counting cell nuclei and the IC_{50} for each was chosen for future experiments. Bio was the only inhibitor that seemed to have a significant effect on rMVSC cell growth at

low doses. The inhibitors were then compared for their inactivation of GSK3β as determined by the phosphorylation of the serine 9 residue of GSK3β. SB216763 and 1-Aza were found to have the best inactivation response of GSK3β whereas Bio had the least response.

Notch signalling has been previously associated with neointimal formation (Sakata et al. 2004; Gridley, 2010; Caolo et al. 2011, Morrow et al., 2009; Redmond et al., 2015). It has also been shown to promote myogenic differentiation of various stem cells (Doi et al. 2006; Kurpinski et al. 2010; Mooney et al. 2015; Chang et al. 2011; Tang et al., 2012). For these reasons, the effect of each inhibitor on Notch mediated myogenic differentiation was compared. Jag-1 significantly increased the levels of CNN1 and Myh11 mRNA levels and immunocytochemical protein levels compared to the IgG-Fc control in rMVSCs. The increase in myogenic markers was concomitant with an increase in Notch target gene expression of Hey1 and HeyL. When rMVSCs were treated with Jag-1 in the absence or presence of each inhibitor, SB216763 and 1-Aza significantly attenuated the Myh11 mRNA response whereas Bio did not have this effect. On the other hand, 1-Aza and Bio had a significant effect on the CNN1 mRNA response, where SB216763 did not. As 1-Aza did not have a significant effect on rMVSC cell growth but successfully inactivated GSK3β (as evidenced by an increase in the inactive GSK3β-ser9 levels) and subsequently attenuated the Jag-1 induction of myogenic markers Myh11 and CNN1, this inhibitor was chosen as the drug of choice for future experiments by incorporating it into PLGA-coated MNPs. Reduced GSK3β levels has been associated with stem cell self renewal and pluripotency in the literature (Wray et al., 2011; Sato et al., 2011; Kirby et al., 2012) so the results are not entirely surprising. Inhibition of GSK3β has also been shown to attenuate cardiomyocyte differentiation of mesenchymal stem cells (Cho et al., 2009) and adipocyte differentiation of adipose derived stem cells (Zaragosi et al., 2008). The results presented herein, and with supporting evidence in the literature, propose

GSK3β inhibitors such as 1-Aza to be an ideal pharmacological inhibitor of stem cell differentiation.

To determine whether the inhibition of myogenic differentiation by 1-Aza was associated with the Notch signalling pathway, rMVSCs were treated with Jag-1 in the absence or presence of 1-Aza before Notch target gene Hey1 and HeyL mRNA expression and SMC differentiation marker expression was assessed. 1-Aza significantly reduced Jag-1 stimulation of Notch target gene expression concomitant with reduction in SMC markers suggesting that GSK3β may modulate Notch control of myogenic differentiation in vitro. Other well known associated pathways to GSK3β are of course the β-catenin/Wnt pathway and the sonic hedgehog (Shh) pathway (Komiya et al., 2008; Guha et al., 2011). As mentioned in chapter 1, GSK3β is responsible for tightly regulating the Wnt/β-catenin pathway during embryogenesis (Komiya et al., 2008). There is also evidence of cross-talk between Wnt and Notch signalling (Espinosa et al., 2003; Rodilla et al., 2008) which provides a possible mechanism of control of GSK3β over Notch signalling, however this was not addressed in this study. Similarly, previous studies have demonstrated that the hedgehog signalling pathway positively regulates Notch signalling in vSMCs (Morrow et al., 2009; Guha et al., 2011) and embryonic stem cells (Kim et al., 2013). Conversely, pharmacological inhibition of GSK3β and targeted siRNA knockdown of GSK3β was shown to attenuate Gli1 mRNA expression in C3H T10 1/2 cells and mMSCs (see supplemental Figure 1). This suggests that GSK3β may also regulate Notch signalling through sonic hedgehog signalling. This is supported by a previous report in our lab that demonstrated targeted siRNA knockdown of GSK3β inhibited Patched1 (Ptch1) expression and sonic hedgehog signalling in rat vascular smooth muscle cells (Guha et al., 2011). Moreover, it is supported by previous reports that show decreased sonic hedgehog signalling in GSK3β null embryos (Nelson et al., 2011).

On the other hand, inhibition of GSK3β had little effect on the jag stimulation of collagen 3. As outlined in Chapter 3, elastin and collagen1 and collagen3 mRNA increases across three stem cell platforms with two different myogenic stimuli. This is concomitant with an increase in AF at the 565 nm± 20 nm wavelength which can be blocked with a collagen 3 siRNA. Jag-1 has been shown to increase collagen3 mRNA and AF. In this chapter, the addition of 1-Aza has attenuated Jag-1 stimulated myogenic differentiation. However, the addition of 1-Aza to Jag-1 treated cells had no effect on the collagen 3 transcript or AF profile at the 565 nm ± 20 nm. Therefore, notch driven collagen 3 up-regulation must occur in a pathway independent of GSK3β. The role of GSK3β in collagen 3 signalling is not currently understood in the literature.

The use of nanoparticles as a drug delivery system is becoming increasingly popular. In particular, magnetic nanoparticles have shown great promise for drug delivery due to their small controllable size and easily functionalised structure. There are also further advantages such as prolongation of the half-life of drugs in circulation and specific targeting to the site of interest for more efficient drug use with limiting side effects (Singh et al., 2011). There has been much success in targeting drugs to tumours in cancer models using nanoparticles and magnetic nanoparticles (Muhammod et al., 2017). However, there is still concern about the toxic effect of magnetic nanoparticles such as the build up of magnetic nanoparticles and bi-products in organs, the risk of an inflammatory response to the particles and the possibility of aggregation that might result in stenosis within the circulatory system. Therefore, novel drug-loaded magnetic nanoparticles require rigorous characterisation before considering in vivo studies (Markides et al., 2012).

In this chapter, 1-Aza loaded PLGA-MNPs were successfully fabricated and characterised. They were round, reproducible and relatively uniform in size and stable. The incorporation efficiency of 1-Aza into the PLGA-

MNP was very high and the rate of release of the drug from the nanoparticle steady in the presence of a uniform magnetic field.

The most similar study published to date was carried out by Chorny et al., who fabricated paclitaxel (PTX) loaded PLGA-MNPs by a similar method and successfully targeted the MNPs to rat carotid arteries to attenuate in-stent restenosis (ISR) (See Table 6.1; Chorny et al., 2010). The PTX-PLGA-MNPs were similar in size, if slightly larger, which suggests the 1-Aza-PLGA-MNPs to be small enough for rat carotid models and thus human arterial models. The zeta potential of the PTX-PLGA-MNPs was lower than the MNPs in this study which would mean they are more likely to aggregate. Nevertheless, this was not an issue when the PTX-PLGA-MNPs were introduced in vivo and therefore aggregation would not be expected with the MNPs produced in this study. The incorporation efficiency of PTX into the PLGA-MNPs was significantly lower than that of the 1-Aza-PLGA-MNPs, this could be due to the method of fabrication of the nanoparticle. Chorny and colleagues fabricated the nanoparticles based on a single emulsion evaporation method whereas the nanoparticles described here were formulated using a double emulsion method. Paclitaxel is also a hydrophobic drug which may have been dissolved in the solvent during the solvent evaporation phase (Chorny et al., 2010). The release of paclitaxel from the PTX-PLGA-MNPs was significantly higher than from the 1-Aza-PLGA-MNPs. Release kinetics for the PTX-PLGA-MNPs were performed in octanol and 1-heptane (1:1) and while the solvent may be the ideal sink conditions to release PTX from PLGA-MNPs, it does not mimic the pH and aqueous environment of the body, therefore a direct comparison with the drug release from the 1-Aza-PLGA-MNPs would be unfair (Chorny et al., 2010). The low release of 1-Aza from the PLGA-MNPs was surprising.

One possible reason for the low level of release of drug is that PLGA has been shown to form covalent bonds with amine containing drugs (Lanao et al., 2013) which may increase the retention of drugs such as 1-Aza

within the nanoparticle. However, the low release did not effect the functional property of the 1-Aza-PLGA-MNP. Indeed, 1-Aza remained functional after release from the PLGA-MNPs and attenuated myogenic differentiation of rMVSCs in a comparable manner to free drug. The levels of CNN1 mRNA expression was evaluated following Jag-1 stimulation of rMVSCs in the absence or presence of varying dilutions of 1-Aza-loaded MNPs. The anti-myogenic effect of the 1-Aza loaded PLGA-MNPs was assessed following 8 fold dilutions (which corresponded to a concentration of 2.5μM 1-Aza), after which the attenuation of CNN1 response reduced before no anti-myogenic effect was observed at a 32-fold dilution.

	1-Aza-PLGA-MNP	Chorny PTX-PLGA-MNP
Size (nm)	232±2.97 nm	263±7 nm
Zeta Potential (mV)	-24.1±6.9mV	-12±2mV
Drug encapsulation Efficiency	96±2.4%	30%
Percentage drug release	3.4±1.56%	72%

Table 5.1 Comparison of the PLGA-MNP and 1-Aza-PLGA-MNP in this study to the published PTX-PLGA-MNPs fabricated by Chorny et al., (2010).

Finally, as the overall objective of this chapter and future work is to target the 1-Aza loaded PLGA-MNPs to stents to attenuate restenosis, the ability to target this type of nanoparticle formulation to stents was evaluated in vitro. PLGA-MNPs were fabricated as before but this time functionalised with fluorescently tagged PLGA, fluorescent tagged siRNA or a fluorescent tagged IgG. The tagged PLGA-MNPs were then targeted to the stent in the presence and absence of a magnetic field to determine the ability of a magnetic field to target PLGA-MNPs towards the stent. Similarly, the siRNA-PLGA-MNPs and IgG-PLGA-MNPs were targeted to

the stent using an external magnetic field and specific binding to the stent was observed [Figure 5.5.4]. This is consistent with the findings by Chorny et al. (2010) who noted a 4- to 10- fold higher binding efficiency of PTX-PLGA-MNPs *in vivo* with the use of an external magnetic field (Chorny et al., 2010).

The results presented in this chapter have been limited to an *in vitro* model however previous reports *in vivo* studies have demonstrated the ability of GSK3β inhibitors to attenuate ISR in rabbit models and PLGA-MNPs have been shown to specifically target bare-metal stents and inhibit restenosis in rat carotid models (Ma et al., 2014; Chorny et al., 2010). The GSK3β inhibitor of choice was shown to reproducibly attenuate Notch mediated myogenic differentiation and the GSK3βi-loaded-PLGA-MNPs remained functional and were further shown to have similar properties to published PTX-PLGA-MNP (Chorny et al., 2010). Together these studies suggest that targeting of the 1-Aza-PLGA-MNPs to bare-metal stents *in vivo* is possible and would likely attenuate restenosis due to inhibiting myogenic differentiation in response to injury.

5.3.2. Conclusion

The aims and objectives of this chapter were achieved. A successful inhibitor of GSK3β was characterised and selected and further demonstrated its ability to inhibit myogenic differentiation of rMVSCs *in vitro*. This inhibitor was efficiently incorporated into appropriately sized, relatively stable, PLGA-MNPs and the released 1-Aza retained its anti-myogenic function. Finally, the formulations of PLGA-MNPs and loaded-PLGA-MNPs showed specific binding to stents, *in vitro*, in the presence of an external magnetic field suggesting them as the ideal drug delivery system for vascular stent targeting.

Chapter 6

Final Discussion

CVD remains the leading cause of death world-wide (WHO, 2017). The most common form of heart disease is atherosclerosis which in response to various risk factors culminates in a build up of cholesterol, lipids, smooth muscle-like cells and inflammatory cells within a intimal lesion (Insull et al., 2009). The current treatment option for this disease involves balloon angioplasty and subsequent deployment of a drug-eluting vascular stent (White et al., 2005), typically loaded with paclitaxel (Taxol™) or rapamycin (Sirolimus™) (Jeremias et al., 2008). Despite the presence of such DES, the phenomenon of ISR may still prevail (Dangas et al., 2002). ISR is characterised by a (neo)intimal thickening of the vessel wall due to the accumulation of a high proportion of smooth muscle-like cells (Schiele et al., 2005). One key question in vascular biology that remains controversial is the potential source of these neointimal cells. Are they derived from differentiated SMC through a re-programming event (de-differentiated) or or are they stem cell-derived myogenic progeny from circulating or resident stem/endothelial cells (Tang et al., 2012). Moreover, what therapeutic strategy best targets these cells using DES platforms? The overall aims of this thesis are to address these compelling questions using both photonic platforms to discriminate vascular phenotypes and novel functionalised magnetic nanoparticles loaded on vascular stents to specifically target these cells.

6.1 Photonics can be used as a label free platform to characterise and identify cells.

To establish whether healthy differentiated SMCs from aorta and carotid arteries could be discriminated from arteriosclerotic neointimal SMC-like cells following carotid injury using photonics, cells from each population were enzymatically isolated from murine tissue, captured on a microfluidic

device and exposed to broadband light. The auto-fluorescence of vascular tissue has been studied since the late 1980's. Reports in the literature compare auto-fluorescence differences in atherosclerotic versus healthy human arteries and attribute them to collagen, elastin, lipids and calcium deposits (Fitzmaurice et al., 1989). The use of auto-fluorescence to diagnose vascular diseases has more recently been reported mainly using skin auto-fluorescence (Noordzig et al., 2012; Dekker et al., 2013; Wong et al., 2014). Information on the auto-fluorescence of vascular cells is limited. Although, there are studies evaluating the changes in auto-fluorescence of undifferentiated stem cells undergoing differentiation but only at 460 nm and 525 nm emission wavelengths (Quinn et al., 2013; Rice et al., 2007; 2010; Thimm et al., 2015; Squirrel et al., 2012), there is a significant lack of information about the autofluorescence signatures for undifferentiated stem cells undergoing myogenic differentiation.

As differences in AF has been noted before in the literature for healthy and diseased arteries (Fitzmaurice et al., 1989) it is not surprising that individual medial and neointimal SMC-like cells from arteriosclerotic (ligated) vessels exhibited much higher AF signatures across all wavelengths than the healthy medial SMCs. These SMC-like cells have been widely reported to be of a more immature, stem-like/de-differentiated phenotype (Schwartz et al., 1998).

Lineage tracing analysis and epigenetic profiling of neointimal cells have since provided compelling evidence for the involvement of stem cell-derived progeny (Torsney et al., 2011; Hu et al., 2004; Klein et al., 2011; Klein 2016; Sata et al. 2002; Hoglund et al. 2010; Tang et al., 2012; Wan et al., 2012; Shikitani et al., 2016; Kramann et al., 2015; Cooley et al., 2014; Yuan et al., 2017), in addition to ‘re-programmed’ differentiated SMCs (Nemenoff et al., 2011; Herring et al., 2014; Shankman et al., 2015; Cherepanova et al., 2016; Majesky et al., 2016; Chappell et al., 2016; Gomez et al., 2015) as well as SMC derived from endothelial-mesenchymal transition (EndMT)(Cooley et al., 2014; Yuan et al., 2017)

in progressing neointimal formation in murine models or arteriosclerotic disease. An important caveat for all of these studies is that stem cells may acquire SMC promoters as they undergo myogenic differentiation while SMCs may acquire specific stem cell promoters as they de-differentiate/re-programme. The use of a time dependent switch is an essential pre-requisite for appropriately designed lineage tracing experiments. Inducible models were developed using cell-specific promoters modified to include a regulatory element that controls Cre expression only when activated by specific exogenous inducing molecules (e.g, tamoxifen, Tm). As a consequence, Cre will recombine the DNA in target cells that express the marker gene only during the administration of the inducing Tm molecule, thus opening a transient window in which the cells can be labelled. Upon withdrawal of the inducing molecule, no additional cells can undergo genetic recombination, even if they express the cell-specific promoter. In many of these landmark lineage tracing studies, Tm was given prior to injury to mark cells and then withdrawn for up to a week. It was then assumed only cells expressing the cell-specific promoter and all their progeny are marked and tracked *in vivo*. However, a recent study using an in vivo bioassay to directly assess the length of time that a given dose of Tm can induce Cre-loxP recombination has seriously questioned this assumption. These studies elegantly demonstrated that a significant number of cells are marked long after Tm is stopped, potentially confounding the interpretation of time-sensitive studies using Tm-dependent models to track differentiated cells (Reinert et al,, 2012).

In this context, the AF profile of mMSCs, mC3H cells and rMVSCs following myogenic differentiation with TGF-β_1 and Jag-1 was assessed to determine whether multipotent stem cells could acquire a neointimal SMC-like AF photonic signature following differentiation. The benefit of using a microfluidic and auto-fluorescence platform over lineage tracing and epigenetic markers is that it is label free, cheap, easy to use and cells can be analysed singularly or as a population. Following

confirmation of myogenic differentiation using various biochemical and epigenetic markers, including epigenetic data confirming mMSCs acquire the SMC histone H3K4me2 di-methylation mark at the Myh11 promoter. the stem cell-derived progeny shared the greatest photonic similarity with the neointimal cells from ligated vessels, particularly at the 565 ± 20 nm wavelength. In particular, when mMSCs were treated with myogenic inductive media for up to 28 days, the AF profile at the 565 ± 20 nm wavelength resembled that of neointimal SMC-like cells.

One of the main drawbacks of this technique is the limited information generated from assessing auto-fluorescence patterns alone. In an effort to identify the molecule(s) involved in exhibiting the high AF signature at 565 ± 20 nm in neointimal SMC-like cells and stem cell-derived myogenic progeny, the role of auto-fluorescent matrix proteins, elastin and collagen were investigated (Richards-Kortum and Sevick-Muraca, 1996; Masters and So, 1999; Agarwal et al., 2001). Indeed, neointimal SMC-like cells exhibit high levels of collagen and elastin (Merrilees et al., 2011; Xu & Shi et al., 2014). Elastin and collagen were also up-regulated in myogenic progeny from mMSCs and rMVSCs regardless of the inductive stimulus (TGF-β_1 or Jag-1). This result is in agreement with other studies that have shown that stem cell-derived myogenic progeny produce collagen and elastin (Swaminathan et al., 2014; Li et al., 2016). In order to determine whether this increased collagen and/or elastin expression contributed to the high AF signature observed at the 565 ± 20 nm, the AF profile at this wavelength was assessed following collagen and elastin knockdown using specific targeted siRNA duplexes. Elastin knockdown reduced, but not significantly, the AF signature at this wavelength. In contrast, collagen knockdown significantly reduced the AF signature at 565 ± 20 nm. This suggests that collagen is responsible in part for the increase in AF at 565 ± 20 nm during myogenic differentiation. Collectively, these photonic data support the concept that stem cell-derived progeny may contribute to SMC-like cells that accumulate at the site of injury to form a (neo)intima.

This AF profiling of cells is also dependent on microfluidic capture of cells thereby rendering it more suitable for interrogating cells within fluid biopsies. Indeed, it is known that tumours shed circulating cells and microfluidics can be adapted as a “liquid biopsy” that enables tumour characterisation by minimally invasive means. Multiple studies have described how molecular information about parent tumours can be extracted from these cellular components (Perakis and Speicher, 2017). In this context, microvesicles are shed from vascular lesions (Bobryshev et al., 2013) and it is not inconceivable that vascular lesions may also shed circulating cells as the neointima enlarges.

Importantly, these data were generated using rodent models of vascular injury and multipotent stem cells *in vitro.* While widely used in vascular research, the mechanism(s) for injury, pathogenesis of the disease and overall structure of the artery (no intima) are significantly different to human outcomes (Shanks et al., 2009). It will therefore be necessary to assess whether similar AF signature differences are evident between cells from human arteriosclerotic vessels and human stem cell-derived myogenic progeny. Finally, as one further disadvantage of assessing AF signatures is the specific identity of the discriminant molecules, vibrational spectroscopic methods were employed for a more rigorous approach at discriminating stem cells from their myogenic progeny and further to compare these cells with ‘de-differentiated’ SMCs *in vitro*.

Vibrational spectroscopy has shown great promise as a diagnostic tool to characterise changes in cell phenotype. Much of the work to date has focused on cancer models which include *in vitro*, *ex vivo* and *in vivo* studies on prostate, cervical, uteri, skin, breast, colon, oesophagus, bladder, oral mucosal cancers with the aim of generating a reliable diagnostic platform to reduce false negatives obtained from conventional diagnostic techniques (Butler et al., 2016; Vardaki et al., 2016; Crow et al., 2005; Baker et al., 2014). The same has been applied to diagnosing bone diseases such as osteoporosis, with the added benefit that it does

not require prior sample prep such as homogenisation or de-calcification of the sample. Similarly, Raman and FTIR have bene applied to kidney and gallstones for label-free detection of the stones. In particularly, they hydroxyapatite band of the kidney stone makes detection reliable and easy. Finally in terms of diagnosis, some research has been carried out comparing atherosclerotic and healthy tissue *in vivo* (mice) and *ex vivo* carotids (human) (Krafft et al., 2009). Although the results of these studies are very promising, a few issues are currently preventing this technology becoming clinically translated. The first being that the data processing of the acquired spectra can be tricky (Smith et al., 2016). Background signals and scattering require removal from spectral datasets and normalisation of the data to a reference spectrum is usually required. Background subtraction and normalisation are applied through computational algorithms such as the Extended Multiplicative Scatter Correction protocol, which requires software and training (Byrne et al., 2016). The next issue is the difference in tissue thickness and density, this can cause issues with IR and Raman signals and can result in longer acquisition times for spectra which can be detrimental to biological specimen (Byrne et al., 2016; Smith et al., 2016). Finally, for *ex vivo* analysis in relation to pathological tissue, expensive substrates such as CaF_2 are necessary to reduce background signals for reliable spectra. The substrates may be too expensive for clinical feasibility. Even with the current limitations, the foundation exists for a spectral based diagnostic platform for disease (Byrne et al., 2016).

In this context, the application of vibrational spectroscopy to characterise stem cells from their myogenic and osteogenic progeny was assessed and the spectral data obtained can be used as a biomarker for the accumulation of myogenic progeny in the neointima in future studies. There are already reports in the literature using vibrational spectroscopy to characterise stem cells and their progeny such as hESCs and cardiomyocytes and neural stem cells from glial cells (Smith et al., 2016) and therefore the technique was adapted for stem cells, myogenic

progeny and also 'de-differentiated' SMCs to characterise differences between the cells at a molecular level.

To test whether vibrational spectroscopic methods could discriminate undifferentiated stem cells from their differentiated progeny, rMSCs were initially differentiated to osteocytes and analysed by FTIR and Raman. These techniques have previously been shown to discriminate undifferentiated stem cells from their osteogenic progeny and provided a standard to be compared against (McManus et al., 2012). Principle component analysis with linear discriminant analysis (PCA-LDA) of FTIR and Raman spectra generated for rMSCs and their osteogenic progeny facilitated successful discrimination of both cell populations.

With both platforms validated, rMSCs were treated with TGF-β_1 and Jag-1 to induce myogenic differentiation. This was validated biochemically, including epigenetic data confirming rMSCs acquire the SMC histone H3K4me2 di-methylation mark at the Myh11 promoter. Subcultured rSMCs (ddSMCs) exhibiting a ‘de-differentiated’ phenotype were compared with undifferentiated rMSCs and their myogenic progeny. PCA-LDA of FTIR spectra from individual cell populations demonstrated significant overlap between the undifferentiated rMSC and the ddSMC spectra, indicating there were stem cell-like cells within the de-differentiated population. De-differentiated SMCs and stem cell derived SMCs were fully discriminated 100% of the time using FTIR. This suggests that FTIR could be used as a useful tool to identify the SMC-like cell in the neointimal lesion as it can specifically identify and discriminate de-differentiated ddSMCs and stem cell derived SMCs.

The more sensitive Raman analysis successfully discriminated individual nuclei of undifferentiated rMSCs from ddSMCs 100% of the time. There was significant overlap however, in the spectra and PCA plot between the ddSMCs and stem cell-derived progeny indicating that ddSMCs and stem cell-derived myogenic progeny are notably similar at the nuclear level.

This result was very interesting, but not altogether surprising. In particular the epigenetic data from stem cell-derived SMCs have a remarkably similar profile to SMCs in culture, typically referred to as 'de-differentiated' SMCs, in both mice and rats [Figure 6.1 (a), (b)]. The presence of either stem cell derived SMCs or 'de-differentiated' SMCs are accepted as being the contributing cell to neointimal lesions, and the autofluorescence profile in this study demonstrated the likeness of stem cell myogenic progeny with the neointimal SMC-like cells [Figure 6.1 (c). Finally, high resolution spectral recordings of the nucleus of stem cell derived progeny and de-differentiated SMCs generated overlapping spectra that when subjected to Principle Component Analysis could not be uniquely discriminated from one another with 100% accuracy [Figure 6.1 (d)].

It has previously been demonstrated that the sudden high proliferative capacity of ‘de-differentiated’ ddSMC in culture is due in part to the expansion of the naturally highly proliferative small subpopulation of stem cells in the culture that eventually take over the population yielding stem cell derived progeny (Tang et al., 2012; 2013, Yuan et al., 2017). This phenomenon was also observed in this study when freshly isolated differentiated SMCs became a rapidly proliferating population over four passages with decreased Myh11 gene expression. It is known that $Sox10^{+}$ resident medial multipotent vascular stem cells (MVSCs) are present in SMC cultures and more than likely dominated the culture (Kennedy et al., 2014a, Kennedy et al., 2014b). It is therefore possible that the stem cell-derived progeny and the so called ‘de-differentiated’ SMCs are actually the same type of cells (myogenic progeny) but from different stem cell origins i.e. bone marrow derived mesenchymal stem cells versus resident multipotent vascular stem cells

In summary of this data, stem cell-derived progeny are likely to contribute to the SMC-like cells in the neointima. Moreover, at an epigenetic and

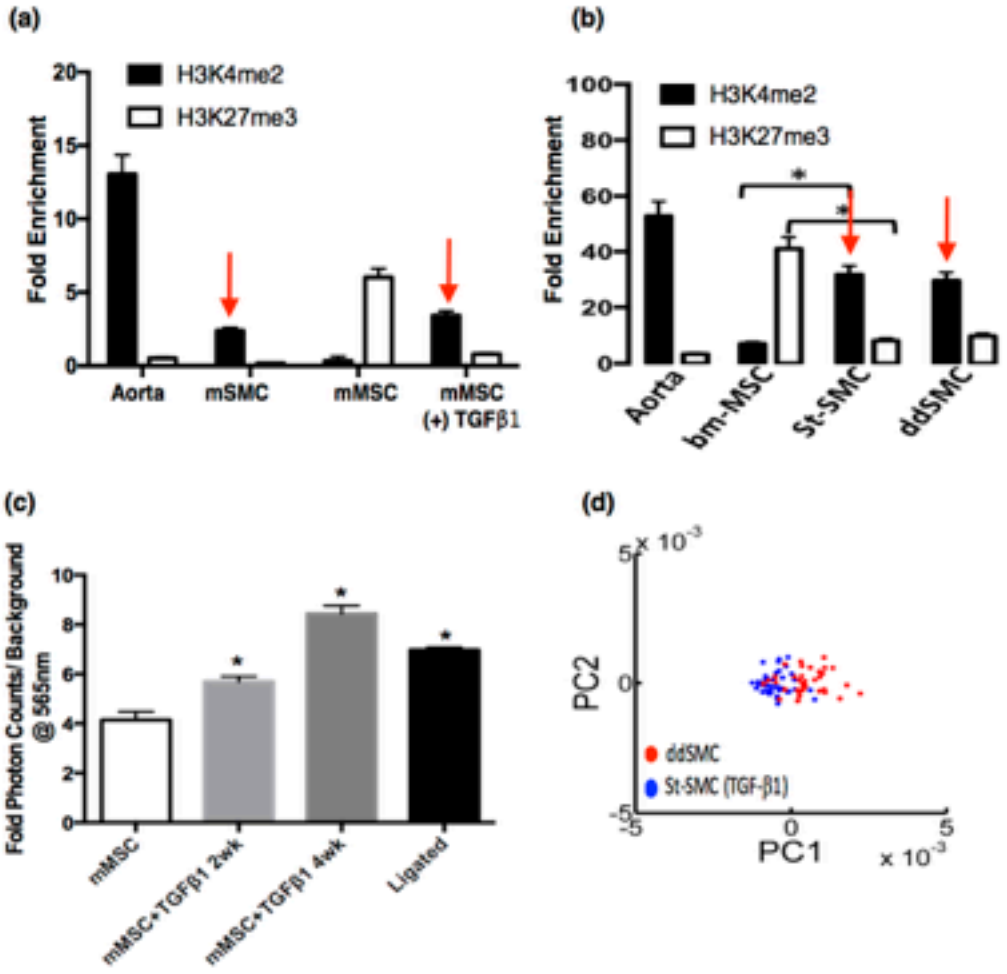

molecular level, stem cell-derived SMCs and 'de-differentiated' SMCs in culture are essentially and photonically the same cell.

Figure 6.1 Summary of photonic and vibrational spectroscopy analysis of SMC-like cells. (a) Fold enrichment of SMC dimethylation marker H3K4Me2 and stem cell methylation marker H3K27me3 in mice cell models (b) rat cell models; (c) Representative autofluorescence profiles of mMSCs with TGF-β_1 and neointimal SMC-like cells; (d) PCA score plot of de-differentiated SMCs and stem cell derived SMCs (TGF-β_1). Data analysis as described in previous chapters. Arrows point to similar fold enrichment values.

A primary limitation of the current study is that the stem cell populations were of rodent origin, heterogeneous in nature and expanded in culture media that is different from protocols required for pre-clinical and clinical

studies. Moreover, spectral measurements were taken with cell cultures, or *ex vivo* rather than being obtained from an intact vessel *in situ.* Culturing the progeny of a single CFU or phenotype-isolated single clonogenic human stem cell would give rise to a more homogenous “true” human MSC population that could serve to provide similar results and further validate vibrational spectroscopic for clinical applications. Nevertheless, the presence of resident multipotent vascular stem cells and their myogenic capacity has been reported in human cells (Tang et al., 2012, 2013).

Vibrational spectroscopy was successfully applied to the study of undifferentiated MSCs before and after myogenic differentiation in vitro to identify discrete spectral characteristics that could facilitate localisation and detection of myogenic differentiation of resident vascular stem cell populations in vivo. The vasculature is unique in that it has a well-defined spatial geography of cells either side and within the internal (IEL) and external elastic lamina (EEL) that could facilitate acquisition of label-free analysis of cell spectra with relative confidence. The initial step in the development of arteriosclerotic disease is IMT and neointimal formation that facilitates the build-up of LDL (low density lipoprotein) particles within the intimal layer of the vessel wall (Sun et al, 2000; Subbotin et al., 2016). Interrogation of early atherosclerotic vessels *in situ* using vibrational spectroscopy could discriminate the presence of stem cell-derived progeny not readily available in current diagnostic imaging techniques such as IVUS, MRI, and angiography (Tarkin et al., 2017). Indeed, significant progress has already been made towards in vivo application of vibrational spectroscopy. Raman spectroscopy in particular, as an optical probe, lends itself naturally to endoscopic application and has recently been deployed for intra-operative guidance of brain surgery (Jermyn et al., 2015) and endoscopic gastrointestinal procedures (Wang et al., 2015). A smart Raman needle probe has also been developed and tested for potential in vivo and ex vivo use, capable of measuring Raman molecular tissue signals in <1-2 seconds down a hypodermic needle (Day

et al., 2013). Because of its high sensitivity to water, there have been relatively fewer in vivo applications of IR spectroscopy, although the recent emergence of high brightness, tunable Quantum Cascade Lasers has opened the door towards their development (Michel et al., 2013). This suggests that, with further development, FTIR could provide initial selection of cells for interrogation before quantitative chemical and morphological evaluation by Raman discriminates these cells within vascular lesions in situ, such as the presence of stem cell derived myogenic or osteogenic progeny so that more targeted therapies against these discrete phenotypes can be introduced. Finally, circulating vascular cells and progenitor cells shed from the vessel wall during IMT and disease progression could be retrieved from blood and interrogated using vibrational spectroscopy for clinical evaluation to provide a more definitive tool for early diagnosis (Perakis et al., 2017). The ability to assess the accumulation of stem cell-derived progeny using label free platforms in situ or the shedding of these progeny into the blood during disease progression may further facilitate interrogation of these phenotypes by their discrete spectroscopic signatures using liquid biopsies and microfluidic platforms.

6.2 GSK3β inhibitors can be incorporated into PLGA-MNPs as a novel therapeutic platform for drug eluting stents.

To address the issue of SMC-like cell accumulation during in-stent restenosis (ISR), and given the likelihood of a contribution from stem cell-derived myogenic progeny to the lesion, a novel inhibitor of myogenic differentiation was incorporated into PLGA-MNPs and investigated for its ability to bind to bare metal stents under magnetic conditions and control myogenic differentiation of undifferentiated stem cells.

Stents coated with a GSK3β inhibitor have previously shown success in reducing neointimal lesions in animal models of ISR (Ma et al., 2010). However, the GSK3β inhibitor was primarily evaluated for its 're-endothelialisation' potential rather than its effect on myogenic differentiation (Ma et al., 2010). GSK3β has been reported to be involved in the progression of vascular diseases in many other studies. Deletion and pharmacological inhibition of GSK3β has improved vessel diameter and atherogenesis in mice (Woulfe et al., 2010; Bowes et al., 2009) and pigs (Potz et al., 2016) and elevated levels of GSK3β have been found in atherosclerotic plaques and in the neointima following carotid ligation in rats (Wang et al., 2013; Guha et al., 2011). GSK3β inhibition has been well characterised in terms of maintaining pluripotency of stem cells (Wray et al., 2011; Sato et al., 2011; Kirby et al., 2012) and even increasing embryonic stem cell resistance to differentiation (Wray et al., 2011). However, there is very little reported in the literature about the role of GSK3β in stem cell differentiation models. Of the available reports in the literature, conflicting results have been presented. For example, inhibition of GSK3β has been shown to enhance neuronal differentiation of neural stem cells (Maurer et al., 2007) and somatic stem cells (Dastjerdi et al., 2012), promote epithelial transition of colorectal cancer stem cells (Costabile et al., 2017), induce endothelial differentiation from iPSCs and mESCs (Kitajima et al., 2016) and promote cancer stem cell tumour differentiation (Korur et al., 2009). However it has also been

shown to attenuate cardiomyocyte differentiation of MSCs (Cho et al., 2009) adipocyte differentiation from adipose stem cells (Zaragosi et al., 2008) and reduced GSK3β levels have been associated with inhibition of embryonic stem cell differentiation to neurons and skeletal muscle (Bain et al., 2016).

The majority of the studies implicating the inactivation of GSKβ in stem cell differentiation are associated with enhanced Wnt/β-Catenin signalling (Maurer et al., 2007; Dastjerdi et al., 2012) which is an essential process in embryogenesis (Komiya et al., 2008) however it is usually switched off in adult systems (Ring et al., 2014). GSKβ has been demonstrated to be the indirect mediator between Wnt/β-catenin signalling and another highly conserved signalling pathway, hedgehog (Ring et al., 2014). Supportive reports in our lab have shown GSKβ inhibition attenuated hedgehog signalling (ptch1 levels) in vascular SMCs (Guha et al., 2011). GSK inhibition also attenuated hedgehog signalling in MSCs and C3H T10 1/2 stem cells (Supplemental Figure 1). GSKβ has also been associated with Wnt and Notch signalling (Espinosa et al., 2003; Ring et al., 2014). Notch signalling is commonly associated with vascular disease models (Liedner et al., 2001; Li et al., 2009; Morrow et al., 2009; Redmond et al., 2014; Caolo et al., 2011) and myogenic differentiation of various stem cells such as MSCs (Doi et al., 2006; Mooney at al., 2015), hESCs (Kurpinski et al., 2010), neural crest stem cells (High et al., 2007) and multipotent vascular stem cells (Tang et al., 2010). GSKβ has been shown to regulate Notch through phosphorylation of the Notch intracellular domain and inhibition of GSKβ results in an attenuation of Notch target gene transcription (Foltz et al., 2002; Guha et al., 2011). In this study, Notch activation was chosen as the driver of myogenic differentiation to evaluate the effect of GSKβ on Notch mediated myogenic differentiation.

Three pharmacological inhibitors of GSK3β were evaluated for their inhibitory effect on myogenic differentiation. Cultured undifferentiated rMVSCs were treated with the Notch ligand, Jag-1 to induce myogenic

differentiation. Jag-1 induced myogenic differentiation of undifferentiated resident stem cells (MVSCs) was confirmed before rMVSCs were treated with Jag-1 in the absence or presence of each GSK3β inhibitor. The most specific inhibitor for GSK3β, 1-Aza (1-Aza), was also the most effective at attenuating Jag-1 induced myogenic differentiation. To determine whether the effect of 1-Aza on myogenic differentiation was due to regulation of Notch signalling, Jag-1 induced Notch target gene expression was evaluated in the absence or presence of 1-Aza. The GSK3β inhibitor significantly inhibited Jag-1 induced Notch target gene expression concomitant with a reduction in myogenic differentiation. The results clearly show that Notch drives myogenic differentiation and GSK3β has a role in this pathway that can be manipulated therapeutically to block this process. The results in this work supports several studies reporting that GSK3β positively regulates Notch signalling (Ruel et al., 1993; Foltz et al., 2002; Guha et al., 2011).

Finally, a current issue with all DES is the problem with depletion of drugs over time (Halkin et al., 2004). Researchers are beginning to utilise nanoparticles to deliver drugs and agents to stents (Danenberg et al., 2002; 2003; Cohen-Sela et al., 2006; Chan et al., 2011). The small size of nanoparticles make them ideal for systemic drug delivery (Siafaka et al., 2016). More recently, magnetic nanoparticles have been employed for drug delivery in cancer and vascular models as they have the added benefit that they can be manipulated using an external magnetic field for specific targeting which therefore reduces systemic drug exposure and less drug is required for a therapeutic effect (Tietze et al., 2015; et al., 2010; Vosen et al., 2016; Chorny et al., 2011).

With this in mind, 1-Aza was encapsulated with PLGA-MNPs using the double oil in water emulsion method (McCall et al., 2013). Using an adaptation of this method (see Chapter 2.6.1), 1-Aza-PLGA-MNPs were formulated and characterised based on their size, stability, drug release kinetics and stent targeting. The 1-Aza-PLGA-MNPs were sized at

approximately 232±2.97 nm and were relatively round in size and small enough to be transported around human arteries (Dodge et al., 1992). The zeta potential of -24.1mV for the 1-Aza-PLGA -MNPs was albeit less than the -30mV recommended (Clogston & Patri, 2011) which would suggest that they have the potential to aggregate. However, in a similar study where PTX-PLGA-MNPs were generated and introduced in vivo, the zeta potential was 12mV, the researchers did not report any aggregation or coagulation of the nanoparticles and they still maintained the ability to reduce restenosis *in vivo* (Chorny et al., 2010). Therefore, aggregation of the 1-Aza-PLGA-MNPs would not be expected when subjected to *in vivo* studies. A very high incorporation efficiency, approximately 96±2.4%, was found for 1-Aza in the PLGA-MNPs with low levels of drug released after 72 hours. Release studies were carried out for up to 14 days with no additional release. The high incorporation efficiency and low release of 1-Aza from the PLGA-MNPs is possibly due to covalent bonds forming between the polymer and amine groups of 1-Aza (Lanao et al., 2013) causing retention of the drug within the PLGA-MNP. However, even with the low release rates and short duration times for 1-Aza, the released 1-Aza remained functional and attenuated Notch mediated myogenic differentiation.

To track targeting of this formulation of nanoparticles to the bare-metal stent *in vitro,* FITC labelled PLGA-MNPs were generated and the presence of an external magnetic field was critical for targeting the nanoparticles to the bare metal stent. This supports a similar *in vivo* study where PTX-PLGA-MNPs were found to bind the stent in rat carotid arteries with four- to ten- fold more specificity in the presence of an external magnetic field (Chorny et al., 2010).

6.3 Future Work

Using three novel diagnostic photonic platforms to interrogate normal (healthy) and arteriosclerotic (diseased) cells, in addition to undifferentiated stem cells and their myogenic and osteogenic progeny *in vitro,* the major findings from this study contribute significantly to the ongoing debate about the source of the SMC-like cells that populate neointimal lesions and moreover, present a clinically translatable strategy to specifically target the source of these cells *in vivo* using novel magnetic nanoparticles to deliver targeted therapies against these cells.

The main limitation of this work is the lack of *in vivo* studies. The microfluidic photonic platform contained some *ex vivo* work when comparing the healthy differentiated SMCs from the carotid artery and aorta with the arteriosclerotic cells from ligated carotid vessel. In addition, the stem cells before and after myogenic differentiation were from cell culture models *in vitro.* The vibrational spectroscopy approach to characterising and identifying stem cells, myogenic progeny and de-differentiated SMCs, while powerful was limited to cell culture models and may display different spectral characteristics for human cells *in vivo.* Moreover, microfluidic platforms using liquid biopsy samples from healthy and diseased vessels could form the basis for AF, FTIR and Raman interrogation and profiling of cells, these studies. This would be a more feasible diagnostic platform using this photonic approach as patient vessels cannot be isolated and digested as outlined in this study. This approach has already been described for blood samples in liver assays (Nwankire et al., 2015) and adapted with Raman spectroscopy in urine samples for bacterial detection for urinary tract infections (Shroder et al., 2015).

The AF platform described in this study used non-specified broadband light which yielded a low resolution. To gain more information about the samples in future and to achieve higher resolution, ‘narrow band imaging’

could be employed whereby narrow band filters, particularly for the 565 ± 20 nm wavelength, can focus the illumination for more precise analysis of the autofluorescence of these cells (Filip et al., 2011). Alternatively, the increasingly popular multi-photon microscopy could be used for a more focused excitation bandwidth through the simultaneous absorption of two photons emitted by a laser source. Multi-photon microscopy has many benefits over broadband AF microscopy such as the ability to optically section a sample with little photodamage or out of focus bleaching (Tauer, 2002) so therefore would be the next logical step in the development of this particular technology. Furthermore, in addition to the concentration of fluorophores and fluorescent intensity, fluorescence lifetime analysis has been utilised in the literature to describe the molecular environment of the cell and in particular differentiate the contributing fluorophores. As previously mentioned, the metabolic state of cells can be assessed by analysing the fluorescent lifetime of the fluorophore NADH as it loses its fluorescence when it becomes oxidised, whereas FAD exhibits AF when it is oxidised and loses it when it is reduced. The ratio between the two fluorophore AF levels indicates protein binding, phosphorylation and glycolysis within a cell. In a similar manner, fluorescent lifetime imaging microscopy (FLIM) could be applied to this study to gain more information about the contributing fluorophores to the AF levels detected (Becker, 2015).

FTIR and Raman spectroscopy have been widely reported for *ex-vivo* characterisation of tumours and tissues (Verdaki et al., 2016; Ooi et al., 2008; Backhaus et al., 2010). In some cases, vibrational spectroscopy was found to be a more reliable approach to cancer diagnosis than typical histology (Njoroge et al., 2006; El-Tawil et al., 2008). Therefore, the next step in this study would be to isolate normal and diseased cells using microfluidic platforms and obtain specific spectra from these tissue samples before the platform is miniaturised to interrogate cells *in situ* to become a minimally invasive diagnostic platform for CVD. Alternatively, as an *in vivo* approach, miniaturised Raman or FTIR fibre optic probes

could be developed on a catheter based system for guidance to the site of a suspected vascular occlusion (Motz et al., 2006; Savastano et al., 2017). Vibrational spectra can be recorded using this technology to yield the discrete information within the vascular vessels and in conjunction with this, colour maps can be generated based on the chemical and structural information within the vessel by Raman or FTIR mapping. Using this technology, the structural information and molecular composition of an obstruction could be simultaneously identified with high speed and specificity (Coman & Leopold, 2017).

The analysis of GSK3β control of Notch mediated myogenic differentiation and subsequent targeting of GSK3β inhibitor loaded nanoparticles to the cells was also an *in vitro* study. There are concerns for the toxicity of magnetic nanoparticles for cells and tissues *in vivo*, such as the build up of MNPs and by products in organs, aggregation of particles to cause a stenosis or interference with cell-cell interactions (Markides et al., 2012). These concerns were addressed in this *in vitro* study however and the less toxic iron oxide was chosen as the nanoparticle and the aggregation potential (zeta potential) of the nanoparticle formulation was assessed and compared to a previous *in vivo* model and was found to be favourable to the previous published work (Chorny et al., 2010). Therefore, the 1-Aza-PLGA-MNPs are ready to progress to *in vivo* studies.

A recently reported platform that may prove useful before applying this therapy *in vivo* would be the use of a mock vascular phantom (Colombo et al., 2013). This mock vascular phantom fabricated using Sylgard™ supports both stent deployment and cell growth within the stented region when connected to a cell culture chamber where *in vivo* hemodynamic conditions of pulsatile flow and circumferential strain are fully incorporated (Colombo et al., 2013). This technology could be adapted by seeding rMVSCs to the mock vascular phantom containing a stent coated

with Jag-1 followed by the addition of 1-Aza-PLGA-MNPs and guidance of the nanoparticles to the cells on the stent (as described in Figure 6.2)

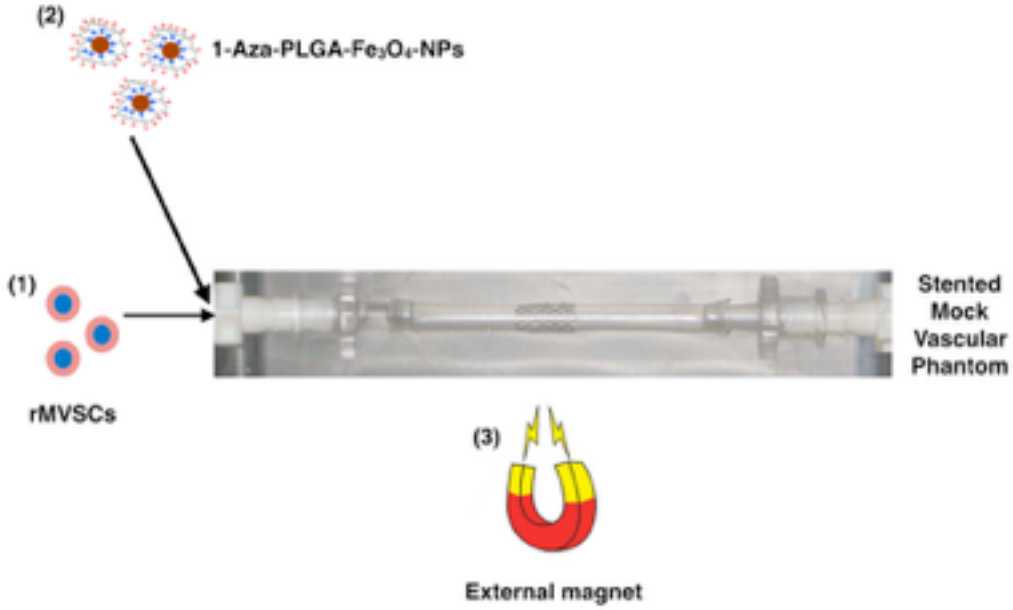

Figure 6.2 Mock vascular phantom system. Figure 6.2 depicts a suggested future experiment where a stent is inserted into a mock vascular phantom that is hooked up to a cell culture chamber. rMVSCs can be added to the system followed by the 1-Aza-PLGA-MNPs and guided the stent using an external magnetic field.

Should this experiment be successful, the technology should be considered for *in vivo* studies, perhaps starting in rat carotid models following the success of neointimal reduction following PTX-PLGA-MNP targeting (Chorny et al., 2010).

6.4 Final Conclusion

The overall aims and objectives of this thesis were to apply a photonic platform to discriminate individual cells from healthy and diseased (arteriosclerotic) vessels *ex vivo* and to compare their profiles to de-differentiated SMCs, undifferentiated stem cells and their myogenic and osteogenic progeny *in vitro*. Specific vibrational spectroscopy techniques were further used to compare ddSMCs and undifferentiated stem cells from their myogenic and osteogenic progeny at a molecular level. Finally, a novel therapeutic platform was developed using functionalised MNP's to specifically target stem cell-derived progeny in a localised, replenishable manner to a bare-metal stents *in vitro.*

Significant data has been presented that demonstrates the feasibility of photonic methods such as the microfluidic-AF platform and vibrational spectroscopy to identify and discriminate differentiated cells from undifferentiated stem cells and their myogenic and osteogenic progeny. The findings also support the putative role of stem cell-derived SMCs and their contribution to the neointimal formation(Tang et al., 2012; Kramann et al., 2015) and that so termed 'de-differentiated SMCs' are possibly stem cell-derived progeny in culture (Tang et al., 2012; Yuan et al., 2017). This study also agrees with reports that GSK3β positively regulates Notch mediated myogenic differentiation (Foltz et al., 2002; Guha et al., 2011) and that this process can be manipulated pharmacologically. Finally, a method to incorporate the inhibitor into a novel delivery system has been evaluated and described to hopefully aid researchers working with similar technology in this field and others.

Bibliography

Abubaker, M., Taylor, A., Ferns, G., & Herman, H. (2007). Differences in Raman Spectra of Aluminium Treated Brain Tissue Sample. *ISPUB.COM The Internet Journal of Toxicology Internet Journal of Toxicology*, *4*(2).

Agarwal, A., Coleno, M. L., Wallace, V. P., Wu, W.-Y., Sun, C.-H., Tromberg, B. J., & George, S. C. (2001). Two-Photon Laser Scanning Microscopy of Epithelial Cell-Modulated Collagen Density in Engineered Human Lung Tissue. *Tissue Engineering*, *7*(2), 191–202.

Aksoy, C., & Severcan, F. (2012). Role of Vibrational Spectroscopy in Stem Cell Research. *Spectroscopy: An International Journal*, *27*(3), 167–184.

Al-Muslet, N. A., & Ali, E. E. (2011). In vivo Spectral Analysis of Bladder Cancer Using Fourier Transform Infrared Spectroscopy, A comparative Study. *Australian Journal of Basic and Applied Sciences*, *5*(9), 1734–1739.

Alberts, B., Johnson, A., Lewis, J., Raff, M., Roberts, K., & Walter, P. (2002). Blood Vessels and Endothelial Cells. *Garland Science.*

Alexander, M. R., & Owens, G. K. (2012). Epigenetic Control of Smooth Muscle Cell Differentiation and Phenotypic Switching in Vascular Development and Disease. *Annual Review of Physiology*, *74*(1), 13–40.

Ami, D., Neri, T., Natalello, A., Mereghetti, P., Doglia, S. M., Zanoni, M., Zuccoti, M., Gargna, S., Redi, C. A. (2008). Embryonic stem cell differentiation studied by FT-IR spectroscopy. *Biochimica et Biophysica Acta (BBA) - Molecular Cell Research*, *1783*(1), 98–106.

Andersson, E. R., & Lendahl, U. (2014). Therapeutic modulation of Notch signalling — are we there yet? *Nature Reviews Drug Discovery*, *13*(5), 357–378.

Ashton, L., Lau, K., Winder, C. L., & Goodacre, R. (2011). Raman spectroscopy: lighting up the future of microbial identification. *Future Microbiology*, *6*(9), 991–997.

Avci, E., Kaya, N. S., Ucankus, G., & Culha, M. (2015). Discrimination of urinary tract infection pathogens by means of their growth profiles using surface enhanced Raman scattering. *Analytical and Bioanalytical Chemistry*, *407*(27), 8233–8241.

Awonusi, A., Morris, M. D., & Tecklenburg, M. M. J. (2007). Carbonate Assignment and Calibration in the Raman Spectrum of Apatite. *Calcified Tissue International, 81*(1), 46–52.

Backhaus, J., Mueller, R., Formanski, N., Szlama, N., Meerpohl, H.-G., Eidt, M., & Bugert, P. (2010). Diagnosis of breast cancer with infrared spectroscopy from serum samples. *Vibrational Spectroscopy*, *52*(2), 173–177.

Bain, L., Liu, J.-T., & League, R. (2016). Arsenic inhibits stem cell differentiation by altering the interplay between the Wnt3a and Notch signaling pathways. *Toxicology Reports*, *3*, 405–413.

Baker, M. J., Trevisan, J., Bassan, P., Bhargava, R., Butler, H. J., Dorling, K. M., Fielden, Peter, R., Fogarty, S.W., Fullwood, N.J., Heys, K.A., Hughes, C., Lasch, P., Martin-Hirsch, P., Obinaju, B., Sockalingum, G.D., Sulé-Suso, J., Strong, R., Walsh, M.J., Wood, B.R., Gardner, P., Martin, F. L. (2014). Using Fourier transform IR spectroscopy to analyze biological materials. *Nature Protocols*, *9*(8), 1771–91.

Bank, A. J., Wang, H., Holte, J. E., Mullen, K., Shammas, R., & Kubo, S. H. (1996). Contribution of Collagen, Elastin, and Smooth Muscle to In Vivo Human Brachial Artery Wall Stress and Elastic Modulus. *Circulation*, *94*(12).

Barrett, H. E., Mulvihill, J. J., Cunnane, E. M., & Walsh, M. T. (2015). Characterising human atherosclerotic carotid plaque tissue composition and morphology using combined spectroscopic and imaging modalities. *BioMedical Engineering OnLine*, *14*(Suppl 1), S5.

Bartolomé, F., & Abramov, A. Y. (2015). Measurement of Mitochondrial NADH and FAD Autofluorescence in Live Cells. In *Methods in molecular biology (Clifton, N.J.) 1264,* pp. 263–270).

Bazak, R., Houri, M., El Achy, S., Kamel, S., & Refaat, T. (2015). Cancer active targeting by nanoparticles: a comprehensive review of literature. *Journal of Cancer Research and Clinical Oncology*, *141*(5), 769–84.

Becker, W. (2015) Fluorescence lifetime imaging by multidimensional time correlated single photon counting. *Medical Photonics, 27:* 41-61.

Beekes, M., Lasch, P., & Naumann, D. (2007). Analytical applications of Fourier transform-infrared (FT-IR) spectroscopy in microbiology and prion research Analytical applications of Fourier transform- infrared (FT-IR) spectroscopy in microbiology. *Veterinary Microbiology*, *123*(4).

Beljebbar, A., Dukic, S., Amharref, N., & Manfait, M. (2010). Ex vivo and in vivo diagnosis of C6 glioblastoma development by Raman spectroscopy coupled to a microprobe. *Analytical and Bioanalytical Chemistry*, *398*(1), 477–487.

Benjamin, E. J., Blaha, M. J., Chiuve, S. E., Cushman, M., Das, S. R., Deo, R., de Ferranti, S.D., Floyd, J., Fornage, M., Gillespie, C., Isasi, C.R., Jiménez, M.C., Jordan, L.C., Judd, S.E., Lackland, D., Lichtman, J.H., Lisabeth, L., Liu, S., Longenecker, C.T., Mackey, R.H., Matsushita, K., Mozaffarian, D., Mussolino, M.E., Nasir, K., Neumar, R.W., Palaniappan, L., Pandey, D.K., Thiagarajan, R.R., Reeves, M.J., Ritchey, M., Rodriguez, C.J., Roth, G.A., Rosamond, W.D., Sasson, C., Towfighi, A., Tsao, C.W., Turner, M.B., Virani, S.S., Voeks, J.H., Willey, J.Z., Wilkins, J.T., Wu, J.H.Y., Alger, H.M., Wong, S.S., Muntner, P.,(2017). Heart Disease and Stroke Statistics—2017 Update: A Report From the American Heart Association. *Circulation*.

Bird, B., Miljkovic, M., Romeo, M. J., Smith, J., Stone, N., George, M. W., & Diem, M. (2008). The application of Fourier transform infrared microspectroscopy for the study of diseased central nervous system tissue. *BMC Clinical Pathology.*, *8*(8).

Bobryshev, Y. V., Killingsworth, M. C., & Orekhov, A. N. (2013). Increased Shedding of Microvesicles from Intimal Smooth Muscle Cells in Athero-Prone Areas of the Human Aorta: Implications for Understanding of the Predisease Stage. *Pathobiology*, *80*(1), 24–31.

Boiret, M., Gorretta, N., Ginot, Y.-M., & Roger, J.-M. (2016). An iterative approach for compound detection in an unknown pharmaceutical drug product: Application on Raman microscopy. *Journal of Pharmaceutical and Biomedical Analysis*, *120*, 342–351.

Bonnier, F., Bertrand, D., Rubin, S., Ventéo, L., Pluot, M., Baehrel, B., Mainfait, M., Sockalingum, G. D. (2008). Detection of pathological aortic tissues by infrared multispectral imaging and chemometrics. *The Analyst*, *133*(6), 784.

Böse, D., Eggebrecht, H., Haude, M., Schmermund, A., & Erbel, R. (2006). First Absorbable Metal Stent Implantation in Human Coronary Arteries. *The American Heart Hospital Journal*, *4*(2), 128–130.

Bowes, A. J., Khan, M. I., Shi, Y., Robertson, L., & Werstuck, G. H. (2009). Valproate Attenuates Accelerated Atherosclerosis in Hyperglycemic ApoE-Deficient Mice Evidence in Support of a Role for Endoplasmic Reticulum Stress and Glycogen Synthase Kinase-3 in Lesion Development and Hepatic Steatosis. *The American Journal of Pathology. 174*(1), 330-42.

Buckley, K., & Matousek, P. (2011). Recent advances in the application of transmission Raman spectroscopy to pharmaceutical analysis. *Journal of Pharmaceutical and Biomedical Analysis*, *55*(4), 645–652.

Burger, R., Kurzbuch, D., Gorkin, R., Kijanka, G., Glynn, M., McDonagh, C., & Ducrée, J. (2015). An integrated centrifugo-opto-microfluidic platform for arraying, analysis, identification and manipulation of individual cells. *Lab Chip*, *15*(2), 378–381.

Buschman, H. P., Deinum, G., Motz, J. T., Fitzmaurice, M., Kramer, J. R., van der Laarse, A., Bursche, A., Feld, M. S. (2001). Raman microspectroscopy of human coronary atherosclerosis: Biochemical assessment of cellular and extracellular morphologic structures in situ. *Cardiovascular Pathology*, *10*(2), 69–82.

Butler, H. J., Ashton, L., Bird, B., Cinque, G., Curtis, K., Dorney, J., Fullwood, N.J., Gardner, B., Martin-Hirsch, P.L., Walsh, M.J., McAinsh, M. R., Stone, N., Martin, F. L. (2016). Using Raman spectroscopy to characterize biological materials. *Nature Protocols*, *11*(4), 664–687.

Byrne, H., Knief, P., Keating, M., & Bonnier, F. (2016). Spectral Pre and Post Processing for Infrared and Raman Spectroscopy of Biological Tissues and Cells. *Chemical Society Reviews, 45*, 1865–1878.

Caine, S., Heraud, P., Tobin, M. J., McNaughton, D., & Bernard, C. C. A. (2012).The application of Fourier transform infrared microspectroscopy for the study of diseased central nervous system tissue. *NeuroImage*, *59*(4), 3624–3640.

Caolo, V., Schulten, H. M., Zhuang, Z. W., Murakami, M., Wagenaar, A., Verbruggen, S., Molin, D.G.M., Post, M. J. (2011). Soluble Jagged-1 Inhibits Neointima Formation by Attenuating Notch-Herp2 Signaling. *Arteriosclerosis, Thrombosis, and Vascular Biology*, *31*(5), 1059–1065

Carlo, D. Di, Wu, L. Y., & Lee, L. P. (2006). Dynamic single cell culture array. *Lab on a Chip*, *6*(11), 1445.

Chan, J. W., Taylor, D. S., Lane, S. M., Zwerdling, T., Tuscano, J., & Huser, T. (2008). Nondestructive Identification of Individual Leukemia Cells by Laser Trapping Raman Spectroscopy. *Analytical Chemistry, 80*(6), 2180-287.

Chan, J. W., Lieu, D. K., Huser, T., & Li, R. A. (2009). Label-Free Separation of Human Embryonic Stem Cells and Their Cardiac Derivatives Using Raman Spectroscopy. *Analytical Chemistry*, *81*(4), 1324–1331.

Chan, J. M., Rhee, J.-W., Drum, C. L., Bronson, R. T., Golomb, G., Langer, R., & Farokhzad, O. C. (2011). In vivo prevention of arterial restenosis with paclitaxel-encapsulated targeted lipid-polymeric nanoparticles. *Proceedings of the National Academy of Sciences of the United States of America*, *108*(48), 19347–52.

Chappell, J., Harman, J. L., Narasimhan, V. M., Yu, H., Foote, K., Simons, B. D., Bennett, M.R., Jorgensen, H. F. (2016). Extensive Proliferation of a Subset of Differentiated, Yet Plastic, Medial Vascular Smooth Muscle Cells Contribute to Neointimal Formation in Mouse Injury and Atherosclerosis Models. *Circulation Research,* 116.

Cheheltani, R., McGoverin, C. M., Rao, J., Vorp, D. A., Kiani, M. F., & Pleshko, N. (2014). Fourier transform infrared spectroscopy to quantify collagen and elastin in an in vitro model of extracellular matrix degradation in aorta. *The Analyst*, *139*(12), 3039–47.

Chen, K., Qin, Y., Zheng, F., Sun, M., & Shi, D. (2006). Diagnosis of colorectal cancer using Raman spectroscopy of laser-trapped single living epithelial cells. *Optics Letters*, *31*(13), 2015.

Chen, S., Crawford, M., Day, R. M., Briones, V. R., Leader, J. E., Jose, P. A., & Lechleider, R. J. (2006b). RhoA Modulates Smad Signaling during Transforming Growth Factor-β-induced Smooth Muscle Differentiation. *Journal of Biological Chemistry,* 281(3), 1765–1770.

Chen, P.-Y., Qin, L., Baeyens, N., Li, G., Afolabi, T., Budatha, M., Tellides, G., Schwartz, M.A., Simons, M. (2015). Endothelial-to-mesenchymal transition drives atherosclerosis progression. *The Journal of Clinical Investigation*, *125*(12), 4514–28.

CHENG, C., XIONG, W., & TIAN, Y. (2009). Classification of Rat FTIR Colon Cancer Data Using Wavelets and BPNN. *Chinese Journal of Chemistry*, *27*(5), 911–914.

Cheng, J.-X., & Xie, X. S. (2016). Coherent Raman Scattering Microscopy. *CRC Press.*

Cherepanova, O. A., Gomez, D., Shankman, L. S., Swiatlowska, P., Williams, J., Sarmento, O. F., Alencar, G., Hess, D., Bevard, M., Greene, E., Murgai, M., Turner, S., Geng, Y-J., Bekiranov, S., Connelly, J., Tomilin, A., Owens, G. K. (2016). Activation of the pluripotency factor OCT4 in smooth muscle cells is atheroprotective. *Nature Medicine*, *22*(6), 657–665.

Cho, J., Rameshwar, P., & Sadoshima, J. (2009). Distinct Roles of Glycogen Synthase Kinase (GSK)-3α and GSK-3β in Mediating Cardiomyocyte Differentiation in Murine Bone Marrow-derived Mesenchymal Stem Cells. *Journal of Biological Chemistry*, *284*(52), 36647–36658.

Chonanant, C., Jearanaikoon, N., Leelayuwat, C., Limpaiboon, T., Tobin, M. J., Jearanaikoon, P., & Heraud, P. (2011). Characterisation of chondrogenic differentiation of human mesenchymal stem cells using synchrotron FTIR microspectroscopy. *The Analyst*, *136*(12), 2542.

Chorny, M., Fishbein, I., Yellen, B. B., Alferiev, I. S., Bakay, M., Ganta, S., Adamo, R., Amiji, M., Friedman, G., Levy, R. J. (2010). Targeting stents with local delivery of paclitaxel-loaded magnetic nanoparticles using uniform fields. *Proceedings of the National Academy of Sciences of the United States of America*, *107*(18), 8346–51.

Cohen-Sela, E., Rosenzweig, O., Gao, J., Epstein, H., Gati, I., Reich, R., Danenberg, H.,Golomb, G. (2006). Alendronate-loaded nanoparticles deplete monocytes and attenuate restenosis. *Journal of Controlled Release : Official Journal of the Controlled Release Society*, *113*(1), 23–30.

Colley, C. S., Kazarian, S. G., Weinberg, P. D., & Lever, M. J. (2004). Spectroscopic imaging of arteries and atherosclerotic plaques. *Biopolymers*, *74*(4), 328–335.

Colombo, A., Guha, S., Mackle, J. N., Cahill, P. A., Lally, C. (2013). Cyclic strain amplitude dictates the growth response of vascular smooth muscle cells in vitro: role in in-stent restenosis and inhibition with a sirolimus drug-eluting stent. *Biomechanical Model Mechanobiology*, *12*, 671–683.

Coman, C., Leopold, L.F. (2017). Raman Mapping: Emerging Applications. *Raman Spectroscopy & Applications.* Chapter 3. Dr. Chan Maaz (Ed.).

Cooley, B. C., Nevado, J., Mellad, J., Yang, D., Hilaire, C. S., Negro, A., Fang, F., Chen, G., San, H., Waltz, A., Schwartzbeck, R., Taylor, B.,Lanzer, J., Wragg, A., Elagha, A, Beltran, L., Berry, C., Feil, R., Virmani, R., Ladich, E., Kovacic, J., Boehm, M. (2014). TGF-β signaling mediates endothelial-to-mesenchymal transition (EndMT)

during vein graft remodeling. *Science Translational Medicine*, *6*(227), 227-34.

Costabile, V. (2017). Epithelial to mesenchymal transition (EMT) and cell plasticity in human colorectoral cancer. *Archivioeddelle tesi di dottorato.*

Crow, P., Stone, N., Kendall, C. A., Uff, J. S., Farmer, J. A. M., Barr, H., & Wright, M. P. J. (2003). The use of Raman spectroscopy to identify and grade prostatic adenocarcinoma in vitro. *British Journal of Cancer*, *89*(1), 106–108.

Crow, P., Molckovsky, A., Stone, N., Uff, J., Wilson, B., & WongKeeSong, L.-M. (2005). Assessment of fiberoptic near-infrared raman spectroscopy for diagnosis of bladder and prostate cancer. *Urology*, *65*(6), 1126–1130.

Danenberg, H. D., Fishbein, I., Epstein, H., Waltenberger, J., Moerman, E., Mönkkönen, J., Gao, J., Gathi, I., Reichi, R., Golomb, G. (2003). Systemic depletion of macrophages by liposomal bisphosphonates reduces neointimal formation following balloon-injury in the rat carotid artery. *Journal of Cardiovascular Pharmacology*, *42*(5), 671–9.

Danenberg, H. D., Fishbein, I., Gao, J., Mönkkönen, J., Reich, R., Gati, I., Moerman, E., Golomb, G. (2002). Macrophage depletion by clodronate-containing liposomes reduces neointimal formation after balloon injury in rats and rabbits. *Circulation*, *106*(5), 599–605.

Dangas, G. (2002). Restenosis: Repeat Narrowing of a Coronary Artery: Prevention and Treatment. *Circulation*, *105*(22), 2586–2587.

Dastjerdi, F. V., Zeynali, B., Tafreshi, A. P., Shahraz, A., Chavoshi, M. S., Najafabadi, I. K., Vardanjani, M., Astashi, A., Soleimani, M. (2012). Inhibition of GSK-3β enhances neural differentiation in unrestricted somatic stem cells. *Cell Biology International*, *36*(11), 967–972.

Day JCC, Stone N. (2013) A Subcutaneous Raman Needle Probe. *Applied Spectroscopy.* 67:349–354.

den Dekker, M. A. M., Zwiers, M., van den Heuvel, E. R., de Vos, L. C., Smit, A. J., Zeebregts, C. J., Oudkerk, M., Vliegenthart, R., Lefrandt, J., Mulder, D. J. (2013). Skin autofluorescence, a non-invasive marker for AGE accumulation, is associated with the degree of atherosclerosis. *PloS One*, *8*(12), e83084.

Doble, B. W., & Woodgett, J. R. (2003). GSK-3: tricks of the trade for a multi-tasking kinase. *Journal of Cell Science*, *116*(Pt 7), 1175–86.

Dodge, J. T., Brown, B. G., Bolson, E. L., & Dodge, H. T. (1992). Lumen diameter of normal human coronary arteries. Influence of age, sex, anatomic variation, and left ventricular hypertrophy or dilation. *Circulation*, *86*(1), 232–46.

Doi, H., Iso, T., Sato, H., Yamazaki, M., Matsui, H., Tanaka, T., Manabe, I., Arai, M., Nagai, R., Kurabayashi, M. (2006). Jagged1-selective Notch Signaling Induces Smooth Muscle Differentiation via a RBP-J -

dependent Pathway. *Journal of Biological Chemistry*, *281*(39), 28555–28564.

Domenga, V., Fardoux, P., Lacombe, P., Monet, M., Maciazek, J., Krebs, L. T., Klonjkowski, B., Berrou, E., Mericskay, M., Li, Z., Tournier-Lasserve, E., Gridley, T., Joutel, A. (2004). Notch-3 is required for arterial identity and maturation of vascular smooth muscle cells. *Genes & Development, 18*(22), 2730–2735.

Downes, A., Mouras, R., Bagnaninchi, P., & Elfick, A. (2011). Raman spectroscopy and CARS microscopy of stem cells and their derivatives. *Journal of Raman Spectroscopy : JRS*, *42*(10), 1864–1870.

Draga, R. O. P., Grimbergen, M. C. M., Vijverberg, P. L. M., Swol, C. F. P. van, Jonges, T. G. N., Kummer, J. A., & Ruud Bosch, J. L. H. (2010). In Vivo Bladder Cancer Diagnosis by High-Volume Raman Spectroscopy. *Analytical Chemistry*, *82*(14), 5993–5999.

Efeoglu, E., Casey, A., & Byrne, H. (2016). In Vitro Monitoring of Time and Dose Dependent Cytotoxicity of Aminated Nanoparticles using Raman Spectroscopy. *Analyst, 141,* 5417–5431.

El-Said, W. A., Kim, S. U., & Choi, J.-W. (2015). Monitoring in vitro neural stem cell differentiation based on surface-enhanced Raman spectroscopy using a gold nanostar array. *Journal of Material Chemistry*, *3*(16), 3848–3859.

El-Tawil, S. G., Adnan, R., Muhamed, Z. ., & Othman, N. H. (2008). Comparative study between Pap smear cytology and FTIR spectroscopy: a new tool for screening for cervical cancer. *Pathology*, *40*(6), 600–603.

ELLIOTT, A., & AMBROSE, E. J. (1950). Structure of Synthetic Polypeptides. *Nature*, *165*(4206), 921–922.

Espinosa, L., Inglés-Esteve, J., Aguilera, C., & Bigas, A. (2003). Phosphorylation by glycogen synthase kinase-3 beta down-regulates Notch activity, a link for Notch and Wnt pathways. *The Journal of Biological Chemistry*, *278*(34), 32227–35.

Espulgar, W., Aoki, W., Ikeuchi, T., Mita, D., Saito, M., Lee, J.-K., & Tamiya, E. (2015). Centrifugal microfluidic platform for single-cell level cardiomyocyte-based drug profiling and screening. *Lab Chip*, *15*(17), 3572–3580.

Evrard, S. M., Lecce, L., Michelis, K. C., Nomura-Kitabayashi, A., Pandey, G., Purushothaman, K.-R., D'Escamard, V., Li, J., Hadri, L., Fujitani, K., Moreno, P., Benard, L., Rimmele, P., Cohain, A., Mecham, B., Randolph, G., Nabel, E., Hajjar, R., Fuster, V., Boehm, M., Kovacic, J. C. (2016). Endothelial to mesenchymal transition is common in atherosclerotic lesions and is associated with plaque instability. *Nature Communications*, *7*, 11853.

Fang, J.-H., Lai, Y.-H., Chiu, T.-L., Chen, Y.-Y., Hu, S.-H., & Chen, S.-Y. (2014). Magnetic Core-Shell Nanocapsules with Dual-Targeting

Capabilities and Co-Delivery of Multiple Drugs to Treat Brain Gliomas. *Advanced Healthcare Materials,* 3(8), 1250–1260.

Falk, R., Falk, A., Dyson, M. R., Melidoni, A. N., Parthiban, K., Young, J. L., Roake, W., McCafferty, J. (2012). Generation of anti-Notch antibodies and their application in blocking Notch signalling in neural stem cells. *Methods (San Diego, California)*, *58*(1), 69–78.

Félix Lanao, R. P., Jonker, A. M., Wolke, J. G. C., Jansen, J. A., van Hest, J. C. M., & Leeuwenburgh, S. C. G. (2013). Physicochemical properties and applications of poly(lactic-co-glycolic acid) for use in bone regeneration. *Tissue Engineering. Part B, Reviews*, *19*(4), 380–90.

Filip, M., Iordache, S., Saftoiu, A., Ciureda, T. (2011) Autofluorescence imaging and magnification endoscopy. *World Journal of Gastroenterology. 17*(1): 9-14.

Fishbein, G. A., & Fishbein, M. C. (2009). Arteriosclerosis: rethinking the current classification. *Archives of Pathology & Laboratory Medicine*, *133*(8), 1309–16.

Fitzmaurice, M., Bordagaray, J. O., Engelmann, G. L., Richards-Kortum, R., Kolubayev, T., Feld, M. S., Ratliff, N.B., Kramer, J. R. (1989). Argon ion laser-excited autofluorescence in normal and atherosclerotic aorta and coronary arteries: morphologic studies. *American Heart Journal*, *118*(5 Pt 1), 1028–38.

Fleckenstein, M., Schmitz-Valckenberg, S., & Holz, F. (2010). Fundus Autofluorescence Imaging in Clinical Use. *Review of Opthamology.*

Foltz, D. R., Santiago, M. C., Berechid, B. E., & Nye, J. S. (2002). Glycogen synthase kinase-3beta modulates notch signaling and stability. *Current Biology : CB*, *12*(12), 1006–11.

Force, T., & Woodgett, J. R. (2009). Unique and overlapping functions of GSK-3 isoforms in cell differentiation and proliferation and cardiovascular development. *The Journal of Biological Chemistry*, *284*(15), 9643–7.

Friend, J., & Yeo, L. (2010). Fabrication of microfluidic devices using polydimethylsiloxane. *Biomicrofluidics, 4*(2).

Gajjar, K., Heppenstall, L. D., Pang, W., Ashton, K. M., Trevisan, J., Patel, I. I., Llabjani, V., Stringfellow, H., Martin-Hirsch, P., Dawson, T., Martin, F. L. (2012). Diagnostic segregation of human brain tumours using Fourier-transform infrared and/or Raman spectroscopy coupled with discriminant analysis. *Analytical Methods : Advancing Methods and Applications*, *5*, 89–102.

Gershinowitz, H. (1979). The first infrared spectrometer. *The Journal of Physical Chemistry*, *83*(11), 1363–1365.

Ghita, A., Pascut, F. C., Sottile, V., Denning, C., & Notingher, I. (2015). Applications of Raman micro-spectroscopy to stem cell technology: label-free molecular discrimination and monitoring cell differentiation. *EPJ Techniques and Instrumentation*, *2*(1), 6.

Go, A. S., Mozaffarian, D., Roger, V. L., Benjamin, E. J., Berry, J. D., Borden, W. B., Bravata, D., Dai, S., Ford, E., Fox, C., Franco, S., Fullerton, H., Gillespie, C., Hailpern, S., Heit, J., Howard, V.J., Huffman, M., Kissela, B.M., Kittner, S., Lackland, D.T., Lichtman, J., Lisabeth, L., Magid, D., Marcus, G., Marelli, A., Matchar, D., McGuire, D., Mohler, E., Moy, C., Mussolino, M., Nichol, G., Paynter, N., Schreiner, P., Sorlie, P., Turan, T., Virani, S., Stein, J., Wong, N., Woo, D., Turner, M. B. (2013). Heart disease and stroke statistics--2013 update: a report from the American Heart Association. *Circulation*, *127*(1), e6–e245.

Godin, J., Chen, C.-H., Cho, S. H., Qiao, W., Tsai, F., & Lo, Y.-H. (2008). Microfluidics and photonics for Bio-System-on-a-Chip: a review of advancements in technology towards a microfluidic flow cytometry chip. *Journal of Biophotonics*, *1*(5), 355–76.

Gok, S., Aydin, O. Z., Sural, Y. S., Zorlu, F., Bayol, U., & Severcan, F. (2016). Bladder cancer diagnosis from bladder wash by Fourier transform infrared spectroscopy as a novel test for tumor recurrence. *Journal of Biophotonics*, *9*(9), 967–975. Gomez, D., & Owens, G. K. (2015). Abstract 60: Histone Modification H3k4me2 Controls Vascular Smooth Muscle Cell Lineage Memory during Vascular Injury. *Arteriosclerosis, Thrombosis, and Vascular Biology*, *35*(Suppl 1).

González-Solís, J. L., Martínez-Espinosa, J. C., Salgado-Román, J. M., & Palomares-Anda, P. (2014). Monitoring of chemotherapy leukemia treatment using Raman spectroscopy and principal component analysis. *Lasers in Medical Science*, *29*(3), 1241–1249.

Gridley, T. (2010). Notch signaling in the vasculature. *Current Topics in Developmental Biology*, *92*, 277–309.

Gittenberger-de Groot, A. C., Vrancken Peeters, M. P., Mentink, M. M., Gourdie, R. G., & Poelmann, R. E. (1998). Epicardium-derived cells contribute a novel population to the myocardial wall and the atrioventricular cushions. *Circulation Research*, *82*(10), 1043–52.

Greiner, M., Carter, P., Korn, B., & Zink, D. (2004). New approach to complete automation in sizing and quantitation of DNA and proteins by the Automated Lab-on-a-Chip Platform from Agilent Technologies. *Nature Methods*, *1*(1), 87–89.

Guha, S., Cullen, J. P., Morrow, D., Colombo, A., Lally, C., Walls, D., Redmond, E., Cahill, P. A. (2011). Glycogen synthase kinase 3 beta positively regulates Notch signaling in vascular smooth muscle cells: role in cell proliferation and survival. *Basic Research in Cardiology*, *106*(5), 773–85.

Guo, X., & Chen, S.-Y. (2012). Transforming growth factor-β and smooth muscle differentiation. *World Journal of Biological Chemistry*, *3*(3), 41–52.

Hachani, R., Dab, H., Sakly, M., Sercombe, R., Callebert, J., Vicaut, E., & Kacem, K. (2011). The profile of the extracellular matrix changes in

the aorta after sympathectomy in the hypercholesterolemic rats. *Autonomic Neuroscience*, *164*(1–2), 67–73.

Haka, A. S., Shafer-Peltier, K. E., Fitzmaurice, M., Crowe, J., Dasari, R. R., & Feld, M. S. (2005). Diagnosing breast cancer by using Raman spectroscopy. *Proceedings of the National Academy of Sciences of the United States of America*, *102*(35), 12371–6.

Halkin, A., & Stone, G. W. (2004). Polymer-based paclitaxel-eluting stents in percutaneous coronary intervention: a review of the TAXUS trials. *Journal of Interventional Cardiology*, *17*(5), 271–82.

Hall, J., C, John (2001). Upregulation of Glucose Metabolism During Intimal Lesion Formation Is Coupled to the Inhibition of Vascular Smooth Muscle Cell Apoptosis Role of GSK3b. *Diabetes.* 50, 1171-1179.

Hands, J. R., Dorling, K. M., Abel, P., Ashton, K. M., Brodbelt, A., Davis, C., Dawson, T., Jenkinson, M., Lea, R., Walker, C., Baker, M. J. (2014). Attenuated Total Reflection Fourier Transform Infrared (ATR-FTIR) spectral discrimination of brain tumour severity from serum samples. *Journal of Biophotonics*, *7*(3–4), 189–199.

Happillon, T., Untereiner, V., Beljebbar, A., Gobinet, C., Daliphard, S., Cornillet-Lefebvre, P., Quinquenel, A., Delmer, A., Troussard, X., Klossa, J.,m Manfait, M. (2015). Diagnosis approach of chronic lymphocytic leukemia on unstained blood smears using Raman microspectroscopy and supervised classification. *Analyst*, *140*. Heikal, A. A. (2010). Intracellular coenzymes as natural biomarkers for metabolic activities and mitochondrial anomalies. *Biomarkers in Medicine*, *4*(2), 241–63.

Herman, B. C., Kundi, R., Yamanouchi, D., Kent, K. C., Liu, B., & Pleshko, N. (2009). Molecular analysis of arterial remodeling: a novel application of infrared imaging. *International Society for Optics and Photonics. (p. 71821H).*

Herring, B., Hoggatt, A. M., Burlak, C., & Offermanns, S. (2014). Previously differentiated medial vascular smooth muscle cells contribute to neointima formation following vascular injury. *Vascular Cell*, *6*(1), 21.

High, F. A. (2007). Notch signaling in cardiac development. *Dissertations Available from ProQuest*.

High, F. A., Zhang, M., Proweller, A., Tu, L., Parmacek, M. S., Pear, W. S., & Epstein, J. A. (2007). An essential role for Notch in neural crest during cardiovascular development and smooth muscle differentiation. *The Journal of Clinical Investigation*, *117*(2), 353–63.

Höglund, P., & Brodin, P. (2010). Current perspectives of natural killer cell education by MHC class I molecules. *Nature Reviews Immunology*, *10*(10), 724–734.

Hollander, W. (1976). Role of hypertension in atherosclerosis and cardiovascular disease. *The American Journal of Cardiology*, *38*(6), 786–800.

Holman, H.-Y. N., Miles, R., Hao, Z., Wozei, E., Anderson, L. M., & Yang, H. (2009). Real-Time Chemical Imaging of Bacterial Activity in Biofilms Using Open-Channel Microfluidics and Synchrotron FTIR Spectromicroscopy. *Analytical Chemistry*, *81*(20), 8564–8570.

Hu, Y., Zhang, Z., Torsney, E., Afzal, A. R., Davison, F., Metzler, B., & Xu, Q. (2004). Abundant progenitor cells in the adventitia contribute to atherosclerosis of vein grafts in ApoE-deficient mice. *The Journal of Clinical Investigation*, *113*(9), 1258–65.

Hughes, C., Liew, M., Sachdeva, A., Bassan, P., Dumas, P., Hart, C. A., Brown, M., Clarke, N.W., Gardner, P. (2010). SR-FTIR spectroscopy of renal epithelial carcinoma side population cells displaying stem cell-like characteristics. *The Analyst*, *135*(12), 3133.

Hutsebaut, D., Vandenabeele, P., & Moens, L. (2005). Evaluation of an accurate calibration and spectral standardization procedure for Raman spectroscopy. *The Analyst*, *130*(8), 1204.

Insull, W. (2009). The pathology of atherosclerosis: plaque development and plaque responses to medical treatment. *The American Journal of Medicine*, *122*(1 Suppl), S3–S14.

Ioan Notingher, Bisson, I, Bishop, A.E., Randle, W.L., Polak, J.J.M and, & Hench, L. L. (2004). In Situ Spectral Monitoring of mRNA Translation in Embryonic Stem Cells during Differentiation in Vitro. *Analytical Chemistry, 76*(11), 3185-3193.

Jähme, H., Di Florio, G., Conti Nibali, V., Esen, C., Ostendorf, A., Grafen, M., Henke, E., Soetebier, J., Brenner, C., Havenith, M., Hofmann, M. R. (2016). Recognition of pharmaceuticals with compact mini-Raman-spectrometer and automized pattern recognition algorithms. *International Society for Optics and Photonics.* 98992.

Jahnke, H.-G., Steel, D., Fleischer, S., Seidel, D., Kurz, R., Vinz, S., Dahlenborg, K., Sartipy, P., Robitzki, A. A. (2013). A Novel 3D Label-Free Monitoring System of hES-Derived Cardiomyocyte Clusters: A Step Forward to In Vitro Cardiotoxicity Testing. *PLoS ONE*, *8*(7), e68971.

Jia, X., Wang, W., Han, Q., Wang, Z., Jia, Y., & Hu, Z. (2016). Micromixer Based Preparation of Functionalized Liposomes and Targeting Drug Delivery. *ACS Medicinal Chemistry Letters, 7*(4), 429–434.

Jiang, L., Li, X., Liu, L., & Zhang, Q. (2013). Thiolated chitosan-modified PLA-PCL-TPGS nanoparticles for oral chemotherapy of lung cancer. *Nanoscale Research Letters, 8*(1), 66.

Jarvis, R.M & Goodacre*, R. (2003). Discrimination of Bacteria Using Surface-Enhanced Raman Spectroscopy. *Analytical Chemistry. 76*(1) 40-47.

Jeremias, A., & Kirtane, A. (2008). Balancing efficacy and safety of drug-eluting stents in patients undergoing percutaneous coronary intervention. *Annals of Internal Medicine*, *148*(3), 234–8.

Jermyn, M., Desroches, J., Mercier, J., St-Arnaud, K., Guiot, M.-C., Leblond, F., & Petrecca, K. (2016). Raman spectroscopy detects distant invasive brain cancer cells centimeters beyond MRI capability in humans. *Biomedical Optics Express*, *7*(12), 5129.

Jermyn, M., Mok, K., Mercier, J., Desroches, J., Pichette, J., Saint-Arnaud, K., Bernstein, L., Guiot, M., Petrecca, K., Leblond, F. (2015). Intraoperative brain cancer detection with Raman spectroscopy in humans. *Science Translational Medicine*, *7*(274).

Jess, P. R. T., Smith, D. D. W., Mazilu, M., Dholakia, K., Riches, A. C., & Herrington, C. S. (2007). Early detection of cervical neoplasia by Raman spectroscopy. *International Journal of Cancer*, *121*(12), 2723–2728.

Jope, R. S. (2003). Lithium and GSK-3: one inhibitor, two inhibitory actions, multiple outcomes. *Trends in Pharmacological Sciences*, *24*(9), 441–443.

Jusman, Y., Mat Isa, N. A., Ng, S.-C., Hasikin, K., & Abu Osman, N. A. (2016). Automated cervical precancerous cells screening system based on Fourier transform infrared spectroscopy features. *Journal of Biomedical Optics*, *21*(7), 75005.

Kallaway, C., Almond, M., Barr, H., Wood, J., Hutchings, J., Kendall, C., Stone, N. Advances in the clinical application of Raman spectroscopy for cancer diagnostics. (2013). *Photodiagnosis and Photodynamic Therapy*, *10*(3), 207–219.

Kanzaki, T., Tamura, K., Takahashi, K., Saito, Y., Akikusa, B., Oohashi, H., Kasayuki, N., Ueda, M., Morisaki, N. (1995). In vivo effect of TGF-beta 1. Enhanced intimal thickening by administration of TGF- beta 1 in rabbit arteries injured with a balloon catheter. *Arteriosclerosis, Thrombosis, and Vascular Biology*, *15*(11), 1951–7.

Karrer, H. E. (1961). An electron microscope study of the aorta in young and in aging mice. *Journal of Ultrastructure Research*, *5*(1), 1–27.

Kaznowska, E., Depciuch, J., Szmuc, K., & Cebulski, J. (2017). Use of FTIR spectroscopy and PCA-LDC analysis to identify cancerous lesions within the human colon. *Journal of Pharmaceutical and Biomedical Analysis*, *134*, 259–268.

Kennedy, E., Mooney, C., Hakimjavadi R., Cahill, PAC. Adult vascular smooth muscle cells in culture express neural stem cell markers typical of resident vascular stem cells. (2014) *Vascular Cell,* 6,6.

Kennedy E., Hakimjavadi, R., Green, C., Mooney, C., Fitzpatrick, E., Collins, L., Loscher, C., Guha, S., Morrow, D., Redmond E., Cahill, P. Embryonic rat vascular smooth muscle cells revisited - a model for neontimal SMC or differentiated vascular stem cells? (2014) *Vascular Cell, 6.6*

Kerr, L. T., Lynn, E. M., Cullen, I. M., Daly, P. J., Shah, N., O 'dea, S., Malkin, A., Hennelly, B. M. (2016). Methodologies for bladder cancer detection with Raman based urine cytology. *Analytical Methods.* 8, 4991-5000

Kibos, A., Campeanu, A., & Tintoiu, I. (2007). Pathophysiology of coronary artery in-stent restenosis. *Acute Cardiac Care*, *9*(2),

Kidd, S., & Lieber, T. (2002). Furin cleavage is not a requirement for Drosophila Notch function. *Mechanisms of Development*, 115(1–2), 41–51.

Kim, H.-S., Skurk, C., Thomas, S. R., Bialik, A., Suhara, T., Kureishi, Y., Birnbaum, M., Keaney, J., Walsh, K. (2002). Regulation of angiogenesis by glycogen synthase kinase-3beta. *The Journal of Biological Chemistry*, *277*(44), 41888–96.

Kim, P. G., Albacker, C. E., Lu, Y., Jang, I., Lim, Y., Heffner, G. C., Arora, N., Bowman, T., Lin, M., Lensch, M., De Los Angeles, A., Zon, L., Loewer, S., Daley, G. Q. (2013). Signaling axis involving Hedgehog, Notch, and Scl promotes the embryonic endothelial-to-hematopoietic transition. *Proceedings of the National Academy of Sciences of the United States of America*, *110*(2), E141-50.

Kim, Y.-H., Chang, B., Choi, J.-H., Park, H.-K., & Choi, S. (2016). Biochemical fingerprints of human papillomavirus infection and cervical dysplasia using cervical fluids: Spectral pattern investigation. *Microscopy Research and Technique*, *79*(10), 966–972.

Kinnunen, M., & Karmenyan, A. (2015). Overview of single-cell elastic light scattering techniques. *Journal of Biomedical Optics*, *20*(5), 51040.

Kirby, L. A., Schott, J. T., Noble, B. L., Mendez, D. C., Caseley, P. S., Peterson, S. C., Routledge, T., Patel, N. V. (2012). Glycogen Synthase Kinase 3 (GSK3) Inhibitor, SB-216763, Promotes Pluripotency in Mouse Embryonic Stem Cells. *PLoS ONE*, *7*(6), e39329.

Kiselev, R., Schie, I. W., Aškrabić, S., Krafft, C., & Popp, J. (2016). Design and first applications of a flexible Raman micro-spectroscopic system for biological imaging. *Biomedical Spectroscopy and Imaging*, *5*(2), 115–127.

Kitajima, K., Nakajima, M., Kanokoda, M., Kyba, M., Dandapat, A., Tolar, J., Saito, M., Toyoda, M., Umezawa, A., Hara, T. (2016). GSK3β inhibition activates the CDX/HOX pathway and promotes hemogenic endothelial progenitor differentiation from human pluripotent stem cells. *Experimental Hematology*, *44*(1), 68-74–10.

Klein, D. (2016). Vascular Wall-Resident Multipotent Stem Cells of Mesenchymal Nature within the Process of Vascular Remodeling: Cellular Basis, Clinical Relevance, and Implications for Stem Cell Therapy. *Stem Cells International*, 1905846.

Klein, D., Weisshardt, P., Kleff, V., Jastrow, H., Jakob, H. G., & Ergün, S. (2011). Vascular wall-resident CD44+ multipotent stem cells give rise to pericytes and smooth muscle cells and contribute to new vessel maturation. *PloS One*, *6*(5), e20540.

Kochan, K., Chrabaszcz, K., Szczur, B., Maslak, E., Dybas, J., & Marzec, K. M. (2016). IR and Raman imaging of murine brains from control and ApoE/LDLR $^{-/-}$ mice with advanced atherosclerosis. *The Analyst*, *141*(18), 5329–5338.

Kohler, N., Sun, C., Fichtenholtz, A., Gunn, J., Fang, C., & Zhang, M. (2006). Methotrexate-Immobilized Poly(ethylene glycol) Magnetic Nanoparticles for MR Imaging and Drug Delivery. *Small, 2*(6), 785–792.

Koljenović, S., Choo-Smith, L.-P., Bakker Schut, T. C., Kros, J. M., van den Berge, H. J., & Puppels, G. J. (2002). Discriminating Vital Tumor from Necrotic Tissue in Human Glioblastoma Tissue Samples by Raman Spectroscopy. *Laboratory Investigation*, *82*(10), 1265–1277.

Komiya, Y., & Habas, R. (2008). Wnt signal transduction pathways. *Organogenesis*, *4*(2), 68–75.

Korur, S., Huber, R. M., Sivasankaran, B., Petrich, M., Morin, P., Hemmings, B. A., Merlo, A., Lino, M. M. (2009). GSK3β Regulates Differentiation and Growth Arrest in Glioblastoma. *PLoS ONE*, *4*(10), e7443.

Kostogrys, R. B., Franczyk-Zarow, M., Gasior-Glogowska, M., Kus, E., Jasztal, A., Wrobel, T. P., Baranska, M., Czyzynska-Cichon, I., Drahun, A., Manterys, A., Chlopicki, S. (2017). Anti-atherosclerotic effects of pravastatin in brachiocephalic artery in comparison with en face aorta and aortic roots in ApoE/LDLR–/– mice. *Pharmacological Reports*, *69*(1), 112–118.

Krafft, C., Salzer, R., & Siesler, H. W. (2009). Disease Recognition by Infrared and Raman Spectroscopy. *Journal of Biophotonics.* 2(1-2), 13-28.

Kramann, R., Schneider, R. K., DiRocco, D. P., Machado, F., Fleig, S., Bondzie, P. A., Henderson, J., Ebert, B., Humphreys, B. D. (2015). Perivascular Gli1+ progenitors are key contributors to injury-induced organ fibrosis. *Cell Stem Cell, 16(1), 51–66.*

Kretzschmar, K., & Watt, F. M. (2012). Lineage Tracing. *Cell*, *148*(1–2), 33–45.

KREUTER, J. (2007). Nanoparticles—a historical perspective. *International Journal of Pharmaceutics*, *331*(1), 1–10.

Krimm, S. (1962). Infrared spectra and chain conformation of proteins. *Journal of Molecular Biology*, *4*(6), 528–540.

Krishna, C. M., Sockalingum, G. D., Vadhiraja, B. M., Maheedhar, K., Rao, A. C. K., Rao, L., Venteo, L., Pluot, M., Fernandes, D. J., Vidyasagar, M.S., Kartha, V.B., Manfait, M. (2006). Vibrational

Spectroscopy Studies of Formalin-Fixed Cervix Tissues. *Biopolymers.* 85(3), 214-221.

Krishnan, P., Purushothaman, K.R., Purushothaman, M., Baber, U., Tarricone, A., Vascquez, M., Wiley, J., Kini, A., Sharma, S.K., O'Connor, W.N., Moreno, P.R., Relation of Internal Elastic Lamellar Layer Disruption to Neointimal Cellular Proliferation and Type III Collagen Deposition in Human Peripheral Artery Restenosis. (2016). *The American Journal of Cardiology*, *117*(7), 1173–1179.

Kuo, J.-N., & Jiang, L.-R. (2014). Design optimization of micromixer with square-wave microchannel on compact disk microfluidic platform. *Microsystem Technologies*, *20*(1), 91–99.

Kurpinski, K., Lam, H., Chu, J., Wang, A., Kim, A., Tsay, E., Agrawal, S., Schaffer, D.V., Li, S. (2010). Transforming growth factor-beta and notch signaling mediate stem cell differentiation into smooth muscle cells. *Stem Cells (Dayton, Ohio)*, *28*(4), 734–42.

Kusters, J. G., van Leeuwen, W. B., Maquelin, K., Blok, H. E. M., Willemse, H. F. M., de Graaf-Miltenburg, L. A. M., Fluit, A. C., Troelstra, A. (2016). Raman spectroscopy-based identification of nosocomial outbreaks of the clonal bacterium Escherichia coli. *European Journal of Clinical Microbiology & Infectious Diseases*, *35*(1), 83–87.

Lattermann, A., Matthäus, C., Bergner, N., Beleites, C., Romeike, B. F., Krafft, C., Brehm, B., Popp, J. (2013). Characterization of atherosclerotic plaque depositions by Raman and FTIR imaging. *Journal of Biophotonics*, *6*(1), 110–121.

Lawson, N. D., Vogel, A. M., & Weinstein, B. M. (2002). sonic hedgehog and vascular endothelial growth factor act upstream of the Notch pathway during arterial endothelial differentiation. *Developmental Cell, 3*(1), 127–36.

Lee, H.-C., Lin, Y.-Z., Lai, Y.-T., Huang, W.-J., Hu, J.-R., Tsai, J.-N., & Tsai, H.-J. (2014). Glycogen synthase kinase 3 beta in somites plays a role during the angiogenesis of zebrafish embryos. *FEBS Journal*, *281*(19), 4367–4383.

Li, C., Li, L., & Keate, A. C. (2012). Targeting Cancer Gene Therapy with Magnetic Nanoparticles. *Oncotarget*, *3*(4), 365–370. Li, J., Jiang, C., Lang, X., Kong, M., Cheng, X., Liu, Y., Feng, C., Chen, X. (2016). Multilayer sodium alginate beads with porous core containing chitosan based nanoparticles for oral delivery of anticancer drug. *International Journal of Biological Macromolecules,* 85, 1–8.

Li, Q.-B., Xu, Z., Zhang, N.-W., Zhang, L., Wang, F., Yang, L.-M., Wang, J-S., Zhou, S., Zhang, Y-F., Zhou, X-S., Shi, J-S., Wu, J.-G. (2005). In vivo and in situ detection of colorectal cancer using Fourier transform infrared spectroscopy. *World Journal of Gastroenterology*, *11*(3), 327–30.

Li, S., Zhang, Y., Xu, J., Li, L., Zeng, Q., Lin, L., Guo, Z., Liu, Z., Xiong, H., Liu, S. (2014). Noninvasive prostate cancer screening based on

serum surface-enhanced Raman spectroscopy and support vector machine. *Applied Physics Letters*, *105*(9), 91104.

Li, X., Yang, T., Li, S., Wang, D., Song, Y., Zhang, S.(2016). Raman spectroscopy combined with principal component analysis and k nearest neighbour analysis for non-invasive detection of colon cancer. *Laser Physics*, *26*(3), 35702.

Li, Y., Wen, Y., Wang, Z., Wei, Y., Wani, P., Green, M., Swaminathan, G., Ramamurthi, A., Pere, R.R., Chen, B. (2016). Smooth Muscle Progenitor Cells Derived From Human Pluripotent Stem Cells Induce Histologic Changes in Injured Urethral Sphincter. *STEM CELLS Translational Medicine*, *5*(12), 1719–1729.

Li, Y., Igne, B., Drennen, J. K., & Anderson, C. A. (2016). Method development and validation for pharmaceutical tablets analysis using transmission Raman spectroscopy. *International Journal of Pharmaceutics*, *498*(1), 318–325.

Li, Y., Takeshita, K., Liu, P.-Y., Satoh, M., Oyama, N., Mukai, Y., Chin, M., Chin, M., Krebs, L., Kotlikoff, M., Radtke, F., Gridley, T., Liao, J. K. (2009). Smooth muscle Notch-1 mediates neointimal formation after vascular injury. *Circulation*, *119*(20), 2686–92.

Liao, J., Chen, X., Li, Y., Ge, Z., Duan, H., Zou, Y., & Ge, J. (2012). Transfer of Bone-Marrow-Derived Mesenchymal Stem Cells Influences Vascular Remodeling and Calcification after Balloon Injury in Hyperlipidemic Rats. *Journal of Biomedicine and Biotechnology*, *2012*, 1–7.

Liao, M., Zhou, J., Yang, P., Ali, Y., Wang, F., & Jiang, Z. (2017). Abstract 369: SMC-Specific Tgfbr1 Deficiency Inhibits Neointimal Hyperplasia In Injured Arteries. *Arteriosclerosis, Thrombosis, and Vascular Biology*, *36*(Suppl 1).

Libby, P., & Theroux, P. (2005). Pathophysiology of coronary artery disease. *Circulation*, *111*(25), 3481–8.

Lieber, C. A., Majumder, S. K., Ellis, D. L., Billheimer, D. D., & Mahadevan-Jansen, A. (2008). In vivo nonmelanoma skin cancer diagnosis using Raman microspectroscopy. *Lasers in Surgery and Medicine*, *40*(7), 461–467.

Lilly, L. S. (2012). Fundamentals of cardiovascular disease; molecular biology and genetics; evaluation of the plant. *Braunwald's Heart Disease: A Textbook of Cardiovascular Medicine*. Section 1, Elsevier Health Sciences.

Lindström, S., & Andersson-Svahn, H. (2011). Miniaturization of biological assays — Overview on microwell devices for single-cell analyses. *Biochimica et Biophysica Acta (BBA) - General Subjects*, *1810*(3), 308–316.

Ling, J., Weitman, S. D., Miller, M. A., Moore, R. V, & Bovik, A. C. (2002). Direct Raman imaging techniques for study of the subcellular distribution of a drug. *Applied Optics*, *41*(28), 6006–17.

Liu, Y., Sinha, S., & Owens, G. (2003). A Transforming Growth Factor-β Control Element Required for SM α-Actin Expression in Vivo Also Partially Mediates GKLF-dependent Transcriptional Repression. *Journal of Biological Chemistry*, *278*(48), 48004–48011.

Lopes, R. M., Silveira, L., Silva, M. A. R. S., Leite, K. R. M., Pasqualucci, C. A. G., & Pacheco, M. T. T. (2011). Diagnostic model based on Raman spectra of normal, hyperplasia and prostate adenocarcinoma tissues in vitro. *Journal of Spectroscopy*, *25*(2), 89–102.

Lui, H., Zhao, J., McLean, D., & Zeng, H. (2012). Real-time Raman Spectroscopy for In Vivo Skin Cancer Diagnosis. *Cancer Research*, *72*(10), 2491–2500.

Liu, Z.-J., Shirakawa, T., Li, Y., Soma, A., Oka, M., Dotto, G. P., Fairman, R., Velasquez, O., Herlyn, M. (2003). Regulation of Notch-1 and Dll4 by vascular endothelial growth factor in arterial endothelial cells: implications for modulating arteriogenesis and angiogenesis. *Molecular and Cellular Biology, 23*(1), 14–25.

Luo, Y.-L., Huang, R.-J., Xu, F., & Chen, Y.-S. (2014). pH-Sensitive biodegradable PMAA2-b-PLA-b-PMAA2 H-type multiblock copolymer micelles: synthesis, characterization, and drug release applications. *Journal of Materials Science,* 49(22), 7730–7741.

Louguet, S., Rousseau, B., Epherre, R., Guidolin, N., Goglio, G., Mornet, S.,Duguet,E.,Lecommandoux,S.Schatz, C.(2012). Thermoresponsive polymer brush-functionalized magnetic manganite nanoparticles for remotely triggered drug release. *Polymer Chemistry, 3*(6), 1408.

Lüscher, T. F., Steffel, J., Eberli, F. R., Joner, M., Nakazawa, G., Tanner, F. C., & Virmani, R. (2007). Drug-eluting stent and coronary thrombosis: biological mechanisms and clinical implications. *Circulation*, *115*(8), 1051–8.

Lyng, F. M., Faoláin, E. ., Conroy, J., Meade, A. D., Knief, P., Duffy, B., Hunter, M.B., Byrne, M.J., Kelehan, P., Byrne, H. J. (2007). Vibrational spectroscopy for cervical cancer pathology, from biochemical analysis to diagnostic tool. *Experimental and Molecular Pathology*, *82*(2), 121–129.

Ma, X., Hibbert, B., Dhaliwal, B., Seibert, T., Chen, Y.-X., Zhao, X., & O ’brien, E. R. (2010). Delayed re-endothelialization with rapamycin-coated stents is rescued by the addition of a glycogen synthase kinase-3b inhibitor. *Cardiovascular research.* 86(2), 338-345.

Majesky, M. W., Lindner, V., Twardzik, D. R., Schwartz, S. M., & Reidy, M. A. (1991). Production of transforming growth factor beta 1 during repair of arterial injury. *The Journal of Clinical Investigation*, *88*(3), 904–10.

Majesky, M. W. (2015). Adventitia and perivascular cells. *Arteriosclerosis, Thrombosis, and Vascular Biology*, *35*(8), e31-5.

Majesky, M. W., Dong, X. R., Hoglund, V., Mahoney, W. M., & Daum, G. (2011). The adventitia: a dynamic interface containing resident

progenitor cells. *Arteriosclerosis, Thrombosis, and Vascular Biology*, *31*(7), 1530–9.

Majid, S., Saini, S., & Dahiya, R. (2012). Wnt signaling pathways in urological cancers: past decades and still growing. *Molecular Cancer*, *11*(1), 7.

Managò, S., Valente, C., Mirabelli, P., Circolo, D., Basile, F., Corda, D., & De Luca, A. C. (2016). A reliable Raman-spectroscopy-based approach for diagnosis, classification and follow-up of B-cell acute lymphoblastic leukemia. *Scientific Reports*, *6*, 24821.

Mangaiyarkarasi, R., Chinnathambi, S., Karthikeyan, S., Aruna, P., & Ganesan, S.(2016). Paclitaxel conjugated Fe3O4@LaF3:Ce3+,Tb3+ nanoparticles as bifunctional targeting carriers for Cancer theranostics application. *Journal of Magnetism and Magnetic Materials, 399*(399), 207–215.

Manoharan, R., Wang, Y., & Feld, M. S. (1996). Histochemical analysis of biological tissues using Raman spectroscopy. *Spectrochimica Acta Part A: Molecular and Biomolecular Spectroscopy*, *52*, 215–249.

Maquelin, K., Kirschner, C., Choo-Smith, L.-P., van den Braak, N., Endtz, H. P., Naumann, D., & Puppels, G. (2002). Identification of medically relevant microorganisms by vibrational spectroscopy. *Journal of Microbiological Methods*, *51*(3), 255–271.

Mark, D., Haeberle, S., Roth, G., von Stetten, F., Zengerle, R., Garcia, E. W., Lebruska, L. L., Laurent, M., Shen, R., Barker, D., Doucet, D., Milewski, M., Yang, R., Siegmund, C., Haas, J., Zhou, L. X., Oliphant, A., Fan, J. B., Barnard, S., Chee, M. S., Alenquer, M. L. I., Jarvie, T. P., Jirage, K. B., Kim, J. B., Knight, J. R., Lanza, J. R., Leamon, J. H., Lefkowitz, S. M., Lei, M., Li, J., Lohman, K. L., Lu, H., Makhijani, V. B., Mcdade, K. E., McKenna, M. P., Myers, E. W., Nickerson, E., Nobile, J. R., Plant, R., Puc, B. P., Ronan, M. T., Roth, G. T., Sarkis, G. J., Simons, J. F., Simpson, J. W., Srinivasan, M., Tartaro, K. R., Tomasz, A., Vogt, K. A., Volkmer, G. A., Wang, S. H., Wang, Y., Weiner, M. P., Yu, P. G., Begley, R. F., Rothberg, J. M. (2010). Microfluidic lab-on-a-chip platforms: requirements, characteristics and applications. *Chemical Society Reviews*, *39*(3), 1153.

Markides, H., Rotherham, M., & El Haj, A. J. (2012). Biocompatibility and Toxicity of Magnetic Nanoparticles in Regenerative Medicine. *Journal of Nanomaterials*, *2012*, 1–11.

Maurer, M.H., O. Brömme, J., Feldmann, R.E., Järve, A., Sabouri, F., Bürgers, H.F., Schelshorn, D., Krüger, C., Armin S., Kuschinsky†, W. (2007). Glycogen Synthase Kinase 3β (GSK3β) Regulates Differentiation and Proliferation in Neural Stem Cells from the Rat Subventricular Zone. *Journal of Proteome Research, 6*(3), 1198-1208.

Marzec, K. M., Wróbel, T. P., Fedorowicz, A., Mateuszuk, Ł., Maślak, E., Jasztal, A., & Chlopicki, S. (2014). Vibrational Microspectroscopy for

Analysis of Atherosclerotic Arteries. In *Optical Spectroscopy and Computational Methods in Biology and Medicine* (pp. 505–535).

Marzec, K. M., Rygula, A., Gasior-Glogowska, M., Kochan, K., Czamara, K., Bulat, K., Malek, K., Kaczor, A., Baranska, M. (2015). Vascular diseases investigated ex vivo by using Raman, FT-IR and complementary methods. *Pharmacological Reports*, *67*(4), 744–750.

Massart, R. (1981). Preparation of aqueous magnetic liquids in alkaline and acidic media. *IEEE Transactions on Magnetics*, *17*(2), 1247–1248.

Mata-Miranda, M. M., Vazquez-Zapien, G. J., Rojas-Lopez, M., Sanchez-Monroy, V., Perez-Ishiwara, D. G., & Delgado-Macuil, R. J. (2017). Morphological, molecular and FTIR spectroscopic analysis during the differentiation of kidney cells from pluripotent stem cells. *Biological Research*, *50*(1), 14.

Matkovic, S. R., Valle, G. M., & Briand, L. E. (2005). Quantitative analysis of ibuprofen in pharmaceutical formulations through FTIR spectroscopy. *Latin American Applied Research*, *35*(3), 189–195.

McCall, R. L., & Sirianni, R. W. (2013). PLGA Nanoparticles Formed by Single- or Double-emulsion with Vitamin E-TPGS. *Journal of Visualized Experiments,* (82), e51015–e51015.

McCubrey, J. A., Steelman, L. S., Bertrand, F. E., Davis, N. M., Sokolosky, M., Abrams, S. L., Montalto, G., D'Assoro, A., Libra, M., Nicoletti, F., Maestro, R., Basecke, J., Gizak, A., Demidenko, Z., Cocco, L., Martelli, A.M., Cervello, M. (2014). GSK-3 as potential target for therapeutic intervention in cancer. *Oncotarget*, *5*(10), 2881–2911.

Mcgregor, H. C., Short, M. A., Mcwilliams, A., Shaipanich, T., Ionescu, D. N., Zhao, J., Wang, W., Chen, G., Lam, S., Zeng, H. (2016). Real-time endoscopic Raman spectroscopy for in vivo early lung cancer detection. *Journal of Biophotonics.* 10(1), 98-110.

McIntyre, N. J., Fluck, R. J., McIntyre, C. W., & Taal, M. W. (2011). Skin autofluorescence and the association with renal and cardiovascular risk factors in chronic kidney disease stage 3. *Clinical Journal of the American Society of Nephrology : CJASN*, *6*(10), 2356–63.

McManus, L. L., Burke, G. A., McCafferty, M. M., O'Hare, P., Modreanu, M., Boyd, A. R., & Meenan, B. J. (2011). Raman spectroscopic monitoring of the osteogenic differentiation of human mesenchymal stem cells. *The Analyst*, *136*(12), 2471.

Meek, C., Hoe, J., Evans, J., Thurman, R., Ashworth, L., & Leff, R. (2016). Raman Spectroscopy: A Sensitive and Specific Technique for Determining the Accuracy of Compounded Pharmaceutical Formulations. *The Journal of Pediatric Pharmacology and Therapeutics*, *21*(5), 413–418.

Merrilees, M. J., Beaumont, B. W., Braun, K. R., Thomas, A. C., Kang, I., Hinek, A., Passi, A., Wight, T. N. (2011). Neointima formed by arterial smooth muscle cells expressing versican variant V3 is resistant to

lipid and macrophage accumulation. *Arteriosclerosis, Thrombosis, and Vascular Biology*, *31*(6), 1309–16.

Michel APM, Liakat S, Bors K, Gmachl CF. In vivo measurement of mid-infrared light scattering from human skin. (2013) *Biomedical Optical Express. 4*(520).

Miller, L. M., Bourassa, M. W., & Smith, R. J. (2013). FTIR spectroscopic imaging of protein aggregation in living cells. *Biochimica et Biophysica Acta*, *1828*(10), 2339–46.

Min, K. A., Shin, M. C., Yu, F., Yang, M., David, A. E., Yang, V. C., & Rosania, G. R. (2013). Pulsed magnetic field improves the transport of iron oxide nanoparticles through cell barriers. *ACS Nano*, *7*(3), 2161–71.

Miranda-Lorenzo, I., Dorado, J., Lonardo, E., Alcala, S., Serrano, A. G., Clausell-Tormos, J., Cioffi, M., Diego, M., Zagorac, S., Balic, A., Hildago, M., Erkan, M., Kleef, J., Scarpa, A., Sainz, B., Heeschen, C. (2014). Intracellular autofluorescence: a biomarker for epithelial cancer stem cells. *Nature Methods*, *11*(11), 1161–1169.

Miyazawa, T., & Blout, E. R. (1961). The Infrared Spectra of Polypeptides in Various Conformations: Amide I and II Bands. *Journal of the American Chemical Society*, *83*(3), 712–719.

Mohammed, L., Gomaa, H. G., Ragab, D., & Zhu, J. (2017). Magnetic nanoparticles for environmental and biomedical applications: A review. *Particuology*, *30*, 1–14.

Mohan, S., & Dhall, A. (2010). A comparative study of restenosis rates in bare metal and drug-eluting stents. *The International Journal of Angiology : Official Publication of the International College of Angiology, Inc*, *19*(2), e66-72.

Moitra, K., Lou, H., & Dean, M. (2011). Multidrug Efflux Pumps and Cancer Stem Cells: Insights Into Multidrug Resistance and Therapeutic Development. *Clinical Pharmacology & Therapeutics*, *89*(4), 491–502.

Molckovsky, A., Song, L.-M. W. K., Shim, M. G., Marcon, N. E., & Wilson, B. C. (2003). Diagnostic potential of near-infrared Raman spectroscopy in the colon: Differentiating adenomatous from hyperplastic polyps. *Gastrointestinal Endoscopy*, *57*(3), 396–402.

Mooney, C. J., Hakimjavadi, R., Fitzpatrick, E., Kennedy, E., Walls, D., Morrow, D., Redmond, E., Cahill, P. A. (2015). Hedgehog and Resident Vascular Stem Cell Fate. *Stem Cells International*, 468428.

Morrow, D., Cullen, J. P., Liu, W., Guha, S., Sweeney, C., Birney, Y. A., Redmond, E., Cahill, P. A. (2009). Sonic Hedgehog induces Notch target gene expression in vascular smooth muscle cells via VEGF-A. *Arteriosclerosis, Thrombosis, and Vascular Biology*, *29*(7), 1112–8.

Motz, J. T., Fitzmaurice, M., Miller, A., Gandhi, S. J., Haka, A. S., Galindo, L. H., Dasari, R., Kramer, J., Feld, M. S. (2006). In vivo Raman

spectral pathology of human atherosclerosis and vulnerable plaque. *Journal of Biomedical Optics*, *11*(2), 21003.

Mourant, J. R., Bigio, I. J., Boyer, J., Conn, R. L., Johnson, T., & Shimada, T. (1995). Spectroscopic diagnosis of bladder cancer with elastic light scattering. *Lasers in Surgery and Medicine*, *17*(4), 350–357.

Movasaghi, Z., Rehman, S., & ur Rehman, I. (2007). Raman Spectroscopy of Biological Tissues. *Applied Spectroscopy Reviews*, *42*(5), 493.

Nakashima, Y., Chen, Y.-X., Kinukawa, N., & Sueishi, K. (2002). Distributions of diffuse intimal thickening in human arteries: preferential expression in atherosclerosis-prone arteries from an early age. *Virchows Archiv*, *441*(3), 279–288.

Narayanan, A. S., Sandberg, L. B., Ross, R., & Layman, D. L. (1976). The smooth muscle cell. III. Elastin synthesis in arterial smooth muscle cell culture. *The Journal of Cell Biology*, *68*(3), 411–9.

National Academy of Sciences (U.S.). (1915). *Proceedings of the National Academy of Sciences of the United States of America.* The Academy.

Naumann, D., Helm, D., & Labischinski, H. (1991). Microbiological characterisations by FT-IR spectroscopy. *Nature*, *351*(6321), 81–82.

Nemenoff, R. A., Horita, H., Ostriker, A. C., Furgeson, S. B., Simpson, P. A., VanPutten, V., Crossno, J.. Offermans, S., Weiser-Evans, M. C. M. (2011). SDF-1 Induction in Mature Smooth Muscle Cells by Inactivation of PTEN Is a Critical Mediator of Exacerbated Injury-Induced Neointima Formation. *Arteriosclerosis, Thrombosis, and Vascular Biology*, *31*(6), 1300–1308.

Neugebauer, U., Rösch, P., Schmitt, M., Popp, J., Julien, C., Rasmussen, A., Budich, C., Deckert, V. (2006). On the Way to Nanometer-Sized Information of the Bacterial Surface by Tip-Enhanced Raman Spectroscopy. *ChemPhysChem*, *7*(7), 1428–1430.

Newton, I. Opticks: Or a treatise of the reflexions, refractions, inflexions and colours of light (1704).

Nguyen, A. T., Gomez, D., Bell, R. D., Campbell, J. H., Clowes, A. W., Gabbiani, G., Giachelli, C., Giachelli, C., Parmacek, M., Raines, E.W., Rusch, N.J., Speer, M., Sturek, M., Sturek, M., Thyberg, J., Towler, D., Weiser-Evans, M., Yan, C., Miano, J., Owens, G. K. (2013). Smooth Muscle Cell Plasticity. *Circulation Research*, *112*(1).

Nica Rodilla, V., Villanueva, A., Obrador-Hevia, A., Robert-Moreno, A., Ferná Ndez-Majada, V., Grilli, A., Ló Pez-Bigas, N., Bellora, N.S., Albà, M.M., Torres, F., Duñ Ach, M., Sanjuan, X., Gonzalez, S., Gridley, T., Capella, G., Bigas, A., Espinosa, L. (2009). Jagged1 is the pathological link between Wnt and Notch pathways in colorectal cancer. *PNAS*. *106(*15), 6315-6320.

Nichols, M., Townsend, N., Scarborough, P., & Rayner, M. (2014). Cardiovascular Disease in Europe 2014: Epidemiological Update. *European Heart Journal. 38*(37).

Njoroge, E., Alty, S. R., Gani, M. R., & Alkatib, M. (2006). Classification of Cervical Cancer Cells using FTIR Data. In *2006 International Conference of the IEEE Engineering in Medicine and Biology Society* (Vol. 1, pp. 5338–5341).

Noordzij, M. J., Lefrandt, J. D., Loeffen, E. A. H., Saleem, B. R., Meerwaldt, R., Lutgers, H. L., Smit, A., Zeebregts, C. J. (2012). Skin autofluorescence is increased in patients with carotid artery stenosis and peripheral artery disease. *The International Journal of Cardiovascular Imaging*, *28*(2), 431–8.

Nwankire, C. E., Venkatanarayanan, A., Glennon, T., Keyes, T. E., Forster, R. J., & Ducrée, J. (2015). Label-free impedance detection of cancer cells from whole blood on an integrated centrifugal microfluidic platform. *Biosensors and Bioelectronics*, *68*, 382–389.

Okada, Y., Katsuda, S., Matsui, Y., Watanabe, H., & Nakanishi, I. (2008). Collagen Synthesis by Cultured Arterial Smooth Muscle Cells during Spontaneous Phenotypic Modulation. *Pathology International*, *40*(3), 157–164.

Ollesch, J., Heinze, M., Heise, H. M., Behrens, T., Brüning, T., & Gerwert, K. (2014). It's in your blood: spectral biomarker candidates for urinary bladder cancer from automated FTIR spectroscopy. *Journal of Biophotonics*, *7*(3–4), 210–221.

Ooi, G. J., Fox, J., Siu, K., Lewis, R., Bambery, K. R., McNaughton, D., & Wood, B. R. (2008). Fourier transform infrared imaging and small angle x-ray scattering as a combined biomolecular approach to diagnosis of breast cancer. *Medical Physics*, *35*(5), 2151–2161.

Otsuka, G., Agah, R., Frutkin, A. D., Wight, T. N., & Dichek, D. A. (2006). Transforming Growth Factor Beta 1 Induces Neointima Formation Through Plasminogen Activator Inhibitor-1–Dependent Pathways. *Arteriosclerosis, Thrombosis, and Vascular Biology*, *26*(4).

Owens, G. K., Kumar, M. S., & Wamhoff, B. R. (2004). Molecular Regulation of Vascular Smooth Muscle Cell Differentiation in Development and Disease. *Physiological Reviews*, *84*(3), 767–801.

Pahk, K., Joung, C., Jung, S.-M., Young Song, H., Yong Park, J., Woo Byun, J., Lee, Y-S., Chul, P-J., Kim, C., Kim, S., Kim, W.-K. (2017). Visualization of Synthetic Vascular Smooth Muscle Cells in Atherosclerotic Carotid Rat Arteries by F-18 FDG PET. *Scientific Reports*, *7*(1), 6989.

Pahlow, S., Meisel, S., Cialla-May, D., Weber, K., Rösch, P., & Popp, J. (2015). Isolation and identification of bacteria by means of Raman spectroscopy. *Advanced Drug Delivery Reviews*, *89*, 105–120.

Palmaz, J. C. (1993). Intravascular stents: tissue-stent interactions and design considerations. *AJR. American Journal of Roentgenology*, *160*(3), 613–8.

Pascut, F. C., Goh, H. T., Welch, N., Buttery, L. D., Denning, C., & Notingher, I. (2011). Noninvasive detection and imaging of molecular markers in live cardiomyocytes derived from human embryonic stem cells. *Biophysical Journal*, *100*(1), 251–9.

Pascut, F. C., Kalra, S., George, V., Welch, N., Denning, C., & Notingher, I. (2013). Non-invasive label-free monitoring the cardiac differentiation of human embryonic stem cells in-vitro by Raman spectroscopy. *Biochimica et Biophysica Acta (BBA) - General Subjects*, *1830*(6), 3517–3524.

Patel, I. I., Trevisan, J., Singh, P. B., Nicholson, C. M., Gopala Krishnan, R. K., Matanhelia, S. S., & Martin, F. L. (2011). Segregation of human prostate tissues classified high-risk (UK) versus low-risk (India) for adenocarcinoma using Fourier-transform infrared or Raman microspectroscopy coupled with discriminant analysis. *Analytical Bioanalytical Chemistry., 401*(3), 969.

Pearl, L. H., & Barford, D. (2002). Regulation of protein kinases in insulin, growth factor and Wnt signalling. *Current opinion in structural biology.* 12(6), 761-767.

Perakis, S., & Speicher, M. R. (2017). Emerging concepts in liquid biopsies. *BMC Medicine*, *15*(1), 75.

Peres, M. B., Silveira, L., Zângaro, R. A., Tavares Pacheco, M. T., & Pasqualucci, C. A. (2011). Classification model based on Raman spectra of selected morphological and biochemical tissue constituents for identification of atherosclerosis in human coronary arteries. *Lasers Medical Science., 26*(5), 645.

Perez-Guaita, D., Heraud, P., Marzec, K. M., de la Guardia, M., Kiupel, M., & Bayden, R. W. (2015). Comparison of transflection and transmission FTIR imaging measurements performed on differentially fixed tissue sections. *Analyst*, *140*(null), 2376.

Pichardo-Molina, J. L., Frausto-Reyes, C., Barbosa-García, O., Huerta-Franco, R., González-Trujillo, J. L., Ramírez-Alvarado, C. A., Gutiérrez-J., Medina-Gutiérrez, C. (2007). Raman spectroscopy and multivariate analysis of serum samples from breast cancer patients. *Lasers in Medical Science*, *22*(4), 229–236.

Pijanka, J. K., Kumar, D., Dale, T., Yousef, I., Parkes, G., Untereiner, V., Yang, Y., Dumas, P., Collins, D., Manfait, M., Sockalingum, G D., Forsyth, N RSulé-Suso, J. (2010). Vibrational spectroscopy differentiates between multipotent and pluripotent stem cells. *Analyst*, *135*(null), 3126.

Piva, J. A. de A. C., Silva, J. L. R., Raniero, L. J., Lima, C. S. P., Arisawa, E. A. L., Oliveira, C. de, Canevari, R., Feirera, J., Martin, A. A. (2015). Biochemical imaging of normal, adenoma, and colorectal adenocarcinoma tissues by Fourier transform infrared spectroscopy

(FTIR) and morphological correlation by histopathological analysis: preliminary results. *Research on Biomedical Engineering*, *31*(1), 10–18.

Polyak, B., Medved, M., Lazareva, N., Steele, L., Patel, T., Rai, A., Rotenberg, M., Wasko, K., Kohut, A.R., Sensenig, R., Friedman, G. (2016). Magnetic Nanoparticle-Mediated Targeting of Cell Therapy Reduces In-Stent Stenosis in Injured Arteries. *ACS Nano*, *10*(10), 9559–9569.

Popescu, G., Ikeda, T., Best, C. A., Badizadegan, K., Dasari, R. R., & Feld, M. S. (2005). Erythrocyte structure and dynamics quantified by Hilbert phase microscopy. *Journal of Biomedical Optics*, *10*(6), 60503.

Potz, B. A., Sabe, A. A., Elmadhun, N. Y., Clements, R. T., Robich, M. P., Sodha, N. R., & Sellke, F. W. (2016). Glycogen Synthase Kinase 3β Inhibition Improves Myocardial Angiogenesis and Perfusion in a Swine Model of Metabolic Syndrome. *Journal of the American Heart Association*, *5*(7).

Pudlas, M., Berrio, D. A. C., Votteler, M., Koch, S., Thude, S., Walles, H., & Schenke-Layland, K. (2011). Non-contact discrimination of human bone marrow-derived mesenchymal stem cells and fibroblasts using Raman spectroscopy. *Medical Laser Application*, *26*(3), 119–125.

Qavi, A. J., Washburn, A. L., Byeon, J.-Y., & Bailey, R. C. (2009). Label-free technologies for quantitative multiparameter biological analysis. *Analytical and Bioanalytical Chemistry*, *394*(1), 121–135.

Quinn, K. P., Sridharan, G. V, Hayden, R. S., Kaplan, D. L., Lee, K., & Georgakoudi, I. (2013). Quantitative metabolic imaging using endogenous fluorescence to detect stem cell differentiation. *Scientific Reports*, *3*, 3432.

Redmond, E. M., Liu, W., Hamm, K., Hatch, E., Cahill, P. A., & Morrow, D. (2014). Perivascular Delivery of Notch 1 siRNA Inhibits Injury-Induced Arterial Remodeling. *PLoS ONE*, *9*(1), e84122.

Rensen, S. S. M., Doevendans, P. A. F. M., & van Eys, G. J. J. M. (2007). Regulation and characteristics of vascular smooth muscle cell phenotypic diversity. *Netherlands Heart Journal : Monthly Journal of the Netherlands Society of Cardiology and the Netherlands Heart Foundation*, *15*(3), 100–8.

Reinert, R. B., Kantz, J., Misfeldt, A. A., Poffenberger, G., Gannon, M., Brissova, M., & Powers, A. C. (2012). Tamoxifen-Induced Cre-loxP Recombination Is Prolonged in Pancreatic Islets of Adult Mice. *PLoS ONE*, *7*(3), e33529.

Rice, W. L., Kaplan, D. L., & Georgakoudi, I. (2007). Quantitative biomarkers of stem cell differentiation based on intrinsic two-photon excited fluorescence. *Journal of Biomedical Optics*, *12*(6), 60504.

Rice, W. L., Kaplan, D. L., & Georgakoudi, I. (2010). Two-Photon Microscopy for Non-Invasive, Quantitative Monitoring of Stem Cell Differentiation. *PLoS ONE*, *5*(4), e10075.

Richards-Kortum, R., & Sevick-Muraca, E. (1996). QUANTITATIVE OPTICAL SPECTROSCOPY FOR TISSUE DIAGNOSIS. *Annual Review of Physical Chemistry*, *47*(1), 555–606.

Ring, A., Kim, Y.-M., & Kahn, M. (2014). Wnt/catenin signaling in adult stem cell physiology and disease. *Stem Cell Reviews*, *10*(4), 512–25.

Romero, G., Qiu, Y., Murray, R. A., & Moya, S. E. (2013). Study of Intracellular Delivery of Doxorubicin from Poly(lactide- *co* -glycolide) Nanoparticles by Means of Fluorescence Lifetime Imaging and Confocal Raman Microscopy. *Macromolecular Bioscience*, *13*(2), 234–241.

Rubina, S., Amita, M., Kedar K., D., Bharat, R., & Krishna, C. M. (2013). Raman spectroscopic study on classification of cervical cell specimens. *Vibrational Spectroscopy*, *68*, 115–121.

Ruel, L., Bourouis, M., Heitzler, P., Pantesco, V., & Simpson, P. (1993). Drosophila shaggy kinase and rat glycogen synthase kinase-3 have conserved activities and act downstream of Notch. *Nature*, *362*(6420), 557–560.

Sakata, Y., Xiang, F., Chen, Z., Kiriyama, Y., Kamei, C. N., Simon, D. I., & Chin, M. T. (2004). Transcription Factor CHF1/Hey2 Regulates Neointimal Formation In Vivo and Vascular Smooth Muscle Proliferation and Migration In Vitro. *Arteriosclerosis, Thrombosis, and Vascular Biology*, *24*(11), 2069–2074.

Salari, A., & Young, R. E. (1998). Application of attenuated total reflectance FTIR spectroscopy to the analysis of mixtures of pharmaceutical polymorphs. *International Journal of Pharmaceutics*, *163*(1), 157–166.

Salvas, J., Simard, J.-S., & Abatzoglou, N. (2010). Raman Spectroscopy to Analyze Intact Pharmaceutical Tablets: Factors Influencing MVPM-based PAT Methods. *American Pharmaceutical Review.*

Samouillan, V., Dandurand, J., Nasarre, L., Badimon, L., Lacabanne, C., & Llorente-Cortés, V. (2012). Lipid loading of human vascular smooth muscle cells induces changes in tropoelastin protein levels and physical structure. *Biophysical Journal*, *103*(3), 532–40.

Sata, M., Saiura, A., Kunisato, A., Tojo, A., Okada, S., Tokuhisa, T., Hirai, H., Makuuchi, M., Hirata, Y., Nagai, R. (2002). Hematopoietic stem cells differentiate into vascular cells that participate in the pathogenesis of atherosclerosis. *Nature Medicine*, *8*(4), 403–409.

Sathyanarayana D. N. (2004). *Vibrational Spectroscopy: Theory and Applications.* Second Edition. New Age International Ltd.

Sato, N., Meijer, L., Skaltsounis, L., Greengard, P., & Brivanlou, A. H. (2004). Maintenance of pluripotency in human and mouse embryonic

stem cells through activation of Wnt signaling by a pharmacological GSK-3-specific inhibitor. *Nature Medicine*, *10*(1), 55–63.

Savastano, L. E., Zhou, Q., Smith, A., Vega, K., Murga-Zamalloa, C., Gordon, D., McHugh, J., Zhao, L., Wang, M.M., Pandey, A., Thompson, B. G., Xu, J., Zhang, J., Chen, Y. E., Seibel, EJ., Wang, T. D. (2017). Multimodal laser-based angioscopy for structural, chemical and biological imaging of atherosclerosis. *Nature Biomedical Engineering, 1*(2), 23.

Schiele, T. M. (2005). Current understanding of coronary in-stent restenosis. Pathophysiology, clinical presentation, diagnostic work-up, and management. *Zeitschrift Für Kardiologie*, *94*(11), 772–90.

Schröder, U.-C., Bokeloh, F., O'Sullivan, M., Glaser, U., Wolf, K., Pfister, W., Popp, J., Ducrée, J., Neugebauer, U. (2015). Rapid, culture-independent, optical diagnostics of centrifugally captured bacteria from urine samples. *Biomicrofluidics*, *9*(4), 44118.

Shanahan, C. M., & Weissberg, P. L. (1998). Smooth muscle cell heterogeneity: patterns of gene expression in vascular smooth muscle cells in vitro and in vivo. *Arteriosclerosis, Thrombosis, and Vascular Biology*, *18*(3), 333–8.

Shankman, L. S., Gomez, D., Cherepanova, O. A., Salmon, M., Alencar, G. F., Haskins, R. M., Swiatlowska, P., Newman, A.C., Greene, E.S., Straub, A.C., Isakson, B., Randolph, G.J., Owens, G. K. (2015). KLF4-dependent phenotypic modulation of smooth muscle cells has a key role in atherosclerotic plaque pathogenesis. *Nature Medicine*, *21*(6), 628–637.

Shanks, N., Greek, R., & Greek, J. (2009). Are animal models predictive for humans? *Philosophy, Ethics, and Humanities in Medicine : PEHM,* 4, 2.

Shapiro, A., Gofrit, O. N., Pizov, G., Cohen, J. K., & Maier, J. (2011). Raman Molecular Imaging: A Novel Spectroscopic Technique for Diagnosis of Bladder Cancer in Urine Specimens. *European Urology*, *59*(1), 106–112.

Shen, Y., Wu, Y., Zheng, Y., Ao, F., Kang, K., Wan, Y., & Song, J. (2016). Responses of adventitial CD34+ vascular wall-resident stem/progenitor cells and medial smooth muscle cells to carotid injury in rats. *Experimental and Molecular Pathology*, *101*(3), 332–340.

Sharif, F., & Murphy, R. T. (2009). Current status of vulnerable plaque detection. *Catheterization and Cardiovascular Interventions*, *75*(1), 135–144.

Shikatani, E. A., Chandy, M., Besla, R., Li, C. C., Momen, A., El-Mounayri, O., Robbins, C., Husain, M. (2016). c-Myb Regulates Proliferation and Differentiation of Adventitial Sca1 + Vascular Smooth Muscle Cell Progenitors by Transactivation of MyocardinHighlights. *Arteriosclerosis, Thrombosis, and Vascular Biology*, *36*(7), 1367–1376.

Siafaka, P. I., Üstündağ Okur, N., Karavas, E., & Bikiaris, D. N. (2016). Surface Modified Multifunctional and Stimuli Responsive Nanoparticles for Drug Targeting: Current Status and Uses. *International Journal of Molecular Sciences*, *17*(9).

Singh, S., Pandey, V. K., Tewari, R. P., & Agarwal, V. (2011). Nanoparticle Based Drug Delivery System: Advantages and Applications. *Indian Journal of Science and Technology*, *4*(3), 177–180.

Siqueira, L. F. S., & Lima, K. M. G. (2016). A decade (2004 – 2014) of FTIR prostate cancer spectroscopy studies: An overview of recent advancements. *TrAC Trends in Analytical Chemistry*, *82*, 208–221.

Sjölund, M., Madsen, K., von der Mark, K., & Thyberg, J. (1986). Phenotype modulation in primary cultures of smooth-muscle cells from rat aorta. Synthesis of collagen and elastin. *Differentiation; Research in Biological Diversity*, *32*(2), 173–80.

Smith, R., Wright, K. L., & Ashton, L. (2016). Raman spectroscopy: an evolving technique for live cell studies. *The Analyst*, *141*(12), 3590–3600.

Song, S., Qi, H., Xu, J., Guo, P., Chen, F., Li, F., Yang, Xi, Sheng, N., Wu, Y., Pan, W. (2014). Hyaluronan-Based Nanocarriers with CD44-Overexpressed Cancer Cell Targeting. *Pharmaceutical Research,* 31(11), 2988–3005.

Squirrell, J. M., Fong, J. J., Ariza, C. A., Mael, A., Meyer, K., Shevde, N. K., Roopra, A., Lyons, G., Kamp, T., Eliceiri, K., Ogle, B. M. (2012). Endogenous Fluorescence Signatures in Living Pluripotent Stem Cells Change with Loss of Potency. *PLoS ONE*, *7*(8), e43708.

Stuart, B. H. (2005). Infrared Spectroscopy: Fundamentals and Applications. In D. J. Ando (Ed.), *Analytical Techniques in the Sciences*. John Wiley & Sons.

Subbotin, V. M. (2016). Excessive intimal hyperplasia in human coronary arteries before intimal lipid depositions is the initiation of coronary atherosclerosis and constitutes a therapeutic target. *Drug Discovery Today*, *21*(10), 1578–1595.

Sulé-Suso, J., Forsyth, N. R., Untereiner, V., & Sockalingum, G. D. (2014). Vibrational spectroscopy in stem cell characterisation: is there a niche? *Trends Biotechnology*, *32*(5), 254.

Sun P, Dwyer KM, Merz VN, Sun W, Johnson CA, Shircore AM, Dwyer JH. (2002). Blood pressure, LDL cholesterol, and intima-media thickness: a test of the 'response to injury' hypothesis of atherosclerosis. *Arterioscler Thromb Vasc Biol*, *20* (8) pp. 2005-2010.

Swaminathan, G., Gadepalli, V. S., Stoilov, I., Mecham, R. P., Rao, R. R., & Ramamurthi, A. (2017). Pro-elastogenic effects of bone marrow mesenchymal stem cell-derived smooth muscle cells on cultured aneurysmal smooth muscle cells. *Journal of Tissue Engineering and Regenerative Medicine*, *11*(3), 679–693.

Tang, Z., Wang, A., Wang, D., & Li, S. (2013). Smooth muscle cells: to be or not to be? Response to Nguyen et Al. *Circulation Research*, *112*(1), 23–6.

Tang, Z., Wang, A., Yuan, F., Yan, Z., Liu, B., Chu, J. S., Helms, J., Li, S. (2012). Differentiation of multipotent vascular stem cells contributes to vascular diseases. *Nature Communications*, *3*, 875.

Tang, X., Cai, S., Zhang, R., Liu, P., Chen, H., Zheng, Y., & Sun, L. (2013). Paclitaxel-loaded nanoparticles of star-shaped cholic acid-core PLA-TPGS copolymer for breast cancer treatment. *Nanoscale Research Letters,* 8(1), 420.

Tanthanuch, W., Thumanu, K., Lorthongpanich, C., Parnpai, R., & Heraud, P. (2010). Neural differentiation of mouse embryonic stem cells studied by FTIR spectroscopy. *Journal of Molecular Structure*, *967*(1–3), 189–195.

Tarkin, J. M., Joshi, F. R., Evans, N. R., Chowdhury, M. M., Figg, N. L., Shah, A. V, Starks, L.T., Martin-Garrido, A., Manavaki, R., Yu, E., Kuc, R., Grassi, L., Kreuzhuber, R., Kostadima, M., Frontini, M., Kirkpatrick, P.J., Coughlin, P.A., Gopalan, D., Fryer, T.D., Buscombe, J.R., Groves, A.M., Ouwehand, W.H., Bennett, M.R., Warburton, E.A., Davenport, A., Rudd,J.H. F. (2017). Detection of Atherosclerotic Inflammation by (68)Ga-DOTATATE PET Compared to [(18)F]FDG PET Imaging. *Journal of the American College of Cardiology*, 69(14), 1774–1791.

Tauer, U., (2002). Advantages and risks of multi photon microscopy in physiology. *Experimental Physiology. 87*(6): 709-14.

Teh, S. K., Zheng, W., Ho, K. Y., Teh, M., Yeoh, K. G., & Huang, Z. (2008). Diagnostic potential of near-infrared Raman spectroscopy in the stomach: differentiating dysplasia from normal tissue. *British Journal of Cancer*, *98*(2), 457–65.

Teirstein, P. S. (2010). Drug-Eluting Stent Restenosis. *Circulation*, *122*(1).

Thimm, T. N., Squirrell, J. M., Liu, Y., Eliceiri, K. W., & Ogle, B. M. (2015). Endogenous Optical Signals Reveal Changes of Elastin and Collagen Organization During Differentiation of Mouse Embryonic Stem Cells. *Tissue Engineering. Part C, Methods*, *21*(10), 995–1004.

Tidy, R. J., Lam, V., Fimognari, N., Mamo, J. C., & Hackett, M. J. (2016). FTIR studies of the similarities between pathology induced protein aggregation in vivo and chemically induced protein aggregation ex vivo. *Vibrational Spectroscopy*. 91, 68-76.

Tien, N., Chen, H.-C., Gau, S.-L., Lin, T.-H., Lin, H.-S., You, B.-J., Tsai, Po-Chuan., Chen, I-R., Tsai, M-F., Wang, I-K., Chen, C-J., Chang, C.-T. (2016). Diagnosis of bacterial pathogens in the dialysate of peritoneal dialysis patients with peritonitis using surface-enhanced Raman spectroscopy. *Clinica Chimica Acta*, *461*, 69–75.

Tietze, R., Zaloga, J., Unterweger, H., Lyer, S., Friedrich, R. P., Janko, C., Pöttler, M., Durr, S., Alexiou, C. (2015). Magnetic nanoparticle-based

drug delivery for cancer therapy. *Biochemical and Biophysical Research Communications, 468(*3), 463–470.

Togkalidou, T., Tung, H.H., Sun, Y., Andrews, A.,Braatz, R. D. (2002). Solution Concentration Prediction for Pharmaceutical Crystallization Processes Using Robust Chemometrics and ATR FTIR Spectroscopy. *Organic Process Research and Development.* 6(3), 317-322.

Torsney, E., Xu, Q., Liu, D., Hickey, R., Krause, D. S., Giordano, F. J., & al., et. (2011). Resident vascular progenitor cells. *Journal of Molecular and Cellular Cardiology*, *50*(2), 304–11.

Tsai, S., Hollenbeck, S. T., Ryer, E. J., Edlin, R., Yamanouchi, D., Kundi, R., Wang, C., Liu, B., Kent, K. C. (2009). TGF-beta through Smad3 signaling stimulates vascular smooth muscle cell proliferation and neointimal formation. *American Journal of Physiology. Heart and Circulatory Physiology*, *297*(2), H540-9.

Utzinger, U., Heintzelman, D. L., Mahadevan-Jansen, A., Malpica, A., Follen, M., & Richards-Kortum, R. (2001). Near-Infrared Raman Spectroscopy for *in Vivo* Detection of Cervical Precancers. *Applied Spectroscopy*, *55*(8), 955–959.

Utzinger, U., & Richards-Kortum, R. R. (2003). Fiber optic probes for biomedical optical spectroscopy. *Journal of Biomedical Optics*, *8*(1), 121–47.

Van der Meulen, J., Sanghvi, V., Mavrakis, K., Durinck, K., Fang, F., Matthijssens, F., Rondou, P., Rosen, M., Pieters, T., Vandenberghe, P., Delabesse, E., Lammens, T., De Moerloose, B., Menten, B., Van Roy, N., Verhasselt, B., Poppe, B., Benoit, Y., Taghon, T., Melnick, A. M., Speleman, F., Wendel, H.-G. Van Vlierberghe, P. (2015). The H3K27me3 demethylase UTX is a gender-specific tumor suppressor in T-cell acute lymphoblastic leukemia. *Blood, 125*(1), 13–21.

Vangara, K. K., Liu, J. L., & Palakurthi, S. (2013). Hyaluronic acid-decorated PLGA-PEG nanoparticles for targeted delivery of SN-38 to ovarian cancer. *Anticancer Research, 33*(6), 2425–34.

Vardaki, M., & Martha. (2016). Advanced Raman Techniques for Real Time Cancer Diagnostics. *Open Research Exeter.* Doctoral thesis.

Vazquez-Zapien, G. J., Mata-Miranda, M. M., Sanchez-Monroy, V., Delgado-Macuil, R. J., Perez-Ishiwara, D. G., & Rojas-Lopez, M. (2016). FTIR Spectroscopic and Molecular Analysis during Differentiation of Pluripotent Stem Cells to Pancreatic Cells. *Stem Cells International*, *2016*, 1–10.

Verdonck, M., Denayer, A., Delvaux, B., Garaud, S., De Wind, R., Desmedt, C., Chorn, G. (2016). Characterization of human breast cancer tissues by infrared imaging. *The Analyst*, *141*(2), 606–619.

Vladimirskaya, T., Shved, I., Kryvorot, S., Yudina, O., Federov, A. Immunohistochemical evaluation of remodeling of coronary artery restenosis. (2017). *Atherosclerosis*, *263*, e127.

Vosen, S., Rieck, S., Heidsieck, A., Mykhaylyk, O., Zimmermann, K., Bloch, W., Eberbeck, D., Plank, C., Gleich, B., Pfeifer, A., Fleischmann, B.K. Wenzel, D. (2016). Vascular Repair by Circumferential Cell Therapy Using Magnetic Nanoparticles and Tailored Magnets. *ACS Nano*, *10*(1), 369–376.

Walsh, M. J., Holton, S. E., Kajdacsy-Balla, A., & Bhargava, R. (2012). Attenuated total reflectance Fourier-transform infrared spectroscopic imaging for breast histopathology. *Vibrationaly Spectroscopy*, *60*(null), 23.

Wan, M., Li, C., Zhen, G., Jiao, K., He, W., Jia, X., Wang, W., Shi, C., Xing, Q., Chen, Y-F., Jan De Beur, S., Bing, Y., Cao, X. (2012). Injury-Activated Transforming Growth Factor β Controls Mobilization of Mesenchymal Stem Cells for Tissue Remodeling. *STEM CELLS*, *30*(11), 2498–2511.

Wang, A. Y.-M., Wong, C.-K., Yau, Y.-Y., Wong, S., Chan, I. H.-S., & Lam, C. W.-K. (2014). Skin autofluorescence associates with vascular calcification in chronic kidney disease. *Arteriosclerosis, Thrombosis, and Vascular Biology*, *34*(8), 1784–90.

Wang, G., Jacquet, L., Karamariti, E., & Xu, Q. (2015). Origin and differentiation of vascular smooth muscle cells. *Journal of Physiology*, *59314*(593), 3013–303014.

Wang, H., Li, Z., Moore, S., & Alavi, M. Z. (1998). Collagen biosynthesis by neointimal smooth muscle cells cultured from rabbit aortic explants 15 weeks after de-endothelialization. *International Journal of Experimental Pathology*, *79*(1), 47–53.

Wang, J., Yin, H., Huang, Y., Guo, C., Xia, C., & Zhang, L. (2013). Expression changes of Akt and GSK-3β during vascular inflammatory response and oxidative stress induced by high-fat diet in rats. *J. Biomedical Science and Engineering*, *6*, 1–5.

Wang, Z., Zhang, X., Chen, S., Wang, D., Wu, J., Liang, T., & Liu, C. (2013). Lithium Chloride Inhibits Vascular Smooth Muscle Cell Proliferation and Migration and Alleviates Injury-Induced Neointimal Hyperplasia via Induction of PGC-1α. *PLoS ONE*, *8*(1), e55471.

Wang J, Lin K, Zheng W, Ho KY, Teh M, Yeoh KG, Huang Z. (2015) Comparative study of the endoscope-based bevelled and volume fiber-optic Raman probes for optical diagnosis of gastric dysplasia in vivo at endoscopy. *Analytical and Bioanalytical Chemistry.* 407:8303–8310.

Wanjare, M., Agarwal, N., & Gerecht, S. (2015). Biomechanical strain induces elastin and collagen production in human pluripotent stem cell-derived vascular smooth muscle cells. *American Journal of Physiology - Cell Physiology*, *309*(4).

Watson, D., Hagen, N., Diver, J., Marchand, P., Chachisvilis, M., Simons, L. A., McMullin, L., Hagen, N., Lykstad, K., Tu, E., Pestana, L.M., Sur, S., Zhang, H., Butler, W.F., Kariv, I. Marchand, P. J. (2004). Elastic

light scattering from single cells: orientational dynamics in optical trap. *Biophysical Journal*, *87*(2), 1298–306.

White. (2005). Drug-Eluting Stents: Advanced Applications for the Management of Coronary Disease. *CRC Press.* Taylor & Francis.

WHO | Cardiovascular diseases (CVDs). (2017). *WHO*. http://www.who.int/mediacentre/factsheets/fs317/en/

Wigren, M., Rattik, S., Hultman, K., Björkbacka, H., Nordin-Fredrikson, G., Bengtsson, E., Hedblad, B., Siegbahn, A., Gonçalves, I. Nilsson, J. (2016). Decreased levels of stem cell factor in subjects with incident coronary events. *Journal of Internal Medicine*, *279*(2), 180–191.

Woodgett, J. R. (1990). Molecular cloning and expression of glycogen synthase kinase-3/factor A. *The EMBO Journal*, *9*(8), 2431–8.

Woulfe, K. C., Gao, E., Lal, H., Harris, D., Fan, Q., Vagnozzi, R., DeCaul, M., Shang, X., Patel, S., Woodgett, J.R., Force, T., Zhou, J. (2010). Glycogen Synthase Kinase-3β Regulates Post–Myocardial Infarction Remodeling and Stress-Induced Cardiomyocyte Proliferation In Vivo. *Circulation Research*, *106*(10).

Wray, J., Kalkan, T., Gomez-Lopez, S., Eckardt, D., Cook, A., Kemler, R., & Smith, A. (2011). Inhibition of glycogen synthase kinase-3 alleviates Tcf3 repression of the pluripotency network and increases embryonic stem cell resistance to differentiation. *Nature Cell Biology*, *13*(7), 838–845.

Wrobel, T. P., Marzec, K. M., Chlopicki, S., Maślak, E., Jasztal, A., Franczyk-Żarów, M., Czyżyńska-Cichoń, I., Moszkowski, T., Kostogrys, R.B., Baranska, M. (2015). Effects of Low Carbohydrate High Protein (LCHP) diet on atherosclerotic plaque phenotype in ApoE/LDLR-/- mice: FT-IR and Raman imaging. *Scientific Reports*, *5*, 14002.

Wu, W., Wu, Z., Yu, T., Jiang, C., & Kim, W.-S. (2015). Recent progress on magnetic iron oxide nanoparticles: synthesis, surface functional strategies and biomedical applications. *Science and Technology of Advanced Materials*, *16*(2), 23501.

Wu, Y., Cui, L., Li, G., Yin, S., Gao, Y., & Cao, Y. (2007). [PDGF-BB initiates vascular smooth muscle-like phenotype differentiation of human bone marrow mesenchymal stem cells in vitro]. *Zhonghua Zheng Xing Wai Ke Za Zhi = Zhonghua Zhengxing Waike Zazhi = Chinese Journal of Plastic Surgery*, *23*(4), 335–9.

Xu, J., Shi G.P. Vascular wall extracellular matrix proteins and vascular diseases. (2014). *Biochimica et Biophysica Acta (BBA) - Molecular Basis of Disease*, *1842*(11), 2106–2119.

Yamashita, S., Tsubakio-Yamamoto, K., Ohama, T., Nakagawa-Toyama, Y., & Nishida, M. (2010). Molecular mechanisms of HDL-cholesterol elevation by statins and its effects on HDL functions. *Journal of Atherosclerosis and Thrombosis*, *17*(5), 436–51.

Ye, D., Tanthanuch, W., Thumanu, K., Sangmalee, A., Parnpai, R., Heraud, P., Wood, B. R., Goldstein, J., Argov, S., Bulvik, S., Melamed, E., Offen, D., Matsunaga, T.,Ohtani, S., Matsuura, A., Hamada, H. Niitsu, Y. (2012). Discrimination of functional hepatocytes derived from mesenchymal stem cells using FTIR microspectroscopy. *The Analyst*, *137*(20), 4774.

Yin, R.-X., Yang, D.-Z., & Wu, J.-Z. (2014). Nanoparticle drug- and gene-eluting stents for the prevention and treatment of coronary restenosis. *Theranostics*, *4*(2), 175–200.

Yuan, F., Wang, D., Xu, K., Wang, J., Zhang, Z., Yang, L., Yang, G., Li, S. (2017). Contribution of Vascular Cells to Neointimal Formation. *PLOS ONE, 12*(1), e0168914.

Yun, H., Kim, K., & Lee, W. G. (2013). Cell manipulation in microfluidics. *Biofabrication*, *5*(2), 22001.

Yun, S. H., & Kwok, S. J. J. (2017). Light in diagnosis, therapy and surgery. *Nature Biomedical Engineering*, *1*(1), 8.

Zaragosi, L.-E., Wdziekonski, B., Fontaine, C., Villageois, P., Peraldi, P., & Dani, C. (2008). Effects of GSK3 inhibitors on in vitro expansion and differentiation of human adipose-derived stem cells into adipocytes. *BMC Cell Biology*, *9*(1), 11.

Zeisberg, E. M., Tarnavski, O., Zeisberg, M., Dorfman, A. L., McMullen, J. R., Gustafsson, E., Chandraker, A., Yuan, X., Pu, W.T., Roberts, A.B., Neilson, E.G., Sayegh, M.H., Izumo, S.R. (2007). Endothelial-to-mesenchymal transition contributes to cardiac fibrosis. *Nature Medicine*, *13*(8), 952–961.

Zelig, U., Dror, Z., Iskovich, S., Zwielly, A., Ben-Harush, M., Nathan, I., Mordechai, S., Kapelushnik, J. (2010). Biochemical analysis and quantification of hematopoietic stem cells by infrared spectroscopy. *Journal of Biomedical Optics*, *15*(3), 37008.

Zeng, X., Tao, W., Mei, L., Huang, L., Tan, C., & Feng, S.-S. (2013). Cholic acid-functionalized nanoparticles of star-shaped PLGA-vitamin E TPGS copolymer for docetaxel delivery to cervical cancer. *Biomaterials, 34*(25), 6058–6067.

Zhang, Y., Yang, M., Portney, N. G., Cui, D., Budak, G., Ozbay, E., Ozkan, M., Ozkan, C. S. (2008). Zeta potential: a surface electrical characteristic to probe the interaction of nanoparticles with normal and cancer human breast epithelial cells. *Biomedical Microdevices*, *10*(2), 321–328.

Zhao, J., Lui, H., McLean, D. I., & Zeng, H. (2008). Real-time raman spectroscopy for non-invasive skin cancer detection - preliminary results. In *2008 30th Annual International Conference of the IEEE Engineering in Medicine and Biology Society* (pp. 3107–3109). IEEE.

Zhou, Y., Liu, C.-H., Sun, Y., Pu, Y., Boydston-White, S., Liu, Y., & Alfano, R. R. (2012). Human brain cancer studied by resonance Raman spectroscopy. *Journal of Biomedical Optics*, *17*(11), 116021.

Zhou, Y.-X., Shi, Z., Singh, P., Yin, H., Yu, Y., Li, L., … Zheng, X.-L. (2016). Potential Role of Glycogen Synthase Kinase-3β in Regulation of Myocardin Activity in Human Vascular Smooth Muscle Cells. *Journal of Cellular Physiology*, *231*(2), 393–402.

Appendix A

List of Materials

Cell culture

Material	Product Code	Company
1-Azakenpaullone	A3734	Sigma-Aldrich, Arklow, Ireland
2-Mercaptoethanol	M7522	Sigma-Aldrich, Arklow, Ireland
B27 supplement	17504-044	Gibco/Bio-sciences, Dun Laoghaire
Bio	B1686	Sigma-Aldrich, Arklow, Ireland
C3H T10 1/2 Cells	ATCC-CCL-226	ATCC, Middlesex, UK
Chick Embryo Extract	Seralab CE-650-J	Seralab, West Sussex, UK
Col1A1 SiRNA	sc-44044	Santa-Cruz Biotechnology, Heidelberg, Germany
Col3A1 siRNA	sc-43063	Santa-Cruz Biotechnology, Heidelberg, Germany
Collagenase Type 1A	C9891	Sigma-Aldrich, Arklow, Ireland
DMEM	D5796	Sigma-Aldrich, Arklow, Ireland
DMEM	ATCC-30-2002	ATCC, Middlesex, UK
Elastase Type III	E0127	Sigma-Aldrich, Arklow, Ireland
Elastin siRNA	sc-43361	Santa-Cruz Biotechnology, Heidelberg, Germany
EMEM	ATCC-30-2003	ATCC, Middlesex, UK
FBS	F9665	Sigma-Aldrich, Arklow, Ireland
FBS	ATCC-SCRR-30-2020	ATCC, Middlesex, UK
Hanks Balanced Salt Solution	H6649	Sigma-Aldrich, Arklow, Ireland
IgG-Fc	110-HG-100	R&D, Abingdon, UK
Jagged-1-Fc	599-JG-100	R&D, Abingdon, UK
Luciferase Assay System	E1500	Promega, Madison, WI

Material	Product Code	Company
Mesencult Proliferation Kit with Mesenpure	5512	StemCell Technologies, Cambridge, UK
Mirus TransIT-X2	MIR 6003	MSC, Mulhuddart, Ireland
Mouse Mesenchymal Stem Cells	S1502-01	Gibco/Bio-sciences, Dun Laoghaire
Myh11 Reporter Plasmid	MPRM16957-PG02	GeneCopoeia, Maryland, USA
N2 Supplement	A13707-01	Gibco/Bio-sciences, Dun Laoghaire
Opti-MEM 1 Reduced Serum Media	11058021	Biosciences, Dun Laoghaire, Ireland
Penicillin/streptomycin	P4333	Sigma-Aldrich, Arklow, Ireland
Protein G	21193	MSC, Mulhuddart, Ireland
Rat Mesenchymal Stem Cells	S1601-01	Gibco/Bio-sciences, Dun Laoghaire
Renilla Reporter Plasmid	E2231	Promega, Madison, WI
Retanoic Acid	R2625	Sigma-Aldrich, Arklow, Ireland
rmFGF	3139-FB-025	R&D/Biotechne
SB-216763	S3442	Sigma-Aldrich, Arklow, Ireland
Soybean Trypsin Inhibitor in MEM	10109886001	Roche, Dublin, Ireland
StemPro Osteogenesis Medium	A1007201	Thermo-fisher, Paisley, UK
$\mathrm{TGF}\text{-}\beta_1$	7666-MB-05	R&D, Abingdon, UK

Photonics

Material	Product Code	Company
PDMS	Sylgard 184	Dow Corning, GmbH, Germany
TrypleE Select	12563029	Thermo-fisher, Paisley, UK

Cell Characterisation

Antibodies and Reagents (ICC and Western Blot)

Material	Product Code	Company
anti-beta actin	2228	Sigma-Aldrich, Arklow, Ireland
anti-calponin 1	ab46794	Abcam, Cambridge, UK
anti-CD44	ab24504	Abcam, Cambridge, UK
anti-nestin	ab11306	Abcam, Cambridge, UK
anti-SM-MHC (Myh11)	sc-79079	Santa-Cruz Biotechnology, Heidelberg, Germany
anti-sox10	MAB2864	R&D, Abingdon, UK
APS	A3678	Sigma-Aldrich, Arklow, Ireland
BCA Assay	23225	Thermo Fisher, Paisley, UK
Bis Acrylamide	A3699	Sigma-Aldrich, Arklow, Ireland
BSA	A4503-50g	Sigma-Aldrich, Arklow, Ireland
Collagen Probe	Gift	TCD
DAPI	D9542-5 mg	Sigma-Aldrich, Arklow, Ireland
donkey anti-goat alexafluor488	A-11055	Bio-sciences, Dun Laoghaire, Ireland
Dynamag PCR Magnet	492025	Bio-sciences, Dun Laoghaire, Ireland
goat anti-mouse alexafluor488	A11030	Bio-sciences, Dun Laoghaire, Ireland
goat anti-rabbit alexafluor488	A11008	Bio-sciences, Dun Laoghaire, Ireland
GSK-3β XP®	5676S	Cell Signalling, Leiden, Netherlands
H3K27me3 mAb	9733S	Cell Signalling, Leiden, Netherlands
H3K4me2 mAb	9725S	Cell Signalling, Leiden, Netherlands
Laemlli Buffer	161-0747	Fannin & Co, Dublin, Ireland
MAGnify™ Chromatin Immunoprecipitation System	492024	Bio-sciences, Dun Laoghaire, Ireland
phospho-GSK3β-(ser9)	9336S	Cell Signalling, Leiden, Netherlands

Material	Product Code	Company
Phosstop	4906845001	Roche, Dublin, Ireland
Ponceau S Solution	P7170	Sigma-Aldrich, Arklow, Ireland
Protease Inhibitor Cocktail	P8340	Sigma-Aldrich, Arklow, Ireland
Protein G Dynabeads		Bio-sciences, Dun Laoghaire, Ireland
RIPA Buffer	R0278	Sigma-Aldrich, Arklow, Ireland
SDS	L3771	Sigma-Aldrich, Arklow, Ireland
TEMED	T9281	Sigma-Aldrich, Arklow, Ireland
TMB	T0565	Sigma-Aldrich, Arklow, Ireland
Triton X-100	X-100	Sigma-Aldrich, Arklow, Ireland
Trizma Base	T1503	Sigma-Aldrich, Arklow, Ireland

Real Time q PCR Reagents

Material	Product Code	Company
PrimeTime Calponin1 forward		IDT Technologies, Leuven, Belgium
PrimeTime Calponin1 reverse		IDT Technologies, Leuven, Belgium
PrimeTime Hey1		IDT Technologies, Leuven, Belgium
PrimeTime HeyL		IDT Technologies, Leuven, Belgium
PrimeTime mHPRT Forward		IDT Technologies, Leuven, Belgium
PrimeTime mHPRT Reverse		IDT Technologies, Leuven, Belgium
PrimeTime Myh11 forward		IDT Technologies, Leuven, Belgium
PrimeTime Myh11 reverse		IDT Technologies, Leuven, Belgium
Quantitect Col1A1_1 Primer Assay	QT01055572	Qiagen, Hilden, Germany

Material	Product Code	Company
Quantitect Col1A1_2 Primer Assay	QT02325736	Qiagen, Hilden, Germany
Quantitect Col3A1_1 Primer Assay	QT01055516	Qiagen, Hilden, Germany
Quantitect Col3A1_2 Primer Assay	QT02331301	Qiagen, Hilden, Germany
Quantitect Elastin Primer Assay	QT01070482	Qiagen, Hilden, Germany
Quantitect mHPRT Primer Assay	QT00166768	Qiagen, Hilden, Germany
Reliaprep RNA Miniprep spin columns	Z6012	
Rotor-Gene SYBR® Green RT-PCR Kit	204174	Qiagen, Hilden, Germany
Sensifast SYBR no-rox	Bio-72005	MSC, Mulhuddart, Ireland

Nanoparticle Formulation & Analysis

Material	Product Code	Company
poly(lactic-co-glycolic acid) (PLGA)	P2066	Sigma-Aldrich, Arklow, Ireland
dichloromethane	650463	Sigma-Aldrich, Arklow, Ireland
Iron(II)(III) Oxide in solution	700312	Sigma-Aldrich, Arklow, Ireland
Poly(vinyl)alcohol (PVA)	363138	Sigma-Aldrich, Arklow, Ireland
Supelco Discovery C18 Column	568523-U	Sigma-Aldrich, Arklow, Ireland
Acetonitrile	34851	Sigma-Aldrich, Arklow, Ireland
Dextran Magnet	2501008	Dexter Magnetic Technologies, IL, USA

Appendix B

Supplementary Figure 1

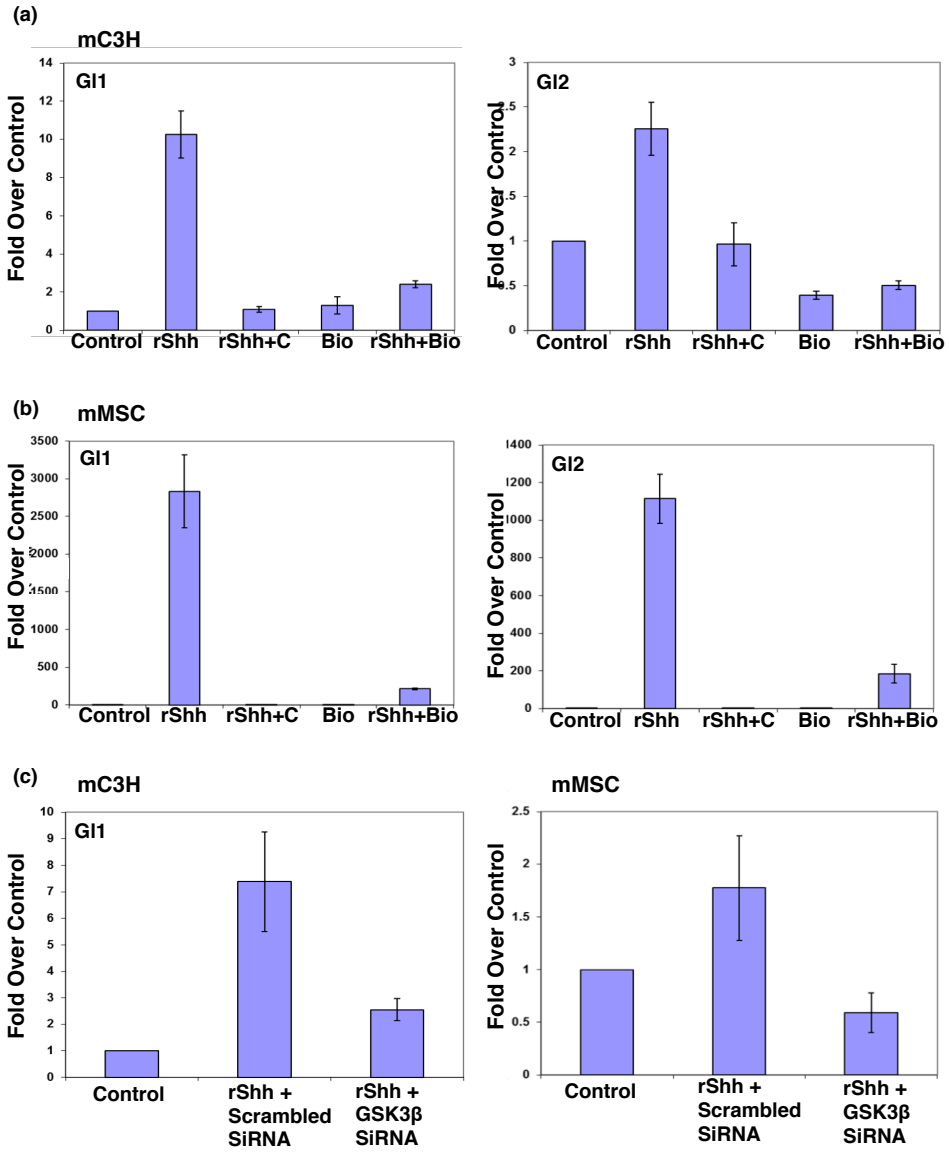

Supplemental Figure 1: Effect of GSK3β inhibitor on hedgehog signalling in stem cells. (a) Representative Gli1 and Gli2 mRNA expression in response to rShh (0.5 µg/ml), rShh + Cycoplamine (15µM) (c), Bio (5µM) alone and rShh+Bio for 24hrs in C3H T10 1/2 cells. (b) Representative Gli1 and Gli2 mRNA expression in response to rShh (0.5 µg/ml), rShh + Cycoplamine (15µM) (c), Bio (5µM) alone and rShh+Bio for 24hrs in mMSCs. (c) Gli1 mRNA expression in mC3H T10 1/2 and mMSCs in response to rShh + scrambled siRNA and rShh + GSK3β siRNA.